https://doi.org/10.15388/vu.thesis.421
https://orcid.org/0000-0002-2343-2821

VILNIUS UNIVERSITY
CENTER FOR PHYSICAL SCIENCES AND TECHNOLOGY

Ričardas Norkus

Terahertz Pulse Excitation Spectroscopy of Semiconductor Materials and Structures

DOCTORAL DISSERTATION

Natural Sciences,
Physics N 002

VILNIUS 2022

This dissertation was written between 2018 and 2022 in Center for Physical sciences and technology. The research was supported by Research Council of Lithuania:
Mobility funding: P-DAK-19-165.
Academic accomplishments: P-DAP-19-144; P-DAP-20-299; P-DAP-21-192.
Doctoral studies were financed from the EU structural funds: 09.3.3-LMT-K-712-01-0032.

Academic supervisor:
Prof. Habil. Dr. Arūnas Krotkus (Center for Physical Sciences and Technology, Natural Sciences, Physics - N 002).

This doctoral dissertation will be defended in a public meeting of the Dissertation Defence Panel:
Chairman –Dr. Gediminas Račiukaitis (Center for Physical Sciences and Technology, Natural Sciences, Physics - N 002).
Members:
Dr. Kęstutis Grigoras (VTT Technical Research Centre of Finland, Natural Sciences, Physics - N 002).
Dr. Irmantas Kašalynas (Center for Physical Sciences and Technology, Natural Sciences, Physics - N 002).
Dr. Tadas Malinauskas (Vilnius University, Natural Sciences, Physics - N 002).
Prof. Habil. Dr. Valdas Sirutkaitis (Vilnius University, Natural Sciences, Physics - N 002).
The dissertation shall be defended at a public meeting of the Dissertation Defence Panel at 3 p.m. on 14th December 2022 in Room D401 of the Center for Physical Sciences and Technology.
Address: Saulėtekio av. 3, D401, Vilnius, Lithuania.
Tel:+37052648884; e-mail: office@ftmc.lt.
The text of this dissertation can be accessed at the libraries of Vilnius University and the Center for Physical Sciences and Technology, as well as on the website of Vilnius University: www.vu.lt/lt/naujienos/ivykiu-kalendorius

https://doi.org/10.15388/vu.thesis.421
https://orcid.org/0000-0002-2343-2821

VILNIAUS UNIVERSITETAS
FIZINIŲ IR TECHNOLOGIJOS MOKSLŲ CENTRAS

Ričardas Norkus

Puslaidininkinių medžiagų ir darinių tyrimas terahercinių impulsų žadinimo spektroskopijos metodu

DAKTARO DISERTACIJA

Gamtos mokslai,
Fizika N 002

VILNIUS 2022

Disertacija rengta 2018– 2022 metais Fizinių ir technologijos mokslų centre.
Mokslinius tyrimus rėmė Lietuvos mokslo taryba:
Parama akademiėms išvykoms: P-DAK-19-165.
Stipendija už akademinius pasiekimus: P-DAP-19-144; P-DAP-20-299; P-DAP-21-192.
Doktorantūra buvo finansuojama ES struktūrinių fondų lėšomis: 09.3.3-LMT-K-712-01-0032.

Mokslinis vadovas:
Prof. habil. dr. Arūnas Krotkus (Fizinių ir technologijos mokslų centras, gamtos mokslai, fizika - N 002).

Gynimo taryba:
Pirmininkas – **dr. Gediminas Račiukaitis** (Fizinių ir technologijos mokslų centras, gamtos mokslai, fizika - N 002).
Nariai:
dr. Kęstutis Grigoras (VTT Suomijos techninių tyrimų centras, gamtos mokslai, fizika - N 002).
dr. Irmantas Kašalynas (Fizinių ir technologijos mokslų centras, gamtos mokslai, fizika - N 002).
dr. Tadas Malinauskas (Vilniaus universitetas, gamtos mokslai, fizika - N 002).
Prof. habil. dr. Valdas Sirutkaitis (Vilniaus universitetas, gamtos mokslai, fizika - N 002).

Disertacija ginama viešame Gynimo tarybos posėdyje 2022 m. Gruodžio mėn. 14 d. 15 val. Fizinių ir technologijos mokslų centro D401 auditorijoje. Adresas: Saulėtekio al. 3 D401 Vilnius, Lietuva, tel. +37052648884; el. paštas office@ftmc.lt.
Disertaciją galima peržiūrėti Vilniaus universiteto ir Fizinių ir technologijos centro bibliotekose ir VU interneto svetainėje adresu: https://www.vu.lt/naujienos/ivykiu-kalendorius

Acknowledgements

Fizinių ir technologijos mokslų centre dirbu jau 6 metus ir per šiuos metus teko susidurti su daugybę žmonių kurie turėjo didesnės ar mažesnės įtakos šio darbo atsiradimui. Norėčiau jiems padėkoti.

Esu dėkingas savo darbo vadovui prof. habil. dr. Arūnui Krotkui už neblėstančia energija, idėjų generavimą bei diskusijas įvairiomis temomis. Taip pat už suteiktą galimybę atlikti tyrimus FTMC ultrasparčios optoelektronikos laboratorijoje.

Taip pat noriu padėkoti kolegai dr. Ignui Nevinskui už pozityvumą ir naudingas diskusijas įvairiomis eksperimentinės metodikos temomis ir ne tik. Taipogi pirmiesiems vadovams dr. Juozui Adamoniui ir dr. Andriui Arlauskui, kurie supažindino su THz impulsų generavimo būdais ir padėjo atlikti pirmuosius eksperimentus. Už naudingas eksperimentines žinias ir mokslines diskusijas noriu padėkoti dr. Andžej Urbanovič ir dr. Ramūnui Adomavičiui.

Dėkoju Optoelektronikos technologijų laboratorijos darbuotojams – dr. Vaidui Pačebutui, dr. Renatai Butkutei ir dr. Jan Devenson už užaugintus bismidų ir bismuto bandinius naudotus atliktuose tyrimuose. Taip pat dr. L. Kulyuk ir jo kolegoms už suteiktus pereinamųjų metalų dichalkogenidų bandinius ir prof. habil. dr. E. Norkui ir jo kolegoms už suteiktus plonus bismuto sluoksnius.

Esu dėkingas prof. dr. V. Karpui ir dr. V.L Malevich už atliktus teorinius skaičiavimus.

Taip pat noriu padėkoti už atliktus darbus charakterizuojant tyrinėtus bandinius kitomis metodikomis: dr. Sandrai Stanionytei ir dr. habil. proc. Remigijui Juškėnui už matavimus Rentgeno spindulių difraktrometru; dr. Andrejui Geižučiui ir dr. Andriui Bičiūnui už Hall‘o matavimus ir dr. Bronislovui Čechavičiui už fotoliuminescencijos matavimus.

Galiausiai noriu padėkoti savo šeimai už palaikymą: tėvams Vaidui ir Indrei, močiutei Adelei, tetai Jūratei ir broliui Nedui.

TABLE OF CONTENTS

1 INTRODUCTION

In recent years THz technology continues to rapidly develop and find applications in various fields of science and industry. One of the applicable techniques – THz time-domain spectroscopy could be used in systems for drugs and explosives detection [1], in a car manufacturing for assuring quality control and resource conservation of exterior painting [2], in the art for heritage conservation [3], as a non – invasive way for cancer detection in the medicine [4], and for the food quality control [5]. Also, such a system can be useful both for quality control of electrical and photonic components [6] as well as in fundamental research of semiconductor properties [7, 8]. Such a plethora of possible applications and proof of concept demonstrations was allowed by the rapid development of THz radiation detection and emission capabilities in previous few decades.

Ultrashort optical pulse, with photon energy higher than the bandgap of the semiconductor, generates photo-excited carriers at the illuminated surface. These carriers are separated by built-in electric field or due to different propagation velocities of holes and electrons towards the bulk of the material. That, in turn, creates a transient photocurrent at the surface, which results in emission of electromagnetic radiation in the THz frequency range. Material properties, the intrinsic surface electric fields, the excess energy of photoexcited carriers and the angle at which exciting pulse impinges the sample determine the efficiency of the THz pulse generation. Such dependencies and estimation of generation mechanisms can be used to determine important properties of the semiconductor band structure. Previously it was shown that using THz pulse excitation spectroscopy (TES) such semiconductor band structure parameters as the direct bandgap [9], subsidiary valley position [8, 9], intrinsic fields on the surface of the material [10] could be evaluated. Mostly, A3B5 semiconductors were investigated and subsidiary valley positions in the conduction band were determined for GaAs [9], InAs [8], InSb [8], InP [OP1], InGaAs [11].

Conduction and valence band offsets at the interface between two materials composing a heterojunction is an important parameter for engineering modern micro- and opto- electronic devices. Such parameters are widely investigated theoretically and experimentally [12]. There are already several established experimental techniques for band offset determination such as quantum well spectroscopy, X-ray photoemission spectroscopy, and ballistic electron emission. In this work, for the first time TES is used to evaluate the band offset of the heterojunction. This is achieved by employing the ballistic nature of carriers excited by

femtosecond laser pulse [13]. Dilute bismides containing heterojunctions – GaAsBi/GaAs and GaInAsBi/InP were investigated. Also, the photoconductive antenna was fabricated from GaInAsBi layer. It emitted THz pulse when excited with 2 μm wavelength optical pulses. Dilute bismides are of high interest lately due to their potential to be used as energy efficient near-infrared devices.

Even though THz pulse emission spectroscopy has been applied for cubic A3B5 semiconductors, there is still a need to investigate other crystal structure materials. Recently layered materials have been widely investigated due to their unique properties when they are of a few layers, their electronic [14] and mechanical properties [15] are superior to their bulk counterparts. Also a transition from indirect gap to direct band gap [16] could be observed. In this work, THz emission spectroscopy was used for investigation of layered Transition Metal Dichalcogenides (TMD) and GaSe crystals.

Ultrathin bismuth layers are of high interest, due to their large Fermi wavelength (~30 nm), the quantum confinement effects in these layers appear quite early [17] that lead to a semimetal – semiconductor transition. Also, theoretical studies predict them to be topological insulators [18]. Therefore, the emission from crystalline polycrystalline ultrathin bismuth layers were investigated in this work.

This work extends previous work performed at CPST on TES methodology development. Techniques versatility is shown by applying measurements to a wide range of materials. TES main advantage is the contactless measurement, with a possibility to directly determine semiconductor band structure parameters.

1.1 Major Goal

To investigate various bandgap and crystal structure semiconductors, and to determine semiconductor heterostructures band offset values using the THz excitation spectroscopy technique.

1.2 Tasks of this Work

- To develop a THz excitation spectroscopy methodology for the determination of energy band offset values in semiconductor heterostructures.

- To determine the conduction band offset of GaAsBi/GaAs and GaInAsBi/InP heterojunctions using the developed THz excitation spectroscopy methodology.
- To investigate indirect bandgap and layered hexagonal crystal structure semiconductors using THz excitation spectroscopy.
- To determine band structure parameters of Transition Metal Dichalcogenides and GaSe crystals.
- To investigate THz generation from ultrathin monoelemental bismuth layers.

1.3 Scientific Novelty

- THz pulse excitation spectroscopy methodology was used for the first time to determine energy band offsets in semiconductor heterojunctions.
- Photoconductive antenna based on GaInAsBi layer grown on InP substrate showed the most efficient THz pulse generation when illuminated by 2 μm wavelength laser pulses.
- Terahertz pulse excitation spectra were used to determine the electron energy band structure of layered materials - GaSe and transition metal chalcogenides ($MoSe_2$, MoS_2, and WSe_2).
- It was shown that germanium crystals can intensively emit THz pulses after being illuminated with femtosecond 1.55 μm laser pulses.
- THz emission from thin electrodeposited polycrystalline bismuth layers was linked to rapid photoelectron thermalisation and the photo-Dember effect.
- The emission of THz pulses observed in thin crystalline layers of bismuth grown by MBE on silicon substrates testified to the semimetal-to-semiconductor transitio.
- Azimuthal angle-dependent THz emission observed in nanometer-thick MBE-grown Bi layers is explained by anisotropic lateral photocurrents.

1.4 Statements of Defense

- The ballistic motion of electrons excited by femtosecond optical pulses in a semiconductor heterostructure results in the distinct changes of the THz pulse excitation spectrum at photon energies corresponding to electron transitions from the valence band of the narrow-band semiconductor to the conduction band of the wide-band semiconductor layers. This allows to determine the energy band line-ups in semiconductor heterostructures directly from THz excitation spectrum.
- The conduction band offset of GaAsBi-GaAs heterojunction has about 45% ± 5% energy gap difference between these materials; while, for another heterojunction containing dilute bismide, GaInAsBi-InP, this value is equal to 34% ± 3 %.
- The THz emission mechanism in thin polycrystalline Bi layers obtained by electrodeposition on noble metal substrates is due to faster electron diffusion from the surface than the hole diffusion – photo-Dember effect. While in crystalline layers grown on Si (111) substrates by molecular beam epitaxy the THz emission is due to lateral photocurrent arising from ballistic propagation of charge carriers.

1.5 Author Contribution

Author was responsible for assembling the experimental setups and most of the measurements of THz pulse emission, azimuthal angle dependence and optical pump – THz probe. He was also involved in discussions, preparation and writing of manuscripts. He presented the results in 16 international and national conferences both in oral and poster format.

The sample growth using MBE and the characterisation were done in the optoelectronics department of the Centre for Physical Sciences and Technology based in Vilnius, while TMD samples were grown in the Institute of Physics of the Moldovan Academy of Sciences in Chisinau.

1.6 Publications

P1. V. Karpus, R. Norkus, R. Butkutė, S. Stanionytė, B. Čechavičius, and A. Krotkus, "THz-excitation spectroscopy technique for band-offset determination" Opt. Express 26, 33807-33817 (2018)

P2. V. Pačebutas, S.Stanionytė, R.Norkus, A.Bičiūnas, A.Urbanowicz and A.Krotkus, „Terahertz pulse emission from GaInAsBi“, J. Appl. Phys. 125, 174507 (2019)

P3. R. Norkus, I. Nevinskas, and A. Krotkus, „Spectral dependencies of terahertz emission from femtosecond laser excited surfaces of germanium crystals“, Journal of Applied Physics 126:22, (2019)

P4. V. Pačebutas, R. Norkus, V. Karpus, A. Geižutis, V. Strazdienė, S. Stanionytė, A. Krotkus „Band-offsets of GaInAsBi–InP heterojunctions“, Infrared Physics and Technology , 109, 103400 (2020)

P5. R. Norkus, I.Nevinskas, A.Krotkus, "Terahertz emission from a bulk GaSe crystal excited by above bandgap photons", J. Appl. Phys. 128, 225701 (2020);

P6. I. Nevinskas, R. Norkus, A. Geižutis, L. Kulyuk, A. Miku, K. Sushkevich and A. Krotkus, „Terahertz pulse emission from photoexcited bulk crystals of transition metal dichalcogenides“ J. Phys. D: Appl. Phys. 54 115105 (2020)

P7. I. Nevinskas; Z. Mockus; R. Juškėnas; R. Norkus; A. Selskis , E. Norkus; A. Krotkus “Terahertz Photoconductivity Spectra of Electrodeposited Thin Bi Films”, Materials, 14, 3150. (2021)

P8. V.L Malevich, P.A. Ziaziulia; R. Norkus; V. Pačebutas, I. Nevinskas; A. Krotkus, “Terahertz Pulse Emission from Semiconductor Heterostructures Caused by Ballistic Photocurrents”, Sensors, 21, 4067. (2021)

P9. J. Devenson, R. Norkus, R. Juškėnas, A. Krotkus, "Terahertz emission from ultrathin bismuth layers," Optic Letters 46, 3681-3684 (2021)

1.7 Other Publications

OP1.R. Norkus, A. Arlauskas and A. Krotkus, „Terahertz excitation spectra of InP single crystals“, Semicond. Sci. Technol. 33 07501 (2018).

OP2.V. Pačebutas, S. Stanionytė, A. Arlauskas, R. Norkus, R. Butkutė, A. Geižutis, B.Čechavičius, A. Krotkus, „Terahertz excitation spectra of GaAsBi alloys“ Journal of Physics D: Applied Physics 51, 474001 (2018)

OP3.Ričardas Norkus, Ramūnas Aleksiejūnas, Arūnas Kadys, Marek Kolenda, Gintautas Tamulaitis and Arūnas Krotkus , „Spectral

dependence of THz emission from InN and InGaN layers“, Scientific Reports , 9, 7077 (2019)

1.8 Conferences

C1. R.Norkus, Puslaidininkių juostinės struktūros charakterizavimas naudojant Terahercų emisijos spektroskopiją, --8-oji doktorantų ir jaunųjų mokslininkų konferencija, Vilnius, Lithuania 2018-10-17 - 18, (oral presentation)

C2. Ričardas Norkus, Sandra Stanionytė, Bronislovas Čechavičius, Renata Butkutė, Vytautas Karpus, Arūnas Krotkus, GaAs1-x Bix/GaAs heterosandūros laidumo juostos trūkio nustatymas terahercų emisijos spektroskopijos metodu, 9-oji Jaunųjų mokslininkų konferencija „Fizinių ir technologijos mokslų tarpdalykiniai tyrimai“. Vilnius, Lietuva 2019-03-12, (oral presentation)

C3. Ričardas Norkus, Sandra Stanionytė, Bronislovas Čechavičius , Renata Butkutė, Vytautas Karpus, Arūnas Krotkus „THz-excitation spectroscopy technique for band-offset determination“, 62nd international conference for students of physics and natural sciences open readings 2019, March 19-22, Vilnius, Lietuva (oral presentation)

C4. R. Norkus, V. Karpus, B. Čechavičius, S. Stanionytė, R. Butkutė, A. Krotkus, „Terahertz excitation spectroscopy for semiconductor band structure characterization“, The IV edition of TERAMETANANO, the International Conference on Terahertz Emission, Metamaterials and Nanophotonics (TERAMETANANO-4), 2019, May 27-31, Lecce, Italy (poster presentation)

C5. R.Norkus, I.Nevinskas, A.Krotkus „THz pulse emission from germanium crystals“, Advanced Materials and Technologies 2019, Palanga, Lithuania 2019 August 19-23. (poster presentation (best poster presentation award)).

C6. Ričardas Norkus; Sandra Stanionytė; Andzej Urbanowicz; Andrius Bičiūnas; Vaidas Pačebutas; Arūnas Krotkus, „Terahertz Pulse Emission From GaInAsBi“, 44th International Conference on Infrared, Millimeter, and Terahertz Waves (IRMMW-THz 2019), Paris, France, 1-6 September 2019 (poster presentation)

C7. Ričardas Norkus, Ignas Nevinskas, Arūnas Krotkus, „Spektrinės terahercinių impulsų emisijos priklausomybės iš germanio kristalų“, 43-

oji nacionalinė fizikos konferencija, Kaunas, Lithuania, 3-5 October 2019. (poster presentation)

C8. Ričardas Norkus, Ignas Nevinskas, Arūnas Krotkus „THz impulsų generacijos iš germanio kristalų paviršiaus tyrimas“ , 9-oji doktorantų ir jaunųjų mokslininkų konferencija FizTeCh2019, Vilnius, Lietuva, 23-24 Spalio 2019 (oral presentation)

C9. R. Norkus, A. Krotkus, I. Nevinskas, V. Pacebutas, V. Karpus „THz - excitation spectroscopy of photoexcited semiconductor surfaces and hetero-interfaces“, 9th International Workshop on Terahertz Technology and Applications, Kaiserslautern, Germany, 3-5 March 2020. (poster presentation).

C10. Ričardas Norkus, Ignas Nevinskas, Arūnas Krotkus, „Terahertz emission from a bulk GaSe crystal excited by above-bandgap photons“, Advanced Properties and Processes in Optoelectronic Materials and Systems - APROPOS-17, Vilnius, Lithuania, 30 September – 1 October 2020.(oral presentation).

C11. Ričardas Norkus, Ignas Nevinskas, Vaidas Pačebutas, Sandra Stanionytė, Vytautas Karpus, Arūnas Krotkus, „Terahercinės spinduliuotės žadinimo spektroskopija“ , 10-oji doktorantų ir jaunųjų mokslininkų konferencija FizTeCh2020, Vilnius, Lietuva, 22-23 Spalio 2020 (oral presentation)

C12. Ričardas Norkus, Jan Devenson, Remigijus Juškėnas, Arūnas Krotkus, „Terahertz Emission From Ultrathin Bismuth Layers“, 64th International Conference For Students Of Physics And Natural Sciences Open readings 2021, Vilnius, Lietuva, Kovo 16-19 d. 2021 (oral presentation)

C13. Ričardas Norkus, Ignas Nevinskas, Arūnas Krotkus, „THz Excitation Spectroscopy of the Layered Semiconductor Crystals“, „Advanced Materials And Technologies 2021“ 23-rd International Conference – School, Palanga, Lithuania, 23 – 27 August, 2021 (poster presentation)

C14. Ričardas Norkus, Ignas Nevinskas, Arūnas Krotkus, „THz Excitation Spectroscopy of the Layered Semiconductor Crystals“, „The 46th International Conference on Infrared, Millimeter and Terahertz Waves (IRMMW-THZ 2021)“ , Chengdu, China, Aug 29 - Sep 3, 2021 (online) (oral presentation)

C15. Ričardas Norkus, Vitaly Leonidovich Malevich , Pavel Aliaksandravich Ziaziulia, Vaidas Pačebutas, Ignas Nevinskas ir Arūnas Krotkus,

„Balistinių fotosrovių sukelta terahercinių impulsų emisija iš puslaidininkinių heterosandūrų“, 44-oji Lietuvos nacionalinė fizikos konferencija, Vilnius, Lithuania 6-8 october, 2021(oral presentation)

C16. Ričardas Norkus, Vitaly Leonidovich Malevich , Pavel Aliaksandravich Ziaziulia, Vaidas Pačebutas, Ignas Nevinskas ir Arūnas Krotkus, „THz impulsų emisijos spektroskopija“, FizTeCh 2021 - 11-toji doktorantų ir jaunųjų mokslininkų konferencija, Vilnius, Lithuania 20-21 October 2021(oral presentation)

2 LITERATURE OVERVIEW

2.1 THz frequency range: technology and its applications

The terahertz (THz) electromagnetic wave region is typically defined by a range from 0.1 THz up to 10 THz [19]. This denotation is common in electronics, while the wavelength and photon energy are common in the optical region. In the latter, the THz region is defined by the wavelengths ranging from 3 mm to 30 μm or photon energies from 0.4 meV to 41 meV.

The THz spectral region lies between microwave and infrared (Fig. 2.1). Previously, this region was referred to as the submillimetre or far-infrared electromagnetic waves as well as the “THz gap” [20] due to low brightness of available THz emitters and limited sensitivity of the detectors, strong atmospheric absorption [21], and because of fundamental problems arising when coming from the electronic and photonic sides of the spectra. In the first case, this limit was originates from the relatively low speed of the electronic components and a rapid attenuation of the signal at higher frequencies. The use of photonic approaches impairs by the scarcity of materials in which the electron population inversion could be possible, because the photon energy of a large part of the THz region is lower than thermal energy of 25 meV at room temperature (293 K).

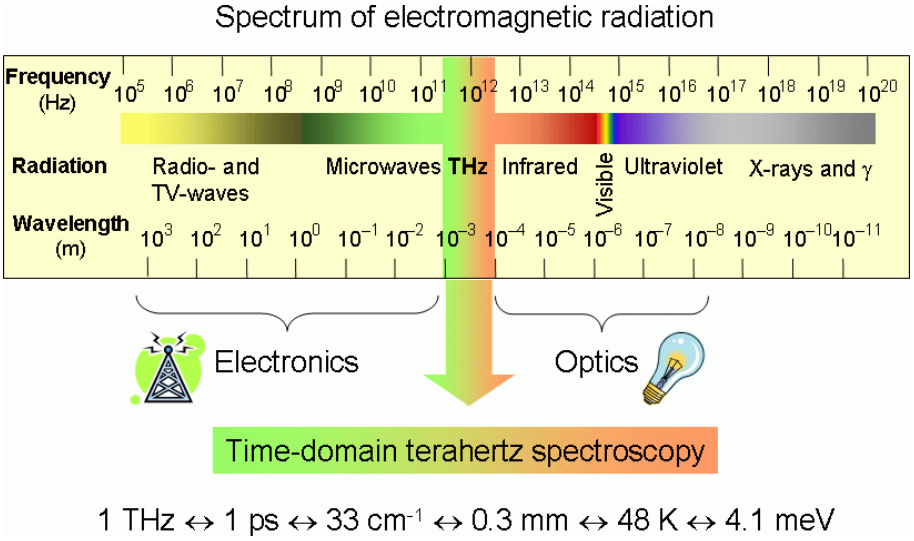

Fig. 2.1 Electromagnetic spectrum and THz region. Adapted from [22]

The photonics side offers several high power THz lasers as a source. The THz quantum cascade laser (QCL) [23] contains several quantum wells

coupled into a superlattice where certain levels are created in the conduction band and are structured in such a way that an electron undergoes several lasing transitions by emitting THz photons multiple times while passing through a device [24]. Such a device was shown to operate in the 1 - 5 THz range with power in the range of tens of mW; it has narrow bandwidth while working in pulsed or CW regimes. Cryogenic temperatures are required, but the devices' operation temperature is rapidly increasing with the latest research showing a maximum operating temperature of 250 K [25]. The main advantages of QCLs would be their portability and relatively high output power. Another solid-state device – the p-Ge laser [26] also demonstrated a high output power and tunable THz wavelength [27]. In this device, the population inversion is achieved between the light and the heavy hole valence bands or due to the Landau splitting of the light hole band in crossed or parallel magnetic and electric fields [28]. This source allows to tune of the THz frequency from 1 THz to 4 THz, its achievable power can reach several watts, but the operating temperature is below 40 K. Photonic instrumentation also employs non-linear optical effect - optical rectification [29], in this case, lower power, but extremely broadband THz pulses can be achieved. While employing difference frequency generation together with an infrared range QCL, in such a way monolithic emitter is demonstrated [30].

The electronic THz equipment uses high-speed transistors and diodes as well as mixers for frequency up-conversion. GaAs Schottky diodes are used for detection and generation of THz radiation, state of the art devices achieve frequencies up to 3 THz [31]. The average power of the silicon-based emitters increased substantially and the range is starting to extend beyond 1 THz [32]. In recent years silicon-based integrated technology systems achieved output power reaching up to 100 μW at 1 THz [33]. Meanwhile, the THz signal detection is achieved using electronic components such as bolometers, Golay cells, and pyroelectric diodes[19].

Rapid development both in the electronics and photonics field, as well as novel optoelectronic methods appearing in the 1980s, started to fill the THz gap quite rapidly. The number of scientific publications with the term "Terahertz" had exponential growth in the following decades [34]. The main catalysts for such a rapid development were the introduction of ultrashort lasers in the laboratories across the globe. The methods of generation and detection of THz radiation based on such lasers were found to have a great potential for numerous applications: security [35]; quality control of integrated circuits [36], non-destructive testing of biological macromolecules [37], as well as in medical imaging and diagnostics [38]. A higher than in the

case of radio waves frequency opens up the possibility for faster next-generation communications [39].

It is also worth mentioning numerous physical characteristics of semiconductors that can be determined when using pulsed THz measurements. For example, electrical conductivity measurement in nanowires using classical Hall-effect is not efficient due to the need for contacts. A noncontact alternative could be offered by THz conductivity spectroscopy [40]. Another powerful tool to investigate dynamical parameters of semiconductors is time-resolved THz spectroscopy (TRTS) [41]. Parameters such as charge carrier lifetimes, their mobilities, dopant concentrations, and surface recombination velocities can be measured with high accuracy [42]. *E.g.*, TRTS was used to characterize the onset of Coulomb screening and plasmon scattering after photogeneration of electron-hole plasma in GaAs on a 10–100 fs time scale [43].

Overall, even with recent advances in THz field the research to improve sources, detectors and components is ongoing.

2.2 THz time-domain spectroscopy

In the 1970s, when the first ultrafast laser systems became available, the optical pulses were three orders of magnitude shorter than the electrical pulses generated by traditional electronic equipment. So developing a system that could use optical pulses for the gating of electrical signals became an important issue. Such a system was proposed in D.H. Auston's [44] pioneering work. In this work, electrical pulses with picosecond rise times were generated in a silicon-based transmission-line structure with a gap illuminated by the second-harmonics of a few ps duration Nd:glass laser pulse. Short electrical pulse switch-off times were achieved by short-circuiting the transmission line using the first harmonic laser pulses. Such an approach became to be known as the Auston switch. The main issues for getting shorter electrical pulses with Auston switches were the long carrier lifetime in silicon and strong dispersion inside the transmission line. A similar method was used in a system where THz pulse was radiated directly into the free space and shorter carrier lifetimes in ion-implanted silicon on the sapphire substrate were used [45]. In this case, dipole antennas were used to generate and detect the electromagnetic radiation. In such experiments sub-ps electrical pulses propagating in the air with almost 2 THz bandwidth were demonstrated [46]. This experiment had limitations since the width of the dipole antenna was around 10 μm - much shorter than the THz wavelength and huge diffraction losses, which resulted in free space

propagation of only a few mm, appeared. A competing group led by D. Grischkowsky used hemispheric sapphire lens and parabolic mirrors to reduce the diffraction losses [47]. In their experiment, 1 m propagation without THz pulse distortion was shown. Later on, an extensive research work was performed on the improvement of the photoconductive material, and with the advancement of 800 nm wavelength lasers, a low temperature grown GaAs was developed [48]. At a similar time, an electro-optical sampling THz system [49] was developed that used non–linear optical effects to generate THz pulses.

THz time-domain-spectroscopy (TDS) is a coherent detection method where both amplitude and phase of the broadband THz pulse are measured. The scheme of such a method is shown in Fig 2.2. Here a femtosecond laser's beam is split into two branches: for illuminating emitter and detector. THz pulse generated in the PCA may pass through the sample and a single data point of THz electric field amplitude is measured. Using a delay line THz pulse is probed by the laser pulse at equally differing time intervals. Measurement is done in the time domain, but, by applying the fast Fourier transform, the spectra of the electrical pulses can also be obtained.

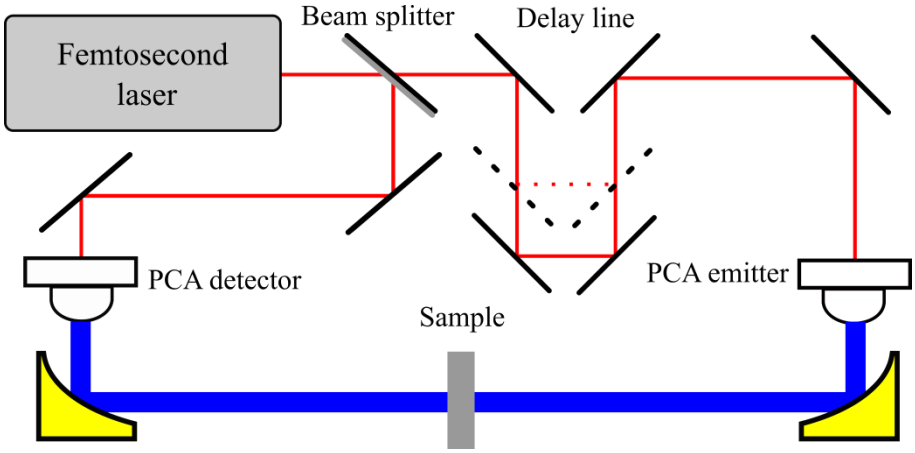

Fig. 2.2 Principle scheme of THz time-domain spectroscopy setup

PCAs do not require high optical pulse energy. The main requirements for semiconductors, from which the antennas are fabricated, are a short carrier lifetime, a high dark resistivity, and a large electrical breakdown field. At present, several materials are having optimal physical characteristics for a successful operation in TDS systems operating at important (due to commercial laser availability) laser wavelengths: ~800 nm

LT–GaAs, ~1000 nm GaAsBi [50], ~1550 nm Rh or Fe doped InGaAs [51, 52].

Another way of generating broadband THz pulse is based on the optical rectification effect in a non-linear medium. Similarly, THz detection is possible via the Pockels effect in such a medium. In the Pockels effect, the electric field of THz pulse induces birefringence in a non-linear optical crystal proportional to the electric field amplitude. Change of polarisation is measured afterward using a couple of photodiodes. With such a method a complete THz electric field characterisation can be achieved by applying the transfer function method [53]. Non-linear optical TDS systems require higher optical pulse energy. The main parameters for nonlinear optical material are an optical nonlinearity coefficient, phonon absorption frequencies, and a walk-off thickness determined by the difference between optical and THz beam group velocities inside the material.

Optical nonlinearity leading to the THz pulse emission and detection can be also obtained when using high-power femtosecond laser pulses in air and other gases via their breakdown and the plasma creation [54]. Such a method has several advantages over solid-state media, the most important of which is the absence of phonon absorption. The only limiting emitted frequency factor, in this case, is the optical pulse width.

2.3 THz pulse emission from semiconductor surfaces

THz pulse emission from semiconductor surfaces illuminated by a femtosecond laser beam was at first shown by X.C. Zhang et al. [55]. Since then a lot of research was done on identifying THz emission mechanisms responsible for this effect [10], as well as its manifestations in other substances, e.g., metals [56], liquids [57], gases [58]. Photoexcited semiconductor emits broadband THz electromagnetic pulse with frequencies ranging up to several THz. Such an effect is common for almost any photo-excited semiconductor, differing mainly by the generated pulse magnitude.

In the majority of cases, the THz pulse emission from illuminated surfaces is due to the accelerated charged particle propagation, leading to electromagnetic radiation. The underlying microscopic explanation of this phenomenon is clearly explained in the book by Longair [59]. A final derived equation for an electric field created by accelerated carriers in spherical coordinates is given there as:

$$E_\theta = \frac{q|a|sin\theta}{4\pi\varepsilon_0 c^2 r}, \quad (1)$$

where q – charge of the carrier, E_θ – tangential component of the electric field, a – acceleration of the charge carrier, r - the radial distance from the carrier, ε_0 – electric permittivity of free space, c – speed of light, θ – angle with respect to acceleration vector direction.

Main properties of the radiation of an accelerated charged particle:

- Stronger acceleration creates stronger electric field/pulse.
- The polar diagram of the radiation is of dipolar form, so electric field strength varies as sin θ and the power radiated per solid unit angle varies as $\sin^2 \theta$. From Fig 2.3 (a) there is no radiation along the acceleration vector and the field strength is greatest at a right angle to the vector.
- The radiation is polarised, the electric field vector in a far field is parallel to the direction of the acceleration vector of a charged particle.

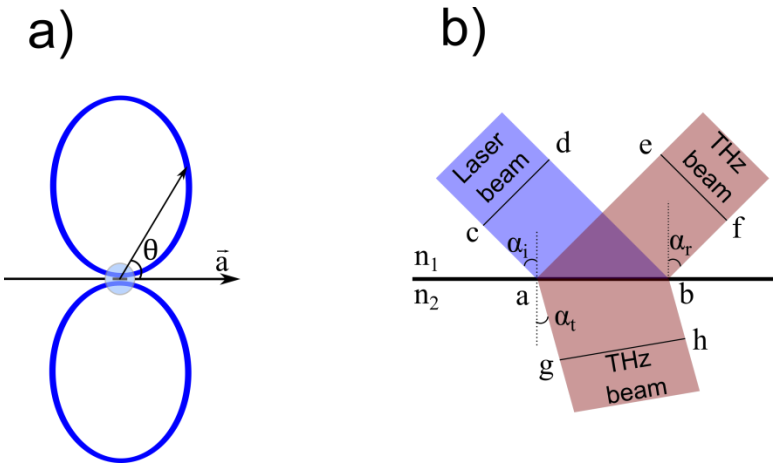

Fig. 2.3 a) Radiated dipole of accelerated charged carrier, b) THz radiation propagation when exciting with optical pulse, when illuminate diameter is higher than THz wavelength

The main mechanisms of THz radiation from semiconductor surfaces can be separated into two broad categories: induced transient photo-current or non-linear optical effects. Their microscopic origin is similar. In the first case, the semiconductor is resonantly excited and source of THz electromagnetic wave will be the accelerated or decelerated free carriers and transient current j induced by them. In the second case, electrons inside the atom will be oscillating (will have an acceleration) creating THz radiation in

such a way, which will depend on nonlinear polarisation P. Therefore, the equation (1) could be expressed in a different form [60]:

$$E_{THz} = -\frac{S}{\varepsilon_0 c^2 r}\int_0^{\infty}\left(\frac{\partial j}{\partial t}+\frac{\partial^2 P}{\partial t^2}\right)dz, \qquad (2)$$

where S is the area of laser excited spot on the semiconductor surface, z – the distance from the surface, ε – vacuum dielectric permittivity. Relation (2) is applicable when the diameter of the illuminated spot is smaller than the wavelength of the emitted THz radiation. If it is not the case and photoexcited area is larger, radiation direction will be governed by interference between dipoles radiating from separate surface elements. Radiation direction will be governed by interference between dipoles radiating from separate surface elements when the diameter of the illuminated spot is bigger than the wavelength of the emitted THz radiation. Because of this, THz radiation will propagate mostly along a specific direction.

In the majority of experiments, THz generation is achieved when illuminating the semiconductor surface at an oblique angle (Fig 2.3b). It can be seen that the laser beam's front edge reaches the semiconductor at different moments, where at point *a* it arrives earlier than at point *b*. Constructive interference will be created when at the wave-front *e-f* optical paths *c-a-e* and *d-b-f* are equal. Otherwise, destructive interference will occur or the intensity of the radiation will be much smaller in all other directions. Optical paths *c-a-e* and *d-b-f* are equal when a relation:

$$n_1^{opt}\sin\alpha_i = n_1^{THz}\sin\alpha_r, \qquad (3)$$

is satisfied, here α_i, α_r – angle of incidence and reflection respectively, n_1^{opt} and n_1^{THz} – refractive index of the first medium for optical and THz radiation. When the medium is air or vacuum, which is usually the case $n_i^{opt} \approx n_r^{THz} \approx 1$, then $\alpha_i = \alpha_r$. The THz beam is emitted in the same direction as the laser beam would be reflected. Similarly, one can derive the propagation angle in the transmission direction. Here optical paths *c-a-g* and *d-b-h* have to be equal, and the THz beam in this direction will be refracted according to Snell's law:

$$n_1^{opt}\sin\alpha_i = n_2^{THz}\sin\alpha_t, \qquad (4)$$

here n_2^{THz}- THz radiation refractive index in the second material, α_t – the angle of refraction of transmitted THz beam. Since in the second material (semiconductor) the refractive index for THz and optical regions might be different, propagation direction could differ as well.

If the spot diameter is smaller than THz wavelength, emission will be as a point source. Experimental example of this was shown in [61]. Here semiconductor was excited at a 30 ° angle, while detector was rotated around the sample in reflection geometry. The photoexcited spot diameter was changed from 30 μm to ~300 μm. It was shown that a wider beam results in a more directional emission from the surface, while a more focused beam acted as a point source and radiated at a wider angle.

The described THz emission mechanism due to dynamic electric dipoles created by the surface photocurrent occurs in two main cases: photocurrent surge in the built-in surface electric field and the electron and hole spatial separation due to their different movement from the photoexcited surface (o called photo-Dember effect. These mechanisms will be briefly characterized below.

Different densities of lattice defects and/or impurity states in the semiconductor volume and on its surface cause the bending of the electron energy bands. This results in an electric field near the surface of many semiconductors, which is stronger when the energy bandgap of the material is larger. The electrons and holes created by the femtosecond optical pulse at the surface will cause a rapidly changing surge of the photocurrent and in turn create an electromagnetic radiation of THz frequency. This process is illustrated in Fig. 2.4. The built-in surface electric field directions are usually opposite to each other for p and n doped samples, so are also the polarities of the emitted THz transients.

Comparison of the polarity of THz pulses emitted from the surfaces of crystals of a certain semiconductor with different conductivity types is the most important feature to identify the mechanism of photocurrent surge [10]. This mechanism was shown to prevail in InP [62] and GaAs [63]. Recently THz generation due to surface electric field was shown to be dominant mechanism in solution-processed metal halide perovskites [64].

The built-in electric fields at the semiconductor surfaces could also appear due to the piezoelectric effect [65], or due to intentionally created differently doped layer structures such as p-i-n [66]. THz field amplitude will depend on such material parameters like the carrier mobility, electric field strength, depletion region width and absorption depth.

A fast surge of photocurrent at the illuminated surface of a semiconductor can occur even when there is no energy band bending at the surface. This may be due to different mobilities and diffusion coefficients of the light-excited electrons and holes. Electrons are usually more mobile than holes and will diffuse into the semiconductor volume faster, leaving less mobile holes at the surface (Fig 2.4). In this way, a rapidly changing electric dipole

directed in a direction perpendicular to the surface of the semiconductor will appear and a pulse of THz radiation will be emitted. By analogy with the known phenomenon, when electric field formation was observed at the surface of a semiconductor illuminated by continuous wave (CW) radiation, this mechanism of THz radiation generation was called the photo-Dember effect [67, 68]. The authors of these works [67, 68] explained their experimental results for narrow-gap semiconductor tellurium.

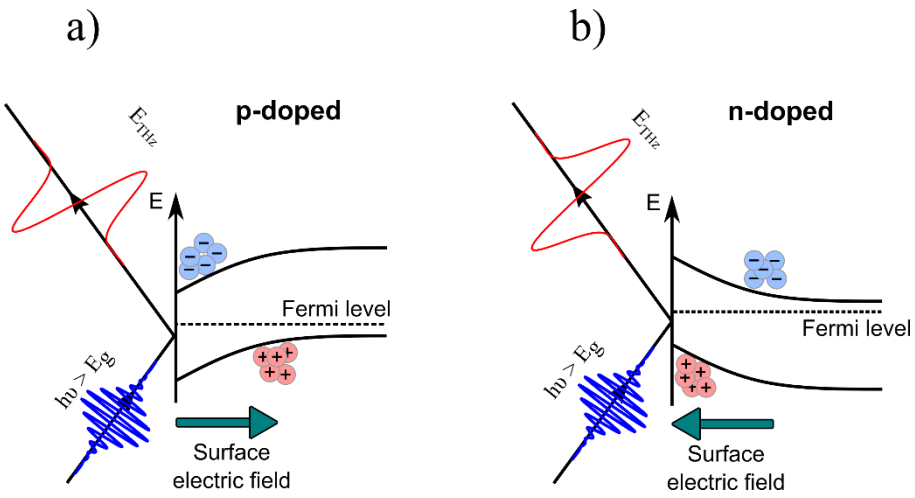

Fig. 2.4 Band bending of p (a) and n (b) doped semiconductors

Photo-Dember field is created parallel to the surface normal. It is not optimal for efficient outcoupling of THz radiation from the material. Oblique photo excitation angle is required to detect emitted THz pulse. There is a method used where lateral photo-Dember currents are created [69]. For this, array of gold stripes is deposited on the surface of semiconductor. When optical pulse excites the material, carriers will be excited only at the gaps between metal. Gradient of excited photocariers parallel to the surface will be created. This will create lateral photocurrent and outcoupling of the THz radiation will be very efficient. In some works efficiency was comparable to a PCA antenna [70]. Another way of enhancing THz outcoupling from semiconductor surface would be due to external magnetic field [71]. Here charged carriers will change their propagation direction due to Lorenz force. Effective radiating dipole will be rotated depending on strength of magnetic field [72] to outcouple THz radiation more efficiently.

Since excess electron energy and electron mobility is one of the most important parameters. The narrow gap semiconductors like InSb (E_g = 0.17 eV) and InAs (E_g= 0.36 eV) has high potential to be a great surface

emitter and the latter is shown to be the best surface emitter for the most common femtosecond laser wavelengths [73]. It is important to note that even though InSb has superior electron mobility and higher excess energy at 800 nm and 1000 nm wavelength excitation THz emission is worse than in InAs [74]. That is because electrons are scattered into higher satellite conduction band valley (~0.53 eV [8]). Timeframe of this effect is comparable to transient current formation time [75]. Generation from InSb and InAs are commonly attributed to photo-Dember effect [76, 77]. Also, it has to be noted that most of the time several mechanism are at play and depending on material properties and excitation conditions dominant mechanism can be different [62]. Temperature dependence in SI-InP showed a THz pulse reversal which was attributed to change of main emission mechanism from diffusion to drift current.

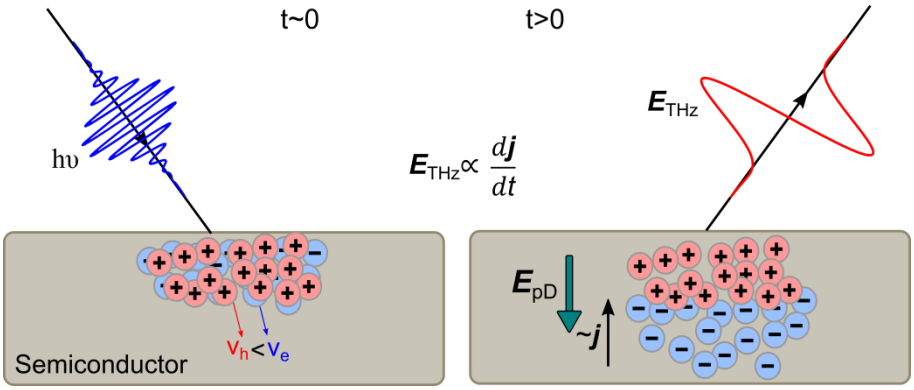

Fig. 2.5 Principle scheme of photo-Dember created electric field and THz generation.

Investigation of THz emission from such materials as InAs [77], InSb[74], GaAs[78], InP[10] also shows a azimuthal angle dependence. This is a THz pulse amplitude dependence on crystallographic surface plane while rotating around the semiconductor surface normal. Non-linear optical effects are commonly used to account for it. We depict polarisation ($\vec{P}$) of the material as dipole moment per unit volume. It's dependence on optical field ($\boldsymbol{E}$) strength [79]:

$$\boldsymbol{P}(t) = \varepsilon_0\left(\chi^{(1)}\boldsymbol{E}(t) + \chi^{(2)}\boldsymbol{E}^2(t) + \chi^{(3)}\boldsymbol{E}^3(t) + \cdots\right) = \varepsilon_0\chi^{(1)}\boldsymbol{E}(t) + \boldsymbol{P}_{\mathrm{NL}}(t), \quad (5)$$

where $\chi^{(1)}$, $\chi^{(2)}$, $\chi^{(3)}$ are the first-, second- and third-order electric susceptibility tensors respectively, ε_0 – dielectric permittivity, $\boldsymbol{P}_{\mathrm{NL}}(t)$ – non-

linear polarisation. It can be seen that non-linear polarisation would start to take effect at higher intensities of electric field. Lowest order non-linearity will depend on $\chi^{(2)}$ for non-centrosymmetric (without point inversion) crystals and will have anisotropic dependence on crystallographic orientation of the crystal. Optical rectification (OR) is one of the processes, where constant voltage appears when optical beam is propagating through crystal [80]. When an optical pulse is propagating electromagnetic pulses with lower frequency could be created.

First to suggest OR as a mechanism from semiconductor surfaces to explain azimuthal angle dependence was Zhang et al [78]. THz radiation in (111)-cut GaAs was measured in transmission geometry where under normal optical incidence THz signal had $\sin 3\varphi$ azimuthal dependence, which could not be explained by photocurrent effects. Also THz pulse phase reversal occurred near GaAs bandgap energy. It was explained by dispersion relation of the nonlinear susceptibility. Theoretical calculations by Khurgin [81] show that the OR susceptibility coefficients rapidly increase when quanta energy of the optical pulse becomes larger than the bandgap.

Since electric field at the surface can break inversion symmetry and contribute to the OR as well. In such a case second order non-linear susceptibility can be expressed in different form [82]:

$$\chi_{ijk}^{(2)eff} = \chi_{ijk}^{(2)bulk} + \chi_{ijkz}^{(3)} E_z^{surf}, \qquad (6)$$

here $\chi_{ijk}^{(2)eff}$ – effective second-order susceptibility, $\chi_{ijk}^{(2)bulk}$ – second-order susceptibility tensor determined by the symmetry properties of the bulk material, $\chi_{ijkz}^{(3)}$ – third-order susceptibility tensor that specifies the symmetry properties of radiation from the near-surface region, E_z^{surf} - surface electric field.

First to suggest electric field induced optical rectification effect (EFIOR) was Chuang et al [83]. It was explained that excitation will be non-vertical in real space, because of the spatial separation of final electron and hole states. Such a spatial separation would lead to instantaneous polarisation and its second order derivative in time would determine radiated THz signal. It was also shown that $\chi_{ijkz}^{(3)}$ coefficient value would increase at resonant excitation.

Also it is convenient to explain OR in the materials with no inversion symmetry. In such a way azimuthal angle dependence of THz radiation from germanium, a centrosymmetric crystal, was explained by EFIOR effect [84].

To distinguish the closely related OR and EFIOR effects responsible for generation from semiconductor surfaces Reid et al [82] calculated THz

emission azimuthal dependences for several crystallographic orientations of zinc-blende crystals (Table 1). From the table 1 it is clear that for (111) surface plane azimuthal angle dependence will be the same for both effects. However investigating (110) and (100) cut crystal planes will have a difference from which it is possible to distinguish between both effects. By these dependences main mechanism responsible for generation from InAs was EFIOR while OR was attributed for InSb [85].

As with photocurrent effects, both mechanisms can be responsible for THz pulse generation at the same time. By investigating (112) – cut InSb crystal azimuthal angle dependences had a more complicated dependences due to contribution from both OR and EFIOR mechanisms [86].

Table 1. Dependences of THz pulse amplitude of two polarisations radiated due to nonlinear optical effects from different planes of zinc-blende crystals, when excited with p polarised light. Coefficients A and B are azimuthal angle independent.

	E_s^{OR}	E_p^{OR}	E_s^{EFIOR}	E_p^{EFIOR}
(100)	$B\sin(2\varphi)$	$B\cos(2\varphi)$	0	A
(110)	$B(\cos(\varphi)+\cos(3\varphi))$	$B(\sin(\varphi)+\sin(3\varphi))$	$B\sin(2\varphi)$	$A+B\cos(2\varphi)$
(111)	$B\sin(3\varphi)$	$A(B-\cos(3\varphi))$	$B\sin(3\varphi)$	$A-B\cos(3\varphi)$

The alternative explanation of azimuthal angle dependences of THz emission from semiconductors is an anisotropic photocurrent originating from the optical alignment of photoexcited electron momentum and the anisotropy of the conduction band isoenergetic surfaces at elevated electron excess energy. Such a model recently was proposed by V.L Malevich et al [13, 87].

The optical momentum alignment effect in A3B5 crystals will result from the optical selection rules of direct optical transitions. Such an effect was reported by Zemskii et al [88]. Polarized photoluminescence is observed under GaAs photons with energies close to the energy bandgap of the material. Since absorption is opposite effect it will have similar dependence when a semiconductor will be excited with linearly polarised light, carriers will have an anisotropic momentum distribution due to optical alignment

(Fig 2.6 red and blue arrows). The function of photoexcited electron distribution[89]:

$$G(\vartheta) = 1 + \eta P_2(\cos\vartheta), \qquad (7)$$

here η – parameter equal to -1 or 1 for an electron excitation from heavy - or light- hole branch excitation, $P_2(x)$ – the second Legendre polynomial, ϑ – is the angle between the electromagnetic wave electric vector direction and electron momentum. Excitation from heavy hole band will distribute photo-carrier momentum perpendicular (Fig2.6 red) to optical wave electric vector (E_p), [90]. While excitation from the light hole band will be aligned with the direction of E_p (Fig 2.6 blue). Electrons from the heavy hole band will play a key role because the density of states for the heavy hole branch is around 3 times larger than light hole band. The optical alignment effect with stationary excitation requires cryogenic temperatures, because carrier momentum relaxation time is short, of the order of a few ps. However, since the photocurrent responsible for THz emission reaches peak value in a comparable timeframe, the optical alignment effect will be significant even at room temperatures and will be able to cause anisotropy of a photocurrent.

THz pulse generation process is of sub-ps timeframe. This timeframe is shorter than the relaxation time of the electrons and is comparable to scattering time by phonons. Because of that the electrons will move in ballistic or velocity overshoot mode in the direction set by the initial optical alignment. Photo-carrier velocity will be close to the group velocity at the excess energy in the conduction band to which the electron was excited. When electrons are excited with low excess energy just above semiconductor bandgap, the built-in surface field would play an important role. From Fig. 2.6 the electric field (**F**) would start to accelerate electrons moving to the surface and ones moving to the bulk would be slowed down. In such a way perpendicular to the surface photocurrent would arise. A similar explanation could be given for excitation with higher excess energies. Electrons directed towards bulk would move much farther away, while the carriers directed at the surface would be scattered. That would create an electric field directed towards the bulk and eventually transient photocurrent when the field would start to deaccelerate photocarriers Such an explanation is an alternative to the classic photo-Dember effect which depends on difference in mobillity of the photo-carriers. Ballistic propagation is a fast process (carrier relaxation of < 1ps timeframe) and stationary values of mobility and diffusion coefficient would not be established yet.

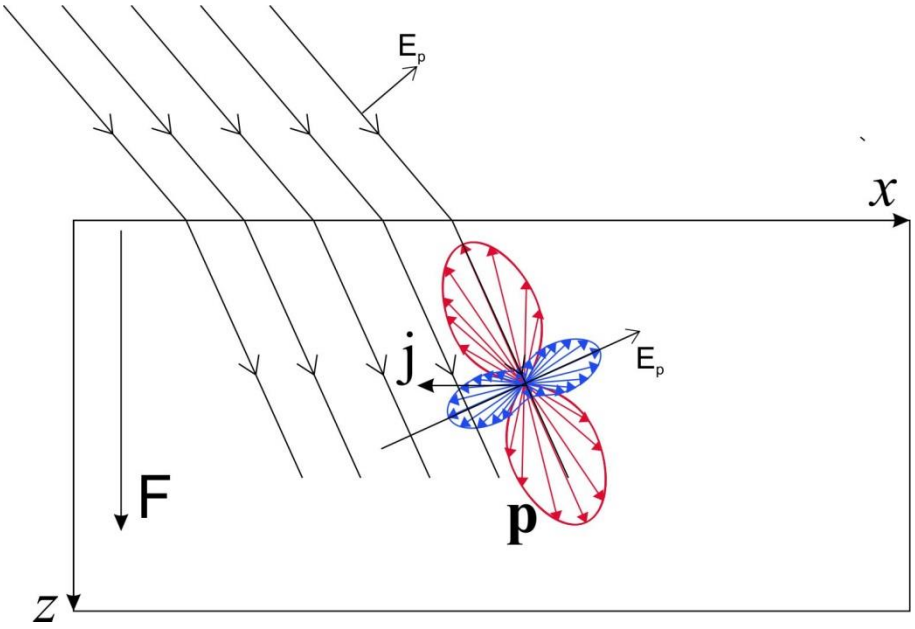

*Fig. 2.6 Photoexcited electron momentum distribution (**p**) in A3B5 semiconductors from heavy hole (red) and light hole (blue) branch.* F *– surface electric field, E_p – electric vector of polarized light, **j** – created lateral current density*

The photocurrent in cubic semiconductors like A3B5 can be represented in the coordinate system of the crystal as follows [13]:

$$\boldsymbol{j} = \alpha \boldsymbol{F}\boldsymbol{E}^2 + \beta \boldsymbol{E}(\boldsymbol{F}\gamma\boldsymbol{E}) + \gamma(F_x E_x^2 \hat{\boldsymbol{x}} + F_y E_y^2 \hat{\boldsymbol{y}} + F_z E_z^2 \hat{\boldsymbol{z}}), \quad (8)$$

here $\hat{\boldsymbol{x}}, \hat{\boldsymbol{y}}, \hat{\boldsymbol{z}}$ – the basic vectors directed along the principal crystallographic axex; α, β, γ coefficients expressed in terms of three non-vanishing tensor components - σ_{zzzz}, σ_{zzxx} and σ_{zxxz} , $\alpha = \sigma_{zzxx}$, $\beta = 2*\sigma_{zxxz}$, $\gamma=\sigma_{zzzz}-\sigma_{zzxx}-2*\sigma_{zxxz}$, $\boldsymbol{F}$ – surface electric field, $\boldsymbol{E}$ – electric field of electromagnetic wave. Such an expression shows that photoconductivity is inherently non-linear process is anisotropic and is characterized by the same dependence on the electric field orientation as the EFIOR effect. This effect generally means that it is possible for the photocurrent to appear which would be perpendicular to electric field direction and the magnitude would depend on angle between its direction and crystallographic plane.

Anisotropic photocurrent would better explain arising azimuthal dependences when excitation is resonant, since OR usually is depicted as a parametric process. Photoexcited electrons (Fig 2.6 red arrows) propagating in different directions compensate each other. But considering nonparabolic

conduction band, carriers moving in built-in electric field will enter the electron dispersion law regions characterized by different effective masses. Accelerated electrons will have reduced mass and higher velocity, while deaccelerated will have the opposite effect. This will make carriers moving towards the bulk and surface have differing velocities parallel to the surface and in turn create the uncompensated lateral photocurrent (Fig. 2.6 ***j***).

Nonparabolicity of the conduction band will be accompanied by their nonsphericity of isoenergetic surface (Fig. 2.7). This would intuitively explain arising azimuthal angle dependences of THz emission. By rotating azimuthal angle the electron momentum distribution would have different velocities depending on isoenergetic surface anisotropy (Fig 2.7). As shown in the picture different petals would create unequal photocurrents which results in a photocurrent lateral to the surface (Fig 2.7 green arrow). It was experimentally observed in [13] where component of THz amplitude dependant on azimuthal angle increased with increasing excess electron energy, which shows an increase of anisotropy of isoenergetic surface. These effects also would be sensitive to subsidiary valley position, when reaching such an energy photoexcited electron momentum would be scattered in timeframes comparable to photocurrent creation and significantly reduce the THz pulse amplitude. Such findings were shown experimentally in [91], where excitation from line of sight geometry was measured in (111) InAs.

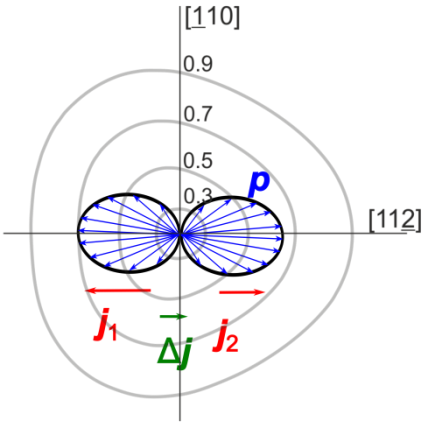

Fig. 2.7 Isoenergetic surfaces of (111) InSb for excitment with differing excess energies in eV [92]*, blue arrrows shows electron impulse in k space after photoexcitation, red arrows shows created lateral currents (j_1 and j_2), while green arrow the uncompensated lateral current (Δj)*

2.4 Investigation of materials with THz pulses

One can differentiate several pulsed THz measurement techniques: THz time-domain spectroscopy (THz-TDS) [93], time-resolved THz spectroscopy (TRTS, which is often called optical pump - THz probe) [41], and THz emission spectroscopy [9, 94]. The first of them is a measurement of static properties of the material absorption, refractive index, conductivity, optical phonon and plasma resonances [95]. The second one offers a dynamic investigation of the material properties since THz radiation is strongly absorbed by free carriers. It is possible to determine carrier lifetime and transient conductivity in a THz spectral range [96]. And the last one uses THz pulse emission from the surface as a probing technique. Here in a THz-TDS system the sample is used as an emitter and changes in THz pulse amplitude, shape, and polarity are investigated [42, 73, 97, 98]. Most studies are done on fixed excitation wavelength (800nm, 1030 nm and 1550 nm, because there are advanced laser systems at those wavelengths), where a change in excitation parameters (fluence, polarisation, beam size),and geometries, dependences on material doping [99], and crystallographic orientation [85] or influence of external forces of magnetic fields [100] or biased sample [101] are analysed. Also, there are several works investigating excitation on range of wavelengths (TES) from near-infrared up to an end of visible range spectrum [9]. All the aforementioned techniques can be complementary and give insight into both material electrical and optical properties.

2.4.1 Nanomaterial characterisation

TES as a contactless technique is especially convenient for the characterisation of nanomaterials such as single-layer or layered 2D materials [102], topological insulators [103], quantum structures [104] (nanowires and dots) and hybrid perovskites [64].

Graphene was the first single-layer material investigated by THz measurement techniques. This material could have potential for future THz devices[105]. Both biased [106] and unbiased [107] graphene samples were measured. The main THz emission mechanism was the photothermic effect, where due to carrier created temperature gradient fast transient photocurrent and photocarrier separation at the graphene–metal interface appears. It was also shown that both layered [108] and single layer graphene could generate [109] THz pulses while excited with ultrashort optical pulses. A photon drag effect was proposed to explain emission from the surface. Where the photons

give up their momentum to photoexcited electrons and holes and transient current is created in the graphene sheet plane. A microscopic mechanism for such phenomenon is that at an oblique angle electron and hole population distributions are not symmetric to the centre of the Dirac cone [108]. This generation mechanism does not depend on the symmetry of the crystal but on the angle between the surface normal and the exciting optical beam wave vector. Later it was shown that the substrate on which single layer graphene is deposited has a great effect on THz pulse emission efficiency. Graphene on randomly structured gold emits two orders of magnitude higher THz pulse amplitude than graphene on the glass substrate which was attributed to the surface plasmon excitation [109].

Layered TMD crystals are heavily investigated at the moment for their indirect to direct bandgap transition when approaching a single layer [16]. THz pulse emission was observed in WSe_2 bulk layered crystal where the generation mechanism was attributed to surface field-driven drift current [110]. At a similar time monolayer WSe_2 was investigated where the generation mechanism was attributed to OR due to an observed azimuthal angle dependence [111]. While the latter work investigated a few-layer sample where due to elliptical THz pulse polarisation: in-plane photocurrent was attributed to the shift current, and out-of-plane photocurrent to drift current [112]. Another TMD material WS_2 has also been investigated where similar results were reported: bulk generation due to drift current [113], while single-layer emission was explained by the OR [114]. Similar findings were obtained when $MoSe_2$ [115, 116], and MoS_2 [117,118] monolayers and multilayers were investigated. There is still no work on THz pulse emission dependence on the excitation wavelength.

Different TMD single layer heterostructures offer possible broad engineering capabilities in the future [119]. Several works employing THz characterisation methods (THz emission spectroscopy and TRTS) were used to investigate heterostructures containing TMD layers. Ma et al [120] investigated WS_2/MoS_2 type 2 heterostructure employing THz emission spectroscopy. The THz pulses were created by carrier transition from MoS_2 layer to WS_2 which was confirmed with THz pulse polarity reversal when stacking of layers was rinverted, while saturation of THz pulse amplitude was attributed to build up of the reverse electric field. Furthermore, theoretical model of created transient current led to the determination of carrier transfer time and efficiency values in the heterostructure. Other work [121] used a TRTS technique to observe carrier dynamics in a graphene/WS_2 heterostructure. Authors showed that the hole transfer from WS_2 to graphene

took around 350 fs. While electron relaxation process is longer and decreases photoconductivity at later times.

A three-dimensional topological insulator (TI) is a perspective material class. They have insulating bulk and a metallic surface that feature a linear Dirac-type electronic energy band. TI material Bi_2Se_3 has been investigated by TES in [103]. Here the surface of this material was excited with a 20 fs duration optical pulses. The emitted THz pulse was decomposed to p and s polarised components. The p-polarisation component was attributed to field-driven drift current in the surface of the material, while the surface states and shift current arising from ultrafast transfer of electrons along a Se-Bi bond were claimed to be responsible for the s-polarized THz pulse component. In another work by Choi et al [122] it was shown that Bi_2Se_2Te thin films emit a THz pulse due to drift photocurrent in a built-in electric field induced by surface band bending. Also, when the sample was annealed the THz pulse changed polarity because the doping type changed from p - to n – type. Furthermore, high frequency THz components appeared for samples annealed at a 250 ℃ temperature which was attributed to the appearance of a metallic surface state. Authors claim that such appearance is the proof of TI state appearance.

InAs nanowires have also been investigated with TES [104]. It was shown that emission mechanisms and dependence on wavelength are different from those in bulk InAs. The main generation mechanism was concluded to be the photo-Dember effect, not the anisotropic photocurrent as in the bulk InAs samples due to the much shorter electron momentum relaxation time of around 50 fs. Later different compositions of $Ga_xIn_{1-x}As$ nanowires were investigated [123]. The best emission was from nanowires with a similar amount of Ga and In attributed to the lowest amount of surface-state donor defects. Lastly wurtzite phase InAs nanowires where optical selection rules depended on optical pulse wavevector with respect to crystal c-axis led to different excitation spectra for different exciting optical pulse polarisations [124]. Two THz emission mechanisms where identified: the carrier separation induced photocurrent when carriers propagate along the nanowire, and the plasma oscillations when due to different optical alignment carriers are spatially confined. Also, phase reversal showed the onset of electron scattering from the high electron mobility conduction band to the lower mobility conduction band valley. These experiments show that more band structure parameters can be determined in hexagonal crystals due to their different optical selection rules.

2.4.2 THz-excitation spectroscopy for subsidiary valley determination

Subsidiary valley energy position is an important parameter of a semiconductor to consider when designing high power field-effect transistors or quantum well based devices. A method to determine this value was proposed by Adomavicius et al [8]. In that work, surface emission from THz InAs and InSb samples was measured when exciting with a broad range of optical pulse wavelengths (0.6 to 2.4 μm) provided by an optical parametric amplifier (OPA). There were clear peaks on TES from both narrow-gap semiconductors, which were attributed to the energy of the onset when electrons started to be scattered to subsidiary L valleys. Reduction of THz pulse amplitude can be explained by fast intervalley scattering processes which disrupt quasi-ballistic propagation and quicker loss of momentum and are on the timeframe of THz pulse generation up to a few hundred femtoseconds. Also, electrons scattered into higher lying valleys will have lower mobility and higher effective mass which lowers the efficiency of accelerating and deaccelerating carriers due to built-in fields. Their main results together with TES spectra of other semiconductors are shown in Fig. 2.8. The shown spectra are normalized to a constant photon number.

In latter works a lot of A3B5 semiconductors were investigated by TES to determine some features of their band structure. Subsidiary valley energy positions were determined in higher bandgap semiconductors - GaAs [9, 11] and InP [OP1]. Also, the technique was used to investigate – GaInAs [11], InN [9], GaSb [125], GaAsBi [OP2].

Recently, a theoretical model to explain TES spectrum shape was proposed [126]. The work presented numerical calculations including drift and diffusion currents while taking into account changes of absorption depth and carrier scattering when reaching the subsidiary valley positions. The model excluded electron energy dispersion due to optical spectral width. Their theoretical model was compared to experimental measurements. The main insights of their work were as follows: surge current effects are of subpicosecond timeframe; shape of THz pulse does not change when electrons start to be scattered; the loss of kinetic energy and momentum are the main reasons for a TES spectrum peak; several valleys could be determined for some materials due to differing scattering rate to X and L valleys, it results in the appearance of different slopes in TES spectra. The monotonous increase of THz pulse amplitude while increasing the exciting pulse photon energy was explained by the increase of electron kinetic energy

and absorption coefficient, which coincides with the Arlauskas et al conclusion [9].

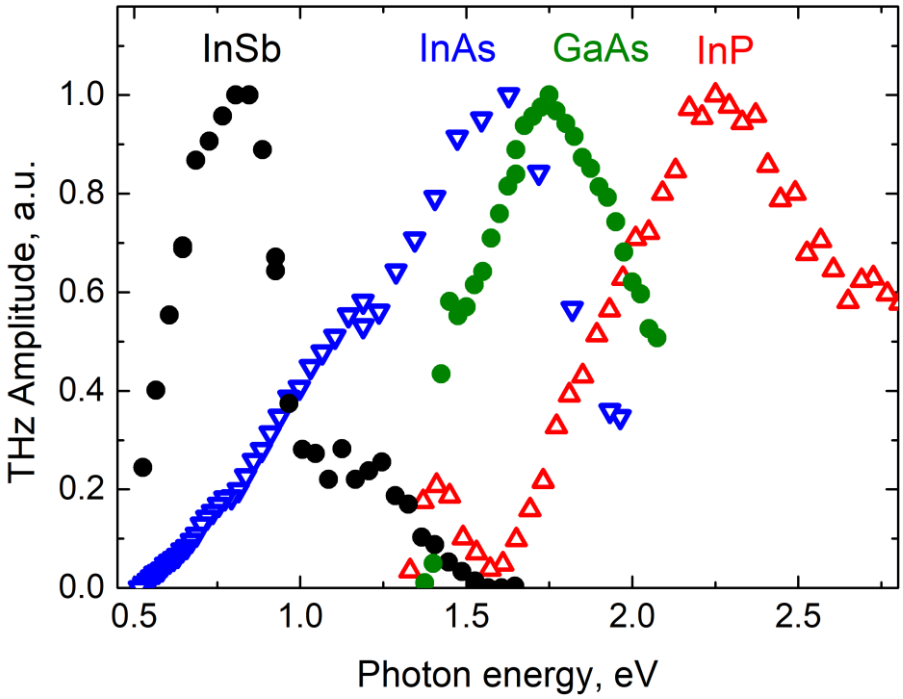

Fig.2.8 TES spectra of various A3B5 semiconductors. Black circles – InSb; blue downward facing triangles – InAs [8]*; green circles – GaAs* [9, 11]*; red upward facing triangles – InP [OP1]*

The technique is versatile and with advancements in THz detectors and expansion of exciting optical pulse wavelength range it will be possible to investigate more semiconductors. Also, it has to be pointed out that most of the mentioned examples are for direct bandgap zinc-blende crystals. The works that investigate different crystal structures and indirect bandgap semiconductors with TES are still lacking.

2.4.3 THz emission imaging of transistors and solar cells

Electronic devices like silicon metal-oxide field effect transistors (SI-MOSFET) [127], integrated circuits [128], and solar cells [129] were shown to generate THz pulses, since most of the devices have pn junctions with built-in fields and depletion layers. At low excitation fluencies the main generation mechanism is drift current; while at high excitation fluencies or large electron excess energies the photo-Dember effect can start to influence

THz pulse generation as well. This should be taken into account when investigating the quality of the devices and characterizing the built-in electric fields of the structure. By scanning the whole device defects could be detected from a change of amplitude or polarity of the THz pulse[128]. The main advantage of THz emission technique in comparison to scanning with THz pulses is a resolution limited by the exciting optical beam width that is a few orders narrower than the THz beam. Micrometre resolution was achieved by employing this technique, referred as laser THz emission microscope (LTEM) [130].

Several types of solar cells were investigated using THz emission: polycrystalline silicon [129], perovskite [131], multi-junction [132], and GaAs based solar cells [133]. From polycrystalline silicon measurements, it was observed that THz pulse amplitude increases with the increasing bias of the structure. Also, saturation when exciting with higher laser fluence was attributed to screening of the electric field by photoexcited carriers. Lastly, polycrystalline boundaries were observed from the images of THz amplitude, and later this technique was compared to conventional ones and showed much better sensitivity to surface defects [134]. Perovskite solar cells showed THz pulse phase reversal when applying reverse bias, which was attributed to internal electric field screening of the perovskite layer. Also, it was shown that THz amplitude would rapidly decrease with the degradation of the sample. Multi-junction cells of Ge/GaAs/InGaP were investigated by exciting the solar cell with different wavelength optical pulses. This led to the observation of differing THz amplitudes from different excited layers depending on the bandgap of the junction. The change of THz amplitude between layers was attributed to changing quantum efficiency of different junctions. Also, THz amplitude images of different junctions show different defects of each layer, for example, surface defects of the most upper junction would only impact the image from that layer. These works show that THz emission from solar cells could be used for quality control or to observe important effects limiting or enhancing solar cell efficiency. More work should be done to get better understanding of the generation mechanisms from these structures and possible application routes.

2.5 Heterojunction band offset

When different semiconductors are in close proximity and create an interface, the energy band structure can take many forms depending on the material. Three types of possible offset configurations are shown in Fig 2.9. For type 1 (Fig. 2.9 a) heterojunctions it is convenient to use the parameter

Q, which is the ratio between conduction band offset (ΔE_c) and the difference ($\Delta E_g = |E_{g1} - E_{g2}|$) of semiconductor bandgaps constituting heterojunction ($Q = \Delta E_c / \Delta E_g$).

A band alignment problem is widely investigated theoretically [12, 135, 136] and by various experimental techniques – optical spectroscopy of quantum wells [137, 138], internal infrared photoemission spectroscopy [139], transport methods [140], x-ray photoemission spectroscopy [141] and ballistic electron emission microscopy (BEEM) [142]. Most of the techniques have their own advantages and disadvantages. For example optical spectroscopy of quantum wells require high quality thin structures with abrupt interfaces as well as good knowledge of semiconductor parameters to calculate possible interband transitions, while being a contactless measurement is an advantage. On the other hand, BEEM requires electric contacts to inject the ballistic carriers through a nanometer dimension tip into a surface of semiconductor of the heterojunction. The structure is simpler in comparison to optical spectroscopy measurements, since multiple quantum well structures are not required. Such a method would also have an unparalleled resolution (the size of a tip - order of nm) on the sample interface position.

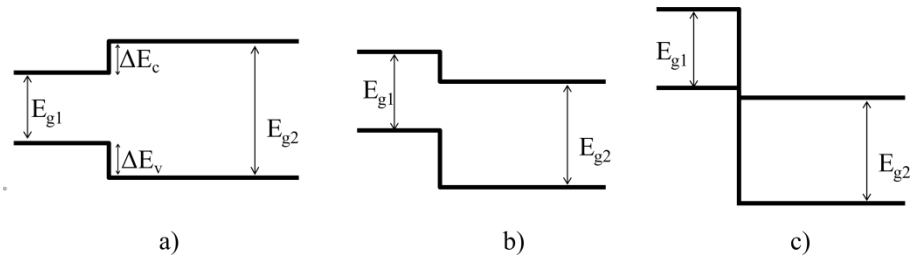

Fig. 2.9 Examples of possible heterojunction offset types a) type 1 (straddling gap), b) type 2 (staggered gap), c) type 3 (broken gap)

The heterojunction offset values are important parameters when engineering modern devices for opto- and micro- electronics, so it is important to find precise or convenient ways to determine them.

2.6 Dilute bismides

Recently A3B5 compounds with small dilute amounts (up to 10%) of embedded Bi have attracted the attention of researchers. Bismuth (the biggest fifth group element) atoms replace As atoms in the crystal and drastically change GaAs and GaInAs energy band structures. First of all, the

band gaps significantly decrease for both GaAsBi and GaInAsBi, by ~ 0.75 meV/% [143] and ~0.56 meV/% [144] respectively. In addition, spin-orbit band splitting is also increasing and at ~10 % Bi for GaAsBi [145] and ~3-4 % Bi for GaInAsBi [146] the respective energy bandgaps are becoming narrower than the spin-orbital splitting, which reduce non-radiative Auger recombination [143]. The temperature dependence of the bandgap in dilute bismides is weaker [147] than in other A3B5 materials, which could be useful when lowering the costs and increasing the operational stability of the devices fabricated from these materials: laser diodes[148], avalanche photodiodes [149], light emitting diodes [150], PCA [50], and photovoltaic cells [151]. More research on their fundamental properties is needed.

Several works were investigating THz pulse emission from unbiased GaAsBi surfaces. Radhampura et al. [152] investigated samples with up to 4 % of bismuth content. In his work, azimuthal angle dependences were investigated for samples of (001) and (311) B orientation substrates. THz pulse generation was attributed to optical rectification discounting transient current effects, because of azimuthal angle dependence on (311) B sample and no emission from (001) sample. In another work, Vaisakh et al. [153] investigated GaAsBi with up to 3.5 % Bi samples of (100) orientation and had different results in comparison to the first work. The main mechanism was attributed to transient currents instead of optical rectification. Also, they observed THz pulse phase reversal when Bi content increased to more than 1.5 %. They concluded that at a low amount of bismuth content the generation was due to surface field, while the photo-Dember effect would prevail for a higher amount of bismuth, because of increased excess electron energy when bandgap was reduced. All of the previous experiments were done with a fixed wavelength laser of around 800 nm. In another work by Pačebutas et al. [OP2] samples with Bi content of up to 8 % with (100) cutw substrates were investigated. Variable wavelength was used to excite the samples. In that work, the THz emission mechanism was due to transient currents – drift current near the bandgap and photo-Dember effect when excess electron energy increases. In addition increasing Bi content lowered the THz pulse amplitude. Overall, the THz emission from GaAsBi is similar to other cubic crystals where several effects (drift current, photo-Dember, optical rectification) are responsible for generation depending on optical excitation fluence and wavelength. Several works investigated offset values theoretically and experimentally for GaAsBi/GaAs heterojunction [145, 154], while only theoretical results were provided for GaInAsBi/InP heterojunction [155, 156].

3 EXPERIMENTAL METHODS

3.1 THz pulse emission

In this work, the main results were acquired using the THz emission spectroscopy setup shown in Fig. 3.1. This setup was based on amplified ytterbium-doped potassium gadolinium tungstate (Yb:KGW) laser system “PHAROS” (“Light conversion”) with 150 fs pulse duration and 200 kHz repetition rate. Typically laser generated around 6.5 W average power which is split into 2 beams. The beam with a higher average power of around 6 W was directed towards optical parametric amplifier (OPA) “Orpheus” which due to collinear optical amplification converts the input beam wavelength into a range from 650 nm to 2600 nm. It was possible to extend the range by using barium borate (BBO) crystal to generate a second harmonic and extending the range up to 325 nm (total range of the system 0.48 eV – 3.8 eV). The optical pulse from OPA was directed at an investigated sample by mirrors and lenses. The beam was impinging the sample either in transmission or reflection geometry at various incidence angles. The generated THz pulse was directed at a silicon lens side of the GaAsBi (Teravil ltd.) PCA. The other beam from “PHAROS” was attenuated to ~ 5 mW average power and was focused onto contacts of the detecting PCA antenna. The emitter branch was chopped with a mechanical chopper and data from the lock-in amplifier was recorded with in-house software. This was a THz –TDS measurement setup where sample was used as an emitter.

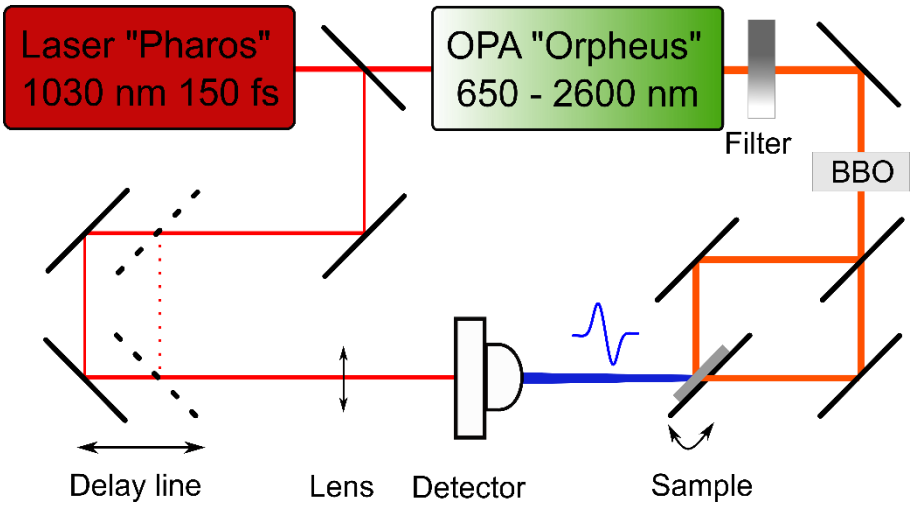

Fig. 3.1 THz emission spectroscopy setup

The TES spectra were acquired by measuring THz pulse amplitude at different exciting optical pulse wavelengths. In some experiments, the values of measured THz pulse integral in time representing photocurrent dependence on exciting photon energy were ploted instead of the THz pulse amplitude. The semiconductor surface was usually excited by the same average optical power at all wavelengths and the obtained spectra were afterwards normalised to a constant photon number. The spectra were measured at the linear part of the THz pulse amplitude dependence on average optical power.

There are several measurement errors to take into account. Firstly the excited electrons have Gaussian distribution of energies around measured point. It is dependant on spectral width of the optical pulse. Since in our measurements optical pulse has 150 fs duration the uncertainty of the energy is around 20 meV. In addition, Laser power could fluctuate up to 5 %, although this limit is around edges of measured wavelengths. These are the biggest value systematic errors and are used to present final results.

In several works, a comparison with highly doped n-type GaAs was made. The n-type GaAs has a THz generation mechanism of built-in surface field that is directed into the surface, the same direction as electrons propagating into the bulk that would create carrier separation.

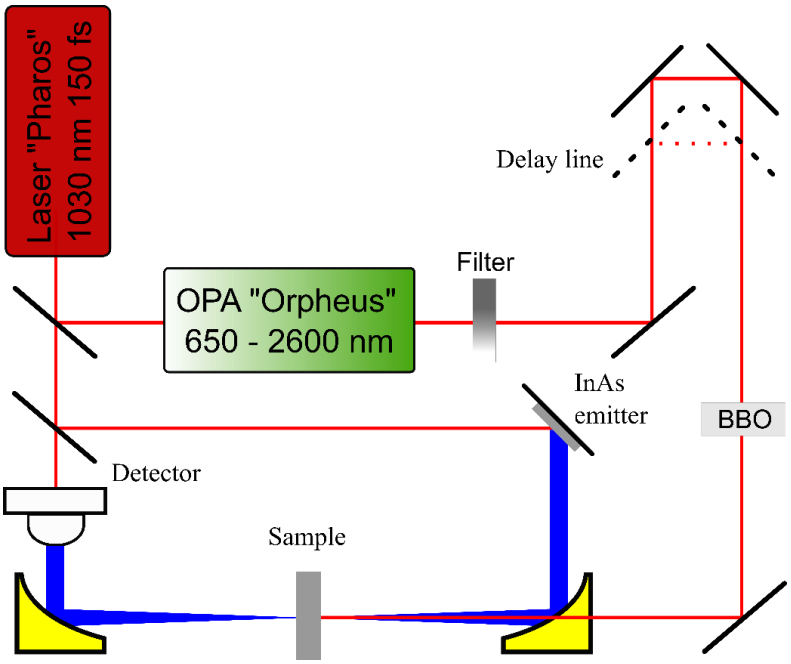

Fig. 3.2 Optical pump THz probe setup

Optical pump THz probe (OPTP) experimental setup is shown in Fig. 3.2. OPTP measurement resolution is similar to the duration of THz pulse emitted from a photoexcited InAs surface. Meanwhile, the sample is located at the THz beam focus spot and is illuminated by the optical pump pulse from OPA. The size of the overlap of both beams is around 2 mm.. The optical pump beam wavelength can be varied from 400 nm to 2600 nm.

3.2 TES for the energy position of subsidiary valleys measurement

As mentioned in the literature overview it is possible by using the TES measurement to determine the subsidiary valley position in direct band gap semiconductors. The TES spectrum of SI-GaAs, together with an inset presenting the energy band structure of this material, is shown in Fig. 3.3. Several specific features are clearly seen on this spectrum. First of all, at the direct bandgap energy of 1.42 eV there is a fast rise in THz pulse amplitude. At 1.76 eV, there is a broad peak showing the position of the first subsidiary valley position. While increasing photon energy further, the THz pulse amplitude starts to decrease due to the onset of electron scattering to lower mobility L valleys; at 1.94 eV the decrease of the THz pulse amplitude becomes even steeper due to the shorter scattering time to X valleys. Intervalley Γ-X scattering times are shorter than 100 fs as compared to ~300 fs for Γ-L scattering [157]. The valley positions can be calculated from corresponding photon energies $h\upsilon$ by using momentum and energy conservation laws for the photocarriers and including the non-parabolicity of the conduction band [158]:

$$\varepsilon_{valley} = \frac{\sqrt{\left(1+\frac{m_e}{m_h}\right)^2 + 4\frac{m_e}{m_h}\beta(h\upsilon - E_g)} - 1 - \frac{m_e}{m_h}}{2\frac{m_e}{m_h}\beta} + \varepsilon_{ph}, \qquad (9)$$

here, m_e, m_h are the electron and hole effective mass respectively, β is the non-parabolicty parameter, $h\upsilon$ – the energy of the measured peak, E_g, ε_{ph} – bandgap and optical phonon energy of the investigated material. It has to be mentioned that such values agree with the already accepted values of GaAs [159].

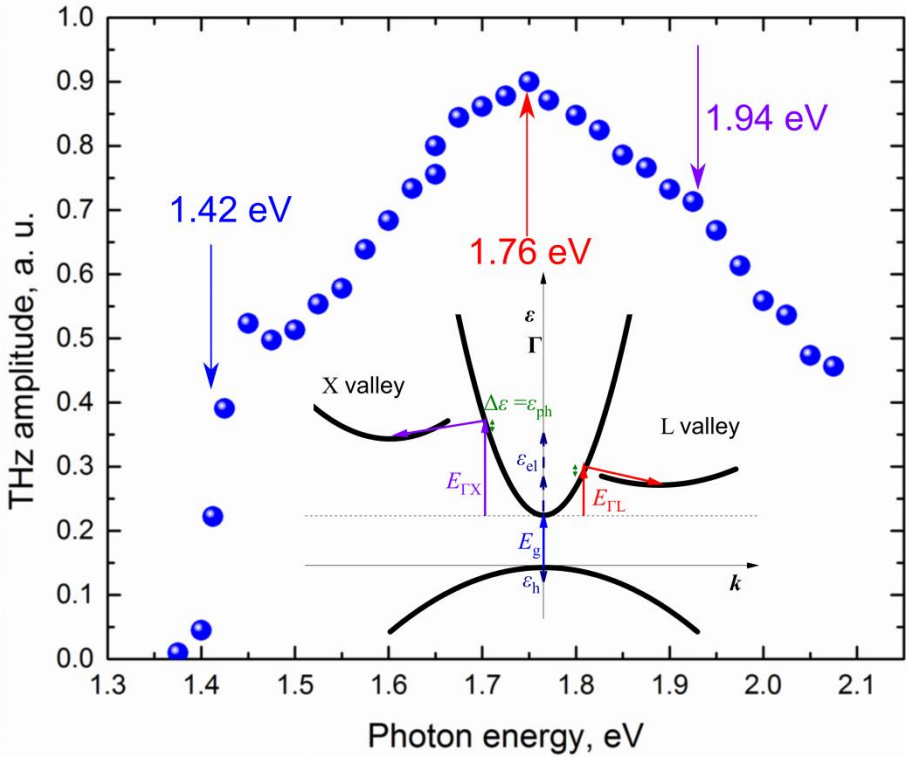

Fig 3.3 TES spectra of SI-GaAs. Inset shows principle band structure scheme of GaAs where $E_{\Gamma X}$– X valley energy, E_g – Band gap energy, $E_{\Gamma L}$ – L valley energy, ε_{el} and ε_h – electron and hole excess energy. *Arrows of the same color represent features in spectra 1.42 eV bandgap of GaAs, 1.76 eV scattering to L valley, 1.94 eV scaterring to X valley [OP2]*

3.3 Growth and sample characterisation methods

Dilute bismide layers and structures containing them were grown in the Optoelectronics department of the Centre for Physical Sciences and Technology using available molecular beam epitaxy (MBE) equipment and various crystalline substrates. Monoelemental bismuth layers with a crystalline structure were also grown using MBE on (111) cut silicon; while an electroplating method was used to grow amorphous Bi layers on various (silver, gold, platinum) precious metals [P1, P3, P6, P7, P8].

In the MBE system several molecular and atomic beams are directed at a substrate with a defined temperature to create a thin layer of crystal material. Most of the layers were grown by Veeco GEN xplor MBE system, with standard In, Ga, Al, and Bi molecular sources and As_2 and Sb crackers. The

device is capable of doping the alloys with Si, Be, and Te. The temperature was controlled by contactless, absolute temperature detector kSA Bandit. Another SVT 3-5 C-V-2 MBE system was also used for several epitaxial layer samples. System had the same molecular beam sources and two temperature zone cracker for As_2 dimer beam. Temperature was controlled by thermocouple.

Samples of TMD's were obtained from the Institute of Physics of the Moldovan Academy of Sciences (Chisinau, Moldova) (Prof. L. Kulyuk). The chemical vapour transport (CVT) technique was used to grow high quality crystalline samples [P5].

To fully investigate the differing concentration bismides and different thickness bismuth layers, additional techniques were used to determine their concentration, bandgap, strain, doping, and crystal structure were needed.

The X-ray diffraction (XRD) measurement is a conventional technique to investigate thin epitaxial layers. In this work, a Rigaku Smartlab diffractometer was used. It had a rotating 9 kW Cu anode source, Ge(200)×2 monochromator, and SC-70 point detector. The measured data were analysed in the GlobalFit database. XRD measurements were used to determine Bi concentration in dilute bismides, by monitoring the (004) diffraction peak with the respect to its position of the substrate material peak, then using Vegard's law to determine the composition assuming lattice constant of GaAs to be 5.653 Å and GaBi 6.234 Å [160]. The strain of epitaxial layers was investigated by analysing the (115) peak in reciprocal space maps (RSM). The thickness could be determined by X-ray reflectivity measurements (XRR).

Photoluminescence measurement is a proven technique to determine the bandgap of the material. This method observes radiative recombination of photoexcited semiconductors, where emitted photon energy is similar to the bandgap value of the material. In these measurements, samples were pumped with a 532 nm wavelength CW laser. The emitted light was separated into different spectral components by monochromator and detected by InGaAs photodetector.

Hall measurements were made to determine the doping of the thin epitaxial layers. Surface quality was observed using a scanning electron microscope (SEM).

OVERVIEW OF INVESTIGATION

The original results obtained during this work and presented below are divided into three groups. The first group consists of articles dedicated to the research of A3B5 group compounds containing bismuth atoms, the second - TES studies carried out using semiconductors with a more complex band structure (indirect bandgap, hexagonal symmetry or van der Waals bonding), and the third – thin polycrystalline and ultrathin crystal Bi layer studies.

Dilute bismides and heterostructures containing them

Paper P1. "THz-excitation spectroscopy technique for band-offset determination"

The experimental technique adopting TES is proposed to determine energy band offsets in semiconducting heterostructures. This is achieved by confining carriers in a thin layer by created barrier in conduction band of heterostructure. It is shown that 100 nm layer is enough to disrupt ballistic carrier propagation while excess electron energy insufficient to overcome the barrier and significantly reduce amplitude of THz pulse. An abrupt increase of THz amplitude is appearing when photoexciting photon energy is sufficient to overcome conduction band heterojunction barrier. A characteristic feature is appearing in TES spectra at that energy. This feature agrees with developed theoretical model, which is fitted to experimental data to determine band offsets of GaAsBi/GaAs heterojunction.

Paper P4. „Band-offsets of GaInAsBi–InP heterojunctions"

TES is used for the analysis of the energy band alignment in $Ga_{0.47}In_{0.53}As_{1-x}Bi_x$-InP heterojunctions. It showed that for bismuth concentrations x in the range from 0 to 0.06, the relative conduction band offset with respect to the energy band difference in unstrained heterostructure is equal to 0.38, and is reduced to approximately 0.34 at x=0.06 by the strain effects.

Paper P8. "Terahertz Pulse Emission from Semiconductor Heterostructures Caused by Ballistic Photocurrents"

TES characteristics were measured, when illuminating the heterostructure from the wider bandgap semiconductor side. The excitation would be at the heterojunction interface. It has been shown that when the photon energy is sufficient enough to excite electrons in the narrower bandgap layer with an energy greater than the conduction band offset generated THz pulse changes its polarity. Theoretical analysis was performed both analytically and by

numerical Monte Carlo simulations. The results shown that photocurrent is created only in the narrow bandgap layer when excess electron energy is insufficient to overcome the conduction band barrier of heterostructure. When photoexcited carriers can overcome the barrier the photocurrent created in wider bandgap semiconductor becomes higher than narrow bandgap layer. This causes the polarity inversion of THz pulse. This effect is used to evaluate the energy band offsets in GaInAs/InP and GaInAsBi/InP heterostructures.

Paper P2. „Terahertz pulse emission from GaInAsBi“

Quaternary GaInAsBi alloy epitaxial layers were grown on InP substrates and used in THz pulse emitters activated by long wavelength femtosecond laser pulses. The energy bandgap of this material was as narrow as 0.4 eV; due to a relatively small lattice mismatch with the substrate (~0.3%), the layers remained fully strained. TES spectra were measured from both unbiased surface and biased PCA fabricated from GaInAsBi layer. PCA fabricated from GaInAsBi layers were the first devices sensitive to the optical pulses with wavelengths longer than 2 μm. Therefore, they can be successfully used with novel femtosecond thulium or holmium doped fibre lasers for which such components are as yet not available.

Investigation of indirect bandgap semiconductors and hexagonal structure layered crystals

Paper P3. „Spectral dependencies of terahertz emission from femtosecond laser excited surfaces of germanium crystals“

TES spectra for variously doped germanium crystals were measured. It showed that a strong emission sets on when the photon energy is higher than the direct energy gap. A new microscopic mechanism for the azimuthal angle dependence below direct band gap is due to anisotropy of L valley isoenergetic surface, which creates lateral photocurrent flowing in the direction opposite to that caused by the optical alignment. Additionally, results of the optical pump – THz probe measurements evidences a fast, sub-picosecond reduction of the Γ valley electron density due to their transfer to low mobility L valleys.

Paper P5. "Terahertz emission from a bulk GaSe crystal excited by above bandgap photons"

THz pulse amplitude dependence on exciting photon energy varying in range from 1.8 to 3.8 eV for a few-μm-thick GaSe hexagonal crystal was

measured in this work. Several features were observed in TES spectrum such as an onset and a peak. These features were attributed to direct bandgap energy and conduction band subsidiary valley position respectively. Additionally, at higher excitation energies THz pulse amplitude started to increase again. Investigation of this feature led to additional measurements of azimuthal angle dependence and TES spectra for different exciting optical pulse polarisation. These experiments showed that due to different optical selection rules in accordance to the c – axis in hexagonal crystal TES spectra for azimuthal angle independent part are different for p and s excitation polarisation. This was used to determine a lower laying valence band position.

Paper P6. „Terahertz pulse emission from photoexcited bulk crystals of transition metal dichalcogenides“

In this work, three multilayer TMD crystals, tungsten diselenide (WSe_2), molybdenum diselenide ($MoSe_2$), and molybdenum disulfide (MoS_2) were investigated. TES spectra and dynamics of photoexcited carriers of these materials were measured. Since we did not observe any azimuthal angle dependences of the THz amplitude or THz emission occurring when illuminating the samples at 0º angle of incidence, the only possible mechanism of THz emission is the appearance of a surface current. Such a current can arise due to unequal diffusion rates of electrons and holes and the formation of a near-surface electric dipole. The measured TES spectra shown peaks at energies coinciding with respective materials direct energy bandgap K-K transition. Unlike other semiconductors, TMD crystals are characterized by intense generation of various excitons after photoexcitation. Part of those excitons, the so-called dark excitons, do not appear in the luminescence, because the electron and the hole are localized in different layers of the material (interlayer excitons) or one of them is caught by a defect. Such excitons can have very long lifetimes, so they will create an internal electric field near the illuminated surface. The presence of that field is evidenced by our experiments of double-pulse optical excitation.

Thz pulse generation in polycrystalline and crystal layers of bismuth

Paper P7. “Terahertz Photoconductivity Spectra of Electrodeposited Thin Bi Films”

TES spectra of thin polycrystalline Bi layers electrochemically deposited on various noble metal substrates depended little on both substrate material

and layer thickness. Therefore, it was concluded that the THz pulse generation occurs in the thin subsurface part of the Bi layer due to the photo-Dember effect. Comparing the phase of the THz pulse generated in the Bi layer with the THz pulses generated on the surfaces of n-type and p-type GaAs crystals, proves that the diffusion of electrons in bismuth is faster than that of holes. Unlike crystalline semiconductors, in which charge carriers thermalize relatively slowly, in semi-metallic bismuth, this process is dominated by inter-electron collisions, which significantly accelerate thermalisation. This conclusion was confirmed by comparing the experimental TES spectra, where sample was illuminated at different angles of incidence, with theory.

Paper P9. **"**Terahertz emission from ultrathin bismuth layers**"**

In this work, MBE grown 8 nm crystal bismuth layers on (111) - cut Si substrate was investigated. Unlike in polycrystalline Bi layers, THz generation started from a certain threshold photon energy equal to 0.45 eV, the pulse amplitude was much higher, depended on the polarisation of the excitation light and had a clear sin (3φ)-type dependence on the azimuthal angle. In addition, layers VS001 and VS002 were similar thickness, differing only in the different thickness ratio of crystal layer and polycrystalline wetting layer. An unequal influence of the azimuth angle-dependent part of the THz pulse was observed in these samples. To explain THz pulse generation a new mechanism was proposed, where lateral currents arise due to scattering at the crystal and wetting layer interface.

MAIN RESULTS AND CONCLUSION

1. Experimental and theoretical results showed that TES technique is suitable to determine offset values of a heterojunction.

2. TES was used to determine the ratio $Q = 0.45 \pm 0.04$ for the Bi content up to 12% for GaAsBi/GaAs heterojunction.

3. The ratio $Q = 0.38 \pm 0.04$ was obtained for Bi content up to 6 % in $Ga_{0.47}In_{0.53}AsBi/InP$ heterojunction. The strain of the bismide layer can reduce Q for GaInAsBi/GaInAs heterojunction down to 0.25 ± 0.03 when the Bi content is approximately 6 %.

4. A photoconductive antenna fabricated on a GaInAsBi layer grown on an InP substrate was shown to have its peak efficiency when activated by 2 μm wavelength optical pulses.

5. For indirect bandgap semiconductors like germanium, the most efficient THz pulse generation was found to coincide with direct bandgap energy.

6. Investigation of TMD (MoS_2, $MoSe_2$, and WS_2) materials showed that the TES peak coincided with their positions of direct gap energies. The THz emission from bulk layered materials was shown to be caused by photocurrent surge in the built-in electric fields.

7. Different optical selection rules in accordance to the c – axis in hexagonal crystal (GaSe) led to a determination of the position of the lower lying valence band. Additionally, a direct bandgap of 2 ± 0.04 eV and conduction band subsidiary valley position of 0.21 ± 0.02 eV above the conduction band bottom was determined.

8. THz pulse emission in thin electrodeposited bismuth layers was attributed to the photo-Dember effect with non-equilibrium carrier diffusion stabilized on the femtosecond timescale by an intense carrier-carrier scattering.

9. Novel THz emission mechanism based on the lateral photocurrent arising due to electron scattering at the wetting layer interface was attributed to THz pulse generation in ultrathin crystal bismuth layers. The onset of THz emission of 0.45 ± 0.02 eV was assigned to the direct bandgap of the bismuth.

CURRICULUM VITAE

About the author

Ričardas Norkus was born in 1993 in Klaipėda, Lithuania. In 2012 he finished Klaipėdos "Ąžuolyno" gimnazija to receive a high school diploma. In 2016 he received a bachelor degree in physics from Kaunas Univeristy of Technology after finishing study programme in Applied Physics. In 2018 he received a Master's degree in physics from Vilnius University after completing Master study programme in Laser Physics and Optical Technologie. In 2018 he started doctoral studies in Center for Physical Sciences and Technology (FTMC).

Apie autorių

Ričardas Norkus gimė 1993 metais Klaipėdoje. 2012 metais baigė Klaipėdos „Ąžuolyno" gimnaziją. 2016 metais baigė bakalauro studijas Kauno technologijos universiteto studijų programą – Taikomoji fizika ir įgijo fizikos bakalauro laipsnį. 2018 metais baigė magistro studijas Vilniaus universiteto studijų programą – Lazerinė fizika ir optinės technologijos ir įgijo fizikos magistro laipsnį. 2018 metais buvo priimtas į doktorantūros studijas Fizinių ir technologijos mokslų centre.

SANTRAUKA

Įvadas

THz bangų ruožo technologijos sparčiai tobulėja ir randa vis naujų taikymų įvairiose mokslo ir pramonės srityse. Viena tokių technologijų – THz laikinės srities spektroskopija (THz-TDS) gali būti panaudota narkotikų ir sprogmenų aptikimo sistemose [1], automobilių dažymo kokybės užtikrinimui [2], restauruojant meno kūrinius [3], neinvaziniu metodu diagnozuojant vėžį [4] bei užtikrinant maisto produktų kokybę [5]. Moksliniuose tyrimuose ji puikiai tinka elektronikos ir fotovoltaikos komponentų parametrų matavimams [6], bei įvairių puslaidininkinių medžiagų charakteristikų tyrimams [7, 8]. Visi minėti pritaikymai yra galimi dėl per pastaruosius kelis dešimtmečius vykusio spartaus THz spinduliuotės impulsų generavimo, bei detektavimo tobulėjimo.

Puslaidininkio paviršių sužadinant itin trumpu optiniu impulsu, kurio fotonų energija didesnė už draustinių energijų tarpą, jame sukuriami nepusiausvyriniai krūvininkai. Šviesos sužadinti elektronai ir skylės atsiskiria erdvėje dėl juos veikiančių vidinio elektrinio lauko arba dėl skirtingo judėjimo greičio link kristalo tūrio. Dėl to paviršiuje atsiranda sparčiai kintanti fotosrovė, kuri yra elektromagnetinių impulsų esančių THz dažnių diapazone šaltinis. THz impulsų generavimo efektyvumas priklausys nuo apšviesto puslaidininkio savybių, vidinių laukų, perteklinės sužadintų krūvininkų energijos ir kampo, kuriuo į paviršių kris žadinantis optinis pluoštas. Tyrinėjant tokias priklausomybes galima nustatyti keletą svarbių elektronų energijos juostos sandaros parametrų. Ankstesniuose darbuose panaudojus THz impulsų žadinimo spektroskopijos (TES) metodiką buvo nustatytas tiesioginis draustinių energijų tarpas [9], vidinis elektrinis laukas puslaidininkio paviršiuje [10] ir laidumo juostos šoninių slėnių padėtis kai kuriuose A3B5 grupės puslaidininkiuose (GaAs [9], InAs [8], InSb [8], InP [OP1], InGaAs [11]).

Modernių mikro- ir optoelektronikos prietaisų kūrime naudojamos heterosandūros, kurių vienas iš svarbiausių parametrų yra laidumo ir valentinės juostos trūkio vertės. Šios vertės randamos tiek iš teorinių, tiek iš eksperimentinių darbų [12]. Tarp įprastinių šio parametro matavimo metodikų galima paminėti kvantinių duobių spektroskopija, Rentgeno spindulių fotoemisijos spektroskopiją ir balistinių elektronų emisijos mikroskopiją (BEEM). Šiame darbe yra pirmą kartą parodoma kaip THz impulsų žadinimo spektroskopija (TES) gali būti panaudota nustatant heterosandūros energijos juostų trūkių vertes. Tai įgalina balistinis elektronų

judėjimas puslaidininkio paviršiuje po sužadinimo optiniu impulsu [13]. Pasiūlytas būdas buvo panaudotas nustatant GaAsBi/GaAs ir GaInAsBi/InP heterosandūrų juostos trūkio vertes. Taip pat iš GaInAsBi sluoksnio užauginto ant InP padėklo buvo pagaminta fotolaidi antena. Ji buvo naudojama generuoti THz impulsus ją žadinant 2 μm bangos ilgio optiniais impulsais.

Iki šiol TES metodika plačiau nagrinėti buvo tiesiatarpiai kubiniai A3B5 grupės puslaidininkiai. Vienas iš šios metodikos privalumų yra bekontaktis tyrimo būdas, dėl to naudinga praplėsti šios metodikos taikymus į dvimates ir sluoksniuotas medžiagas, kuriose elektrinių kontaktų gamyba yra itin problemiška. Van der Walso jėgomis surištiems kristalams artėjant prie kelių ar vieno sluoksnio storio keičiasi jų elektroninės [14] ir mechaninės savybės [15], kartais stebimas puslaidininkio netiesioginio draustinių energijų tarpo virsmas tiesioginiu [16]. Šiame darbe TES metodika buvo pritaikyta būtent tokio tipo medžiagos – pereinamųjų metalų dichalkogenidams (TMD) ir GaSe kristalams.

Ploni bismuto sluoksniai pastaruoju metu taip pat traukia nemažai dėmesio dėl savo unikalių savybių. Viena iš jų didelis Fermi bangos ilgis (~30 nm), dėl ko kvantiniai erdvinės sąspraudos efektai šioje medžiagoje pasireiškia pakankamai storuose sluoksniuose ir galiausiai lemia Bi perėjimą iš pusmetalio į puslaidininkį [17]. Teoriniuose darbuose buvo prognozuota, jog itin ploni bismuto sluoksniai pasižymi topologinio izoliatoriaus savybėmis [18]. Dėl šių priežasčių buvo tyrinėjama THz impulsų generacija itin plonuose kristaliniuose bismuto sluoksniuose ir šiek tiek storesniuose polikristaliniuose bismuto sluoksniuose.

Šis tyrimas yra tęstinis, prieš tai atlikti tyrimai FTMC Optoelektronikos laboratorijoje davė pagrindą šiam darbui, skirtam TES metodikos tobulinimui ir jos galimybių praplėtimui tyrinėjant naujas medžiagas ir ieškant naujų panaudojimo būdų. Šiame darbe tyrinėjamos skirtingos medžiagos parodo TES metodikos universalumą. Pagrindinis metodikos privalumas – bekontaktis matavimas, leidžiantis tiesiogiai nustatyti įvairius fizikinius puslaidininkio parametrus.

Darbo tikslas

Pasitelkus THz emisijos spektroskopijos metodą tirti puslaidininkius su įvairiu draustinių energijų tarpu, bei kristaline struktūra ir puslaidininkinių heterosandūrų energijos juostų trūkio vertes.

Darbo uždaviniai

- Pritaikyti THz sužadinimo spektroskopijos metodą nustatant juostos trūkio vertes puslaidininkinėse heterosandūrose.
- Nustatyti laidumo juostos trūkio vertes GaAsBi/GaAs ir GaInAsBi/InP heterosandūrose naudojant THz sužadinimo spektroskopiją metodą.
- Atlikti THz žadinimo spektroskopijos tyrimą sluoksniuotiems heksagoninės simetrijos ir netiesiatarpiams puslaidininkiniams kristalams.
- Nustatyti juostinės struktūros parametrus ir THz impulsų generacijos mechanizmus pereinamųjų metalų dichalkogeniduose (MoS_2, $MoSe_2$, WS_2) ir GaSe kristaluose.
- Ištirti THz impulsų generaciją plonuose monoelementinio bismuto sluoksniuose.

Mokslinis naujumas

- TES pirmą kartą buvo panaudotas nustatant energijos juostos trūkių vertes puslaidininkio heterosandūroje.
- Fotolaidi antena, pagaminta iš GaInAsBi sluoksnio užauginto ant InP padėklo, žadinama 2 μm bangos ilgio optiniais impulsais efektyviausiai generavo THz impulsus.
- Sluoksniuotų medžiagų – GaSe ir TMD ($MoSe_2$, MoS_2, WSe_2) išmatuoti TES spektrai leido nustatyti keletą juostinės struktūros parametrų.
- Germanio kristalai efektyviausiai generuoja THz impulsus, kai žadinančiojo optinio impulso bangos ilgis yra apie 1.55 μm.
- THz impulsų emisija iš elektrochemiškai nusodintų plonų bismuto sluoksnių yra dėl sparčios foto-elektronų termalizacijos ir jo sukelto foto-Demberio efekto.
- THz impulsų emisija iš MBE metodu užauginto kelių nanometrų storio kristalinių sluoksnių parodo galimą pusmetalio – puslaidininkio perėjimą šioje medžiagoje.

- THz impulsų generacija iš MBE metodu užauginto ultraplono kristalinio bismuto buvo paaiškinta atsirandančiomis lygiagrečiomis paviršiui aniztoropinėmis srovėmis.

Disertacijos ginamieji teiginiai

- Puslaidininkio heterosandūroje femtosekundiniu lazerio impulsu sužadintų elektronų balistinis judėjimas lemia THz impulsų žadinimo spektre atsirandančias skiriamąsias ypatybes, kurios sutampa su elektronų perėjimais iš siauresnio draustinių energijų tarpo puslaidininkio valentinės juostos į platesnio draustinių energijų tarpo puslaidininkio laidumo juostą. Tai leidžia tiesiogiai nustatyti heterosandūros laidumo juostos trūkio vertę.
- GaAsBi-GaAs heterosandūros laidumo juostos trūkio vertė sudaro apie 45 % ± 5% bendro draustinių energijų tarpo skirtumo, o GaInAsBi/InP heterosandūroje ši vertė yra apie 34 % ± 3% šio skirtumo.
- THz impulsų generacijos mechanizmas elektrochemiškai nusodintame polikristaliniame bismuto sluoksnyje ant tauriųjų metalų yra dėl greitesnės elektronų difuzijos nuo paviršiaus lyginant su skylėmis – foto-Demberio efekto. Tuo tarpu ultraploname kristaliniame sluoksnyje užaugintame ant Si padėklų molekulinių pluoštų eptitaksijos būdu THz emisija vyksta dėl balistiškai judančių krūvininkų ir jų generuojamo šoninės nekompensuotos fotosrovės lygiagrečios paviršiui.

Autoriaus indėlis

Šio darbo autorius atliko eksperimentinius tyrimus: THz impulsų emisijos, THz sužadinimo spektroskopijos, azimutinio kampo priklausomybės ir optinio žadinimo – THz zondavimo eksperimentus. Jis taip pat prisidėjo prie rezultatų analizės, diskusijų ir straipsnių ruošimo. Gauti rezultatai paties autoriaus buvo pristatyti keliose tarptautinėse ir vietinėse konferencijose tiek žodinio, tiek plakato pranešimo formatu.

Fizinių ir technologijų mokslų centro optoelektronikos skyriuje MBE metodu buvo auginti visi bismuto ir bismidų bandiniai, tame pačiame skyriuje jie buvo ir charakterizuoti. Tuo tarpu TMD bandiniai buvo išauginti Moldovos mokslų akademijos fizikos institute.

Gautieji rezultatai buvo paskelbti devyniuose moksliniuose straipsniuose. Šie straipsniai disertacijoje yra suskirstyti į tris grupes. Pirmojoje yra nagrinėjami sluoksniai ir heterosandūros, turinčios A3B5 grupės bismidinių junginių. Antrojoje – TES spektrai, matuojami netiesiatarpiai, heksagoninės kristalinės struktūros ar susaistyti van der Waals'o ryšiais puslaidininkiai. Galiausiai, trečiojoje grupėje yra straipsniai, kuriuose pateikiami THz impulsų emisijos iš plonų polikristalinių ir kristalinių bismuto sluoksnių tyrimai.

Bismidų ir su jais sudarytų heterosandūrų tyrimas

Straipsnis P1. „Juostinės struktūros trūkio verčių nustatymas pritaikant THz žadinimo spektroskopijos metodą"

Šiame darbe pristatytas eksperimentinis būdas, skirtas puslaidininkinės heterosandūros laidumo juostos trūkio vertės radimui pasitelkiant TES metodą. Tai pasiekiama žadinant krūvininkus ploname siauresnio draustinių energijų tarpo puslaidininkio sluoksnyje. Buvo parodyta, kad apie 100 nm storio sluoksnis yra pakankamas sutrikdyti balistinį krūvininkų judėjimą, jei perteklinės elektronų energijos nepakanką įveikti heterosandūros barjero, tuo pačiu stipriai sumažinant THz impulso amplitudę. Pasiekus perteklinę elektronų energiją, kuomet barjeras yra elektronų įveikiamas, THz impulso amplitudė pradeda staigiai didėti, tai atsispindi TES spektre. Šis didėjimas sutapo su atliktais teoriniais skaičiavimais ir leido nustatyti GaAsBi/GaAs heterosandūros energijos juostų trūkio vertes.

Staipsnis P4. „GaInAsBi-InP heterosandūrų juostinės struktūros trūkio verčių nustatymas"

Eksperimentinė metodika pristatyta praeitame straipsnyje pritaikoma ir kitai bismidinei heterosandūrai - $Ga_{0.47}In_{0.53}As_{1-x}Bi_x/InP$. Šiame darbe buvo tirti sluoksniai kuriuose bismuto koncentracija x kito nuo 0 iki 0.06. Laidumo juostos trūkio vertės neįtemptuose sluoksniuose sudarė 0.38 draustinių energijų tarpo skirtumo, įvertinus sluoksnių įtempimus ši vertė gali sumažėti iki 0.34, kai x = 0.06.

Straipsnis P8. „Balistinių fotosrovių sukelta THz impulsų emisija iš puslaidininkinių heterosandūrų"

Šiame darbe buvo matuojami TES spektrai apšviečiant heterostruktūrą iš platesnio draustinių energijų tarpo puslaidininkio pusės. Šiuo atveju TES spektre buvo matyti THz impulso fazės apsivertimas, ties energija, kai

elektronų, sužadintų siauresnio draustinių energijų tarpo puslaidininkio sluoksnyje, perteklinė energija yra pakankama įveikti laidumo juostos trūkio sukurtą barjerą. Norint šį procesą ištirti nuodugniau buvo atliktas teorinis tyrimas kuriame skaičiuotos susidarančios srovės analitiškai ir skaitiškai Monte Carlo metodu. Šie tyrimai parodė, jog elektronų perteklinei energijai esant žemiau barjero, fotosrovė kuriama tik siauresnio draustinių energijų tarpo sluoksnyje. Pasiekus energiją, kai barjeras įveikiamas fotosrovės atsiranda abiejuose heterosandūrą sudarančiose puslaidininkiuose - didesnė fotosrovė yra platesnio draustinių energijų tarpo puslaidininkyje. Kadangi ši fotosrovė yra priešingos krypties, tai pakeičia ir spinduliuojamo THz impulso poliarumą. Šis efektas buvo stebimas GaInAs/InP ir GaInAsBi/InP heterosandūrose.

Straipsnis P2. „THz impulsų emisija iš GaInAsBi“

Keturnariai GaInAsBi epitaksiniai sluoksniai buvo užauginti ant InP padėklo ir buvo panaudoti kaip THz impulsų emiteriai, juos žadinant mažomis femtosekundinio optinio impulso fotono energijomis (0.5 -1.2 eV). Šios medžiagos draustinių energijų tarpas buvo ~ 0.4 eV, o dėl pakankamai mažo gardelės neatitikimo su padėklu (~0.3 %) pakankamai stori ~ 600 nm sluoksniai buvo pilnai įtempti. THz impulsų generacijos priklausomybės nuo žadinamo bangos ilgio buvo matuojamos tiek iš sluoksnio paviršiaus, tiek iš ant to sluoksnio suformuotos fotolaidžios antenos. Šie tyrimai parodė, kad fotolaidžios antenos emisija buvo efektyviausia žadinant apie 2 μm bangos ilgio optiniais impulsais. Šis bangos ilgis gali būti pasiekiamas naujais tuliu ir helmiu legiruotais šviesolaidiniais femtosekundiniais lazeriais, o šiems lazeriams THz emiterių iki šiol nebuvo.

Netiesiatarpių puslaidininkių ir heksagoninės struktūros sluoksniuotų kristalų tyrimas

Straipsnis P3. „Spektrinės THz impulsų emisijos priklausomybės iš germanio kristalų“

1. Šiame darbe buvo tyrinėti skirtingo legiravimo germanio kristalai. Išmatuotame TES spektre buvo stebėta, jog THz impulsų generacija yra efektyviausia, kai fotono energija yra didesnė už tiesioginį draustinių energijų tarpą Briuljen‘o zonos Γ taške. THz impulsų generacija buvo stebima ir žadinant su fotonų energijomis žemesnėmis nei tiesioginis energijų tarpas. Tai buvo paaiškinta L slėnių izoenergetinių paviršių anizotropija, dėl kurios atsiranda šoninė fotosrovė, kurios kryptis yra priešinga fotosrovei sukurtai dėl optinės orientacijos. Tuo tarpu optinio

žadinimo – THz strobavimo metodika buvo nustatyta, kad elektronų sklaida iš Γ slėnio į žemesnio judrio L slėnį yra subpikosekundinės trukmės.

Straipsnis P5. „GaSe kristale sukelta THz impulsų emisija žadinant virš draustinių energijų tarpo“

Šiame darbe buvo tirtas kelių μm storio heksagoninės kristalinės struktūros GaSe THz impulso amplitudės priklausomybė nuo žadinančio fotono energijos, kuri buvo keičiama nuo 1.8 iki 3.8 eV. TES spektre rastos charakteringos energijos, atitinkančios THz generacijos pradžią ir jos efektyvumo maksimumą. Šios energijos buvo panaudotos tiesioginiam draustinių energijų tarpui ir laidumo juostos šoninio slėnio energijos padėčiai nustatyti. Kiek netikėtai, didinant žadinančio fotono energiją THz impulso amplitudė vėl pradėjo kilti. Dėl šios priežasties buvo atlikti papildomi azimutinio kampo priklausomybės ir TES spektrų priklausomybės nuo žadinančio optinio impulso poliarizacijos matavimai. Pastarieji eksperimentai parodė, jog dėl optinės atrankos taisyklių heksagoniniame kristale, priklausomai nuo kampo tarp žadinančio impulso elektrinio vektoriaus ir heksagoninio kristalo c – ašies, TES spektrai žadinant p ir s poliarizacijomis skirsis. Taip buvo nustatyta žemiau esančios antros valentinės juostos energinė padėtis GaSe kristale.

Straipsnis P6. „THz impulsų emisija iš pereinamųjų metalų dichalkogenidų kristalų“

Šiame darbe buvo tyrinėjami trys pereinamųjų metalų dichalkogenidų (TMD) kristalai: volframo diselenidas (WSe_2), molibdeno diselenidas ($MoSe_2$) ir molibdeno disulfidas (MoS_2). Šiose medžiagose buvo matuoti THz žadinimo spektrai ir sužadintų krūvininkų dinaminės charakteristikos. THz impulsų amplitudės nepriklausė nuo azimutinio kampo, taip pat nebuvo stebimas THz impulsas kuomet bandiniai buvo apšviečiami 0^o kritmo kampu. Todėl buvo padaryta išvada, kad generacijos mechanizmas yra susijęs su paviršinėmis fotosrovėmis, atsirandančiomis dėl vidinių laukų sluoksnių paviršiuje. Šie vidiniai elektriniai laukai gali susidaryti dėl vadinamųjų tamsiųjų eksitonų, atsirandančių kuomet elektronai ir skylės yra lokalizuoti skirtinguose sluoksniuose (tarpsluoksniniai eksitonai) ar vienas iš jų yra defekte. Šių laukų buvimą paliudijo atlikti papildomi eksperimentai žadinant bandinius dviem skirtingų bangos ilgių impulsais.

THz impulsų generacija iš polikristalinių ir kristalinių bismuto sluoksnių

Straipsnis P7. „Elektrochemiškai nusodintų plonų bismuto sluoksnių THz fotolaidumo spektrai”

Plonų polikristalinių Bi sluoksnių, elektrochemiškai nusodintų ant skirtingų tauriųjų metalų, TES spektrai beveik nepriklauso nuo padėklo medžiagos ir Bi sluoksnio storio. Tai leido daryti išvadą, jog THz impulsai yra generuojami prie pat bismuto paviršiaus dėl foto-Demberio efekto. Buvo palygintos iš bismuto generuojamo THz impulso fazė su n- ir p- tipo GaAs kristalais. Šis eksperimentas parodė, jog elektronai juda greičiau nei skylės nuo paviršiaus. Įprastai kristaliniuose puslaidininkiuose krūvininkų termalizacijos procesai vyksta pakankamai ilgai, tačiau pusmetaliniame bismute šis procesas yra spartesnis dėl stiprios tarpelektroninės sklaidos. Ši išvada buvo patvirtinta palyginus THz žadinimo spektrus, išmatuotus prie žadinančio spindulio kritimo kampų, su teorija.

Straipsnis 9. „THz impulsų emisija iš ultraplonų bismuto sluoksnių“

Šiame darbe buvo tyrinėjami ploni: apie 8 nm storio epitaksinio bismuto sluoksniai, užauginti ant (111) silicio padėklų MBE metodu. Šių bandinių THz impulsų amplitudė buvo daugiau nei eile didesnė už prieš tai tyrinėtų polikristalinio Bi bandinių, taip pat buvo stebima $\sin(3\varphi)$ tipo priklausomybė nuo azimutinio kampo. TES spektre generacija prasidėjo nuo 0.45 eV, tai leido daryti prielaida, jog tiesioginis draustinių energijų tarpas yra ties šia energija. Skirtingose temperatūrose auginti bandiniai turėjo skirtingus kristalinio sluoksnio ir apatinio polikristalinio sluoksnio santykius. Norint paaiškinti stebėtus eksperimentinius rezultatus buvo pasiūlytas naujas THz emisijos mechanizmas, aiškinantis emisijos atsiradimą sluoksnio plokštumoje tekančių dviem priešingomis kryptimis šoninių fotosrovių disbalanso, iššaukto vienos iš jų sklaida ties riba tarp kristalo ir polikristalinio sluoksnio.

Rezultatai ir išvados

1. Eksperimentiniai ir teoriniai rezultatai parodė, jog TES metodika yra tinkama nustatant heterosandūros energijos juostų trūkio vertes.
2. Atlikus TES matavimus buvo nustatytas GaAsBi/GaAs heterosandūros, kurioje yra iki 12 % bismuto, energijos juostų trūkio parametras $Q = 0.45 \pm 0.04$
3. $Ga_{0.47}In_{0.53}AsBi/InP$ heterosandūroje parametras $Q = 0.38 \pm 0.04$ buvo nustatytas esant bismuto kiekiui nuo 3 % iki 6 %. Bismuto sluoksnio įtempimas gali sumažinti Q vertes GaInAsBi/GaInAs heterosandūroje iki ~ 0.25 ± 0,03, kai Bi dalis yra apie 6 %.
4. Fotolaidi antena, pagaminta iš GaInAsBi sluoksnio užauginto ant InP padėklo, demonstravo didžiausią našumą ties 2 μm žadinimo bangos ilgiu.

5. Netiesiatarpiame germanio kristale THz impulsai yra efektyviausiai generuojami, kai žadinimo impulso fotonų energija sutampa su tiesioginio draustinių energijų tarpo energija.

6. TMD (MoS_2, $MoSe_2$, and WS_2) medžiagų tyrimai parodė, jog TES spektro maksimalios vertės sutampa su tiesioginiais draustinių energijų tarpais joje. THz impulsų generacija iš šių medžiagų vyksta dėl vidinių laukų sukurtos ultrasparčiai kintančios fotosrovės.

7. GaSe TES spektrai, išmatuoti naudojant skirtingos poliarizacijos optinius impulsus, leido nustatyti žemiau esančios valentinės juostos energetinę padėtį. Tuo pačiu buvo nustatytas tiesioginis draustinių energijų tarpas lygus – 2 ± 0.04 eV ir laidumo juostos šoninio slėnio energinis atstumas virš laidumo juostos dugno – 0.21 ± 0.02 eV

8. THz impulsų generacija elektrochemiškai nusodintuose plonuose bismuto sluoksniuose vyksta dėl foto-Demberio efekto, krūvininkų difuzijašiuo atveju buvo sub-ps eilės, dėl stiprios tarpelektroninės sklaidos.

9. Naujas THz emisijos mechanizmas paremtas šoninių fotosrovių atsiradimu, dėl elektronų sklaidos ties kristalo ir drėkinamojo polikristalinio sluoksnio sandūra, paaiškino THz impulsų generaciją ultraplonuose kristalinio bismuto sluoksniuose. THz emisijos slenkstis ties 0.45 ± 0.02 eV buvo priskirtas tiesioginiam draustinių energijų tarpui 8 nm storio Bi sluoksnyje.

REFERENCES

1. A. G. Davies, A. D. Burnett, W. Fan, E. H. Linfield, J. E. Cunningham, Terahertz spectroscopy of explosives and drugs. *Mater. Today*. **11**, 18–26 (2008).
2. S. Krimi, J. Klier, J. Jonuscheit, G. Von Freymann, R. Urbansky, R. Beigang, Highly accurate thickness measurement of multi-layered automotive paints using terahertz technology. *Appl. Phys. Lett.* **109**, 021105 (2016).
3. J. P. Guillet, M. Roux, K. Wang, X. Ma, F. Fauquet, H. Balacey, B. Recur, F. Darracq, P. Mounaix, Art Painting Diagnostic Before Restoration with Terahertz and Millimeter Waves. *J. Infrared, Millimeter, Terahertz Waves*. **38**, 369–379 (2017).
4. H. Cheon, H. J. Yang, J. H. Son, Toward Clinical Cancer Imaging Using Terahertz Spectroscopy. *IEEE J. Sel. Top. Quantum Electron.* **23**, 1–9 (2017).
5. C. Feng, C. Otani, Terahertz spectroscopy technology as an innovative technique for food : Current state-of- the-Art research advances. *Crit. Rev. Food Sci. Nutr.* **61**, 2523–2543 (2021).
6. J. True, C. Xi, N. Jessurun, K. Ahi, N. Asadizanjani, Review of THz-based semiconductor assurance. *Opt. Eng.* **60**, 060901 (2021).
7. J. B. Baxter, G. W. Guglietta, Terahertz spectroscopy. *Anal. Chem.* **83**, 4342–4368 (2011).
8. R. Adomavičius, G. Molis, A. Krotkus, V. Sirutkaitis, Spectral dependencies of terahertz emission from InAs and InSb. *Appl. Phys. Lett.* **87**, 1–3 (2005).
9. A. Arlauskas, A. Krotkus, THz excitation spectra of AIIIBV semiconductors. *Semicond. Sci. Technol.* **27**, 115015 (2012).
10. X. C. Zhang, D. H. Auston, Optoelectronic measurement of semiconductor surfaces and interfaces with femtosecond optics. *J. Appl. Phys.* **71**, 326–338 (1992).
11. G. Molis, A. Krotkus, V. Vaičaitis, Intervalley separation in the conduction band of InGaAs measured by terahertz excitation spectroscopy. *Appl. Phys. Lett.* **94**, 091104 (2009).
12. E. T. Yu, J. O. McCaldin, T. C. McGill, Band Offsets in Semiconductor Heterojunctions. *Solid State Phys. - Adv. Res. Appl.* **46**, 1–146 (1992).
13. V. L. Malevich, P. A. Ziaziulia, R. Adomavičius, A. Krotkus, Y. V. Malevich, Terahertz emission from cubic semiconductor induced by a transient anisotropic photocurrent. *J. Appl. Phys.* **112**, 073115 (2012).
14. R. Roldán, J. A. Silva-Guillén, M. P. López-Sancho, F. Guinea, E. Cappelluti, P. Ordejón, Electronic properties of single-layer and multilayer transition metal dichalcogenides MX_2 (M = Mo, W and X = S, Se). *Ann. Phys.* **526**, 347–357 (2014).

15. S. Demirci, N. Avazlı, E. Durgun, S. Cahangirov, Structural and electronic properties of monolayer group III monochalcogenides. *Phys. Rev. B*. **95**, 115409 (2017).
16. K. F. Mak, C. Lee, J. Hone, J. Shan, T. F. Heinz, Atomically thin MoS2: A new direct-gap semiconductor. *Phys. Rev. Lett.* **105**, 2–5 (2010).
17. Y. F. Ogrin, V. N. Lutskii, M. I. Elinson, Observation of Quantum Size Effects in Thin Bismuth Films. *JETP Lett.* **3**, 71 (1966).
18. Y. Ma, Y. Dai, L. Kou, T. Frauenheim, T. Heine, Robust two-dimensional topological insulators in methyl-functionalized bismuth, antimony, and lead bilayer films. *Nano Lett.* **15**, 1083–1089 (2015).
19. Y. S. Lee, *Principles of terahertz science and technology* (Springer, New York, 2009).
20. Gwyn P Williams, Filling the THz gap — high power sources and applications. *RE. Prog. Phys.* **69**, 301–326 (2006).
21. C. M. Armstrong, The truth about terahertz. *IEEE Spectr.* **49**, 36–41 (2012).
22. Laboratory of Terahertz Spectroscopy, Prague – Introduction, (available at https://lts.fzu.cz/en/intro.php).
23. R. Köhler, A. Tredicucci, F. Beltram, H. E. Beere, E. H. Linfield, A. G. Davies, D. A. Ritchie, R. C. Iotti, F. Rossi, Terahertz semiconductor-heterostructure laser. *Nature*, **417**, 156–159 (2002).
24. M. S. Vitiello, A. Tredicucci, Physics and technology of Terahertz quantum cascade lasers. *Adv. Phys. X*. **6** (2021).
25. A. Khalatpour, A. K. Paulsen, C. Deimert, Z. R. Wasilewski, Q. Hu, High-power portable terahertz laser systems. *Nat. Photonics 2020 151*. **15**, 16–20 (2020).
26. S. Komiyama, S. Kuroda, Far-infrared laser oscillation in p-Ge. *Solid State Commun.* **59**, 167–172 (1986).
27. A. Bergner, U. Heugen, E. Bründermann, G. Schwaab, M. Havenith, D. R. Chamberlin, E. E. Haller, New p-Ge THz laser spectrometer for the study of solutions: THz absorption spectroscopy of water. *Rev. Sci. Instrum.* **76**, 063110 (2005).
28. E. Bründermann, Widely Tunable Far-Infrared Hot-Hole Semiconductor Lasers. *Long-Wavelength Infrared Semicond. Lasers*, 279–350 (2005).
29. X. C. Zhang, X. F. Ma, Y. Jin, T. M. Lu, E. P. Boden, P. D. Phelps, K. R. Stewart, C. P. Yakymyshyn, Terahertz optical rectification from a nonlinear organic crystal. *Appl. Phys. Lett.* **61**, 3080–3082 (1992).
30. M. A. Belkin, F. Capasso, A. Belyanin, D. L. Sivco, A. Y. Cho, D. C. Oakley, C. J. Vineis, G. W. Turner, Terahertz quantum-cascade-laser source based on intracavity difference-frequency generation. *Nat. Photonics*, **1**, 288–292 (2007).
31. I. Mehdi, J. V. Siles, C. Lee, E. Schlecht, THz diode technology:

Status, prospects, and applications. *Proc. IEEE*. **105**, 990–1007 (2017).
32. K. Sengupta, T. Nagatsuma, D. M. Mittleman, Terahertz integrated electronic and hybrid electronic–photonic systems. *Nat. Electron.* **1**, 622–635 (2018).
33. Z. Hu, M. Kaynak, R. Han, High-Power Radiation at 1 THz in Silicon: A Fully Scalable Array Using a Multi-Functional Radiating Mesh Structure. *IEEE J. Solid-State Circuits*. **53**, 1313 (2018).
34. T. Hochrein, Markets, Availability, Notice, and Technical Performance of Terahertz Systems: Historic Development, Present, and Trends. *J. Infrared, Millimeter, Terahertz Waves*. **36**, 235–254 (2015).
35. H.-B. Liu, H. Zhong, N. Karpowicz, Y. Chen, X.-C. Zhang, Terahertz Spectroscopy and Imaging for Defense and Security Applications. *Proc. IEEE*. **95**, 1514–1527 (2007).
36. K. Ahi, S. Shahbazmohamadi, N. Asadizanjani, Quality control and authentication of packaged integrated circuits using enhanced-spatial-resolution terahertz time-domain spectroscopy and imaging. *Opt. Lasers Eng.* **104**, 274–284 (2018).
37. L. Wei, L. Yu, H. Jiaoqi, H. Guorong, Z. Yang, F. Weiling, Application of terahertz spectroscopy in biomolecule detection. *Front. Lab. Med.* **2**, 127–133 (2018).
38. A. I. Nikitkina, P. Y. Bikmulina, E. R. Gafarova, N. V. Kosheleva, Y. M. Efremov, E. A. Bezrukov, D. V. Butnaru, I. N. Dolganova, N. V. Chernomyrdin, O. P. Cherkasova, A. A. Gavdush, P. S. Timashev, Terahertz radiation and the skin: a review. *J Biomed Opt*. **26**, 043005 (2021).
39. M. H. Rahaman, A. Bandyopadhyay, S. Pal, K. P. Ray, Reviewing the Scope of THz Communication and a Technology Roadmap for Implementation. *IETE Tech. Rev.* **38**, 465–478 (2020).
40. H. J. Joyce, J. L. Boland, C. L. Davies, S. A. Baig, M. B. Johnston, A review of the electrical properties of semiconductor nanowires: Insights gained from terahertz conductivity spectroscopy. *Semicond. Sci. Technol.* **31** 103003 (2016).
41. M. C. Beard, G. M. Turner, C. A. Schmuttenmaer, Transient photoconductivity in GaAs as measured by time-resolved terahertz spectroscopy. *Phys. Rev. B.* **62**, 15764 (2000).
42. S. Dexheimer, *Terahertz spectroscopy: principles and applications* (CRC press, Boca Raton, 2008).
43. R. Huber, F. Tauser, A. Brodschelm, M. Bichler, G. Abstreiter, A. Leitenstorfer, How many-particle interactions develop after ultrafast excitation of an electron-hole plasma. *Nature*. **414**, 286–289 (2001).
44. D. H. Auston, Picosecond optoelectronic switching and gating in silicon. *Appl. Phys. Lett.* **26**, 101–103 (1975).
45. D. H. Auston, K. P. Cheung, P. R. Smith, Picosecond

photoconducting Hertzian dipoles. *Appl. Phys. Lett.* **45**, 284–286 (1984).
46. P. R. Smith, D. H. Auston, M. C. Nuss, Subpicosecond Photoconducting Dipole Antennas. *IEEE J. Quantum Electron.* **24**, 255–260 (1988).
47. C. Fattinger, D. Grischkowsky, Terahertz beams. *Appl. Phys. Lett.* **54**, 490–492 (1989).
48. S. Kono, M. Tani, P. Gu, K. Sakai, Detection of up to 20 THz with a low-temperature-grown GaAs photoconductive antenna gated with 15 fs light pulses. *Appl. Phys. Lett.* **77**, 4104 (2000).
49. J. A. Valdmanis, G. Mourou, C. W. Gabel, Picosecond electro-optic sampling system. *Appl. Phys. Lett.* **41**, 211–212 (1982).
50. K. Bertulis, A. Krotkus, G. Aleksejenko, V. Pačebutas, R. Adomavičius, G. Molis, S. Marcinkevičius, GaBiAs: A material for optoelectronic terahertz devices. *Appl. Phys. Lett.* **88**, 201112 (2006).
51. R. B. Kohlhaas, S. Breuer, S. Nellen, L. Liebermeister, M. Schell, M. P. Semtsiv, W. T. Masselink, B. Globisch, Photoconductive terahertz detectors with 105 dB peak dynamic range made of rhodium doped InGaAs. *Appl. Phys. Lett.* **114**, 221103 (2019).
52. B. Globisch, R. J. B. Dietz, R. B. Kohlhaas, T. Göbel, M. Schell, D. Alcer, M. Semtsiv, W. T. Masselink, Iron doped InGaAs: Competitive THz emitters and detectors fabricated from the same photoconductor. *J. Appl. Phys.* **121**, 053102 (2017).
53. D. Turchinovich, W. Zhang, Rigorous signal reconstruction in terahertz emission spectroscopy. *Opt. Express, Vol. 29, Issue 15, pp. 24411-24421*. **29**, 24411–24421 (2021).
54. B. Clough, J. Liu, X.-C. Zhang, "All air-plasma" terahertz spectroscopy. *Opt. Lett.* **36**, 2399–2401 (2011).
55. X. C. Zhang, B. B. Hu, J. T. Darrow, D. H. Auston, Generation of femtosecond electromagnetic pulses from semiconductor surfaces. *Appl. Phys. Lett.* **56**, 1011–1013 (1990).
56. B. V. Shishkin, D. A. Fadeev, E. V. Suvorov, I. E. Ilyakov, R. A. Akhmedzhanov, V. A. Mironov, Terahertz emission from a metallic surface induced by a femtosecond optic pulse. *Opt. Lett.* **37**, 2520–2522 (2012).
57. Q. Jin, J. Dai, E. Yiwen, X. C. Zhang, Terahertz wave emission from a liquid water film under the excitation of asymmetric optical fields. *Appl. Phys. Lett.* **113**, 261101 (2018).
58. M. D. Thomson, M. Kreß, T. Löffler, H. G. Roskos, Broadband THz emission from gas plasmas induced by femtosecond optical pulses: From fundamentals to applications. *Laser Photon. Rev.* **1**, 349–368 (2007).
59. M. S. Longair, *High Energy Astrophysics, 3rd edn., by Malcolm S. Longair* (Cambridge University Press, Cambridge, 2011).
60. V. L. Malevich, R. Adomavičius, A. Krotkus, THz emission from

semiconductor surfaces. *Comptes Rendus Phys.* **9**, 130–141 (2008).
61. R. Inoue, K. Takayama, M. Tonouchi, Angular dependence of terahertz emission from semiconductor surfaces photoexcited by femtosecond optical pulses. *Josa B.* **26**, A14–A22 (2009).
62. M. Nakajima, M. Hangyo, M. Ohta, H. Miyazaki, Polarity reversal of terahertz waves radiated from semi-insulating InP surfaces induced by temperature. *Phys. Rev. B - Condens. Matter Mater. Phys.* **67**, 1–7 (2003).
63. J. N. Heyman, N. Coates, A. Reinhardt, G. Strasser, Diffusion and drift in terahertz emission at GaAs surfaces. *Appl. Phys. Lett.* **83**, 5476 (2003).
64. C. S. Ponseca, A. Arlauskas, H. Yu, F. Wang, I. Nevinskas, E. Du Da, V. Vaičaitis, J. Eriksson, J. Bergqvist, X. K. Liu, M. Kemerink, A. N. Krotkus, O. Inganas, F. Gao, Pulsed Terahertz Emission from Solution-Processed Lead Iodide Perovskite Films. *ACS Photonics*. **6**, 1175–1181 (2019).
65. N. Woodward, C. Gallinat, L. E. Rodak, G. D. Metcalfe, H. Shen, M. Wraback, Enhanced THz emission from c-plane $In_xGa_{1-x}N$ due to piezoelectric field-induced electron transport. *Appl. Phys. Lett.* **100**, 191110 (2012).
66. I. Nevinskas, S. Stanionytė, V. Pačebutas, A. Krotkus, Terahertz emission from GaInAs p-i-n diodes photoexcited by femtosecond laser pulses. *Lith. J. Phys.* **55**, 274–279 (2015).
67. T. Dekorsy, H. Auer, H. Bakker, H. Roskos, H. Kurz, THz electromagnetic emission by coherent infrared-active phonons. *Phys. Rev. B.* **53**, 4005–4014 (1996).
68. T. Dekorsy, H. Auer, C. Waschke, H. J. Bakker, H. G. Roskos, H. Kurz, V. Wagner, P. Grosse, Emission of Submillimeter Electromagnetic Waves by Coherent Phonons. *Phys. Rev. Lett.* **74**, 738 (1995).
69. V. Apostolopoulos, M. E. Barnes, THz emitters based on the photo-Dember effect. *J. Phys. D. Appl. Phys.* **47**, 374002 (2014).
70. P. Gow, S. A. Berry, D. McBryde, M. E. Barnes, H. E. Beere, D. A. Ritchie, V. Apostolopoulos, Multiple lateral photo-Dember terahertz emitters illuminated by a cylindrical micro-lens array. *Appl. Phys. Lett.* **103**, 252101 (2013).
71. C. Weiss, R. Wallenstein, R. Beigang, Magnetic-field-enhanced generation of terahertz radiation in semiconductor surfaces. *Appl. Phys. Lett.* **77**, 4160–4162 (2000).
72. M. B. Johnston, D. M. Whittaker, A. Corchia, A. G. Davies, E. H. Linfield, Simulation of terahertz generation at semiconductor surfaces. *Phys. Rev. B.* **65**, 165301 (2002).
73. V. L. Malevich, R. Adomavičius, A. Krotkus, THz emission from semiconductor surfaces. *Comptes Rendus Phys.* **9**, 130–141 (2008).
74. P. Gu, M. Tani, S. Kono, K. Sakai, X. C. Zhang, Study of terahertz

radiation from InAs and InSb. *J. Appl. Phys.* **91**, 5533–5537 (2002).
75. M. C. Nuss, D. H. Auston, F. Capasso, Direct Subpicosecond Measurement of Carrier Mobility of Photoexcited Electrons in Gallium Arsenide. *Phys. Rev. Lett.* **58**, 2355 (1987).
76. A. Reklaitis, Terahertz emission from InAs induced by photo-Dember effect: Hydrodynamic analysis and Monte Carlo simulations. *J. Appl. Phys.* **108**, 053102 (2010).
77. S. Kono, P. Gu, M. Tani, K. Sakai, Temperature dependence of terahertz radiation from n-type InSb and n-type InAs surfaces. *Appl. Phys. B Lasers Opt.* **71**, 901–904 (2000).
78. X. C. Zhang, Y. Jin, K. Yang, L. J. Schowalter, Resonant nonlinear susceptibility near the GaAs band gap. *Phys. Rev. Lett.* **69**, 2303–2306 (1992).
79. R. W. Boyd, *Nonlinear Optics* (Academic Press, Boston, ed. 3rd, 2008).
80. M. Bass, P. A. Franken, J. F. Ward, G. Weinreich, Optical Rectification. *Phys. Rev. Lett.* **9**, 446 (1962).
81. J. B. Khurgin, Optical rectification and terahertz emission in semiconductors excited above the band gap. *JOSA B*. **11**, 2492–2501 (1994).
82. M. Reid, I. V. Cravetchi, R. Fedosejevs, Terahertz radiation and second-harmonic generation from InAs: Bulk versus surface electric-field-induced contributions. *Phys. Rev. B - Condens. Matter Mater. Phys.* **72**, 1–9 (2005).
83. S. L. Chuang, S. Schmitt-Rink, B. I. Greene, P. N. Saeta, A. F. J. Levi, Optical rectification at semiconductor surfaces. *Phys. Rev. Lett.* **68**, 102 (1992).
84. A. Urbanowicz, A. Krotkus, R. Adomavičius, V. L. Malevich, Terahertz emission from femtosecond laser excited Ge surfaces due to the electrical field-induced optical rectification. *Phys. B Condens. Matter*. **398**, 98–101 (2007).
85. A. Arlauskas, L. Subačius, A. Krotkus, V. L. Malevich, Terahertz emission from InSb illuminated by femtosecond laser pulses. *J. Phys. D. Appl. Phys.* **50**, 055101 (2017).
86. V. L. Malevich, A. Krotkus, A. Bičinas, V. Pačebutas, Terahertz emission from femtosecond laser illuminated (112) surfaces of InSb. *J. Appl. Phys.* **104**, 113117 (2008).
87. Y. V. Malevich, R. Adomavičius, A. Krotkus, V. L. Malevich, Anisotropic picosecond photoconductivity caused by optical alignment of electron momenta in cubic semiconductors. *J. Appl. Phys.* **115** (2014), doi:10.1063/1.4865961.
88. V. I. Zemskii, B. P. Zakharchenya, D. N. Mirlin, Polarization of hot photoluminescence in semiconductors of the GaAs type. *JETP lett.* **24**, 82–85 (1976).
89. B. P. Zakharchenya, D. N. Mirlin, V. I. Perel, I. I. Reshina, Optical

alignment of hot carriers in semiconductors. *Reshina, Sov. Phys. Usp.* **25**, 573–612 (1982).
90. C. V. Shank, B. P. Zakharchenya, *Spectroscopy of nonequilibrium electrons and phonons* (North-Holland, Amsterdam, 1992).
91. P. Cicėnas, A. Geižutis, V. L. Malevich, A. Krotkus, Terahertz radiation from an InAs surface due to lateral photocurrent transients. **40**, 5164–5167 (2015).
92. A. Krotkus, A. Trinkūnas, I. Nevinskas, K. Vizbaras, R. Butkutė, Terahertz pulse generation from (111)-cut InSb and InAs crystals when illuminated by 1.55 μm femtosecond laser pulses. *Opt. Lett.* **42**, 2615–2618 (2017).
93. M. van Exter, C. Fattinger, D. Grischkowsky, Terahertz time-domain spectroscopy of water vapor. *Opt. Lett.* **14**, 1128 (1989).
94. H. Němec, A. Pashkin, P. Kužel, M. Khazan, S. Schnüll, I. Wilke, Carrier dynamics in low-temperature grown GaAs studied by terahertz emission spectroscopy. *J. Appl. Phys.* **90**, 1303 (2001).
95. Jean-Louis Coutaz, Frederic Garet, Vincent P Wallace, *Principle of Terahertz Time-Domain Spectroscopy* (Jenny Stanford Publishing, New York, 2018).
96. M. C. Beard, G. M. Turner, C. A. Schmuttenmaer, Subpicosecond carrier dynamics in low-temperature grown GaAs as measured by time-resolved terahertz spectroscopy. *J. Appl. Phys.* **90**, 5915 (2001).
97. A. Krotkus, Semiconductors for terahertz photonics applications. *J. Phys. D. Appl. Phys.* **43**, 273001 (2010).
98. R. V. Mikhaylovskiy, E. Hendry, V. V. Kruglyak, R. V. Pisarev, T. Rasing, A. V. Kimel, Terahertz emission spectroscopy of laser-induced spin dynamics in $TmFeO_3$ and $ErFeO_3$ orthoferrites. *Phys. Rev. B - Condens. Matter Mater. Phys.* **90**, 184405 (2014).
99. R. Adomavičius, A. Urbanowicz, G. Molis, A. Krotkus, E. Šatkovskis, Terahertz emission from p-lnAs due to the instantaneous polarization. *Appl. Phys. Lett.* **85**, 2463 (2004).
100. A. Corchia, R. McLaughlin, M. B. Johnston, D. M. Whittaker, D. D. Arnone, E. H. Linfield, A. G. Davies, M. Pepper, Effects of magnetic field and optical fluence on terahertz emission in gallium arsenide. *Phys. Rev. B*. **64**, 205204 (2001).
101. D. S. Rana, M. Tonouchi, Terahertz Emission Functionality of High-Temperature Superconductors and Similar Complex Systems. *Adv. Opt. Mater.* **8**, 1900892 (2020).
102. Y. Huang, Z. Yao, C. He, L. Zhu, L. Zhang, J. Bai, X. Xu, Terahertz surface and interface emission spectroscopy for advanced materials. *J. Phys. Condens. Matter*. **31**, 153001 (2019).
103. L. Braun, G. Mussler, A. Hruban, M. Konczykowski, T. Schumann, M. Wolf, M. Münzenberg, L. Perfetti, T. Kampfrath, Ultrafast photocurrents at the surface of the three-dimensional topological insulator Bi_2Se_3. *Nat. Commun.* **7**, 1–9 (2016).

104. A. Arlauskas, J. Treu, K. Saller, I. Beleckaite, G. Koblmüller, A. Krotkus, Strong terahertz emission and its origin from catalyst-free InAs nanowire arrays. *Nano Lett.* **14**, 1508–1514 (2014).
105. K. S. Novoselov, V. I. Fal'Ko, L. Colombo, P. R. Gellert, M. G. Schwab, K. Kim, A roadmap for graphene. *Nature*. **490**, 192–200 (2012).
106. X. Xu, N. M. Gabor, J. S. Alden, A. M. Van Der Zande, P. L. McEuen, Photo-thermoelectric effect at a graphene interface junction. *Nano Lett.* **10**, 562–566 (2010).
107. L. Prechtel, L. Song, D. Schuh, P. Ajayan, W. Wegscheider, A. W. Holleitner, Time-resolved ultrafast photocurrents and terahertz generation in freely suspended graphene. *Nat. Commun. 2012 31*. **3**, 1–7 (2012).
108. J. Maysonnave, S. Huppert, F. Wang, S. Maero, C. Berger, W. De Heer, T. B. Norris, L. A. De Vaulchier, S. Dhillon, J. Tignon, R. Ferreira, J. Mangeney, Terahertz generation by dynamical photon drag effect in graphene excited by femtosecond optical pulses. *Nano Lett.* **14**, 5797–5802 (2014).
109. Y. M. Bahk, G. Ramakrishnan, J. Choi, H. Song, G. Choi, Y. H. Kim, K. J. Ahn, D. S. Kim, P. C. M. Planken, Plasmon enhanced terahertz emission from single layer graphene. *ACS Nano*. **8**, 9089–9096 (2014).
110. K. Si, Y. Huang, Q. Zhao, L. Zhu, L. Zhang, Z. Yao, X. Xu, Terahertz surface emission from layered semiconductor WSe_2. *Appl. Surf. Sci.* **448**, 416–423 (2018).
111. D. I. Khusyainov, A. V. Gorbatova, A. M. Buryakov, E. D. Mishina, THz surface emission from bulk and monolayer WSe_2. *AIP Conf. Proc.* **2359**, 020016 (2021).
112. J. Chang, H. Wang, Z. Lei, W. Du, Y. Huang, Y. Zhou, L. Zhu, X. Xu, Coherent Elliptically Polarized Terahertz Wave Generation in WSe_2 by Linearly Polarized Femtosecond Laser Excitation. *J. Phys. Chem. Lett.* **12**, 10068–10078 (2021).
113. L. Zhang, Y. Huang, Q. Zhao, L. Zhu, Z. Yao, Y. Zhou, W. Du, X. Xu, Terahertz surface emission of d -band electrons from a layered tungsten disulfide crystal by the surface field. *Phys. Rev. B*. **96**, 155202 (2017).
114. L. Zhang, Y. Huang, L. Zhu, Z. Yao, Q. Zhao, W. Du, Y. He, X. Xu, Polarized THz Emission from In-Plane Dipoles in Monolayer Tungsten Disulfide by Linear and Circular Optical Rectification. *Adv. Opt. Mater.* **7**, 1801314 (2019).
115. Z. Fan, M. Xu, Y. Huang, Z. Lei, L. Zheng, Z. Zhang, W. Zhao, Y. Zhou, X. Wang, X. Xu, Z. Liu, Terahertz Surface Emission from $MoSe_2$ at the Monolayer Limit. *ACS Appl. Mater. Interfaces*. **12**, 48161–48169 (2020).
116. D. Yagodkin, L. Nádvorník, O. Gueckstock, C. Gahl, T. Kampfrath,

K. I. Bolotin, Ultrafast photocurrents in $MoSe_2$ probed by terahertz spectroscopy. *2D Mater.* **8**, 025012 (2021).
117. Y. Huang, L. Zhu, Z. Yao, L. Zhang, C. He, Q. Zhao, J. Bai, X. Xu, Terahertz Surface Emission from Layered MoS2 Crystal: Competition between Surface Optical Rectification and Surface Photocurrent Surge. *J. Phys. Chem. C*. **122**, 481–488 (2017).
118. Y. Huang, A. Yartsev, S. Guan, L. Zhu, Q. Zhao, Z. Yao, C. He, L. Zhang, J. Bai, J. W. Luo, X. Xu, Hidden spin polarization in the centrosymmetric MoS_2 crystal revealed via elliptically polarized terahertz emission. *Phys. Rev. B*. **102**, 085205 (2020).
119. A. Chaves, J. G. Azadani, H. Alsalman, D. R. da Costa, R. Frisenda, A. J. Chaves, S. H. Song, Y. D. Kim, D. He, J. Zhou, A. Castellanos-Gomez, F. M. Peeters, Z. Liu, C. L. Hinkle, S. H. Oh, P. D. Ye, S. J. Koester, Y. H. Lee, P. Avouris, X. Wang, T. Low, Bandgap engineering of two-dimensional semiconductor materials. *npj 2D Mater. Appl.* **4**, 1–21 (2020).
120. E. Y. Ma, B. Guzelturk, G. Li, L. Cao, Z. X. Shen, A. M. Lindenberg, T. F. Heinz, Recording interfacial currents on the subnanometer length and femtosecond time scale by terahertz emission. *Sci. Adv.* **5**, eaau0073 (2019).
121. L. Zhang, Z. Chen, R. Zhang, Y. Tan, T. Wu, M. Shalaby, R. Xie, J. Xu, Direct Observation of Charge Injection of Graphene in the Graphene/WSe_2 Heterostructure by Optical-Pump Terahertz-Probe Spectroscopy. *ACS Appl. Mater. Interfaces*. **11**, 47501–47506 (2019).
122. H. Choi, T. H. Kim, J. Chae, J. Baeck, C. S. Kee, K. H. Jeong, H. S. Jeong, C. Kang, M. H. Cho, Evolution of the surface state in Bi2Se2Te thin films during phase transition. *Nanoscale*. **7**, 14924–14936 (2015).
123. I. Beleckaitė, J. Treu, S. Morkötter, M. Döblinger, X. Xu, R. Adomavičius, J. J. Finley, G. Koblmüller, A. Krotkus, Enhanced THz emission efficiency of composition-tunable InGaAs nanowire arrays. *Appl. Phys. Lett.* **110**, 201106 (2017).
124. R. Adomavičius, I. Nevinskas, J. Treu, X. Xu, G. Koblmüller, A. Krotkus, Pulsed THz emission from wurtzite phase catalyst-free InAs nanowires. *J. Phys. D. Appl. Phys.* **53**, 19LT01 (2020).
125. I. Nevinskas, K. Vizbaras, A. Vizbaras, A. Trinkunas, A. Krotkus, Magnetic field enhanced terahertz pulse emission from a femtosecond laser excited GaSb epitaxial layer. *Electron. Lett.* **52**, 1627–1629 (2016).
126. J. B. Héroux, M. Kuwata-Gonokami, Photoexcited Carrier Dynamics in InAs, GaAs, and InSb Probed by Terahertz Excitation Spectroscopy. *Phys. Rev. Appl.* **7**, 054001 (2017).
127. M. Yamashita, C. Otani, K. Kawase, K. Nikawa, M. Tonouchi, Noncontact inspection technique for electrical failures in semiconductor devices using a laser terahertz emission microscope.

Appl. Phys. Lett. **93**, 041117 (2008).
128. T. Kiwa, M. Tonouchi, M. Yamashita, K. Kawase, Laser terahertz-emission microscope for inspecting electrical faults in integrated circuits. *Opt. Lett.* **28**, 2058 (2003).
129. H. Nakanishi, S. Fujiwara, K. Takayama, I. Kawayama, H. Murakami, M. Tonouchi, Imaging of a polycrystalline silicon solar cell using a laser terahertz emission microscope. *Appl. Phys. Express*. **5**, 112301 (2012).
130. M. Yamashita, K. Kawase, C. Otani, Imaging of large-scale integrated circuits using laser terahertz emission microscopy. *Optics Express* **13**, 115–120 (2005).
131. T. Mochizuki, I. Kawayama, M. Tonouchi, Y. Nishihara, M. Chikamatsu, Y. Yoshida, H. Takato, Instantaneous Photocarrier Transport at the Interface in Perovskite Solar Cells to Generate Photovoltage. *Photonics*. **9**, 316 (2022).
132. T T. Umegaki, S. Hamauchi, Y. Sakai, A. Ito, H. Nakanishi, I. Kawayama, H. Murakami, M. Tonouchi, 2015 40th International Conference on Infrared, Millimeter, and Terahertz waves (IRMMW-THz) 1-2 (2015). DOI: 10.1109/IRMMW-THz.2015.7327592
133. K. Miyagawa, M. Nagai, G. Yamashita, M. Ashida, C. Kim, H. Akiyama, Y. Kanemitsu, Quantitative monitoring of the internal field in the depletion layer of a GaAs-based solar cell with terahertz radiation. *Appl. Phys. Lett.* **113**, 163501 (2018).
134. H. Nakanishi, A. Ito, K. Takayama, I. Kawayama, H. Murakami, M. Tonouchi, Comparison between laser terahertz emission microscope and conventional methods for analysis of polycrystalline silicon solar cell. *AIP Adv.* **5**, 117129 (2015).
135. I. Vurgaftman, J. R. Meyer, L. R. Ram-Mohan, Band parameters for III-V compound semiconductors and their alloys. *J. Appl. Phys.* **89**, 5815–5875 (2001).
136. A. Franciosi, C. G. Van De Walle, Heterojunction band offset engineering. *Surf. Sci. Rep.* **25**, 1–140 (1996).
137. F. Capasso, G. Margaritondo, *Heterojunction band discontinuities : physics and device applications* (North-Holland, Amsterdam, 1987).
138. H. C. Kuo, J. M. Kuo, Y. C. Wang, C. H. Lin, H. Chen, G. E. Stillman, Determination of the Band Offset of GalnP- GaAs and AllnP- GaAs Quantum Wells by Optical Spectroscopy. *J. Electron. Mater.* **26**, 944–948 (1997).
139. K. W. Goossen, S. A. Lyon, K. Alavi, Conduction-band offset determination in GaAs-AlxGa1-xAs through measurement of infrared internal photoemission. *Phys. Rev. B.* **36**, 9370 (1987).
140. L. J. Brillson, Surfaces and Interfaces: Atomic-Scale Structure, Band Bending and Band Offsets. *Basic Prop. Semicond.*, 281–417 (1992).
141. C. Gao, X. Liu, X. Fang, B. Li, M. Qiu, Q. Zhang, H. Zhang, H. Zhao, D. Wang, D. Fang, Y. Zhai, X. Chu, J. Li, X. Wang, Band

offset measurement at the $MAPbBr_3/Al_2O_3$ heterointerface by X-ray photoelectron spectroscopy. *J. Alloys Compd.* **920**, 165911 (2022).
142. W. Yi, A. J. Stollenwerk, V. Narayanamurti, Ballistic electron microscopy and spectroscopy of metal and semiconductor nanostructures. *Surf. Sci. Rep.* **64**, 169–190 (2009).
143. S. J. Sweeney, S. R. Jin, Bismide-nitride alloys: Promising for efficient light emitting devices in the near- and mid-infrared. *J. Appl. Phys.* **113**, 043110 (2013).
144. J. P. Petropoulos, Y. Zhong, J. M. O. Zide, Optical and electrical characterization of InGaBiAs for use as a mid-infrared optoelectronic material. *Appl. Phys. Lett.* **99**, 031110 (2011).
145. M. Usman, C. A. Broderick, A. Lindsay, E. P. O'Reilly, Tight-binding analysis of the electronic structure of dilute bismide alloys of GaP and GaAs. *Phys. Rev. B - Condens. Matter Mater. Phys.* **84**, 1–13 (2011).
146. S. Jin, S. J. Sweeney, InGaAsBi alloys on InP for efficient near-and mid-infrared light emitting devices. *J. Appl. Phys.* **114**, 213103 (2013).
147. Y. Tominaga, K. Oe, M. Yoshimoto, Low temperature dependence of oscillation wavelength in $GaAs_{1-x}Bi_x$ laser by photo-pumping. *Appl. Phys. Express.* **3**, 062201 (2010).
148. I. P. Marko, S. J. Sweeney, Progress Toward III-V Bismide Alloys for Near- and Midinfrared Laser Diodes. *IEEE J. Sel. Top. Quantum Electron.* **23**, 1501512 (2017).
149. Y. Liu, X. Yi, N. J. Bailey, Z. Zhou, T. B. O. Rockett, L. W. Lim, C. H. Tan, R. D. Richards, J. P. R. David, Valence band engineering of GaAsBi for low noise avalanche photodiodes. *Nat. Commun.* **12**, 1–8 (2021).
150. R. B. Lewis, D. A. Beaton, X. Lu, T. Tiedje, $GaAs_{1-x}Bi_x$ light emitting diodes. *J. Cryst. Growth*. **311**, 1872–1875 (2009).
151. T. Thomas, A. Mellor, N. P. Hylton, M. Fuhrer, D. Alonso-Àlvarez, A. Braun, N. J. Ekins-Daukes, J. P. R. David, S. J. Sweeney, Requirements for a GaAsBi 1 eV sub-cell in a GaAs-based multi-junction solar cell. *Semicond. Sci. Technol.* **30**, 094010 (2015).
152. K. Radhanpura, S. Hargreaves, R. A. Lewis, M. Henini, The role of optical rectification in the generation of terahertz radiation from GaBiAs. *Appl. Phys. Lett.* **94**, 251115 (2009).
153. C. P. Vaisakh, A. Mascarenhas, R. N. Kini, THz generation mechanisms in the semiconductor alloy, $GaAs_{1-x}Bi_x$. *J. Appl. Phys.* **118**, 165702 (2015).
154. R. Kudrawiec, J. Kopaczek, M. P. Polak, P. Scharoch, M. Gladysiewicz, J. Misiewicz, R. D. Richards, F. Bastiman, J. P. R. David, Experimental and theoretical studies of band gap alignment in $GaAs_{1-x}Bi_x/GaAs$ quantum wells. *J. Appl. Phys.* **116**, 233508 (2014).
155. S. Jin, S. John Sweeney, InGaAsBi alloys on InP for efficient near-

and mid-infrared light emitting devices. *J. Appl. Phys.* **114**, 213103 (2013).
156. M. Gladysiewicz, R. Kudrawiec, M. S. Wartak, 8-band and 14-band *kp* modeling of electronic band structure and material gain in Ga(In)AsBi quantum wells grown on GaAs and InP substrates. *J. Appl. Phys.* **118**, 055702 (2015).
157. V. Aninkevičius, V. Bareikis, R. Katilius, J. Liberis, I. Matulionienė, A. Matulionis, P. Sakalas, R. Šaltis, Γ-X intervalley-scattering time constant for GaAs estimated from hot-electron noise spectroscopy data. *Phys. Rev. B*. **53**, 6893 (1996).
158. A. Arlauskas, thesis, Vilnius University (2015).
159. A. Dargys, J. Kundrotas, *Handbook of physical properties of Ge, Si, GaAs and InP* (Science and Encyclopedia Publischers, Vilnius, 1994).
160. G. Feng, M. Yoshimoto, K. Oe, A. Chayahara, Y. Horino, New III-V semiconductor InGaAsBi alloy grown by molecular beam epitaxy. *Jpn. J. Appl. Phys.* **44**, L1161 (2005).

COPIES OF PUBLICATIONS

The main results of the thesis were published in 9 scientific papers:

Paper 1 [P1]

V. Karpus, **R. Norkus**, R. Butkutė, S. Stanionytė, B. Čechavičius, and A. Krotkus, "THz-excitation spectroscopy technique for band-offset determination" *Opt. Express* 26, 33807-33817 (2018)

DOI: 10.1364/OE.26.033807

The article can be accessed online at https://doi.org/10.1364/OE.26.033807

Research Article | Vol. 26, No. 26 | 24 Dec 2018 | OPTICS EXPRESS 33807
Optics EXPRESS

THz-excitation spectroscopy technique for band-offset determination

V. KARPUS,* R. NORKUS, R. BUTKUTĖ, S. STANIONYTĖ, B. ČECHAVIČIUS, AND A. KROTKUS

Optoelectronics Department, Center for Physical Sciences and Technology, Saulėtekio 3, LT-10257 Vilnius, Lithuania
**vytas.karpus@ftmc.lt*

Abstract: The experimental THz-excitation spectroscopy technique for determining heterojunction band offsets is suggested. When photoexcited electrons gain sufficient energy to pass the potential barrier corresponding to a conduction band offset, an amplitude of THz-emission pulse sharply increases, which allows for direct measurements of the offset value. The technique is applied for determining GaAsBi-GaAs band offsets. The deduced conduction band offset of GaAsBi-GaAs heterojunction has about 45% of an energy gap difference at the Bi concentrations $x < 0.12$ investigated.

1. Introduction

The conduction and valence band offsets, ΔE_c and ΔE_v, at a heterojunction of two semiconductors set up the potential barriers for electrons and holes, which essentially affect performance of practically all contemporary micro- and opto-electronic devices. The band alignment problem, due to its importance both for solid-state physics and device engineering, is widely investigated (see, e. g., reviews [1–5]) theoretically and by various experimental techniques – optical spectroscopy, photoemission spectroscopy, transport methods, and ballistic electron emission microscopy. The principle instrumental tool is the optical spectroscopy of quantum wells (QW). However, the energies of interband transitions between QW electron and hole subbands are not sufficiently sensitive to band-offset values – different ratios of the conduction band offset to the energy gap difference, $Q = \Delta E_c/\Delta E_g$, usually correspond to similar sets of the interband-transition energies. As a result, a reliable determination of band offsets for a given heterostructure is not a straightforward task and usually requires integrated studies by optical and other, more sensitive to band-offsets, techniques.

In the present paper we suggest a novel technique for a direct band-offset determination based on a terahertz excitation spectroscopy (TES). The THz emission in semiconductors is due to a spacial separation of charge carriers photoexcited by a short laser pulse. When charge carriers are photoexcited in a heterostructure of semiconductors, an amplitude of the emitted THz-pulse will experience a sharp increase at the photon energies when photoelectrons (holes) gain sufficient kinetic energies to overcome the potential barrier corresponding to a heterojunction band-offset (Fig. 1). This allows for a direct determination of band-offsets from the spectral positions of THz-emission onsets.

The TES technique assumes ballistic propagation of photoexcited carriers in a thin enough layer of a narrower-gap semiconductor. The layer width should be smaller either than the optical penetration length, for photocarriers to be uniformly distributed, or than the distance the carriers travel while THz-pulse emission takes place.

In the present study, the TES technique is applied for a determination of band offsets of GaAsBi-GaAs heterojunction. The dilute bismides – the III-V semiconductors with a few percent of Bi – are in a focus of recent theoretical and experimental studies, which are motivated by a potential use of bismides in GaAs-based near-IR photodetectors, highly-efficient solar cells [6],

#346941 https://doi.org/10.1364/OE.26.033807
Journal © 2018 Received 27 Sep 2018; revised 4 Nov 2018; accepted 13 Nov 2018; published 12 Dec 2018

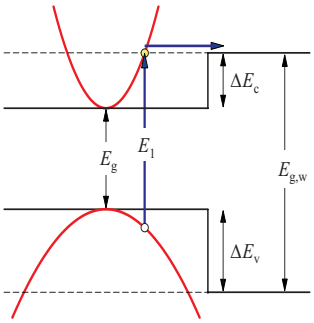

Fig. 1. Scheme of optical transitions corresponding to the threshold photon energy E_1 for THz-emission. The THz pulse is emitted when an electron excess energy is sufficient to overcome the ΔE_c potential barrier.

and laser diodes with reduced temperature-sensitivity of emission-wavelength [7]. Despite the wide-range studies, the GaAsBi-GaAs band offsets are not unambiguously determined. Our measurements, carried out by TES technique, show that the GaAsBi-GaAs conduction band offset is of about 45 % of the bandgap difference at Bi content up to about 12 %.

2. THz excitation spectroscopy

The main mechanism of THz emission in semiconductors is due to a spacial separation of electrons and holes photoexcited by a short, typically ~ 100 fs, laser pulse. The photoexcited electrons move quasi-ballistically leaving less-mobile holes behind themselves and, as a result, induce a dynamically varying electric dipole that eventually leads to a THz-pulse emission [8]. In a bulk semiconductor, the THz-pulse is generated when a photon energy of the laser pulse exceeds the energy gap of semiconductor [9], $\hbar\omega \geq E_g$.

When a heterostructure comprised of two different-bandgap materials, with a thin narrower-bandgap material at a surface, is illuminated, the THz-emission will be generated when photoexcited charge carriers in a top (surface) layer will gain an excess energy to pass the potential barrier corresponding to a conduction (valence) band offset (Fig. 1). Indeed, when the thickness of a top layer is much smaller than the optical absorption depth, photoexcited electrons and holes will be uniformly distributed in the layer. The energy barriers at the heterojunction will prevent their spatial separation, and no electric dipole and subsequent THz-pulse will be generated. With an increase of the exciting photon energy, photoexcited electrons will eventually gain energy enough to pass to the widegap semiconductor and an onset of THz-emission will start at the threshold energy $\hbar\omega = E_1$ which is determined by the conduction band offset ΔE_c,

$$E_1 = E_g + \Delta E_c \left(1 + \frac{m}{m_h}\right). \quad (1)$$

Here E_g is the bandgap of a top-layer semiconductor, m and m_h are the effective electron and hole masses. As it is seen from Eq. (1), the band offset can be directly determined from the spectral position of THz-emission onset.

2.1. Onset of THz-emission

The amplitude of THz-emission pulse is proportional to the electron (hole) flux density along the heterojunction normal (taken as the z-axis),

$$j_z = \frac{2}{(2\pi)^3}\int_{(v_z>0)} \mathrm{d}^3k\, v_z T(\varepsilon_\perp) f_{\boldsymbol{k}}. \tag{2}$$

Here $v_z = \hbar k_z/m$ is the electron velocity along the z-axis, $f_{\boldsymbol{k}}$ is the electron distribution function, and $T(\varepsilon_\perp)$ is the transmission coefficient of the potential barrier (see inset to Fig. 2),

$$T(\varepsilon_\perp) = \frac{4\sqrt{1-\frac{U}{\varepsilon_\perp}}}{\left(\sqrt{1-\frac{U}{\varepsilon_\perp}}+1\right)^2}, \tag{3}$$

$\varepsilon_\perp = \hbar^2 k_z^2/2m$ is the electron kinetic energy of the z-motion, and $U = \Delta E_c$ is the potential barrier corresponding to a conduction band offset.

The distribution function of electrons photoexcited by a short laser pulse is determined by the Gaussian energy-dependence $G(\varepsilon)$ and the angular dependence $F(\boldsymbol{n}_{\boldsymbol{k}})$, which is due to the optical orientation [10] of their quasimomenta $\boldsymbol{k}$,

$$f_{\boldsymbol{k}} = CG(\varepsilon)F(\boldsymbol{n}_{\boldsymbol{k}}), \quad G(\varepsilon) = \frac{1}{\sqrt{2\pi}s}\exp\left[-\frac{(\varepsilon-\varepsilon_0)^2}{2s^2}\right], \quad F(\boldsymbol{n}_{\boldsymbol{k}}) = 1+\alpha_0 P_2(\cos\chi). \tag{4}$$

Here $\varepsilon_0 = (\hbar\omega - E_g)/(1+m/m_h)$ is the electron energy, determined by the photon energy $\hbar\omega$ of the excitation pulse, $s = \sqrt{8\ln 2}\,\hbar(\Delta t)^{-1}/(1+m/m_h)$ is the standard deviation parameter determined by the pulse duration Δt, the α_0 parameter is equal to -1 or $+1$ for an electron excitation from heavy- and light-hole branches, correspondingly, $P_2(x)$ is the second Legendre polynomial, and χ is the angle between the $\boldsymbol{k}$-vector and the electric vector of the exciting light, $\cos\chi = \boldsymbol{n}_{\boldsymbol{k}}\boldsymbol{n}_{\boldsymbol{E}}$. The constant C of the distribution function in Eq. (4) is determined by the normalization condition $2(2\pi)^{-3}\int \mathrm{d}^3k\, f_{\boldsymbol{k}} = n$, where n is the concentration of photoexcited electrons, and can be expressed (at $\varepsilon_0 \gg s$) as $C = n/\varrho(\varepsilon_0)$, where $\varrho(\varepsilon_0) = 4\pi(2m)^{3/2}(2\pi\hbar)^{-3}\sqrt{\varepsilon_0}$ is the electron density of states at ε_0 energy.

The general expression (2) for the flux density, by integrating in the spherical coordinate system with the polar axis taken along z-direction, can be reduced to the form

$$j_z = j_0 A(\varepsilon_0), \quad j_0 = \frac{nU}{2\sqrt{2m\varepsilon_0}}, \quad A(\varepsilon_0) = \frac{2}{U}\int_0^\infty \mathrm{d}\varepsilon\, \varepsilon G(\varepsilon)\int_0^{\pi/2} \mathrm{d}\vartheta\, \sin\vartheta\cos\vartheta\, T(\varepsilon_\perp)\overline{F}. \tag{5}$$

Here $\overline{F}$ is the $F(\boldsymbol{n}_{\boldsymbol{k}})$ function averaged over the azimuthal angle,

$$\overline{F} = \frac{1}{2\pi}\int_0^{2\pi} \mathrm{d}\varphi\, F(\boldsymbol{n}_{\boldsymbol{k}}) = 1+\frac{\alpha_0}{4}(1-3\cos^2\vartheta_{\boldsymbol{E}})(1-3\cos^2\vartheta), \tag{6}$$

$\vartheta_{\boldsymbol{E}}$ is the polar angle of the electric vector of exciting light pulse.

The introduced dimensionless $A(\varepsilon_0)$ function [Eq. (5)] determines an expected spectral shape of an onset of THz-emission. Neglecting the energy spread of photoexcited electrons ($s = 0$) and assuming that the transmission coefficient of potential barrier corresponds to the step function [$T(\varepsilon_\perp) = 0$, for $\varepsilon_\perp < U$, and $T(\varepsilon_\perp) = 1$, for $\varepsilon_\perp > U$], one obtains the linear onset of THz-emission (dashed line in Fig, 2), which is predicted by Eq. (5) at $\varepsilon_0 - U \ll U$,

$$A(\varepsilon_0) = \left[1-\frac{\alpha_0}{2}(1-3\cos^2\vartheta_{\boldsymbol{E}})\right]\frac{\varepsilon_0-U}{U} \propto \hbar\omega - E_1. \tag{7}$$

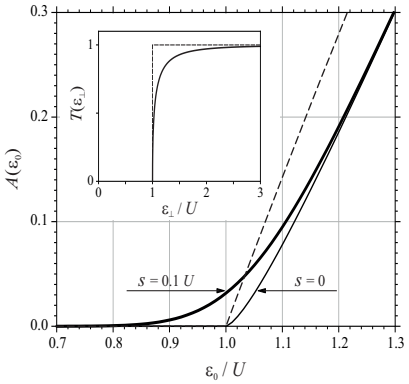

Fig. 2. The theoretical spectral shape of THz-emission onset: The $A(\varepsilon_0)$ function for an electron photoexcitation from the hh band ($\alpha_0 = -1$) at $\vartheta_{\boldsymbol{E}} = 80°$. The inset presents the transmission coefficient of potential barrier.

The energy dependence of the transmission coefficient (3) gives rise to a superlinear behavior of THz-emission onset (thinner full curve in Fig, 2), which can be successfully modeled by a power-law dependence

$$A(\varepsilon_0) \propto (\varepsilon_0 - U)^p \propto (\hbar\omega - E_1)^p \tag{8}$$

with the $p \approx 1.25$ exponent. At immediate vicinity to the $\varepsilon_0 = U$ energy, the onsets starts with the $p = 3/2$ exponent, which corresponds to an initial rise of the transmission coefficient (3). However, this holds true in a very short range of electron energies and subsequently the $A(\varepsilon_0)$ rise becomes less steep. The energy spread of photoexcited electrons ($s \neq 0$) smears the THz-emission edge by its Gaussian convolution, as it seen from the final theoretical spectral shape of the $A(\varepsilon_0)$ function presented by a thick full curve in Fig. 2.

3. Experimental

3.1. TES measurements

The THz excitation spectroscopy measurements have been carried out in the quasi-reflection geometry with samples illuminated at 45° to their surface normal. Experimental setup is shown schematically in Fig. 3. The setup is based on an amplified ytterbium-doped potassium gadolinium tungstate (Yb:KGW) laser system (PHAROS, Light Conversion Ltd.) operating at 1030 nm with the pulse duration of 160 fs and the pulse repetition rate of 200 kHz. Average power of 6 W from the laser is directed into a cavity-tuned optical parametric amplifier (OPA, ORPHEUS, Light Conversion Ltd.) that generates 140–160 fs duration pulses with a central wavelength tunable from 640 nm to 2600 nm. In the THz-TDS arrangement activated by the laser system, the investigated samples were excited by the OPA output beam, while the sample-emitted THz pulses were detected by the GaAsBi photoconducting antenna (TeraVil Ltd.). The THz detector was illuminated by a small fraction (average power of ~ 5 mW) of Yb:KGW-laser beam delayed by different times with respect to the optical beam exciting an investigated sample. All experiments were performed at room temperature. The average power of the optical pulses incident on a sample was of about 10 mW.

The THz pulses emitted by $GaAs_{0.941}Bi_{0.059}As$-GaAs heterostructure at the 1.19–1.89 eV photon energies of OPA beam and the pulse spectrum for $\hbar\omega = 1.89$ eV are presented in Fig. 4.

Optics EXPRESS

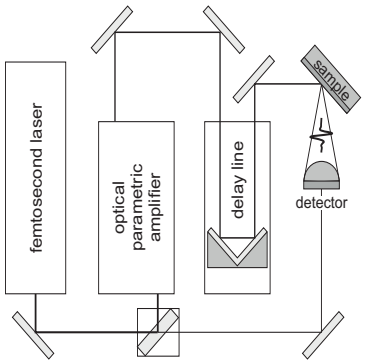

Fig. 3. Experimental setup for THz excitation spectroscopy measurements.

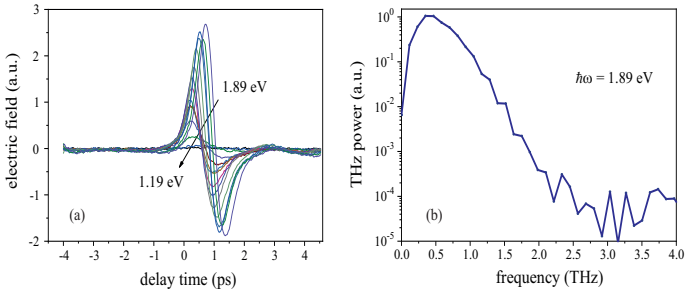

Fig. 4. THz pulses emitted by $GaAs_{0.941}Bi_{0.059}As$-GaAs photoexcited by OPA beams with photon energies in the 1.19–1.89 eV range (a) and the Fourier spectrum of the pulse obtained for $\hbar\omega$ = 1.89 eV (b).

3.2. Growth of heterostructures

The GaAsBi-GaAs heterostructures were molecular-beam-epitaxy (MBE) grown on semi-insulating (001) GaAs substrates at temperatures between 320 and 350 °C. Prior to the bismide layer of d = 100 nm deposition, the native oxide of GaAs-wafer was removed at 630 °C temperature and under maximum arsenic flux. For smoothing of the wafer surface, a 10–20 nm thick GaAs buffer layer was grown. The atomic composition of the $GaAs_{1-x}Bi_x$ layer was varied by adjusting the growth temperature and/or the Bi to As molecular flux ratio.

3.3. Characterization of GaAsBi layers

The atomic compositions x, Bi contents, of the grown $GaAs_{1-x}Bi_x$ layers (Table 1) were determined by X-ray diffraction (XRD) measurements, carried out with SmartLab Rigaku diffractometer, by monitoring shifts of the (004) diffraction peak with respect to its position in GaAs [Fig. 5(a)] and by reciprocal space mapping (RSM) of the (115) diffraction peak.

The recorded RSM patterns clearly indicated [Fig. 5(b)] that epitaxial GaAsBi layers, which were of d = 100 nm thickness, remained to be strained even at the highest Bi content, x = 0.117,

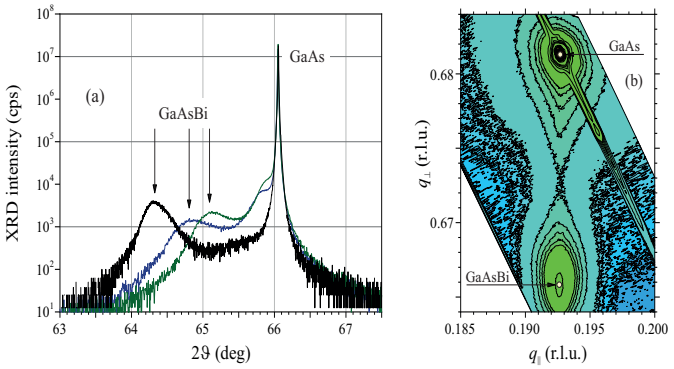

Fig. 5. (a) XRD rocking curves of the (004) diffraction peak of several GaAsBi-GaAs samples, x = 0.068, 0.086, and 0.117. (b) Reciprocal space map of the (115) diffraction peak of GaAsBi-GaAs sample with the highest Bi content, x = 0.117.

achieved in the present study. To determine atomic compositions of strained GaAsBi layers, the Vegard's law for the lattice constant of unstrained GaAsBi,

$$a_{\mathrm{GaAsBi}} = (1 - x)a_{\mathrm{GaAs}} + xa_{\mathrm{GaBi}}, \tag{9}$$

and the known expressions of strain-tensor components

$$\epsilon_{xx} = -\frac{\Delta a}{a}, \qquad \epsilon_{zz} = 2\frac{C_{12}}{C_{11}}\frac{\Delta a}{a} \tag{10}$$

were employed. Here a_{GaAs} = 5.653 Å and a_{GaBi} = 6.234 Å are the lattice constants of GaAs and GaBi [11], $\Delta a = a_{\mathrm{GaAsBi}} - a_{\mathrm{GaAs}}$, $a = (a_{\mathrm{GaAsBi}} + a_{\mathrm{GaAs}})/2$, C_{11} and C_{12} are the elastic constants, which were taken to be equal to those of GaAs [12], C_{11} = 122.1 GPa and C_{12} = 56.6 GPa.

The bandgaps of GaAsBi layers were determined from the spectral positions of their photoluminescence peaks, which were recorded by a standard PL setup with DPSS 532 nm excitation laser. The energy gaps determined (dots in Fig. 6) monotonously decrease with an increase of Bi content and follow the theoretical estimate of $E_{\mathrm{g}}(x)$ dependence (full curve in Fig. 6)

$$E_{\mathrm{g}}(x) = E_{\mathrm{g},0}(x) + (a_{\mathrm{c}} + a_{\mathrm{v}})(2\epsilon_{xx} + \epsilon_{zz}) + |b(\epsilon_{zz} - \epsilon_{xx})|\,. \tag{11}$$

Here $E_{\mathrm{g},0}(x)$ is the energy gap of bulk, unstrained GaAsBi [13], $a_{\mathrm{c}} = -7.17$ eV, $a_{\mathrm{v}} = -1.16$ eV, and $b = -2$ eV are the deformation potential constants (taken to be equal to those of GaAs).

4. GaAsBi-GaAs band-offsets

The band offsets of GaAsBi-GaAs heterojunction is a widely debated problem. The valence band anticrossing (VBAC) model shows [13] that a restructuring of $GaAs_{1-x}Bi_x$ valence band occurs as a result of an anticrossing interaction between the extended states of GaAs valence band and the resonant states of Bi atoms. In addition to the VBAC-induced valence band movement, the recent theoretical studies [14] have predicted that the conduction band also experiences shift, contributing to approximately 40 % of the GaAsBi-GaAs bandgap difference ΔE_{g}. Experimental data on the GaAsBi-GaAs conduction band offset are few and range from 23 %, as determined

Optics EXPRESS

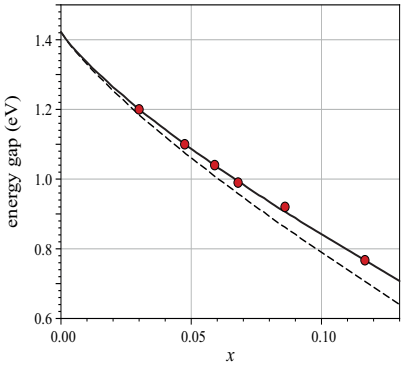

Fig. 6. Dependence of the $GaAs_{1-x}Bi_x$ bandgap on the atomic composition x. Full curve presents the theoretical estimate of strained-layer $E_g(x)$ dependence (11). Dashed curve corresponds to the bandgap dependence of unstrained, bulk GaAsBi [13].

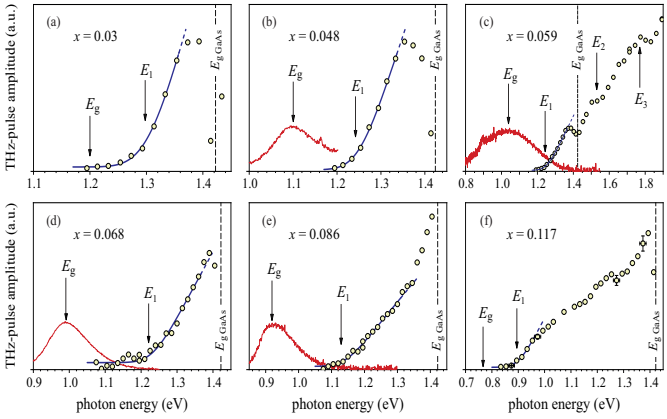

Fig. 7. THz-pulse excitation spectra (dots) of investigated GaAsBi-GaAs heterostructures. Red curves present photoluminescence spectra of the samples. Blue ones correspond to theoretical spectral shapes $A(\varepsilon_0)$ of THz-emission onset [Eq. (5)].

by X-ray photoemission spectroscopy [15] on samples with less than 2.5 % Bi, to nearly 48 % at 2.1 % < x < 5.9 %, as found from a photoreflectance study [16] of GaAsBi-GaAs quantum wells. Moreover, the authors of a recent multi-quantum well photoluminescence study [17] have suggested that GaAsBi-GaAs band offsets correspond to a staggered, type-II, rather than to a more common straddling, type-I, alignment.

The THz-pulse excitation spectra measured on GaAsBi-GaAs heterostructures are presented by dots in Fig. 7. As it is seen, an increase of the signal occurs at energies E_1 above the GaAsBi bandgap E_g and the spectral shape of THz-emission onsets is close to its theoretical estimate $A(\varepsilon_0)$ [Eq. (5), blue curves in Fig. 7]. Since the optical absorption coefficient in GaAsBi

layers does not exceed $2 \cdot 10^4$ cm^{-1} for photon energies up to about $E_g + 0.3$ eV [18, 19], the photoexcited electrons and holes are uniformly distributed in the investigated $d = 100$ nm GaAsBi layers, and THz-pulse is not generated until electrons gain sufficient energy to overcome the conduction-band-offset barrier.

With an increase of the photon energy, the THz-pulse amplitude experiences a drop at a photon energy of 1.42 eV, when a photoexcitation begins in GaAs substrate. With a further increase of $\hbar\omega$, the THz excitation spectrum shows [Fig. 7(c)] additional features E_2 and E_3 which are due to a photoexcitation of electrons in GaAsBi and GaAs layers with excess energies sufficient to pass to GaAs L-valleys [19].

Table 1. Physical parameters of $GaAs_{1-x}Bi_x$ layers (their atomic compositions x and bandgaps E_g), measured onsets of THz-emission E_1 and determined conduction band offsets ΔE_c of investigated GaAsBi-GaAs heterostructures.

x	0.03	0.048	0.059	0.068	0.086	0.117
E_g (eV)	1.2	1.1	1.04	0.99	0.92	0.77
E_1 (eV)	1.30 ±0.01	1.24 ±0.01	1.24 ±0.01	1.22 ±0.01	1.13 ±0.01	0.90 ±0.01
ΔE_c (eV)	0.09	0.13	0.18	0.21	0.19	0.12

The threshold energies of THz-emission E_1 can be determined by fitting the emission onsets with the $A(\varepsilon_0)$-function. The E_1 values obtained are presented in Table 1. The deduced value of the broadening parameter s was of about 36 meV.

The measured shifts of the THz-emission onsets from the bandgap values, $E_1 - E_g$, allow for a straightforward determination of the conduction band offsets [see Eq. (1)]. The values obtained at the $m = 0.067\, m_0$ and $m_h = 0.55\, m_0$ effective electron and hole mases (taken to be equal to those of GaAs) are presented in Table 1 and by open dots in Fig. 9.

The shifts of THz-emission onsets, as seen from Eq. (1), are related both with the band offsets and parameters of energy-band dispersions,– the effective electron and hole masses. Since the band dispersions are affected by strains, a determination of the strained-heterostructure band offsets, in principle, should be carried out taking into account the strain-induced band dispersions.

To estimate an influence of energy spectrum parameters on a band-offset determination, we modeled the strain-induced dispersion of the heavy- and light-hole branches by a simplest, 4×4 Hamiltonian approach [20],

$$\varepsilon_{1,2}(\boldsymbol{k}) = E_{v,0} - a_v(2\epsilon_{xx} + \epsilon_{zz}) - \frac{\hbar^2}{2m_0}\gamma_1 k^2 \mp \sqrt{\mathcal{E}_{\boldsymbol{k}} + \mathcal{E}_{\epsilon\boldsymbol{k}} + \mathcal{E}_{\epsilon}}, \tag{12}$$

$$\mathcal{E}_{\boldsymbol{k}} = \left(\frac{\hbar^2}{2m_0}\right)^2 \left[(2\gamma_2 k^2)^2 + 12(\gamma_3^2 - \gamma_2^2)(k_x^2 k_y^2 + k_y^2 k_z^2 + k_z^2 k_x^2)\right], \tag{13}$$

$$\mathcal{E}_{\epsilon\boldsymbol{k}} = \frac{\hbar^2}{2m_0} 2\gamma_2 b\,(k^2 - 3k_z^2)(\epsilon_{zz} - \epsilon_{xx}), \qquad \mathcal{E}_{\epsilon} = b^2(\epsilon_{zz} - \epsilon_{xx})^2, \tag{14}$$

and the conduction band dispersion by the Kane spectrum,

$$\varepsilon(\boldsymbol{k}) = E_c + \sqrt{\left(\frac{1}{2}E_g\right)^2 + P^2 k^2} - \frac{1}{2}E_g. \tag{15}$$

Here γ_1, γ_2, γ_3 are the Luttinger parameters and P is the Kane parameter.

Optics EXPRESS

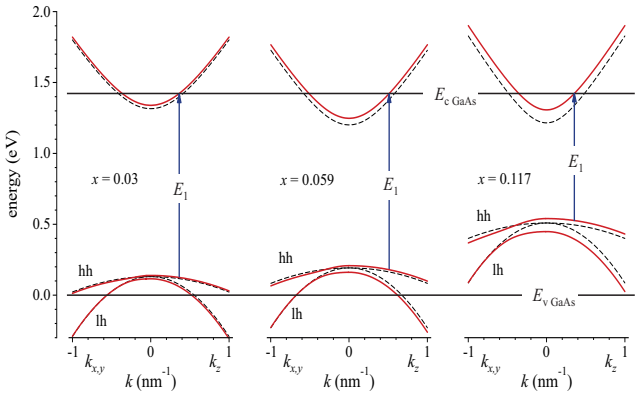

Fig. 8. Energy spectra of several investigated strained GaAsBi layers (thick curves). Dashed curves present spectra of unstrained GaAsBi.

The dispersion of energy bands for several of the investigated GaAsBi layers, calculated by Eqs. (12)–(15) at the $\gamma_1 = 6.98$, $\gamma_2 = 2.06$ and $2m_0P^2/\hbar^2 = 21.23$ eV parameter values (corresponding to those of GaAs), is presented in Fig. 8. The altered dispersion, at the chosen set of parameters, only slightly affected the band-offset values [small full dots in Fig. 9]. By varying the parameters within relevant limits, one can estimate the influence of the band dispersion parameters on the ΔE_c-determination accuracy to be below ~ 25 %.

The determined positions of the GaAsBi conduction and valence bands with respect to those of GaAs are presented graphically in Fig. 9. The band offsets for a given heterojunction of the type-I alignment are conventionally characterized by the Q-parameter which is defined as a ratio of the conduction band offset to a difference of the energy gaps in unstrained semiconductors, $Q = \Delta E_{c,0}/\Delta E_{g,0}$. The curves in Fig. 9 present estimates of the strained-GaAsBi energy band positions corresponding to the $Q = 0.45$ value. As it is seen, the experimental values closely follow the theoretical estimates what allows us to conclude that the conduction band offset of the GaAsBi-GaAs heterojunction, at the Bi concentrations $x < 12$ % investigated, is close to $Q = 0.45 \pm 0.05$. The $Q = 0.45$ value is very close to that, $Q = 0.48$, determined by Kudrawiec *et al.* [16] from a photoreflectance study of GaAsBi-GaAs quantum wells with $x < 5.9$ % bismuth concentrations.

5. Discussion

The determined GaAsBi-GaAs band offsets at the $x < 0.1$ bismuth concentrations, as it is seen from Fig. 9, are close to their values corresponding to $Q = 0.45$, while the offsets at $x = 0.117$ distinctly deviate from the $Q = 0.45$ estimates. Most probably this is due to the band bending effects induced by a redistribution of charge carriers in the $GaAs_{0.883}Bi_{0.117}$-GaAs heterostructure.

Although the MBE-grown epitaxial GaAsBi layers were not intentionally doped, an incorporation of Bi leads to a formation of acceptor levels (see, e. g., [21]) positioned up to 90 meV above the valence band edge [22]. The Hall coefficient R_H measurements carried out on investigated GaAsBi-GaAs samples indicated the $5 \cdot 10^{15}$ cm^{-3} hole concentration in the $x = 0.117$ sample and much lower, $1 \cdot 10^{11} - 5 \cdot 10^{14}$ cm^{-3}, effective charge carrier concentrations $n_H = -1/(ecR_H)$ in the $x = 0.03 - 0.086$ samples. The presumable energy diagram of the $GaAs_{0.883}Bi_{0.117}$-GaAs

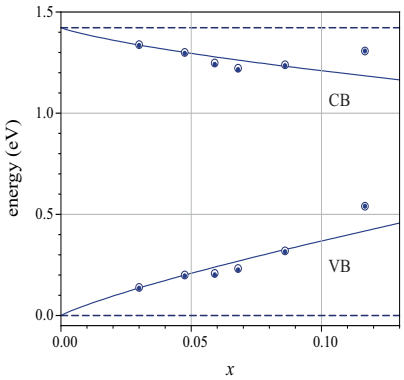

Fig. 9. Positions of the strained-GaAsBi conduction and valence bands (dots) with respect to those of GaAs (dashed lines). Large open and small full dots are obtained disregarding and taking into account an influence of strains on energy-band dispersions.

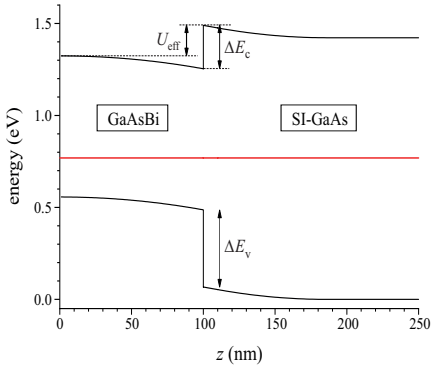

Fig. 10. Presumable energy diagram of the $GaAs_{0.883}Bi_{0.117}$-GaAs heterostructure.

heterostructure is presented in Fig. 10. The diagram was calculated under an assumption of the $N_A = 1 \cdot 10^{16}$ cm^{-3} acceptor concentration with the $\varepsilon_A = 90$ meV binding energy in the $d = 100$ nm GaAsBi layer and a standard doping of SI-GaAs substrate by deep EL2 donors, $N_D = 1.5 \cdot 10^{16}$ cm^{-3}, $\varepsilon_D = 0.684$ eV. (The intermediate $d = 10$ nm GaAs buffer layer was assumed to be undoped.) As seen from Fig. 10, the band bending in GaAsBi layer, ΔV, induced by a charge-carrier redistribution, reduces the potential barrier for electrons, $U_{eff} = \Delta E_c - \Delta V$. Taking into account the calculated $\Delta V = 0.07$ eV value, one obtains the corrected $GaAs_{0.883}Bi_{0.117}$-GaAs conduction band offset of 0.19 eV which is close to the 0.24 eV value expected at $Q = 0.45$.

In summary, the suggested THz excitation spectroscopy technique allows for a straightforward direct determination of band offsets under the flat-band conditions in constituent layers of heterostructure, what is expected at low thicknesses of the narrower-gap layers and at low doping levels. When a charge carrier redistribution affects the potential profile of heterostructure, the

band bending should be taken into account in a determination of band-offset values.

The main advantage of the suggested TES technique with respect to other experimental methods of band-offset determination is a direct relation between the offset values and the experimentally traced spectral TES features, what ensures a high sensitivity of the technique. The technique is contactless and does not require complicatedly sampled structures. An accuracy of the technique is limited by the spectral resolution of the current stage THz spectroscopic equipment. Keeping in mind that an instrumentation of THz spectroscopy is rapidly developing, one can expect the TES technique to become both reliable and precise tool for a band-offset determination.

Funding

Research Council of Lithuania (grant No. 09.3.3-LMT-K-712-01-0032).

References

1. E. T. Yu, J. O. McCaldin, and T. C. McGill, "Band offsets in semiconductor heterojunctions," in *Solid State Physics* **46**, 1–146 (Academic Press, 1992).
2. A. Franciosi and C. G. Van de Walle, "Heterojunction band offset engineering," Surf. Sci. Reports **25**, 1–140 (1996).
3. H. Kroemer, "Quasielectric fields and band offsets: Teaching electrons new tricks," Rev. Mod. Phys. **73**, 783–793 (2001).
4. W. Yi, A. J. Stollenwerk, and V. Narayanamurti, "Ballistic electron microscopy and spectroscopy of metal and semiconductor nanostructures," Surf. Sci. Reports **64**, 169–190 (2009).
5. J. Robertson, "Band offsets, Schottky barrier heights, and their effects on electronic devices," J. Vac. Sci. Technol. A **31**, 050821 (2013).
6. T. Thomas, A. Mellor, N. P. Hylton, M. Führer, D. Alonso-Àlvarez, A. Braun, N. J. Ekins-Daukes, J. P. R. David, and S. J. Sweeney, "Requirements for a GaAsBi 1 eV sub-cell in a GaAs-based multi-junction solar cell," Semicond. Sci. Technol. **33**, 094010 (2015).
7. Y. Tominaga, K. Oe, and M. Yoshimoto, "Low temperature dependence of oscillation wavelength in $GaAs_{1-x}Bi_x$ laser by photo-pumping," Appl. Phys. Express **3**, 062201 (2010).
8. V. L. Malevich, P. A. Ziaziulia, R. Adomavičius, A. Krotkus, and Y. V. Malevich, "Terahertz emission from cubic semiconductor induced by a transient anisotropic photocurrent," J. Appl. Phys. **112**, 073115 (2012).
9. A. Arlauskas and A. Krotkus, "THz excitation spectra of AIIIBV semiconductors," Semicond. Sci. Technol. **27**, 115015 (2012).
10. B. P. Zakharchenya, D. N. Mirlin, V. I. Perel', and I. I. Reshina, "Optical alignment of hot carriers in semiconductors," Sov. Phys. Uspekhi **25**, 143–157 (1982).
11. G. Feng, M. Yoshimoto, K. Oe, A. Chayahara, and Y. Horino, "New III-V semiconductor InGaAsBi alloy grown by molecular beam epitaxy," Jpn. J. Appl. Phys. **44**, L1181 (2005).
12. I. Vurgaftman, J. R. Meyer, and L. R. Ram-Mohan, "Band parameters for III-V compound semiconductors and their alloys," J. Appl. Phys. **89**, 5815–5875 (2001).
13. K. Alberi, O. D. Dubon, W. Walukiewicz, K. M. Yu, K. Bertulis, and A. Krotkus, "Valence band anticrossing in $GaBi_xAs_{1-x}$," Appl. Phys. Lett. **91**, 051909 (2007).
14. C. A. Broderick, M. Usman, S. J. Sweeney, and E. P. O'Reilly, "Band engineering in dilute nitride and bismide semiconductor lasers," Semicond. Sci. Technol. **27**, 094011 (2012).
15. K. Collar, J. Li, W. Jiao, Y. Guan, M. Losurdo, J. Humlicek, and A. S. Brown, "Determination of the impact of Bi content on the valence band energy of GaAsBi using x-ray photoelectron spectroscopy," AIP Adv. **7**, 075016 (2017).
16. R. Kudrawiec, J. Kopaczek, M. P. Ploak, P. Sharoch, M. Gladysiewicz, J. Misiewicz, R. D. Richards, F. Bastiman, and J. P. R. David, "Experimental and theoretical studies of band gap alignment in $GaAs_{1-x}Bi_x$/GaAs quantum wells," J. Appl. Phys. **116**, 233508 (2014).
17. P. Patil, T. Tatabe, Y. Nabara, K. Higaki, N. Nishii, S. Tanaka, F. Ishikawa, and S. Shimomura, "Growth of GaAsBi/GaAs multi quantum wells on (100) GaAs substrates by molecular beam epitaxy," J. Surf. Sci. Nanotechnol. **13**, 469–473 (2015).
18. C. J. Hunter, F. Bastiman, A. R. Mohmad, R. Richards, J. S. Ng, S. J. Sweeney, and J. P. R. David, "Absorption characteristics of $GaAs_{1-x}Bi_x$/GaAs diodes in the near-infrared," IEEE Photonics Technol. Lett. **24**, 2191–2194 (2012).
19. V. Pačebutas, S. Stanionytė, A. Arlauskas, R. Norkus, R. Butkutė, A. Geižutis, B. Čechavičius, and A. Krotkus, "Terahertz excitation spectra of GaAsBi alloys," J. Phys. D: Appl. Phys. **51**, 474001 (2018).
20. G. L. Bir and G. E. Pikus, *Symmetry and Strain-Induced Effects in Semiconductors* (Wiley, 1974).
21. G. Pettinari, A. Patanè, A. Polimeni, M. Capizzi, X. Lu, and T. Tiedje, "Bi-induced *p*-type conductivity in nominally undoped Ga(AsBi)," J. Appl. Phys. **100**, 092109 (2012).
22. M. Yoshimoto, M. Itoh, Y. Tominaga, and K. Oe, "Quantitative estimation of density of Bi-induced localized states in $GaAs_{1-x}Bi_x$ grown by molecular beam epitaxy," J. Cryst. Growth **378**, 73–76 (2013).

Paper 2 [P2]

V. Pačebutas, S.Stanionytė, **R.Norkus**, A.Bičiūnas, A.Urbanowicz and A.Krotkus, „Terahertz pulse emission from GaInAsBi“, J. Appl. Phys. 125, 174507 (2019)

This article may be accessed online https://doi.org/10.1063/1.5089855

Journal of Applied Physics ARTICLE scitation.org/journal/jap

Terahertz pulse emission from GaInAsBi

Cite as: J. Appl. Phys. **125**, 174507 (2019); doi: 10.1063/1.5089855
Submitted: 23 January 2019 · Accepted: 16 April 2019 ·
Published Online: 7 May 2019

V. Pačebutas,[a] S. Stanionytė, R. Norkus, A. Bičiūnas, A. Urbanowicz, and A. Krotkus

AFFILIATIONS

Centre for Physical Sciences and Technology, Saulėtekio av. 3, LT-10257 Vilnius, Lithuania

Note: This paper is part of the Special Topic on Highly Mismatched Semiconductors Alloys: From Atoms to Devices.
[a]vaidas.pacebutas@ftmc.lt

ABSTRACT

Quaternary GaInAsBi alloy epitaxial layers were grown on InP substrates with 6% Bi. It was found that the thick layers remain fully strained. The measured carrier lifetimes were of the order of a few picoseconds. The terahertz (THz) emission was investigated using a GaInAsBi layer as an unbiased surface emitter and as a substrate for photoconductive antenna. It was observed that fabricated THz emitters were sensitive to the optical pulses with wavelengths longer than 2 μm. The demonstrated spectral characteristics of THz pulses obtained when using an Er-doped fiber laser for photoexcitation were comparable with those observed in other emitters used for THz-time-domain spectroscopy systems.

I. INTRODUCTION

The generation of terahertz (THz) pulses by photoconductive antennas (PCAs) is a commonly used technique because of the compact size of PCA components and their flexibility in different uses. THz radiation pulses are presently widely applied to study the physical properties of materials, identification of chemicals, and for nondestructive testing using time-domain spectroscopy (TDS) techniques. These applications would significantly proliferate if inexpensive and maintenance-free fiber laser systems could be used in THz-TDS systems. Such lasers operate at 1 μm and longer wavelengths, and, therefore, require suitable alternatives to low-temperature grown (LTG) GaAs, a material used in TDS systems activated by Ti:sapphire lasers.[1,2] LTG GaAs layers are grown by molecular beam epitaxy (MBE) at As overpressure and at substrate temperatures in the range from 200 °C to 300 °C and contain a large number of nonstoichiometric As antisite (As_{Ga}) defects.[3] The As_{Ga} defect band located approximately in the middle of the energy bandgap of LTG GaAs secures high resistivity and subpicosecond carrier lifetimes—material parameters that are essential for ultrafast optoelectronic switches.

Alternative to LTG GaAs, materials photosensitive at fiber laser wavelengths shall be narrower bandgap semiconductors with fairly high resistivity and short carrier lifetimes. Higher electron mobilities typical for narrow-gap semiconductors and lower photon energies are also expected to yield higher optical-to-THz power conversion efficiencies. PCAs activated by long wavelength optical pulses can be fabricated from LTG GaInAs. For 1 μm wavelength TDS systems, GaInAs can be grown on GaAs substrates, but the performance of PCAs fabricated is greatly reduced by low electron mobility in this material.[4] $Ga_{0.53}In_{0.47}As$ lattice-matched to InP substrates have a bandgap of ~0.74 eV required for PCAs sensitive to 1.5 μm wavelength radiation; however, low-temperature grown layers of that material become highly n-type conductive as the As_{Ga} defect band becomes resonant with the conduction band.[5] The resulting high dark conductivity is not acceptable for THz PCAs. The use of ErAs nanocomposite materials based on InGaAs[6] or GaAs[7] superlattice shortens the carrier lifetimes to a few picoseconds, but is found to have prohibitively low dark resistivities. Heavy doping of low-temperature grown InGaAs with beryllium shows particularly good properties,[8] but due to a high concentration of ionized point defects, the electron mobility becomes low. Due to this effect, alternative techniques have been developed to simultaneously achieve high resistivity and ultrafast behavior of InGaAs. Fe doping of MOVPE grown layers[9] as well as heavy ion bombardment[10] have both been applied, but without achieving material characteristics equivalent to LT GaAs.

Recently, we have proposed to fabricate pulsed THz emitters and detectors from group III element bismides. The introduction of Bi into the crystalline lattice of $A^{III}B^{V}$ semiconductor compounds results in a strong reduction of the energy bandgap accompanied by a relatively small change in the lattice constant. The good performance of THz emitters and detectors activated by 1 μm

solid-state or fiber laser pulses has been achieved when using GaAsBi layers with ~6%Bi grown on GaAs substrates.[11,12] However, these ternary compounds are not suitable when one tries to obtain semiconductor materials for ultrafast photoconductors sensitive in the 1.55 μm range. For reaching a necessary energy bandwidth of 0.8 eV, the GaAsBi layer should contain more than 10%Bi;[13] bismides with such composition are highly conductive because of the large hole density.[14] In Ref. 15, an attempt to solve this problem was made by simultaneous introduction of both In and Bi into GaAs. High resistivity ($\rho > 400\,\Omega$ cm) quaternary GaInAsBi layers were grown on GaAs substrates with the energy bandgaps of ~0.6 eV and subpicosecond electron lifetimes; a THz-TDS system activated by femtosecond pulses generated by an Er-doped fiber laser based on the PCAs fabricated from these layers has been demonstrated.[16] Optimal composition of these layers was achieved for ~20% In and ~10% Bi; the lattice mismatch with the GaAs substrate is larger than 3%, which causes a full relaxation of the crystalline structure and a significant reduction of the carrier mobility. The hole mobility in GaInAsBi grown on GaAs substrates is of the order of 10 cm^2/Vs only.[12]

In this work, we present the results obtained on pulsed THz emitters fabricated from quaternary GaInAsBi grown on InP substrates. The incorporation of 6% Bi into the lattice-matched with the substrate ternary GaInAs caused a 0.3% large mismatch and the layers remain strained; the hole mobility is much higher (~90 cm^2/Vs). Most importantly, the energy bandgap of this alloy is as narrow as 0.4 eV; thus, THz photoconductors fabricated from it can be used even in TDS systems activated by 2 μm wavelength femtosecond pulses generated by thulium (Tm) doped fiber lasers.

II. SAMPLE GROWTH AND CHARACTERIZATION

GaInAsBi samples were grown on semi-insulating (100) InP substrates by solid-source MBE. The growth was performed in the SVT-A reactor equipped with metallic Ga, In, and Bi sources and a two-zone valved-cracker source to produce As_2. Prior to the growth, a native oxide from the InP substrate was removed after being exposed to arsenic flux at 500 °C. Deoxidation was monitored by the reflection high energy electron diffraction (RHEED). Immediately after the appearance of (2 × 4) patterns, the temperature was ramped down to the bismide growth temperature of 240 °C. The growth temperature was monitored by a thermocouple. The nominal growth rate used was ~300 nm/h. Indium and gallium beam ratio was kept the same as for lattice-matched GaInAs grown on the InP substrate. The ratio of arsenic to group III atoms was kept close to 1 as determined from RHEED reconstructions.

The surface quality was critically sensitive to the layer growth conditions, especially to the As/Ga and Bi/As beam ratios. When these ratios are not optimal, metallic droplets appear. The surfaces of the samples grown with optimal growth conditions were rather smooth. Their root mean square (RMS) values were ~1.5 nm measured by atomic force microscopy on an $8 \times 8\,\mu m^2$ image.

The bismuth content in GaInAsBi layers was determined from X-ray diffraction (XRD) rocking curves. XRD curves were measured by a Rigaku Smartlab diffractometer equipped with Ge(400) × 2 monochromator and scintillation detector SC-70 (for 2D measurements, a linear Dtex/Ultra detector was used). XRD trace obtained

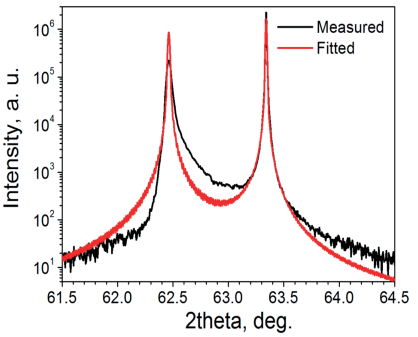

FIG. 1. Measured (black) and fitted (red) HR-XRD (004) plane rocking curve of a 600-nm-thick GaInAsBi layer.

on one of the samples—sample I401—is presented in Fig. 1. This trace was fitted with the calculations performed assuming that the layer is fully strained and that the Ga and In incorporation did not change after the addition of bismuth.[17] By analyzing the XRD data, the lattice parameter for GaBi and InBi was assumed to be 6.324 Å and 6.686 Å,[18] respectively. This fit evidences that sample I401 contains 6% of Bi.

The reciprocal space map (RSM) of sample I401 is presented in Fig. 2. Two strong peaks can be clearly distinguished on that

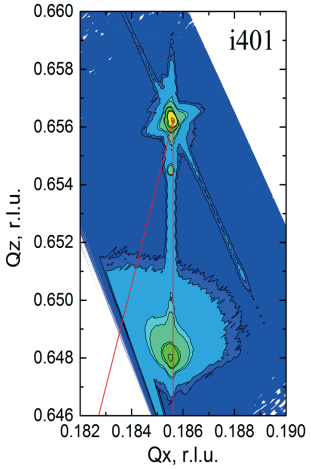

FIG. 2. (115) plane RSM of I401 sample with 6% Bi. The red vertical line corresponds to all strained lattices, and the red tilted line to relaxed lattices.

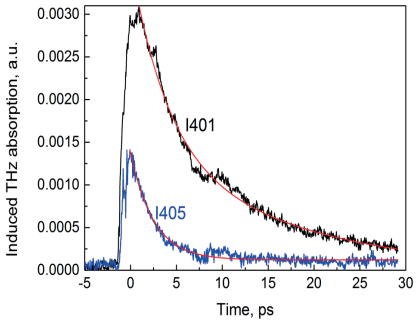

FIG. 3. Optical pump–THz probe traces measured on two GaInAsBi samples. Red lines are fits using a single exponential decay for sample I405 and double-exponential decay for sample I401.

map: the upper peak can be associated with the InP substrate and the lower one with the GaInAsBi layer. It can be seen from this figure that a 600 nm-thick GaInAsBi layer grown on the InP substrate is strained, to the contrary of GaInAsBi layers grown on the GaAs substrate, which are fully relaxed.[12] A similar set of measurements was also performed on another bismide layer (I405) used for fabricating PCAs. This layer has a Bi content of 1.8% and was also fully strained.

Electrical, optical, and dynamical properties of the layers were further characterized by the Hall effect, Fourier transform infrared (FTIR) spectroscopy, and optical pump–THz probe measurements, respectively. Resistivities of the layers were 5 Ω cm and 9.2 Ω cm, and their optical absorption edges were equal to 0.48 eV and 0.63 eV for I401 and I405, respectively.

The carrier lifetime was measured using the optical pump–THz probe technique.[19] In this case, a 70 fs duration and 1030 nm central wavelength pulses generated by a Yb:KGW (potassium gadolinium tungstate) solid-state laser were used both for the sample excitation and for the activation of THz optoelectronic components (PCAs) fabricated from GaAsBi. A femtosecond laser pump pulse with an average pump power of 460 mW and beam diameter at the sample position of 1.9 mm excites electron–hole pairs in the sample, which induces additional free-electron absorption of THz radiation pulses synchronized with the sample photoexcitation. Reduction in THz pulse due to its absorption by photoexcited electrons in the case of low excitation is proportional to the photoelectron density and their mobility.[20] Therefore, the measurement of THz absorption with THz probe beam at different times lets us to investigate ultrafast electron dynamics in semiconductors. The results of such measurements performed on two samples are presented in Fig. 3. Transient THz absorption trace measured on sample I405 gives the lifetime of ~3 ps, whereas the trace measured on sample I401 is best fitted with a double-exponential function with characteristic time constants of 4 ps and 16 ps. It could be assumed that the faster decay component is caused by the capture of electrons at recombination centers, whereas the longer decay component by emptying of these centers after the capture of non-equilibrium holes.

III. RESULTS AND DISCUSSION

THz emission was investigated both using a GaInAsBi layer as an unbiased surface emitter and as a substrate for photoconductive antenna. First, spectral dependences of the emitted THz pulse amplitude on photon energy were measured using 140 fs to 180 fs duration optical pulses from cavity-tuned optical parametric amplifier ORPHEUS (OPA, Light Conversion, Ltd.). Central

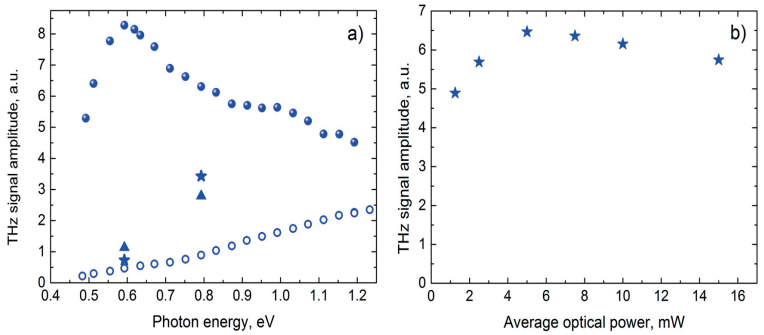

FIG. 4. (a) THz excitation spectra of the GaInAsBi epitaxial layer with 53%In and 6%Bi (layer i401, empty points) and PCA fabricated from that layer (full points) biased cw at 50 V voltage. THz pulse amplitudes emitted from the InAs layer (triangles) and PCA fabricated from GaInAsBi with 53%In and 1.8%Bi (layer i405, stars) excited by 2 μm and 1.5 μm optical pulses are shown for comparison. (b) THz pulse amplitudes emitted by PCA from layer i401 excited at 1.5 μm wavelength pulses at different average optical beam power.

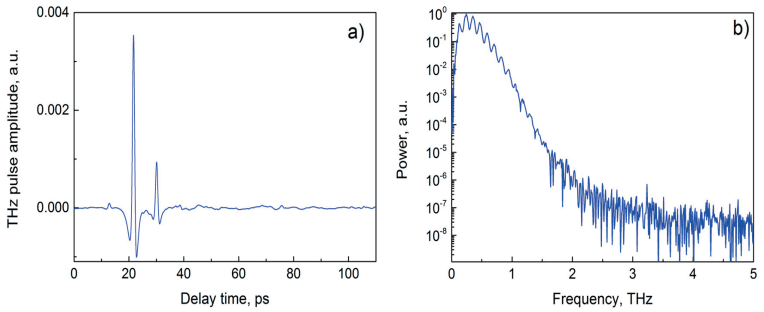

FIG. 5. (a) THz electrical field and (b) its Fourier spectrum emitted by PCA fabricated from the $Ga_{0.53}In_{0.47}As_{0.94}Bi_{0.06}$ layer grown on the InP substrate and biased to 50 V. THz detector was a PCA made from $Ga_{0.8}In_{0.2}As_{0.89}Bi_{0.11}$ on GaAs.[12]

wavelength of the pulses was tunable from 640 nm to 2600 nm, and the pulse repetition rate was 200 kHz. Radiated THz pulses were detected by a PCA fabricated from a GaAsBi layer (TERAVIL Ltd.) illuminated by a part (average power of ∼5 mW) of the Yb:KGW laser beam pumping the OPA ($\lambda = 1030$ nm) and delayed by different times with respect to the optical beam that was exciting the investigated sample. All experiments were performed at room temperature; average power of the optical pulses used for the sample excitation was 5 mW.

Figure 4 compares THz pulse excitation spectra for the bare unbiased GaInAsBi layer with 6% Bi and for the large aperture photoconductive emitter fabricated from the same layer. PCA has 400 μm wide Ti/Au contacts with 480 μm wide gap on the epitaxial layer surface. The photoconductor was mounted on a substrate lens from high resistivity silicon, the incoming laser beam was focused to the part of the gap close to the anode contact, and the diameter of the light spot was about 100 μm. In contrast to that, the THz surface was excited by unfocused 15 mW average power laser beam at 45° incident angle and was measured in the reflection direction. As can be seen from Fig. 4(a), the THz signal amplitude in unbiased surface emitter increases with the photon energy due to a larger excess energy of photoexcited electrons and, accordingly, their higher group velocity. On the other hand, the THz signal amplitude generated by PCA first increases due to enhanced light absorption in its active layer, reaches a maximum at ∼0.6 eV, and then decreases due to the reduced number of photons in the constant power optical pulses with increasing photon energy. PCA fabricated from the layer i401 when excited by 2 μm wavelength femtosecond pulses emits THz pulses with an amplitude nearly 20 times stronger than unbiased surface of this layer photoexcited by a three times stronger optical beam. PCA from quaternary GaInAsBi with 6% Bi is also a rather good THz emitter for 1.5 μm wavelength

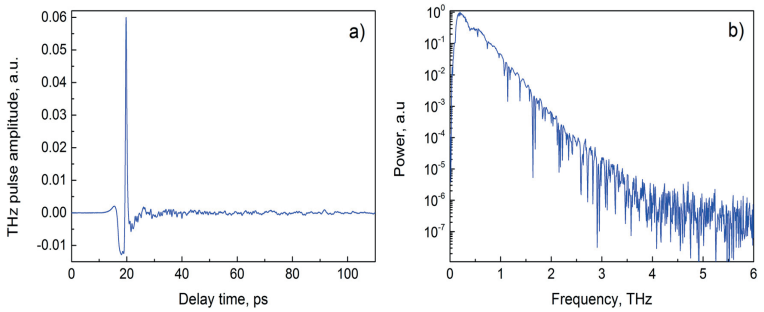

FIG. 6. (a) THz electrical field and (b) its Fourier spectrum emitted by PCA fabricated from the $Ga_{0.53}In_{0.47}As_{0.94}Bi_{0.06}$ layer grown on the InP substrate and biased to 60 V. THz detector was a PCA made from LTG GaAs.

excitation radiating stronger THz pulses than the InAs surface emitter [the point corresponding this emitter shown in Fig. 4(a) corresponds to an optical beam power of 50 mW] and PCA fabricated from GaInAsBi with 1.8% Bi.

It is interesting to point out that emitted by the PCA from quaternary bismide layer i401 THz power shows rather early saturation at average optical power exceeding 5 mW, which corresponds to photoexcited carrier densities of about 2×10^{19} cm^{-3} [see Fig. 4(b)]. Much smaller photoexcitation levels or about 10^{16} cm^{-3} were achieved when 80 MHz repetition rate pulses from the femtosecond fiber laser were used. Figures 5 and 6 present THz pulse amplitudes and their Fourier spectra for PCA from the layer i401 excited by femtosecond first (1550 nm, 100 fs) and second harmonics (770 nm, 90 fs) pulses of an Er-doped fiber laser (Toptica), respectively. In both cases, the signal to noise ratio of the Fourier spectra is exceeding 60 dB and is comparable with PCAs made from Be-doped InGaAs/InAlAs superlattices,[8] but the frequency bandwidth obtained when using second harmonics pulses for the PCA activation (~4 THz) is two times larger than the bandwidth for the first harmonics photoexcitation. This difference is caused by different performance of PCA detectors used in both cases: LTG GaAs for the second harmonics and GaInAsBi on GaAs[12] for the first harmonics excitation.

IV. CONCLUSIONS

In conclusion, relatively thick (600 nm) quaternary GaInAsBi alloy epitaxial layers were grown on InP substrates and used in THz pulse emitters activated by long wavelength femtosecond laser pulses. Energy bandgap of this material was as narrow as 0.4 eV; due to a relatively small lattice mismatch with the substrate (~0.3%), the layers remained fully strained. THz pulse emission was measured from both unbiased surface and biased photoconductive antennas fabricated from GaInAsBi layers. In the second case, spectral characteristics of THz pulses obtained when using Er-doped fiber laser for the photoexcitation were comparable with those observed in other emitters used for THz-TDS systems. Photoconductive THz emitters fabricated from GaInAsBi layers were the first such devices sensitive to the optical pulses with wavelengths longer than 2 μm; therefore, they can be successfully used also with novel femtosecond thulium or holmium doped fiber lasers[21,22] for which such components are as yet not available.

ACKNOWLEDGMENTS

This research was financially supported by the Research Council of Lithuania (Grant No. S-MIP-17-25).

REFERENCES

[1]F. W. Smith, H. Q. Le, V. Diadiuk, M. A. Hollis, A. R. Calawa, S. Gupta, M. Frankel, D. R. Dykaar, G. A. Mourou, and T. Y. Hsiang, "Picosecond GaAs-based photoconductive optoelectronic detectors," Appl. Phys. Lett. **54**, 890 (1989).
[2]A. C. Warren, N. Katzenellenbogen, D. Grischkowsky, J. M. Woodall, M. R. Melloch, and N. Otsuka, Appl. Phys. Lett. **58**, 1512 (1991).
[3]A. Krotkus and J. L. Coutaz, "Non-stoichiometric semiconductor materials for terahertz optoelectronics applications," Semicond. Sci. Technol. **20**(7), S142 (2005).
[4]S. Gupta, J. F. Whitaker, and G. A. Mourou, "Ultrafast carrier dynamics in III-V semiconductors grown by molecular beam epitaxy at very low substrate temperatures," IEEE J. Quantum Electron. **28**, 2464–2472 (1992).
[5]B. Sartorius, H. Roehle, H. Künzel, J. Böttcher, M. Schlak, D. Stanze, H. Venghaus, and M. Schell, "All-fiber terahertz time-domain spectrometer operating at 1.5 μm telecom wavelengths," Opt. Express **16**, 9565 (2008).
[6]M. Sukhotin, E. R. Brown, D. Driscoll, M. Hanson, and A. C. Gossard, "Picosecond photocarrier-lifetime in ErAs:InGaAs at 1.55 μm," Appl. Phys.Lett. **83**, 3921 (2003).
[7]S.-H. Yang, R. Salas, E. M. Krivoy, H. P. Nair, S. R. Bank, and M. Jarrahi, "Characterization of ErAs:GaAs and LuAs:GaAs superlattice structures for continuous-wave terahertz wave generation through plasmonic photomixing," J. Infrared Millim. Terahertz Waves **37**, 640–648 (2016).
[8]B. Globisch, R. J. B. Dietz, D. Stanze, T. Göbel, and M. Schell, "Terahertz detectors from Be-doped low-temperature grown InGaAs/InAlAs: Interplay of annealing and terahertz performance," Appl. Phys. Lett. **104**, 172103 (2014).
[9]C. D. Wood, O. Hatem, J. E. Cunningham, E. H. Linfield, A. G. Davies, P. J. Cannard, M. J. Robertson, and D. G. Moodie, "Terahertz emission from metal-organic chemical vapor deposition grown Fe:InGaAs using 830 nm to 1.55 μm excitation," Appl. Phys. Lett. **96**, 194104 (2010).
[10]M. Suzuki and M. Tonouchi, "Fe-implanted InGaAs THz emitters for 1.56 μm wavelength excitation," Appl. Phys. Lett. **86**, 051104 (2005).
[11]V. Pačebutas, A. Bičiūnas, K. Bertulis, and A. Krotkus, "Optoelectronic terahertz radiation system based on femtosecond 1 μm laser pulses and GaBiAs detector," Electron. Lett. **44**, 1154 (2008).
[12]V. Pačebutas, A. Bičiūnas, S. Balakauskas, A. Krotkus, G. Andriukaitis, D. Lorenc, A. Pugžlys, and A. Baltuška, "Terahertz time-domain-spectroscopy system based on femtosecond Yb:fiber laser and GaBiAs photoconducting components," Appl. Phys. Lett. **97**, 031111 (2010).
[13]K. Alberi, O. D. Dubon, W. Walukiewicz, K. M. Yu, K. Bertulis, and A. Krotkus, "Valence band anticrossing in GaBiAs," Appl. Phys. Lett. **91**, 051909 (2007).
[14]G. Pettinari, A. Polimeni, M. Capizzi, H. Engelkamp, P. C. M. Christianen, J. C. Maan, A. Patane, and T. Tiedje, "Effects of Bi incorporation on the electronic properties of GaAs: Carrier masses, hole mobility, and Bi-induced acceptor states," Phys. Status Solidi B **250**, 779 (2013).
[15]V. Pačebutas, A. Urbanowicz, P. Cicėnas, S. Stanionyte, A. Bičiūnas, I. Nevinskas, and A. Krotkus, "Growth and characterization of quaternary (GaIn)(AsBi) layers for optoelectronic terahertz detector applications," Semicond. Sci. Technol. **30**, 094012 (2015).
[16]A. Urbanowicz, V. Pačebutas, A. Geižutis, S. Stanionytė, and A. Krotkus, "Terahertz time-domain-spectroscopy system based on 1.55 μm fiber laser and photoconductive antennas from dilute bismides," AIP Adv. **6**, 025218 (2016).
[17]J. Devenson, V. Pačebutas, R. Butkutė, A. Baranov, and A. Krotkus, "Structure and optical properties of InGaAsBi with up to 7% bismuth," Appl. Phys. Express **5**, 015503 (2012).
[18]A. Janotti, S.-H. Wei, and S. B. Zhang, "Theoretical study of the effects of isovalent coalloying of Bi and N in GaAs," Phys. Rev. B **65**, 115203 (2002).
[19]M. C. Beard, G. M. Turner, and C. A. Schmuttenmaer, "Subpicosecond carrier dynamics in low-temperature grown GaAs as measured by time-resolved terahertz spectroscopy," J. Appl. Phys. **90**, 5915 (2001).
[20]K. P. H. Lui and F. A. Hegmann, "Ultrafast carrier relaxation in radiation-damaged silicon-on-sapphire studied by optical pump-terahertz-probe experiments," Appl. Phys. Lett. **78**, 3478–3480 (2001).
[21]M. Zhang, E. J. R. Kelleher, F. Torrisi, Z. Sun, T. Hasan, D. Popa, F. Wang, A. C. Ferrari, S. V. Popov, and J. R. Taylor, "Tm-doped fiber laser mode-locked by graphene-polymer composite," Opt. Express **20**, 25077 (2012).
[22]A. Chamorovskiy, A. V. Marakulin, S. Ranta, M. Tavast, J. Rautiainen, T. Leinonen, A. S. Kurkov, and O. G. Okhotnikov, "Femtosecond mode-locked holmium fiber laser pumped by semiconductor disk laser," Opt. Lett. **37**, 1448 (2012).

Paper 3 [P3]

R. Norkus, I. Nevinskas, and A. Krotkus, „Spectral dependencies of terahertz emission from femtosecond laser excited surfaces of germanium crystals“, *Journal of Applied Physics* 126, 225704 (2019)

This article may be accessed online https://doi.org/10.1063/1.5128186

Journal of Applied Physics ARTICLE scitation.org/journal/jap

Spectral dependencies of terahertz emission from femtosecond laser excited surfaces of germanium crystals

Cite as: J. Appl. Phys. **126**, 225704 (2019); doi: 10.1063/1.5128186
Submitted: 19 September 2019 · Accepted: 26 November 2019 ·
Published Online: 12 December 2019

R. Norkus, I. Nevinskas,[a] and A. Krotkus

AFFILIATIONS

Center for Physical Sciences and Technology, Saulėtekio al. 3, LT-10257 Vilnius, Lithuania

[a]**Electronic mail:** ignas.nevinskas@ftmc.lt

ABSTRACT

Pulsed terahertz emission excitation spectra from germanium crystals are being presented. The most intense terahertz pulses from germanium crystals are emitted at quanta energies coinciding with technologically significant telecommunication wavelengths. The terahertz generation mechanisms are an interplay of the photocurrent surge in the surface electric field and the photo-Dember effect. Remarkably, the terahertz emission is also observed at quanta energies below the direct bandgap of this material even when photoexcited at a surface normal. This is the result of a broken symmetry of effective electron mass in the L valleys.

I. INTRODUCTION

Various materials excited by femtosecond laser pulses radiate electromagnetic transients with characteristic frequencies in the terahertz (THz) range. THz radiation was generated first in dielectric crystals by means of optical rectification[1] and later in semiconductor surfaces due to the ultrafast photocurrents.[2] Recently, the list of potential surface THz emitter materials has been widely extended, and it includes laser excited organic crystals,[3] ferromagnetic[4] and ferroelectric[5] materials, their structures, and hybrid organic-inorganic perovskites.[6,7] The physical mechanisms behind the THz emission phenomenon in each case are different, and they provide various important characteristic information about the materials. The most actively investigated group of THz emitting materials is the direct bandgap semiconductors (see, e.g., review papers[8,9]). The radiated THz pulse amplitude from their surfaces depends on the exciting femtosecond laser pulse wavelength that allows to directly determine the energy position of the subsidiary valley conduction band minima.[10,11] Similarly, the conduction and valence energy bands' offsets are estimated at the interfaces of heterojunctions.[12]

Germanium is a semiconductor with an indirect bandgap of 0.66 eV. Its valence band maximum is located at the Brillouin zone center (Γ points), whereas the conduction band has its absolute minima at the L points of this zone. The direct bandgap of Ge at Γ points corresponds to the energy of $\varepsilon_g = 0.8$ eV.[13] At a still higher energetic distance from the valence band maximum, there is an additional set of conduction band valleys located near the X points of the Brillouin zone at $\Delta\varepsilon = 0.85$ eV. It has been recently shown in Ref. 14 that a photoconductive antenna fabricated from Ge efficiently emits broadband THz pulses in time-domain spectroscopy (TDS) systems. Yet, surface THz emission from Ge was only investigated by femtosecond laser pulses with photon energies much higher than the energy bandgap of this material; $h\nu = 1.55$ eV[14–16] and 1.2 eV.[17] At these energies, a complicated redistribution of photoexcited electrons between different conduction band valleys obstructs the investigation of the physical origin of THz emission. Nevertheless, the THz pulse amplitude dependencies on azimuthal angle measured on various crystallographic planes demonstrate the symmetry of a third order optical nonlinearity—the electric-field-induced optical rectification (EFIOR) effect.[16] Moreover, the optical pump–THz probe experiment has shown that the electron intervalley redistribution lasts 3–4 ps, which is much longer than the time it takes to generate a THz pulse.[15]

In the interest of both fundamental and practical points of view, the formerly mentioned THz emission and the intervalley scattering effects should be studied with femtosecond optical pulses of wavelengths close to the absorption edge of this material. Such an investigation could provide new insights into the optical

characteristics of germanium, including its prospects as the substrate for pulsed THz radiation sources activated by technologically significant telecom wavelength lasers. In this contribution, we present the THz excitation spectra (TES) measurements from Ge crystals. The crystals were excited by femtosecond optical pulses with photon energies in the range from 0.6 eV to 1.2 eV. This allowed us to evaluate the contributions of different conduction band valleys to the THz pulse generation and to determine the microscopic origin of the EFIOR effect.

II. EXPERIMENTAL DETAILS

Three Ge crystals were investigated: an unintentionally doped n-Ge crystal with a resistivity of $\rho = 22\,\Omega\,\text{cm}$ and an electron density of $1.5 \times 10^{14}\,\text{cm}^{-3}$ (referred to in the text as i-Ge), a p-type Ge with $\rho = 0.05\,\Omega\,\text{cm}$, and an n-Ge sample with $\rho = 0.02\,\Omega\,\text{cm}$. All of the samples were cut along a (111) crystallographic plane. Surface THz emission experiments were performed in the quasi-reflection geometry with samples being illuminated at 45° to their surface normal. The experimental setup was based on an amplified ytterbium-doped potassium gadolinium tungstate (Yb:KGW) laser system (PHAROS, Light Conversion Ltd.) operating at 1030 nm with a pulse duration of 160 fs and a 200 kHz repetition rate. The average power of 6 W from this laser was directed into a cavity-tuned optical parametric amplifier (OPA, ORPHEUS, Light Conversion Ltd.) that generated 140–160 fs duration pulses with a central wavelength tunable from 640 nm to 2600 nm. In the THz-TDS arrangement, the investigated surface emitters were excited by the output beam from OPA, whereas the radiated THz pulses were detected by a photoconducting antenna fabricated from a GaAsBi layer (TERAVIL Ltd.). This THz detector was illuminated by a small part (an average power of ∼1 mW) of the Yb:KGW laser beam delayed by different times with respect to the OPA beam that was exciting the samples. All experiments were performed at room temperature.

III. THz EXCITATION SPECTRA

Figure 1 compares THz transients emitted from the surfaces of three Ge crystals. The (111) crystallographic planes were excited under identical conditions; the azimuthal angles for all the samples were aligned to correspond to the THz electric field maxima. The polarities of transients radiated from the n- and p-type crystals are opposite, which affirms the photocurrent surge in the surface electric field as the THz pulse emission mechanism. On the other hand, the highest THz pulse amplitude is emitted from the unintentionally doped i-Ge sample that has the widest surface depletion region and the weakest built-in field.[18]

The dependencies of THz pulse amplitude on excitation fluence are also very different for each Ge crystal (Fig. 2). The n-Ge and p-Ge samples show a slight sublinear behavior, whereas the i-Ge sample has a clear THz pulse amplitude saturation at optical fluencies exceeding $\sim 1.9\,\mu\text{J/cm}^2$. In order to eliminate the potential effects of this saturation on the shapes of THz excitation spectra, the spectral measurements were performed with an unfocused optical beam at a rather low fluence of $\sim 0.2\,\mu\text{J/cm}^2$. At a laser wavelength of 1.53 μm corresponding to the photon energy of 0.81 eV, the photoexcited carrier densities were about $10^{15}\,\text{cm}^{-3}$.

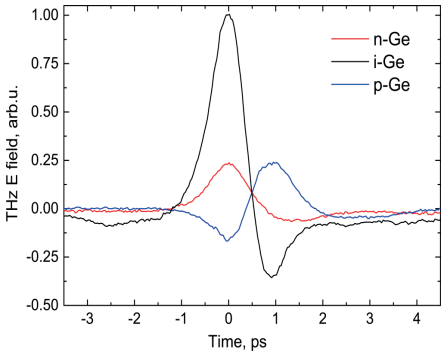

FIG. 1. The shapes of THz transients emitted from the surfaces of various doped germanium crystals after their photoexcitation with femtosecond optical pulses (at a photon energy of 0.83 eV and an excitation fluence of $\sim 1.4\,\mu\text{J/cm}^2$).

The THz excitation spectra of all three germanium samples are presented in Fig. 3. As it is expected, the THz emission sets on when laser photon energies become comparable to the direct energy bandgap of Ge that is equal to 0.8 eV.[13] At higher photon energies, the shapes of the spectra become different for each sample. The THz excitation spectrum of i-Ge is distinguished by a distinctive peak at the vicinity of the direct bandgap; this peak is much lower in a p-Ge sample and it is completely absent in a highly doped n-Ge sample. It indicates a THz emission advantage of i-Ge crystals photoexcited with telecom wavelengths over higher quanta energy lasers.

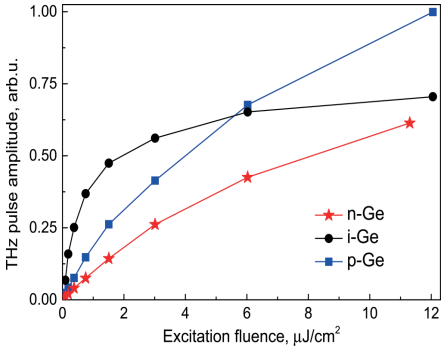

FIG. 2. Peak-to-peak amplitude of THz transients emitted from the surfaces of various doped germanium crystals as a function of an average optical power of femtosecond pulses (at 0.83 eV photon energy).

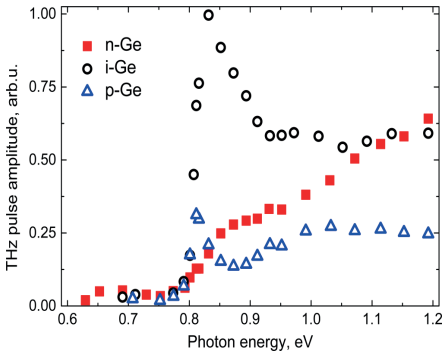

FIG. 3. THz excitation spectra measured for three differently doped Ge crystals. The peak-to-peak amplitudes of THz pulses are obtained at an excitation fluence of $\sim 0.2\,\mu J/cm^2$. The graph is normalized to a constant photon number.

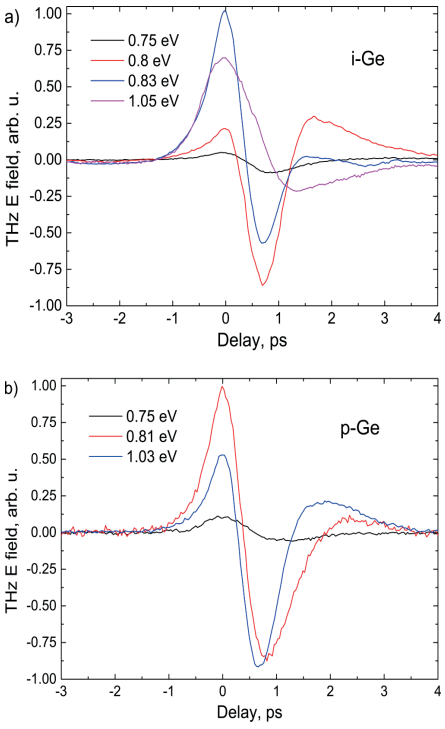

FIG. 4. THz pulses emitted from the i- (a) and p- (b) Ge surfaces at different laser photon energies. The excitation fluence is $\sim 6\,\mu J/cm^2$.

As in the majority of semiconducting materials, one could expect that the THz radiation pulses emitted from photoexcited germanium surfaces are due to two effects, both of which can cause the appearance of a dynamically changing electrical dipole. First is the photoexcited electron and hole separation in the built-in surface electric field, and second is due to different velocities at which these carriers propagate away from the surface (superdiffusion or the photo-Dember effect).[19] On the one hand, the photo-Dember effect is the strongest when the electrons in the high mobility Γ valley are involved, because in germanium only these electrons have much higher mobilities than the holes. On the other hand, the surface field separates carriers even after electrons are scattered to the lower mobility L or X valleys. The THz emission even at below direct gap optical transitions, dependencies on crystal doping and THz pulse polarity reversal, and increasing THz radiation intensities at shorter wavelength photoexcitations for the n-Ge case suggest that the THz generation in germanium is an interplay between the mentioned two mechanisms.

In an undoped i-Ge sample, the surface electric field is weak[18] and so the superdiffusion of quasiballistically moving away from surface photoelectrons is prevailing. This effect in i-Ge is most effective when photons have energies close to those of a direct optical transition; its efficiency decreases when electrons have enough energy to be scattered to subsidiary L and, further to X, valleys. Surface electric fields in the n-Ge and p-Ge samples are 50 and 30 times, respectively, stronger than in an undoped sample; thus, the photocurrent surge becomes the dominant mechanism in these samples. At a first few hundred femtoseconds—the time during which a THz pulse is generated—the majority of photoelectrons remain in Γ valleys, and thus their behavior might be alike as in A3B5 semiconductors, InAs in particular.[8] THz pulses radiated from a p-type Ge surface are stronger than those from an n-type germanium because the built-in field direction in the former facilitates the growth of a lateral photocurrent component and the EFIOR effect.[20] In an n-type Ge, the movement directions of electron superdiffusivity and drift in a surface field coincide; with increasing photon energy, more and more electrons are excited in a narrow (less than 90 nm) surface depletion region and a monotonous increase of the THz pulse amplitude is observed.

The shapes of THz pulses emitted from i- and p-Ge samples when excited by various optical wavelengths show an anomalous behavior (see Fig. 4). The negative and positive polarities of THz transients respond to exciting quanta energy nonproportionally; the polarity of pulses is essentially changing to the opposite. This tendency remains over the whole investigated spectral region including photon energies below the direct energy bandgap of 0.8 eV. The polarity reversal is not present in the n-Ge sample.

IV. OPTICAL PUMP-THz PROBE MEASUREMENTS

Since the THz field strength is proportional to the time derivative of photocurrent, the more pronounced negative pulse polarity

at around direct energy gap excitation, $h\nu$ ~0.8 eV, indicates a sudden decrease of the photocurrent decay time. This could be attributed to the manifestation of a more effective photocurrent decay mechanism. To investigate this possibility, the optical pump–THz probe measurements at different pump wavelengths were performed. The setup was arranged so that the pump and the probe pulses were impinging the sample at its surface normal in transmission geometry. It is noteworthy that the pumped sample generates a THz pulse itself but it is relatively weak at a surface normal photoexcitation, and it was subtracted from the pump-probe signal altogether. The results are presented in Fig. 5.

When photon energies are lower than the direct energy gap at Γ points of the Brillouin zone, <0.8 eV, the optically induced THz absorption increases rather slowly, for about 1 ps. This indirect energy gap absorption does not completely disappear even after 5 μs, which is a time interval between two subsequent laser pulses, and it causes a significant background level of the THz absorption signal. On the other hand, at quanta energies above 0.8 eV, the background practically disappears and a sharp peak becomes apparent at the initial transient part followed by a slower signal increase lasting 3–4 ps. The amplitude of the peak gradually becomes smaller with increasing photon energy, and it nearly disappears at energies higher than 0.9 eV. The energy range at which peaks of THz absorption transients occur coincides with the maximum of the THz excitation spectrum (Fig. 3).

The fast decay of THz absorption can be explained by the electron scattering from high mobility Γ valleys to subsidiary low mobility L valleys. This Γ-L intervalley electron scattering mechanism is characterized to last about 230 fs in Ref. 21. Such time scales are shorter than the temporal resolution of our experiment limited by the photoconducting THz antenna detector response (~400 fs). When quanta energies exceed 0.9 eV, the Γ valley electron excess energies reach the energy position of the X valleys. The intervalley Γ-X scattering is faster than Γ-L; therefore, the initial peak of the THz absorption transient is nearly completely distorted by the insufficient temporal resolution.

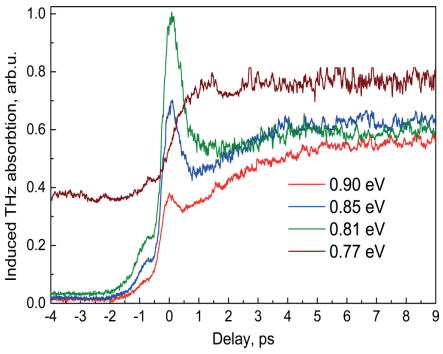

FIG. 5. Optical pump–THz probe experiment transients of the i-Ge sample excited by different wavelength femtosecond laser pulses at an excitation fluence of ~1 μJ/cm^2.

One remaining question is the origin of background THz absorption observed at energies below direct bandgap energy. It indicates different carrier recombination conditions compared to those above 0.8 eV. This difference of the carrier lifetimes can be caused by the surface recombination. While the number of photoexcited carriers is nearly the same slightly above and below 0.8 eV, the optical absorbance changes by more than two orders of magnitude in this spectral range. Therefore, at energies below 0.8 eV, the excited carriers are distributed homogeneously over a thickness comparable to a carrier diffusion length of ~150 μm, implying that not all of them will reach the surface during 5 μs between consecutive optical pulses. Conversely, at energies above 0.8 eV, the absorption length becomes much shorter and most of the carriers are excited at the surface vicinity where they efficiently recombine. Subnanosecond surface recombination times under similar experimental conditions were observed before.[22]

V. AZIMUTHAL ANGLE DEPENDENCIES

As in other semiconducting crystals, the amplitude of THz pulses emitted from laser excited Ge surfaces depends on the angle between optical field vector and crystalline axes—the azimuthal angle. In a centrosymmetric crystal, such as germanium, the second order optical nonlinearities are absent. Optical rectification can be caused by the effective $\chi^{(2)} = \chi^{(3)}E$, where E is a surface electric field due to energy band bending and/or a photoexcited electron and hole separation. This effect is phenomenologically known as the electric-field-induced optical rectification (EFIOR).[16,20] In microscopic terms, the presence of EFIOR in semiconductors is explained by the lateral surface photocurrent components appearing due to an anisotropic electron energy dispersion law.[23] An unmistakable proof of lateral photocurrents is the observation of THz emission in the line-of-sight direction when optical pulses are impinging the crystal along its surface normal.[24,25] Here, we used this experimental geometry to measure the azimuthal angle dependencies of the (111)-cut i-Ge sample.

The measured azimuthal angle, ϕ, dependencies at different laser wavelength photoexcitations are presented in Fig. 6(a). The results confirm a typical sin 3ϕ proportionality of the EFIOR effect for a (111) crystallographic plane. A small angle-independent component is caused by a possible misalignment of the experimental setup. The emitted THz pulse amplitude becomes more dependent on the azimuthal angle when photon energies exceed the direct energy bandgap.

Similar relations observed in the case of THz emission from p-type InAs surfaces are explained by the effects of nonparabolicity and nonsphericity of the main conduction band.[23] The direct energy bandgap of Ge is higher than that of InAs so the excess energy of photoexcited electrons is lower; therefore, the THz emission from Ge is not as efficient as the emission from the later semiconductor. At the photoexcitation wavelength of 1520 nm (~0.82 eV) and a fluence of ~0.2 μJ/cm^2, the peak-to-peak amplitude of a THz transient radiated from a p-type InAs surface is ~6 times higher than that from the surface of i-Ge. A rather unexpected behavior of azimuthal angle dependencies is observed when

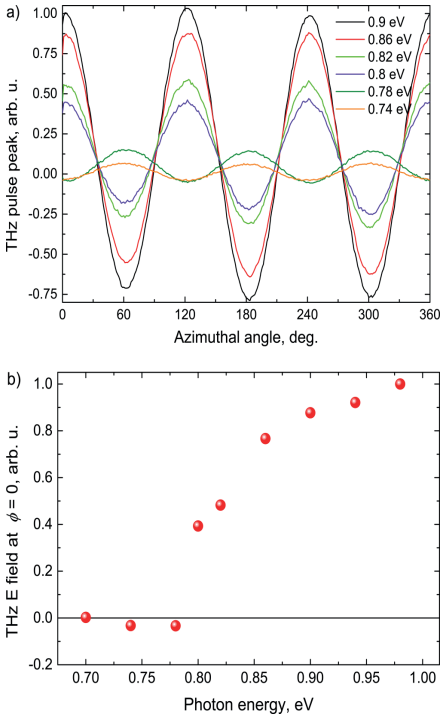

FIG. 6. THz emission azimuthal angle dependencies measured in transmission geometry when the (111)-cut i-Ge sample is excited at its surface normal at different laser photon energies (a) and photon energy dependence on the anisotropic part of THz signal amplitude (b). The excitation fluence is $\sim 2\mu J/cm^2$.

the i-Ge sample is excited with photon energies below the direct bandgap energy. Though the proportionality of sin 3ϕ persists, the pulse phase polarity flips over.

VI. DISCUSSION

Both photoconductive mechanisms of THz pulse emission are documented; the photocurrent surge in the built-in surface electric field and the electron and hole spatial separation are due to their different propagation velocities from the surface. However, this conclusion is applicable only when the photon energies are slightly higher than the direct energy bandgap. The photoexcited electron scattering to L valleys sets on when their excess energy is above the energy of intervalley phonons ($\hbar\omega = 30$–40 meV[26]); scattering to subsidiary X valleys occurs at photon energies exceeding ~0.9 eV. Still, the THz pulses are generated in about 200 fs after photoexcitation while electrons remain in the Γ valleys. In the low doped i-Ge sample, the generation is due to the optical alignment effect, typical for cubic semiconductors,[27] and the quasiballistic electron movement.[23] Nonetheless, the clear azimuthal angle dependencies are most probably caused by the warping of the heavy hole valence band[23] rather than the nonsphericity of the conduction band.

Surprisingly, THz emission, though rather weak, is observed at photon energies lower than 0.8 eV. The THz pulse amplitude dependence on optical power shown in Fig. 7 evidences that the photoexcitation is a linear process involving long wavelength intervalley phonons. In this case, the photoelectron population of all four L valleys is equal and the optical alignment effect is absent. Nevertheless, the azimuthal angle dependence typical for the EFIOR effect is also present. To microscopically explain the origin of this dependence, one needs to involve the anisotropy of L valleys.

Figure 8 shows the two isoenergetic surfaces of L valleys of the conduction band. These surfaces are rotational ellipsoids with their main axes coinciding with $[1\bar{1}1]$ and [111] crystallographic axes lying in the (110) plane. The effective electron mass in the main axis direction (longitudinal mass) is $m_l = 1.57m_0$, whereas the transverse mass is nearly 20 times smaller, $m_t = 0.08m_0$.[13] In a (111)-cut crystal, the surface electric field, $E_{surface}$, is parallel to the main [111] axis of the ellipsoid; therefore, the electrons excited in these valleys will not induce any electron movement parallel to the surface. In contrast, the symmetry of photoelectron masses is broken in the L valleys lying on the $[1\bar{1}1]$ axis. The photocurrent induced in the low-mass direction is higher than that in the high-mass direction, which results in a total current direction off the surface normal, j_{total}. As a consequence, the lateral photocurrent component parallel to the surface, $j_{lateral}$, appears causing THz radiation outcoupling from the crystal.

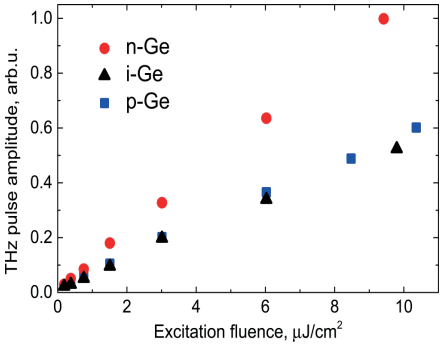

FIG. 7. THz pulse amplitude dependence on excitation power for 3 differently doped Ge samples measured in reflection geometry when the laser photon energy is 0.75 eV.

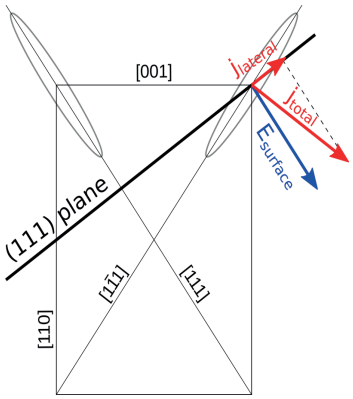

FIG. 8. Germanium's isoenergetic surfaces of L valleys in the (110) plane. The thick black line represents the investigated (111) plane, while the blue arrow is the direction of the surface electric field. Different photoelectron masses in different directions result in a broken photocurrent symmetry inducing a lateral photocurrent component, $j_{lateral}$.

Finally, one has to point out that in this case the lateral photocurrent component is directed toward the [001] side of the (110) plane. The direction of a lateral current component is opposite when this effect is caused by the optical alignment,[24] which explains the phase reversal of the azimuthal angle dependencies measured at different photoexcitation wavelengths (Fig. 6).

VII. CONCLUSIONS

To summarize, the THz emission from various doped germanium crystals was investigated by exciting the samples with different wavelength optical pulses. It was shown that a strong emission sets on when the photon energy is higher than the direct energy gap at Γ points of the Brillouin zone. Results of the optical pump–THz probe measurements evidence a fast, subpicosecond reduction of the Γ valley electron density caused by electron transfer to low mobility L valleys. The small effective mass and high mobility of the Γ valley electrons, fast reduction of their population, and low absorbance at the THz frequencies make germanium a prospective material for applications in optoelectronic THz range components activated by telecom wavelength laser sources.

ACKNOWLEDGMENTS

This research was funded by a grant from the European Social Fund, Measure No. 09.3.3-LMT-K-712-01-0032.

REFERENCES

[1]D. H. Auston, K. P. Cheung, J. A. Valdmanis, and D. A. Kleinman, "Cherenkov radiation from femtosecond optical pulses in electro-optic media," Phys. Rev. Lett. **53**, 1555–1558 (1984).
[2]X. Zhang, B. B. Hu, J. T. Darrow, and D. H. Auston, "Generation of femtosecond electromagnetic pulses from semiconductor surfaces," Appl. Phys. Lett. **56**, 1011–1013 (1990).
[3]J. J. Carey, R. T. Bailey, D. Pugh, J. N. Sherwood, F. R. Cruickshank, and K. Wynne, "Terahertz pulse generation in an organic crystal by optical rectification and resonant excitation of molecular charge transfer," Appl. Phys. Lett. **81**, 4335–4337 (2002).
[4]E. Beaurepaire, G. M. Turner, S. M. Harrel, M. C. Beard, J.-Y. Bigot, and C. A. Schmuttenmaer, "Coherent terahertz emission from ferromagnetic films excited by femtosecond laser pulses," Appl. Phys. Lett. **84**, 3465–3467 (2004).
[5]J. F. Scott, H. J. Fan, S. Kawasaki, J. Banys, M. Ivanov, A. Krotkus, J. Macutkevic, R. Blinc, V. V. Laguta, P. Cevc, J. S. Liu, and A. L. Kholkin, "Terahertz emission from tubular Pb(Zr, Ti)O_3 nanostructures," Nano Lett. **8**, 4404–4409 (2008).
[6]B. Guzelturk, R. A. Belisle, M. D. Smith, K. Bruening, R. Prasanna, Y. Yuan, V. Gopalan, C. J. Tassone, H. I. Karunadasa, M. D. McGehee, and A. M. Lindenberg, "Terahertz emission from hybrid perovskites driven by ultrafast charge separation and strong electron-phonon coupling," Adv. Mater. **30**, 1704737 (2018).
[7]C. S. Ponseca, A. Arlauskas, H. Yu, F. Wang, I. Nevinskas, E. Dūda, V. Vaičaitis, J. Eriksson, J. Bergqvist, X.-K. Liu, M. Kemerink, A. Krotkus, O. Inganas, and F. Gao, "Pulsed terahertz emission from solution-processed lead iodide perovskite films," ACS Photonics **6**, 1175–1181 (2019).
[8]A. Krotkus, "Semiconductors for terahertz photonics applications," J. Phys. D Appl. Phys. **43**, 273001 (2010).
[9]R. A. Lewis, "A review of terahertz sources," J. Phys. D Appl. Phys. **47**, 374001 (2014).
[10]G. Molis, A. Krotkus, and V. Vaičaitis, "Intervalley separation in the conduction band of InGaAs measured by terahertz excitation spectroscopy," Appl. Phys. Lett. **94**, 091104 (2009).
[11]A. Arlauskas and A. Krotkus, "THz excitation spectra of AIIIBV semiconductors," Semicond. Sci. Technol. **27**, 115015 (2012).
[12]V. Karpus, R. Norkus, R. Butkutė, S. Stanionytė, B. Čechavičius, and A. Krotkus, "THz-excitation spectroscopy technique for band-offset determination," Opt. Express **26**, 33807 (2018).
[13]See www.ioffe.ru/SVA/NSM/Semicond/Ge/ for physical properties of germanium (Ge).
[14]A. Singh, A. Pashkin, S. Winnerl, M. Helm, and H. Schneider, "Gapless broadband terahertz emission from a germanium photoconductive emitter," ACS Photonics **5**, 2718–2723 (2018).
[15]A. Urbanowicz, R. Adomavičius, A. Krotkus, and V. L. Malevich, "Electron dynamics in Ge crystals studied by terahertz emission from photoexcited surfaces," Semicond. Sci. Technol. **20**, 1010–1015 (2005).
[16]A. Urbanowicz, A. Krotkus, R. Adomavičius, and V. Malevich, "Terahertz emission from femtosecond laser excited Ge surfaces due to the electrical field-induced optical rectification," Physica B **398**, 98–101 (2007).
[17]A. Bičiūnas, V. Pačebutas, and A. Krotkus, "Terahertz pulse emission from semiconductor surfaces illuminated by femtosecond Yb:KGW laser pulses," Physica B **404**, 3386–3390 (2009).
[18]A. Dimoulas and P. Tsipas, "Germanium surface and interfaces (invited paper)," Microelectron. Eng. **86**, 1577–1581 (2009).
[19]T. Dekorsy, H. Auer, C. Waschke, H. J. Bakker, H. G. Roskos, H. Kurz, V. Wagner, and P. Grosse, "Emission of submillimeter electromagnetic waves by coherent phonons," Phys. Rev. Lett. **74**, 738–741 (1995).
[20]M. Reid, I. V. Cravetchi, and R. Fedosejevs, "Terahertz radiation and second-harmonic generation from InAs: Bulk versus surface electric-field-induced contributions," Phys. Rev. B **72**, 035201 (2005).
[21]G. Mak and H. M. van Driel, "Femtosecond transmission spectroscopy at the direct band edge of germanium," Phys. Rev. B **49**, 16817–16820 (1994).
[22]A. L. Smirl, S. C. Moss, and J. R. Lindle, "Picosecond dynamics of high-density laser-induced transient plasma gratings in germanium," Phys. Rev. B **25**, 2645–2659 (1982).

[23]V. L. Malevich, P. A. Ziaziulia, R. Adomavičius, A. Krotkus, and Y. V. Malevich, "Terahertz emission from cubic semiconductor induced by a transient anisotropic photocurrent," J. Appl. Phys. **112**, 073115 (2012).
[24]P. Cicėnas, A. Geižutis, V. L. Malevich, and A. Krotkus, "Terahertz radiation from an InAs surface due to lateral photocurrent transients," Opt. Lett. **40**, 5164 (2015).
[25]I. Nevinskas, K. Vizbaras, A. Trinkūnas, R. Butkutė, and A. Krotkus, "Terahertz pulse generation from (111)-cut InSb and InAs crystals when illuminated by 1.55 μm femtosecond laser pulses," Opt. Lett. **42**, 2615 (2017).
[26]A. Dargys and J. Kundrotas, *Handbook on Physical Properties of Ge, Si, GaAs and InP* (Science and Encyclopedia, 1994).
[27]C. V. Shank and B. P. Zakharchenya, *Spectroscopy of Nonequilibrium Electrons and Phonons*, 1st ed. (Elsevier, 1992), pp. 291–294.

Paper 4 [P4]

V. Pačebutas, **R. Norkus**, V. Karpus, A. Geižutis, V. Strazdienė, S. Stanionytė, A. Krotkus „Band-offsets of GaInAsBi–InP heterojunctions“ , Infrared Physics and Technology, 109, 103400 (2020)

The article can be accessed online at https://doi.org/10.1016/j.infrared.2020.103400

Infrared Physics and Technology 109 (2020) 103400

Contents lists available at ScienceDirect

Infrared Physics & Technology

journal homepage: www.elsevier.com/locate/infrared

Band-offsets of GaInAsBi–InP heterojunctions

V. Pačebutas*, R. Norkus, V. Karpus, A. Geižutis, V. Strazdienė, S. Stanionytė, A. Krotkus

Center for Physical Sciences and Technology, Saulėtekio 3, LT-10257 Vilnius, Lithuania

ARTICLE INFO

Keywords:
Band offsets
GaInAsBi bismides
THz emission spectroscopy

ABSTRACT

The alignment of band edges in bismide-based $Ga_{0.47}In_{0.53}As_{1-x}Bi_x$–($Ga_{0.47}In_{0.53}As$)–InP heterostructures is examined experimentally by THz emission spectroscopy technique. The determined band offsets of $Ga_{0.47}In_{0.53}As_{1-x}Bi_x$–InP heterojunctions at the $x = 0 - 0.06$ bismuth concentrations correspond to the ≈ 0.38 value of *Q*-parameter, which is defined as the relative conduction band offset with respect to energy gap difference in unstrained heterostructure. The relative conduction band offset is smaller for strained GaInAsBi layers, – it reduces to about 34% at the bismuth concentration of $x = 0.06$. The band offsets of $Ga_{0.47}In_{0.53}As_{1-x}Bi_x$–$Ga_{0.47}In_{0.53}As$ heterojunctions are estimated to correspond to the same value of *Q*-parameter, $Q \approx 0.38$, while the strains are expected to reduce the relative conduction band offset down to about 25% at the $x = 0.06$ Bi concentration.

1. Introduction

The knowledge of conduction and valence band offsets at an interface of two materials composing a heterojunction is of critical importance for an engineering of semiconductor devices. The band alignment problem is widely investigated (see, e.g., reviews [1–5]) theoretically and by various experimental techniques, namely, optical spectroscopy of quantum wells, X-ray photoemission spectroscopy, transport methods, and ballistic electron emission microscopy. Recently we have proposed [6] a novel technique for a direct band-offset determination based on a terahertz excitation spectroscopy (TES). The THz emission in semiconductors is due to a spatial separation of charge carriers photoexcited by a short laser pulse. The TES technique assumes ballistic propagation of photoexcited carriers in a thin enough layer of a narrower-bandgap semiconductor. The layer width should be smaller either than the optical penetration length, for photocarriers to be uniformly distributed, or than the distance which the carriers travel while THz-pulse emission takes place. When charge carriers are photoexcited in a heterostructure of semiconductors, the amplitude of emitted THz-pulse sharply increases at the photon energies when photoelectrons gain sufficient kinetic energy to overcome the potential barrier corresponding to the heterojunction band-offset. This increase can be further facilitated by a refraction of ballistic electrons while passing through the interface [7] that could lead to a more efficient THz wave outcoupling from a semiconductor heterostructure.

In paper [6], the TES technique was applied for a determination of energy band offsets at an interface between the dilute GaAsBi bismide and GaAs. The dilute bismides – the III-V semiconductors with a few percent of Bi – are in a focus of recent theoretical and experimental studies, which are motivated by a potential use of the bismides in GaAs-based near-IR photodetectors [8], highly-efficient solar cells [9], and laser diodes with reduced temperature-sensitivity of emission-wavelength [10].

The quaternary GaInAsBi layers grown on InP substrates is another dilute bismide system of technological importance, because, in principle, it allows for a fabrication of mid-infrared optoelectronic devices operating at up to ~6 μm-wavelengths in the lattice-matched with substrate heterostructures [11–13]. Energy band offsets of GaInAsBi–InP and GaInAsBi–GaInAs heterojunctions are assumed to be of a type-I (see, e.g., [14]), however quantitatively they are not unambiguously determined. In the present work, the band offsets of $Ga_{0.47}In_{0.53}As_{1-x}Bi_x$–InP heterojunctions (with the bismuth concentrations up to 6%) are determined experimentally by TES technique. Experimental results show that the conduction band offset is close to 38% of the energy gap difference $E_{g,InP} - E_{g,GaInAsBi}$ for unstrained layers. In the strained heterostructure, the relative offset is smaller, and reduces to ca. 34% at the bismuth concentration of 6%. Estimates of the $Ga_{0.47}In_{0.53}As_{1-x}Bi_x$–$Ga_{0.47}In_{0.53}As$ band-offsets show that in the strained heterostructures the relative conduction band offset reduces to ca. 25% at 6% Bi.

2. Sample growth and characterization

The $Ga_{1-y}In_yAs_{1-x}Bi_x$ ($y \approx 0.53$) based heterostructures were grown

* Corresponding author.
E-mail address: vaidas.pacebutas@ftmc.lt (V. Pačebutas).

https://doi.org/10.1016/j.infrared.2020.103400
Received 10 April 2020; Received in revised form 28 May 2020; Accepted 2 June 2020
Available online 10 June 2020

on semi-insulating (001) InP:Fe substrates by molecular-beam-epitaxy (MBE) reactor SVT-A, equipped with metallic In, Ga, and Bi sources and a two-zone valved cracker for a production of As_2 molecules. Native oxides were desorbed by heating substrates at 480 °C under arsenic flux and monitoring the deoxidation by observation of a distinctive (2 × 4) surface reconstruction pattern of the reflection high energy electron diffraction. The intermediate $Ga_{0.47}In_{0.53}As$ buffer layers were grown in some of bismide samples at standard growth conditions, keeping the substrate temperature of ~510 °C and the beam equivalent pressure (BEP) ratio As_2/Ga from 7 to 10. The growth temperature was adjusted by a thermocouple-based controller. To enhance an incorporation of bismuth into a growing bismide layer and to avoid Bi segregation on the layer surface, the bismide layer growth was performed at the substrate temperatures of 280 − 300 °C, which are significantly lower than typical MBE growth temperatures for GaInAs. The As_2/Ga BEP ratio was reduced to ~2.3, and the bismide-layer growth rate was of 0.3 μm/h.

Most of the samples, chosen for a band-offset determination, were the 600 nm thick GaInAsBi bismide layers deposited on InP substrates without an intermediate buffer layer. After measuring their physical parameters, for TES measurements, the samples were thinned down to 50 − 150 nm by chemical etching in $H_2SO_4/H_2O_2/H_2O$ solution. The samples with an intermediate GaInAs layer were comprised of 150 nm thick GaInAsBi bismide, 250 nm thick $Ga_{0.47}In_{0.53}As$ layer, and InP substrate. To measure band-offsets of the GaInAs-InP heterojunction, a reference sample of the 1 μm thick $Ga_{0.47}In_{0.53}As$ layer on InP substrate was grown. For TES measurements, the GaInAs layer was etched down to about 20 nm.

The atomic composition of bismide layers was determined by X-ray diffraction (XRD) measurements, carried out with Smart Lab Rigaku diffractometer (see [15] for more details), by monitoring the 004 diffraction peak in rocking-curve diffractograms and the 115 peak in reciprocal space maps (RSM). In analysis of the XRD data, the lattice parameters of GaBi and InBi were taken to be 6.324 Å and 6.686 Å, respectively [16]. It should be noted that the RSM data (Fig. 1) indicated that bismide layers ($x = 0 - 0.06$) remained to be strained despite of their considerable thickness ~600 nm.

The Hall measurements, carried out on thick GaInAsBi layers, indicated that most of the layers were highly *n*-doped, possibly due to a low-temperature growth which causes the creation of a large density of arsenic antisite defects energetically close to the conduction band edge [17]. Only in the samples with the large Bi-content of 3.5 − 6% the electron density in bismide layers was relatively low, of the order of 10^{15} cm^{-3}, which can be explained by the compensating effect of Bi-induced acceptor levels [18,19]. To avoid the band-bowing influence on a band-offset determination, only the samples with low carrier concentrations were chosen for TES measurements.

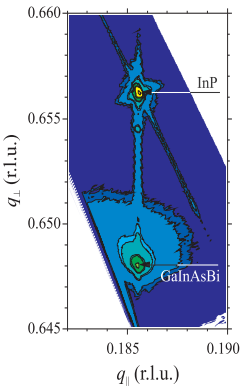

Fig. 1. Reciprocal space map of 115 XRD peak of the 600 nm thick GaInAsBi layer with 6% Bi.

Table 1
Parameters of $Ga_{0.47}In_{0.53}As_{1-x}Bi_x$ layers (their atomic compositions x and bandgaps E_g), measured onsets of THz-emission E_1, determined conduction band offsets ΔE_c of strained GaInAsBi-InP heterojunctions, and estimated conduction band offsets $\Delta E_{c,0}$ for unstrained bismide layers.

x	0	0.035	0.039	0.04	0.055	0.059	0.06
E_g (eV)	0.737	0.564	0.549	0.542	0.485	0.470	0.466
E_1 (eV)	0.986	0.878	–	0.924	0.786	0.803	0.793
ΔE_c (eV)	0.230	0.291	–	0.354	0.279	0.308	0.303
$\Delta E_c/\Delta E_g$	0.38	0.37	–	0.44	0.32	0.35	0.34
$\Delta E_{c,0}$ (eV)	0.230	0.316	–	0.383	0.319	0.351	0.346
$\Delta E_{c,0}/\Delta E_{g,0}$	0.38	0.40	–	0.47	0.36	0.39	0.38

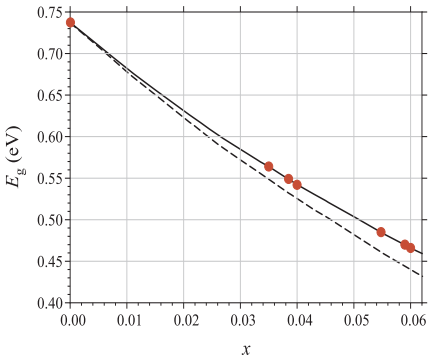

Fig. 2. Dependence of the energy gap of strained $Ga_{0.47}In_{0.53}As_{1-x}Bi_x$ bismide layers (grown on InP-substrates) on bismuth concentration. Dots correspond to samples investigated in the present paper. Dashed curve presents $E_g(x)$ dependence for unstrained bismides [11].

Energy bandgaps E_g of the investigated bismide layers (see Table 1) were determined indirectly, making use of a reference bandgap dependence on Bi concentration, $E_g(x)$, which is presented in Fig. 2 by full curve. The $E_g(x)$ dependence for unstrained bismides (dashed curve in Fig. 2) was adapted from results of the theoretical calculations presented in [11]. To account for strains, the $E_g(x)$ dependence was corrected (see [6] for details) at the following values of elastic constants and deformation potentials: $C_{11} = 101.53$ GPa, $C_{12} = 50.59$ GPa, $a_c = -6.71$ eV, $a_v = -1.08$ eV, and $b = -1.89$ eV (which correspond to those of ternary $Ga_{0.47}In_{0.53}As$) [20]. The obtained values of GaInAsBi energy gaps well corresponded to the spectral positions of an initial rise of THz excitation spectra (see Figs. 3 and 4).

3. Results and discussion

The THz excitation spectroscopy measurements were carried out by experimental setup described in detail in [6].

Fig. 3 presents the THz excitation spectra measured on two 600 nm thick $Ga_{0.47}In_{0.53}As_{1-x}Bi_x$ layers with different Bi concentrations and on the reference 1 μm thick $Ga_{0.47}In_{0.53}As$ layer. The emitted THz-pulse amplitudes monotonously increase with an increase of photon energy $\hbar\omega$. Significant changes in a spectral shape occur first at ca. 1.34 eV and later at ca. 1.6 eV energy. The first of these characteristic energies corresponds to the energy bandgap of InP, 1.344 eV, which influences the THz-pulse emission when a part of optical pulse, not absorbed in a bismide layer, excites current carriers in InP-substrate. Decrease of the THz-pulse amplitude at $\hbar\omega > 1.6$ eV can be attributed to a scattering of photoexcited electrons to subsidiary, high-effective-mass L-valleys of

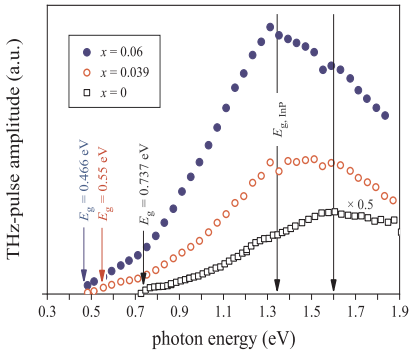

Fig. 3. THz excitation spectra of two 600 nm thick $Ga_{0.47}In_{0.53}As_{1-x}Bi_x$ layers with 6% and 3.9% Bi concentrations and spectrum of $Ga_{0.47}In_{0.53}As$ layer (1 μm).

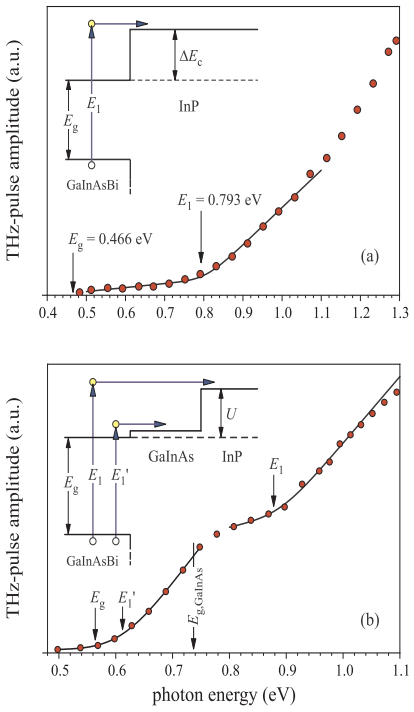

Fig. 4. THz excitation spectra and energy diagrams (insets) of (a) 70 nm thick GaInAsBi layer (6% Bi) on InP substrate and (b) the bismide heterostructure comprised of 150 nm thick GaInAsBi layer (3.5% Bi), 250 nm $Ga_{0.47}In_{0.53}As$ layer, and InP substrate.

conduction band [21]. It should be noted that a value of this characteristic energy, which is a measure of energy separation between conduction band L-valleys and the top of a valence band, does not depend on the Bi content in GaInAsBi alloy and remains approximately the same as in the $Ga_{0.47}In_{0.53}As$ layer lattice-matched to InP. Since the energy gap of GaInAsBi decreases with Bi incorporation, the Γ-L intervalley energy separation presumably increases with an increase of Bi content.

The THz excitation spectra of the bismide heterostructures with thin GaInAsBi layers are presented in Fig. 4. Fig. 4(a) shows the TES spectrum of 70 nm thick GaInAsBi ($x = 0.06$) layer grown directly on InP substrate. As it is seen, a threshold of THz emission, E_1, is blue-shifted from the bandgap of bismide and corresponds to the photon energy when photo-excited electrons gain enough kinetic energy to overcome the potential barrier, set up by a conduction band offset ΔE_c. The indicated value of threshold position, $E_1 = 0.793$ eV, was determined by fitting the experimental data with an energy dependence of the theoretical spectral-shape $A(\hbar\omega)$-function (see [6] for details), which is presented by curves in Fig. 4. This allows for a determination of the conduction band offset ΔE_c, which is related with E_1 as

$$E_1 = E_g + \Delta E_c\left(1 + \frac{m}{m_h}\right). \quad (1)$$

Here m and m_h are the effective electron and heavy hole masses, which were assumed to be equal to those of $Ga_{0.47}In_{0.53}As$, $m = 0.043$ and $m_h = 0.54$ [20]. The determined conduction band offsets ΔE_c of investigated GaInAsBi-InP heterostructures and their estimates for unstrained bismide layers, $\Delta E_{c,0}$, are summarized in Table 1.

The TES spectrum of the bismide heterostructure with an intermediate GaInAs layer exhibits several spectral features [see Fig. 4(b)]. The E_1' onset of THz emission corresponds to an injection of photoelectrons into the intermediate GaInAs layer. Its value, $E_1' = 0.612$ eV, allows for a determination of the conduction band offset of GaInAsBi–GaInAs heterojunction, $\Delta E_c' = 0.045$ eV (which corresponds to the $\Delta E_{c,0}' = 0.07$ eV offset for unstrained bismide layer). The second onset of THz emission, $E_1 = 0.878$ eV, corresponds to an injection of photoelectrons into InP substrate and allows for a determination of potential barrier between the substrate and bismide layer, $U = 0.291$ eV. The difference of the potential barriers, $U - \Delta E_c' = 0.246$ eV, should be equal to the conduction band offset of GaInAs–InP heterojunction. This offset was independently determined from the TES spectrum of a reference GaInAs–InP sample and was of 0.230 eV, what differs from the $U - \Delta E_c'$ value only by 7%. This justifies a reliability of the employed TES technique for a determination of band-offsets and indicates its accuracy to be of about 10%.

The alignment of conduction and valence band edges in the investigated $Ga_{0.47}In_{0.53}As_{1-x}Bi_x$ – $(Ga_{0.47}In_{0.53}As)$ – InP heterostructures, determined by TES measurements, is summarized in Fig. 5. Results obtained on bismide layers grown directly on InP substrates are shown by circles, while squares correspond to the sample with an intermediate GaInAs layer. (Empty and full squares present the bismide band edges determined with respect to InP and GaInAs layer, respectively.) The

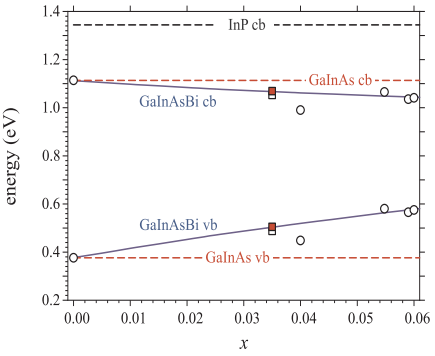

Fig. 5. The energy positions of conduction and valence band edges in GaInAsBi–(GaInAs)–InP heterostructures versus the bismuth concentration x of bismide layers.

energy zero is taken to coincide with InP valence band edge. Full curves in the figure correspond to the theoretical positions of bismide band edges calculated at the relative conduction band offset $Q = 0.38$. The Q-parameter conventionally is defined as the ratio of the conduction band offset and the energy gap difference of unstrained semiconductors comprising a heterojunction, $Q = \Delta E_{c,0}/\Delta E_{g,0}$. For the strained $Ga_{0.47}In_{0.53}As_{1-x}Bi_x$–InP heterostructure, the relative conduction band offset is smaller, and reduces to ca. 34% at the bismuth concentration of 6%. The determined scheme of band alignment (Fig. 5) allows for an estimation of $Ga_{0.47}In_{0.53}As_{1-x}Bi_x$–$Ga_{0.47}In_{0.53}As$ band-offsets. For the GaInAsBi–GaInAs heterojunction, the Q-parameter is the same, $Q = 0.38$, while a strain in bismide layer reduces the relative conduction band offset to ca. 25% at 6% Bi.

The determined conduction and valence band offsets of the lattice-matched, widely investigated, GaInAs–InP heterojunction (which correspond to the $x = 0$ dots in Fig. 5) are of 0.23 eV and 0.377 eV, respectively. Our results agree with the recommended average literature values [20], 0.263 eV and 0.345 eV, with an accuracy of about 10%.

Declaration of Comepeting Interest

None.

Acknowledgements

The authors gratefully acknowledge support by the Research Council of Lithuania (Grant No. S-MIP-17–25).

References

[1] E.T. Yu, J.O. McCaldin, T.C. McGill, Band offsets in semiconductor heterojunctions, Solid State Physics, 46 Academic Press, 1990, p. 1.
[2] A. Franciosi, C.G. Van de Walle, Heterojunction band offset engineering, Surf. Sci. Rep. 2 (1996) 1–140.
[3] H. Kroemer, Nobel Lecture: Quasielectric fields and band offsets: teaching electrons new tricks, Rev. Mod. Phys. 73 (2001) 783–793.
[4] W. Yi, A.J. Stollenwerk, V. Narayanamurti, Ballistic electron microscopy and spectroscopy of metal and semiconductor nanostructures, Surf. Sci. Rep. 64 (2009) 169–190.
[5] J. Robertson, Band offsets, Schottky barrier heights, and their effects on electronic devices, J. Vac. Sci. Technol. A 31 (2013) 050821.
[6] V. Karpus, R. Norkus, R. Butkutė, S. Stanionytė, B. Čechavičius, A. Krotkus, THz-excitation spectroscopy technique for band-offset determination, Opt. Exp. 26 (2018) 33807–33817.
[7] D.W. Wilson, E.N. Glytsis, T.K. Gaylord, Electron waveguiding characteristics and ballistic current capacity of semiconductor quantum slabs, IEEE J. Quant. Electron. 29 (1993) 1364–1382.
[8] Y. Gu, Y.G. Zhang, X.Y. Chen, Y.J. Ma, S.P. Xi, B. Du, Hsby. Li, Nearly lattice-matched short-wave infrared InGaAsBi detectors on InP, Appl. Phys. Lett. 108 (2016) 032102.
[9] T. Thomas, A. Mellor, N.P. Hylton, M. Führer, D. Alonso-Àlvarez, A. Braun, N.J. Ekins-Daukes, J.P.R. David, S.J. Sweeney, Requirements for a GaAsBi 1 eV sub-cell in a GaAs-based multi-junction solar cell, Semicond. Sci. Technol. 33 (2015) 094010.
[10] Y. Tominaga, K. Oe, M. Yoshimoto, Low temperature dependence of oscillation wavelength in $GaAs_{1-x}Bi_x$ laser by photo-pumping, Appl. Phys. Exp. 3 (2010) 062201.
[11] J.P. Petropoulos, Y. Zhong, J.M.O. Zide, Optical and electrical characterization of InGaBiAs for use as a mid-infrared optoelectronic material, Appl. Phys. Lett. 99 (2011) 031110.
[12] J. Devenson, V. Pačebutas, R. Butkutė, A. Baranov, A. Krotkus, Structure and optical properties of InGaAsBi with up to 7% bismuth, Appl. Phys. Exp. 5 (2012) 015503.
[13] I.P. Marko, Z. Batool, K. Hild, S.R. Jin, N. Hossain, T.J.C. Hosea, J.P. Petropoulos, Y. Zhong, P.B. Dongmo, J.M.O. Zide, S.J. Sweeney, Temperature and Bi-concentration dependence of the bandgap and spin-orbit splitting in InGaBiAs/InP semiconductors for mid-infrared applications, Appl. Phys. Lett. 101 (2012) 221108.
[14] M. Gladysiewicz, R. Kudrawiec, M.S. Wartak, 8-band and 14-band kp modeling of electronic band structure and material gain in Ga(In)AsBi quantum wells grown on GaAs and InP substrates, J. Appl. Phys. 118 (2015) 055702.
[15] V. Pačebutas, S. Stanionytė, R. Norkus, A. Bičiūnas, A. Urbanowicz, A. Krotkus, Terahertz pulse emission from GaInAsBi, J. Appl. Phys. 125 (2019) 174507.
[16] A. Janotti, S.-H. Wei, S.B. Zhang, Theoretical study of the effects of isovalent coalloying of Bi and N in GaAs, Phys. Rev. B 65 (2002) 115203.
[17] H. Künzel, J. Böttcher, R. Gibis, G. Urmann, Material properties of $Ga_{0.47}In_{0.53}As$ grown on InP by low-temperature molecular beam epitaxy, Appl. Phys. Lett. 61 (1992) 1347–1349.
[18] G. Pettinari, A. Patanè, A. Polimeni, M. Capizzi, Xianfeng Lu, T. Tiedje, Bi-induced p-type conductivity in nominally undoped Ga(AsBi), Appl. Phys. Lett. 100 (2012) 092109.
[19] S. Zhu, W. Qiu, H. Wang, T. Lin, P. Chen, X. Wang, Raman spectroscopic determination of hole concentration in undoped GaAsBi, Semicond. Sci. Technol. 34 (2019) 015008.
[20] I. Vurgaftman, J.R. Meyer, L.R. Ram-Mohan, Band parameters for III-V compound semiconductors and their alloys, J. Appl. Phys. 89 (2001) 5815–5875.
[21] G. Molis, A. Krotkus, V. Vaičaitis, Intervalley separation in the conduction band of InGaAs measured by terahertz excitation spectroscopy, Appl. Phys. Lett. 94 (2009) 091104.

Paper 5 [P5]

R. Norkus, I.Nevinskas, A.Krotkus, "Terahertz emission from a bulk GaSe crystal excited by above bandgap photons", J. Appl. Phys. 128, 225701 (2020);

This article may be accessed online https://doi.org/10.1063/5.0027944

Journal of Applied Physics ARTICLE scitation.org/journal/jap

Terahertz emission from a bulk GaSe crystal excited by above bandgap photons

Cite as: J. Appl. Phys. **128**, 225701 (2020); doi: 10.1063/5.0027944
Submitted: 1 September 2020 · Accepted: 22 November 2020 ·
Published Online: 8 December 2020

R. Norkus, I. Nevinskas,[a] and A. Krotkus

AFFILIATIONS

Centre for Physical Sciences and Technology, Saulėtekio av. 3, Vilnius LT-10257, Lithuania

[a]**Author to whom correspondence should be addressed:** ignas.nevinskas@ftmc.lt

ABSTRACT

Spectral dependences of the amplitudes of terahertz (THz) transients radiated from a GaSe surface after its excitation by femtosecond optical pulses with photon energies in the range from 1.8 eV to 3.8 eV were used for the study of electron energy band structure of this layered crystal. The energy separation of 0.21 eV between the main Γ valleys and the satellite K valleys in the conduction band was determined from the maximum position of THz excitation spectrum; the polarity of the THz transients became inverted at photon energies higher than 3 eV due to the onset of electron transitions from the second, lower lying valence band.

INTRODUCTION

Gallium selenide is a layered III–VI semiconductor crystal. Each GaSe layer consists of four covalently bonded Se–Ga–Ga–Se atomic planes and the layers are stacked together by a weak van der Waals force. Bulk GaSe crystals have an energy bandgap of approximately 2 eV and an extreme optical transparency in the infrared (IR) spectral region. The optical absorption coefficient of GaSe does not exceed 1 cm^{-1} throughout the transparency range from 0.65 μm to 18 μm.[1] Its nonlinear optical coefficients are among the highest measured in the infrared range for birefringent crystals. GaSe is widely used as a nonlinear optical crystal for applications such as mid-IR and THz radiation generation[2,3] electrooptic sampling,[4] frequency comb generation,[5] and saturable absorbers.[6] The bandwidth-limited IR pulses with frequencies reaching 41 THz are generated in GaSe crystals by nonlinear optical rectification[7] after the photoexcitation by 10 fs duration Ti:sapphire laser pulses (at the wavelength of 780 nm). The same frequency bandwidth is also demonstrated by electrooptic THz detectors fabricated from GaSe.[8]

Moreover, GaSe is a semiconductor with a relatively high bandgap energy, so it has attracted much interest because of its potential applications for photoelectric devices that operate in the visible region.[9,10] Recent theoretical studies have predicted a new phase of GaSe as a three-dimensional topological insulator, indicating its potential applications in spintronics.[11] Other layered crystals such as transition metal dichalcogenides, the two-dimensional (2D) crystals composed of a few or even single atomic layers, can be fabricated from GaSe by mechanical exfoliation[12] or epitaxial growth.[13,14] 2D GaSe monolayers have shown superior properties for applications such as photodetectors,[9,15] light-emitting devices,[16] and field effect transistor.[17] However, despite an enhanced interest on various GaSe applications, the knowledge of semiconducting properties of this material is still rather limited. It is commonly agreed that the energy gap ε_g of stable ε-GaSe polytype bulk crystals at room temperature is ∼2 eV, though the predictions on whether the optical gap are direct or indirect may differ.[18,19] The estimations of energy separation in the conduction band of bulk GaSe crystals between the main Γ valleys and secondary M valleys also vary from −0.13 eV[20] to +0.3 eV.[21]

In this paper, we present a set of measurements that allow us to evaluate the details of the electron energy dispersion law at energies remote from the bandgap edge. The main experiment performed is the measurement of THz pulse amplitudes emitted from a GaSe surface after its photoexcitation by femtosecond optical pulses of different wavelengths. Such dependencies—the THz excitation spectra—have been successfully used before for investigating the electron energy band structure of A_3B_5 semiconductors,[22] semiconductor nanowires,[23] hybrid organic–nonorganic perovskites,[24] and other material systems. An analysis of the experimental data obtained from GaSe provided novel information on the details of the structure of valence and conduction bands of this material.

EXPERIMENTAL DETAILS

The samples investigated were 50 μm thick GaSe sheets cleaved from a Bridgman grown crystal. For this purpose, an adhesive tape was attached to the sample surface and then peeled off carefully, taking with it a thin sheet of GaSe. Hall effect measurements had evidenced a p-type conductivity with a hole density of 4.5×10^{14} cm^{-3} and a mobility of 40 cm^2/Vs. The surface THz emission experiments were performed in a transmission geometry with samples illuminated at 30° or 0° angles to their surface normal. The experimental setup was based on an amplified ytterbium-doped potassium gadolinium tungstate (Yb:KGW) laser system (PHAROS, Light Conversion Ltd.) operating at 1030 nm with a pulse duration of 160 fs and a repetition rate of 200 kHz. The laser beam with an average power of 6 W was directed into a cavity-tuned optical parametric amplifier (OPA, ORPHEUS, Light Conversion Ltd.) that generated 140–180 fs duration pulses with a central wavelength tuneable from 640 nm to 2600 nm. Shorter wavelength femtosecond optical pulses from 640 nm down to 400 nm were reached by generating the second harmonic in a BBO (Beta Barium Borate) crystal. In the THz time-domain spectroscopy (THz-TDS) arrangement, the samples were excited by the OPA output beam, while the sample-emitted THz pulses were detected by the GaAsBi photoconducting antenna (TeraVil Ltd.). The average power of optical pulses incident on a sample during THz excitation spectra measurements was from 10 mW to 350 mW, which corresponded to the irradiation level from ~1 μJ/cm^2 to 20 μJ/cm^2. The THz detector was illuminated by a small fraction of Yb:KGW laser beam (an average power of ~5 mW), which was delayed by different amounts of time with respect to the optical beam exciting the sample. All experiments were performed at room temperature.

RESULTS

Figure 1 shows the THz pulses and their respective Fourier spectra emitted from the GaSe sample when it is illuminated at a 30° angle from surface normal by femtosecond optical pulses of two different wavelengths. The emitted THz pulse shape after photoexcitation with a longer wavelength radiation, that is, corresponding to an optically transparent region, is bipolar and it is characterized by a wider THz frequency bandwidth, whereas the THz pulse radiated from GaSe when illuminated by higher than energy bandgap photons is monopolar and of a narrower Fourier spectral bandwidth. However, the efficiency of THz pulse emission from GaSe becomes much higher when the photon energy exceeds the energy bandgap. This demonstrates an obvious advantage of the semiconducting surface THz emitters over those that are based on the optical rectification effect in dielectric crystals. To reach comparable THz electric field amplitudes (the THz pulse peak-to-peak values) when exciting the sample at sub-bandgap photon energies (1.77 eV), the optical pulse power must be approximately nine times higher than that at a photon energy of 2.2 eV, the emitted THz transient in the former case is narrower and its Fourier spectrum is wider.

The THz pulse emission from the GaSe crystal has a strong dependence of its amplitude on the azimuthal angle, ϕ, between the optical field direction and crystalline axes. For a hexagonal symmetry crystal plane that has the c-axis perpendicular to it, this

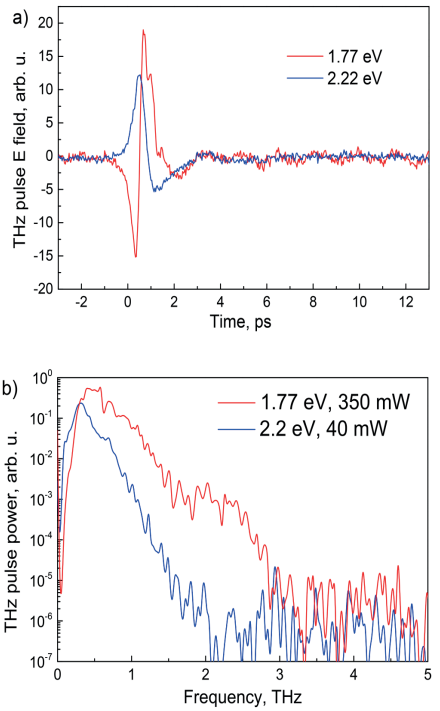

FIG. 1. Electric field dynamics of the THz transients (a) and their Fourier spectra (b) measured when the photon energy of optical pulses is lower ($h\nu$ = 1.77 eV) and higher ($h\nu$ = 2.2 eV) than the energy bandgap of GaSe. Note that the average power of photoexciting pulses is nine times higher for the 1.77 eV photons. The azimuthal angle is at THz emission maximum.

dependence is proportional to sin 3ϕ. Figure 2 shows the azimuthal angle dependencies measured in the transmission direction when the sample is excited by P-polarized optical beams of various wavelengths impinging the surface at a 30° angle. The latter THz curves can be expressed as an angle dependent, A, and independent, B, components as $E_{THz}(\varphi) = A + B \sin 3\varphi$. The amplitude of the azimuthal angle dependent part of the THz signal is higher when the optical beam is of S-polarization; it is the highest when the sample is illuminated along its surface normal.

The spectrum of the azimuthal angle dependent THz pulse amplitude is rather complicated (see Fig. 3). It has two ranges at low and high photon energy sites separated by the region between 3 eV and 3.6 eV at which the THz pulse amplitude is nearly independent on ϕ. The data presented in Fig. 3 are obtained when the sample is excited at its surface normal; however, similar

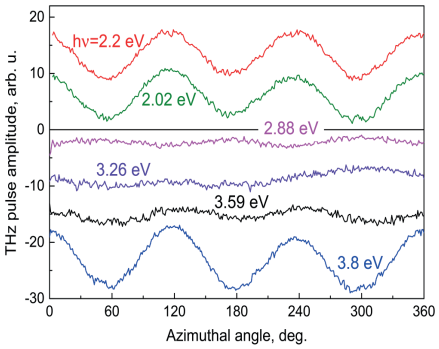

FIG. 2. The azimuthal angle dependencies of THz pulse amplitude for different P-polarized femtosecond optical beam photon energies. The GaSe sample is illuminated at a 30° angle to surface normal; the THz pulses are monitored in transmission geometry.

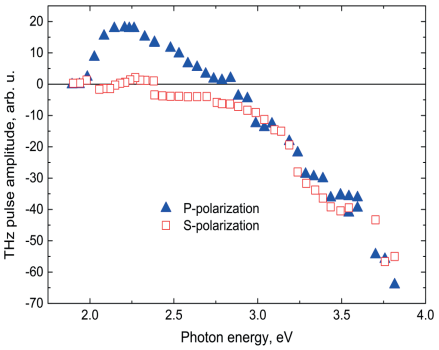

FIG. 4. The azimuthal angle independent THz pulse amplitude spectra of a GaSe crystal illuminated by S- (red squares) and P-polarized (blue triangles) optical beams.

dependences are observed for inclined photoexcitations and for both S- and P-polarized optical beams.

In contrast to the azimuthal angle dependent THz amplitude component, the angle independent THz excitation spectra are different for different polarizations of the optical beam (Fig. 4). The experiments illustrated in this figure are performed in transmission geometry at different exciting wavelengths impinging the surface of GaSe at a 30° angle to its normal.

No angle independent background is observed for photon energies below ∼2.9 eV when optical beams are S-polarized; at higher photon energies, this background is increasing monotonously. For the photoexcitation with P-polarized optical beams, the THz pulse amplitude increases monotonously up to photon energies of ∼2.25 eV, after which a rather steep reduction follows until a minimum of the THz transient field is reached at 2.9 eV. An inversion of the phase of THz transients is taking place at this photon energy (see Fig. 5), while the THz pulse amplitude begins to increase again.

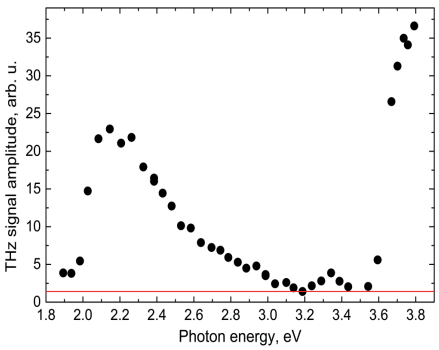

FIG. 3. The amplitude of the azimuthal angle dependent part of THz pulses at various photon energies. The sample is illuminated along its surface normal; the THz pulses are measured in transmission geometry. The red line is the noise floor average.

DISCUSSION

The measurements of azimuthal angle dependencies—the dependence of the THz pulse amplitude on the angle between optical field vector and crystalline axes—are a standard means of characterizing the physical mechanism responsible for the THz emission phenomenon.[25,26] The presence of such a dependence could be considered as the evidence that a nonlinear optical rectification or other effects related to crystal anisotropy play the main role in the THz radiation generation, whereas its absence indicates that the ultrafast electron and hole separation in space caused by their diffusion or drift is the dominating physical mechanism.

The first rather trivial conclusion that could be made after considering the results presented above is that the physical mechanisms responsible for surface THz emission from GaSe depend on whether the exciting photon energies are either lower or higher than the bandgap. In the low photon energy range, this effect is caused by the optical rectification, that is, the nonlinear response of bound electrons, whereas in the high photon energy range, the THz emission is originating from the photoexcited free electron and hole spatial separation and the lateral photocurrents arising due to the anisotropy of the energy dispersion relation.[27,28] For a hexagonal crystal-like GaSe and its c-plane, the optical rectification and the anisotropic lateral photocurrent components follow sin 3ϕ type dependences.[29]

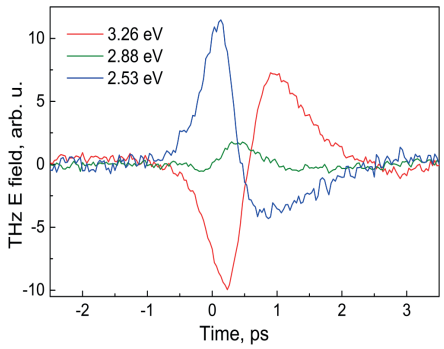

FIG. 5. THz pulses excited in GaSe by different wavelength P-polarized optical beams.

A specific feature of the THz excitation spectra of GaSe is the strong dependence of their shapes on the femtosecond laser beam polarization used for the photoexcitation. It could be concluded that the S-polarized optical radiation has a main influence on the anisotropy of measured characteristics, whereas the P-polarized beams are contributing to the isotropic, the azimuthal angle independent, part of the radiated THz pulse amplitude. These observations are in line with a well-known characteristic of the optical selection rules in hexagonal crystals—the interband optical transitions that are dependent on exciting electric field polarization relative to the ***c*** axis. In hexagonal wurtzite-type crystals where optical selection rules are similar to the ones of GaSe, for example, a considerable role is played by the optical alignment effect[23,30] as the optical field of S-polarized beams is always perpendicular to the ***c*** axis, while the P-polarized beams have parallel as well as perpendicular to ***c***-axis components for off-normal surface excitations. Consequentially, the latter beams excite electrons from different energy levels with different symmetry.

The uppermost valence band (Γ_{v1}) has mainly a Se p_z character, which makes the fundamental transition to the s-character conduction band allowed for the light polarized parallelly to ***c***-axis ($E_{opt} \parallel \boldsymbol{c}$). This band also contains a small component of a Se p_x–p_y character that supports the optical transitions with the polarization $E_{opt} \perp \boldsymbol{c}$. On the other hand, optical selection rules allow the transitions from the Γ_{v2} band to the conduction band only for the light polarized perpendicular to the ***c***-axis.[29] The Γ_{v2} band is highly anisotropic;[31] therefore, the electrons excited from this band would create a lateral photocurrent dependent on the optical field vector angle with respect to the crystal axes. Anisotropic optical transitions excited by $E_{opt} \perp \boldsymbol{c}$ polarization are the main cause of the azimuthal angle dependences of radiated THz pulse amplitude.

The isotropic component of THz excitation spectra is most likely defined by the dynamical dipoles evolving at a surface due to the electron and hole spatial separation. In the photon energy range between 2 eV and 3 eV, the electron–hole pairs are generated due to the transitions from the uppermost valence band, Γ_{v1}. Since the GaSe sample is of a p-type conduction, the energy bands are bent downward at the surface, and the photoexcited electrons are forced to move toward the surface. The transitions from the Γ_{v2} band are activated when the photon energy exceeds 3–3.2 eV.[32,33] In our experiment, the optical beam incidence angle is 30°, so the light is refracted at an 11.5° angle inside the GaSe, and the intensity of the $E_{opt} \perp \boldsymbol{c}$ component of the beam is ∼15 times higher than that of the $E_{opt} \parallel \boldsymbol{c}$ component. This would explain the growth of the emitted THz pulse amplitude at higher than 3 eV photon energies. In a separate experiment, we compared the polarities of THz pulses emitted in this spectral range from GaSe and n-type GaAs samples. These polarities have shown to be of the same sign, which evidences that the electrical dipole is formed by the electrons moving toward the bulk of the GaSe crystal and the holes remaining at the surface. Such a carrier separation can occur due to different electron and hole diffusion rates—the Photo-Dember effect.[34]

Finally, let us discuss the shape of THz excitation spectra dependences in their initial part, close to the energy bandgap (Figs. 3 and 4). The peaks of THz excitation spectra (for GaSe, it is at ∼2.3 eV, Fig. 3) have been documented previously for the majority of group A_3B_5 semiconductors.[22] These peaks have been explained by the onset of photoexcited electron transitions to satellite conduction band valleys with high effective masses, which results in a decreasing THz pulse intensity. Since the nonparabolicity of electronic bands is mostly pronounced in narrow gap semiconductors such as InAs or InSb, these bands of a wide bandgap GaSe can be assumed to be of a parabolic shape. From the momentum and energy conservation laws, one could derive the excess energy of electrons at which the intervalley transfer sets in

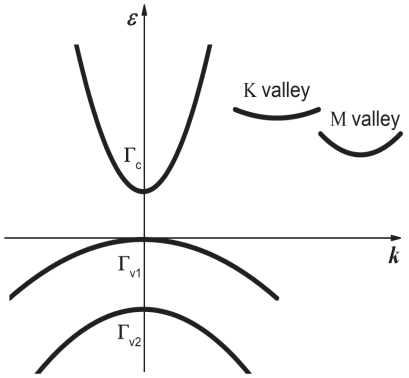

FIG. 6. Schematic energy band structure of a bulk GaSe crystal.

$$\varepsilon_2 = \frac{(\varepsilon_p - \varepsilon_g)}{\left(1 + \frac{m_n}{m_p}\right)} + h\omega, \tag{1}$$

where ε_p is the exciting photon energy, $m_n = 0.24m_o$, and $m_p = 0.4m_o$ are the effective electron and hole masses in Γ_c and Γ_{v1} energy bands, respectively,[1] and $\hbar\omega = 0.0167$ eV is the optical phonon energy of GaSe.[35] After inserting these values and $\varepsilon_p = 2.3$ eV into the equation, we find the intervalley energy separation between conduction band valleys at Γ and K points of the Brillouin zone to be equal to 0.21 eV. High electron effective masses in the K valleys significantly reduce their mobility and diffusion rate; therefore, the emitted THz pulse amplitude decreases. A subsequent increase of this amplitude sets in only when the photon energy is high enough to activate the electron transitions from the Γ_{v2} band to the low effective mass levels in the conduction band (Fig. 6).

CONCLUSIONS

In conclusion, the THz emission from a GaSe crystal excited by femtosecond optical pulses with photon energies higher than energy bandgap was measured over a wide spectral range. The obtained THz excitation spectra revealed several features typical to the specific optical selection rules of hexagonal symmetry crystals. The shape of these spectra was sensitive to the exciting light polarization. The azimuthal angle dependences of the THz pulse amplitude were proportional to $\sin 3\phi$ in the case of *c*-plane photoexcitation. The azimuthal angle dependence for the S-polarized laser beam was stronger than that for the P-polarized beam because it was caused by the lateral photocurrents of electrons excited by an optical field perpendicular to the ***c*** axis. The optical field component parallel to this axis was creating carriers propagating toward the bulk of the crystal and it was responsible for the azimuthal angle independent part of the THz radiation. An analysis of THz excitation spectra was used to estimate the energetic distance between the two upper valence bands. Moreover, the intervalley energy separation between the main G and satellite K valleys of the conduction band was determined from the shape of the initial part of the THz excitation spectrum.

ACKNOWLEDGMENTS

This research was funded by a grant from the European Social Fund, Measure No. 09.3.3-LMT-K-712-01-0032.

DATA AVAILABILITY

The data that support the findings of this study are available from the corresponding author upon reasonable request.

REFERENCES

[1]N. C. Fernelius, "Properties of gallium selenide single crystal," Prog. Cryst. Growth Charact. **28**, 275 (1994).
[2]R. Hegenbarth, A. Steinmann, S. Sarkisov, and H. Giessen, "Milliwatt-level mid-infrared (10.5–16.5μm) difference frequency generation with a femtosecond dual-signal-wavelength optical parametric oscillator," Opt. Lett. **37**, 3513 (2012).
[3]W. Shi, Y. J. Ding, N. Fernelius, and K. Vodopyanov, "Efficient, tunable, and coherent 0.18–5.27-THz source based on GaSe crystal," Opt. Lett. **27**, 1454 (2002).
[4]K. Liu, J. Xu, and X.-C. Zhang, "GaSe crystals for broadband terahertz wave detection," Appl. Phys. Lett. **85**, 863 (2004).
[5]F. Keilmann, C. Gohle, and R. Holzwarth, "Time-domain mid-infrared frequency-comb spectrometer," Opt. Lett. **29**, 1542 (2004).
[6]U. Kurum, M. Yuksek, H. G. Yaglioglu, A. Elmali, A. Ates, M. Karabulut, and G. M. Mamedov, "The effect of thickness and/or doping on the nonlinear and saturable absorption behaviors in amorphous GaSe thin films," J. Appl. Phys. **108**, 063102 (2010).
[7]R. Huber, A. Brodschelm, F. Tauser, and A. Leitenstorfer, "Generation and field-resolved detection of femtosecond electromagnetic pulses tunable up to 41 THz," Appl. Phys. Lett. **76**, 3191 (2000).
[8]K. C. Mandal, S. H. Kang, M. Choi, J. Chen, X.-C. Zhang, J. M. Schleicher, C. A. Schmuttenmaer, and N. C. Fernelius, "III–VI chalcogenide semiconductor crystals for broadband tunable THz sources and sensors," IEEE J. Select. Top. Quantum Electron. **14**, 284 (2008).
[9]P. Hu, Z. Wen, L. Wang, P. Tan, and K. Xiao, "Synthesis of Few-layer GaSe nanosheets for high performance photodetectors," ACS Nano **6**, 5988 (2012).
[10]S. Sorifi, M. Moun, S. Kaushik, and R. Singh, "High-temperature performance of a GaSe nanosheet-based broadband photodetector," ACS Appl. Electron. Mater. **2**, 670–676 (2020).
[11]Z. Zhu, Y. Cheng, and U. Schwingenschloegl, "Topological phase transition in layered GaS and GaSe," Phys. Rev. Lett. **108**, 266805 (2012).
[12]D. J. Late, B. Liu, H. S. S. R. Matte, C. N. R. Rao, and V. P. Dravid, "Rapid characterization of ultrathin layers of chalcogenides on SiO2/Si substrates," Adv. Funct. Mater. **22**, 1894 (2012).
[13]S. D. Lei, L. H. Ge, Z. Liu, S. Najmaei, G. Shi, G. You, J. Lou, R. Vajtai, and P. M. Ajayan, "Synthesis and photoresponse of large GaSe atomic layers," Nano Lett. **13**, 2777 (2013).
[14]Z. Ben Aziza, H. Henck, D. Pierucci, M. G. Silly, E. Lhuillier, G. Patriarche, F. Sirotti, M. Eddrief, and A. Ouerghi, "Van der Waals epitaxy of GaSe/graphene heterostructure: Electronic and interfacial properties," ACS Nano **10**, 9679 (2016).
[15]Y. Cao, K. Cai, P. Hu, L. Zhao, T. Yan, W. Luo, X. Zhang, X. Wu, K. Wang, and H. Zheng, "Strong enhancement of photoresponsivity with shrinking the electrodes spacing in few layer GaSe photodetectors," Sci. Rep. **5**, 8130 (2015).
[16]N. Balakrishnan, Z. R. Kudrynskyi, M. W. Fay, G. W. Mudd, S. A. Svatek, O. Makarovsky, Z. D. Kovalyuk, L. Eaves, P. H. Beton, and A. Patane, "Room temperature electroluminescence from mechanically formed van der Waals III–VI homojunctions and heterojunctions," Adv. Opt. Mater. **2**, 1064 (2014).
[17]D. J. Late, B. Liu, J. J. Luo, A. M. Yan, H. Matte, M. Grayson, C. N. R. Rao, and V. P. Dravid, "GaS and GaSe ultrathin layer transistors," Adv. Mater. **24**, 3549 (2012).
[18]J. Srour, M. Badawi, F. El Haj Hassan, and A. Postnikov, "Comparative study of structural and electronic properties of GaSe and InSe polytypes," J. Chem. Phys. **149**, 054106 (2018).
[19]Y. Ma, Y. Dai, M. Guo, L. Yu, and B. Huang, "Tunable electronic and dielectric behavior of GaS and GaSe monolayers," Phys. Chem. Chem. Phys. **15**, 7098 (2013).
[20]R. Sporken, R. Hafsi, F. Coletti, J. M. Debever, P. A. Thiry, and A. Chevy, "Inverse-photoemission spectroscopy of GaSe and InSe," Phys. Rev. B **49**(11), 11093 (1994).
[21]U. Schwarz, D. Olguin, A. Cantarero, M. Hanfland, and K. Syassen, ""Effect of pressure on the structural properties and electronic band structure of GaSe," Phys. Status Solidi (b) **244**, 244 (2007).
[22]A. Arlauskas and A. Krotkus, "THz excitation spectra of AIIIBV semiconductors," Semicond. Sci. Technol. **27**, 115015 (2012).
[23]R. Adomavičius, I. Nevinskas, J. Treu, X. Xu, G. Koblmüller, and A. Krotkus, "Pulsed THz emission from wurtzite phase catalyst-free InAs nanowires," J. Phys. D: Appl. Phys. **53**, 19LT01 (2020).
[24]C. S. Ponseca Jr, A. Arlauskas, H. Y. Wang, I. Nevinskas, E. Dūda, V. Vaičaitis, J. Eriksson, J. Bergqvist, X.-K. Liu, M. Kemerink, A. Krotkus, O. Inganas, and F. Gao, "Pulsed terahertz emission from solution-processed lead iodide perovskite films," ACS Photonics **6**, 1175 (2019).

[25]J. Dong *et al.*, "Terahertz emission from layered GaTe crystal Due to surface lattice reorganization and In-plane noncubic mobility anisotropy," Photonics Res. **7**(2019), 518 (2019).
[26]J. B. Khurgin, "Optical rectification and terahertz emission in semiconductors excited above the band gap," J. Opt. Soc. Am. B **11**, 2492 (1994).
[27]P. Cicėnas, A. Geižutis, V. L. Malevich, and A. Krotkus, "Terahertz radiation from an InAs surface due to lateral photocurrent transients," Opt. Lett. **40**, 5164 (2015).
[28]I. Nevinskas, K. Vizbaras, A. Trinkūnas, R. Butkutė, and A. Krotkus, "Terahertz pulse generation from (111)-cut InSb and InAs crystals when illuminated by 1.55-μm femtosecond laser pulses," Opt. Lett. **42**, 2615 (2017).
[29]A. Bičiūnas, A. Arlauskas, J. Adamonis, P. Cicėnas, and A. Krotkus, "Physical mechanisms of terahertz pulse emission from photoexcited surfaces of tellurium crystals," J. Appl. Phys. **116**, 093102 (2014).
[30]P. Tronc, Y. E. Kitaev, G. Wang, M. F. Limonov, A. G. Panfilov, and G. Neu, "Optical selection rules for hexagonal GaN," Phys. Status Solidi (b) **216**, 599 (1999).
[31]L. Plucinski R, L. Johnson, B. J. Kowalski, K. Kopalko, B. A. Orlowski, Z. D. Kovalyuk, and G. V. Lashkarev, "Electronic band structure of GaSe (0001): Angle-resolved photoemission and *ab initio* theory," Phys. Rev. B **68**, 125304 (2003).
[32]A. Segura, J. Bouvier, M. V. Andres, F. J. Manjon, and V. Munoz, "Strong optical nonlinearities in gallium and indium selenides related to inter-valence-band transitions induced by light pulses," Phys. Rev. B **56**, 4075 (1997).
[33]S. G. Choi, D. H. Levi, C. Martinez-Tomas, and V. Muñoz Sanjosé, "Above-bandgap ordinary optical properties of GaSe single crystal," J. Appl. Phys. **106**, 053517 (2009).
[34]T. Dekorsy, H. Auer, H. J. Bakker, H. G. Roskos, and H. Kurz, "THz electromagnetic emission by coherent infrared-active phonons," Phys. Rev. B **53**, 4005 (1996).
[35]S. S. Yao, J. Buchert, and R. R. Alfano, "Time-resolved picosecond absorption spectroscopy of the layered compound gallium selenide," Phys. Rev. B **25**, 6534 (1982).

Paper 6 [P6]

I. Nevinskas, **R. Norkus**, A. Geižutis, L. Kulyuk, A. Miku, K. Sushkevich and A. Krotkus, „Terahertz pulse emission from photoexcited bulk crystals of transition metal dichalcogenides“ J. Phys. D: Appl. Phys. 54 115105 (2020)

The published article can be accessed online: https://doi.org/10.1088/1361-6463/abcc26

Terahertz pulse emission from photoexcited bulk crystals of transition metal dichalcogenides

I. Nevinskas*[a)], R. Norkus[a)], A. Geižutis [a)], L. Kulyuk[b)], A. Miku[b)], K. Sushkevich[c)] and A. Krotkus[a)]

a) Centre for Physical Sciences and Technology, Saulėtekio av. 3, Vilnius, LT-10257, Lithuania

b) Institute of Applied Physics, Academiei str. 5, Chisinau, MD-2028, Moldova

c) Moldova State University, Mateevichi str. 60, Chisinau, MD-2009, Moldova

ABSTRACT: Multilayer MoS2, MoSe2, and WSe2 crystals were excited with femtosecond optical pulses of various wavelengths. The emitted terahertz (THz) radiation pulses were found to be the most intense at photon energies coinciding with the direct energy gap at the K points of the Brillouin zone of corresponding materials. It was shown that the transition metal dichalcogenides of different dopant type emit THz pulses of opposite polarity, suggesting that the surface field plays a role in THz emission. Nevertheless, the optical pump–THz probe experiments contradicted THz emission observations, demonstrating a decrease in photoconductivity at higher energy quanta. The proposed THz pulse generation mechanism, therefore, assumes the accumulation of excitonic electric dipoles during optical pulse absorption and a fast build-up of the internal electric field inside the samples. This assumption was supported by double optical pulse investigations.

KEYWORDS: THz, terahertz emission, TMD, transition metal dichalcogenides, MoS_2, $MoSe_2$, WSe_2, excitons, double pulse experiment, femtosecond laser

Transition metal dichalcogenides (TMDs) MX_2 (M = Mo, W and X = S, Se) have attracted recently an enhanced interest because of their distinct electronic, optical, and catalytic properties[1-4] as well as due to promising applications in field-effect transistors[5], photodetectors, optoelectronic memory devices[6] and light-emitting diodes[7]. Crystals of TMDs are composed of vertically stacked weakly interacting layers held together by the van der Waals interaction. The bulk MX_2 crystals are indirect-gap semiconductors and they are built up of van der Waals bonded X-M-X monolayers consisting of two hexagonal planes of S or Se atoms and an intermediate hexagonal plane of transition metal atoms[8]. Because the interaction between monolayers is weak, much weaker than intralayer interactions, it is possible to obtain ultrathin TMD layers by mechanical cleavage or chemical exfoliation techniques[9]. Mono- and few-layer TMDs become direct bandgap semiconductors and thus they exhibit a greatly enhanced photoluminescence yield[10,11]. The physical and chemical properties of many of these materials are still unknown, because they are difficult to grow over large areas and the vast majority of the studies are made on flakes detached from bulk crystals.

Recently, a broadband non-contact terahertz (THz) spectroscopy approaches are used to study the fundamental physics of various materials such as the details of conduction band structure at elevated energies[12], band offsets of heterojunctions[13], electron intervalley redistribution in germanium crystals[14] and wurtzite type InAs nanowires[15]. Exclusively among the spectroscopy approaches, the THz time-domain emission spectroscopy (THz-TDS) under femtosecond laser excitation offers a contactless and a sensitive method to characterize the surfaces and interfaces of semiconducting materials[16]. The THz pulse emission after femtosecond laser excitation is observed in several TMD materials: layered MoS_2[17,18], layered WSe_2[19], and layered and monolayer WS_2[20,21]. The physical mechanisms identified as the cause of this emission from these materials are different: the nonlinear optical rectification in MoS_2[17] and the photocurrent surge in WS_2[20] and WSe_2[19]. Such a discrepancy could be explained by the fact that in all the experiments mentioned above the TMD samples are excited by femtosecond Ti:sapphire laser pulses with photon energies of $h\nu_{ph}$~1.55 eV. For MoS_2 and WS_2 these quanta have energy much lower than their direct bandgaps (1.87 eV for MoS_2 and 2 eV for WS_2[22]), whereas for tungsten diselenide it is comparable to its direct bandgap of 1.65 eV. Moreover, the amplified Ti:sapphire laser systems used before[17-20] generate low repetition rate and high energy optical pulses, therefore all these experiments were performed under extremely high photoexcitation conditions.

The carrier dynamics in TMDs were also investigated by the THz spectroscopy. The optical pump – THz probe experiments were performed several times[23-26]; a plethora of different physical mechanisms responsible for photoexcited carrier density decay in these materials were identified including defect related, Auger recombination, exciton and trion formation. The optical pump – THz probe experiments

were also predominantly performed with amplified Ti:sapphire femtosecond laser systems, which puts some in-advance restrictions on the experimental conditions such as a rather high photoexcitation level and varying photoelectron excess energies for different materials.

In this work we are studying the three samples of multilayered TMD crystals, MoS_2, $MoSe_2$, and WSe_2, by using tunable wavelength femtosecond optical pulses from the optical parametric amplifier (OPA). The THz excitation spectra, i.e. the emitted THz pulse amplitude dependencies on the wavelength of exciting laser, as well as the photoexcited carrier dynamics were investigated over the photon energy range from 1 eV to 2.4 eV. A relatively high pulse repetition rate of 200 kHz and the use of sensitive photoconductive antenna detectors allowed us to perform the experiments at excitation levels three orders of magnitude lower than those used in the references mentioned above.

EXPERIMENTAL METHODS

The synthetic transition metal dichalcogenide single crystals, namely tungsten diselenide (WSe_2), molybdenum diselenide ($MoSe_2$), and molybdenum disulphide (MoS_2) were grown by the chemical vapor transport method (CVT) in a two-zone tube furnaces, using halogens (iodine or chlorine) as transport agents[27]. Tungsten and molybdenum diselenides were grown from primary components in evacuated sealed quartz ampoules using iodine as a transport gas. The crystallization chamber temperature at the growth zone was mainteined at a level of 1100°C. The ampoules were held inside the furnace for a period of up to 10 days, after which they were slowly cooled to room temperature. MoS_2 layered crystals were grown in a similar way, however, along with Mo and S, as a starting material the $MoCl_5$ compound was used, which decomposes at high temperatures, playing the role of a source of chlorine molecules for the CVT[28]. The grown layered bulk crystals were then exfoliated to obtain smooth Van der Waals surfaces. The thickness of each crystalline sample was of an order of a few tens of microns with diameters varying from 3 to 5 mm.

The typical surface THz emission experiments were performed in reflection geometry. The samples were deposited on a sapphire substrate and placed in the optical setup so that the femtosecond pulses were impinging at 45° to surface normal (Figure 1). Since the optical beam spot diameter was much greater than THz wavelengths, the ultrafast photogenerated charges radiated the THz waves that constructively interfered in the quasi-reflection direction, which is where the detector was positioned. The setup was based on an amplified ytterbium-doped potassium gadolinium tungstate (Yb:KGW) laser system (PHAROS, Light Conversion Ltd.) operating at 1030 nm (160 fs pulse duration 200 kHz repetition rate). The laser beam with an average power of 6 W was directed into a cavity-tuned optical parametric amplifier (OPA, ORPHEUS, Light Conversion Ltd.) that generated 140–180 fs duration pulses with a central wavelength tunable from 640 nm to 2600 nm. Shorter wavelength femtosecond optical pulses from 640 nm down to 400 nm were reached by generating the second harmonic in a BBO (Beta Barium Borate) crystal. In the THz-TDS arrangement, the TMD samples were excited by the pulses from OPA, while the sample-emitted THz pulses were detected by the GaAsBi photoconducting antenna (TeraVil Ltd.) that was connected to a lock-in amplifier. The average power of optical pulses incident on samples during THz excitation spectra measurements was about 10 mW, which corresponded to the sample irradiation level of ~1 μJ/cm^2. The THz detector was illuminated by a small fraction (~5 mW) of Yb:KGW laser beam. The THz pulses were registered by varying the delay between the detector optical branch and the THz pulse branch. All experiments were performed at room temperature.

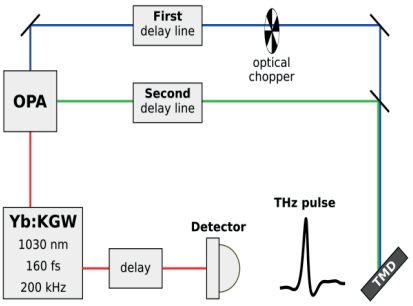

Figure 1. The experimental setup schemes where the second delay line was used for the double pulse experiment.

TERAHERTZ EXCITATION SPECTRA

Figure 2 shows the THz excitation spectra (TES) of all three investigated multilayered TMD materials. In all three cases the emitted THz pulse amplitudes are peaking when the photon energy coincides with the direct bandgap energy observed in the bulk samples of corresponding materials[22]. A clear double-peak structure of the MoS_2 spectrum is obtained; the peaks at 1.85 eV and 2.02 eV coincide with the maxima of room temperature photoluminescence and optical absorption spectra of mono and bilayers[29]. Though the Figure 2 graphs are all normalized to maximum, it is noted that the most intense THz pulses are generated from the MoS_2 sample while for the $MoSe_2$ and WSe_2 it is about ~2.5 and ~6 less intense, respectively. The shape of the TES spectra of bulk TMD samples is similar to the measured Ge TES spectrum, a material that has a similar electron energy dispersion law; a weak THz emission is present at indirect gap energies and a THz emission maximum at direct gap photon energies[14]. However, in contrast to germanium, the investigated TMD samples are characterized by a considerably intense and gradually increasing THz emission starting from indirect gap photon energies up until the direct bandgap energy.

The only possible THz emission physical mechanism from femtosecond laser excited bulk TMD samples is the surface photocurrent. We did not observe any azimuthal angle dependence of radiated THz pulse amplitude nor any THz emission for the normal incidence case. Both of these experiments are the main fingerprints of the nonlinear optical rectification contribution to THz emission. There may be two reasons why the optical nonlinearities responsible for THz emission are not present in our investigations, one

of which is the excitation fluence that is a few orders of magnitude lower than that used by other groups, and another is the fact that our samples are made of stacked layers of TMDs and not monolayers[17,18,20]. The photocurrent appearing due to electron and hole separation by an electric field at the surface or due to different diffusion rates of these carriers towards the bulk (photo-Dember effect) create dynamically changing electric dipoles.

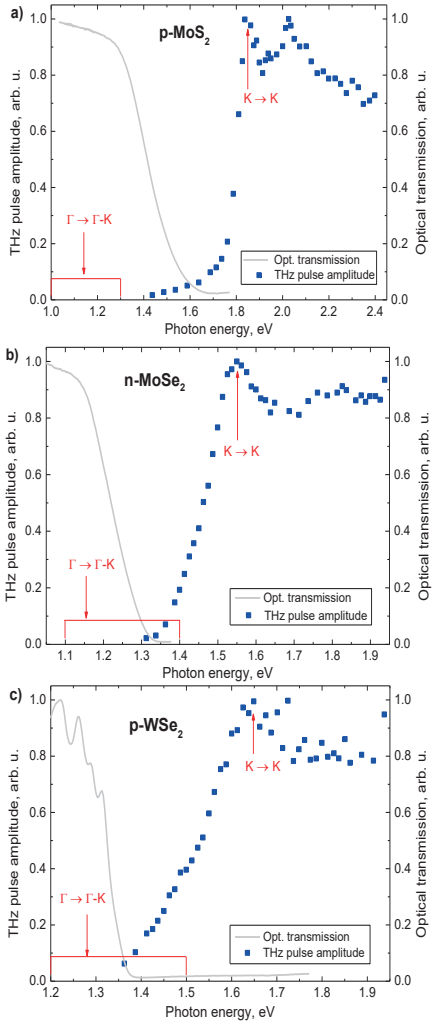

Figure 2. The terahertz excitation spectra of three TMD samples measured in 45° reflection geometry. Excitation fluence ~1 μJ/cm^2. Direct and indirect transition energy ranges are marked by red arrows which are taken from[30]. The optical transmission is represented with grey lines for each sample.

In order to specify whether the effects of surface field have influence on THz emission we compared the polarities of THz pulses emitted from investigated TMDs with those from unintentionally doped n-InSb (n ~ 2x10^{16} cm^{-3}) and n-GaAs (Figure 3). First, it is known that the photo-Dember effect in InSb is dominating the THz emission because the surface field is practically screened in this narrow-gap semiconductor. The free electrons are of higher mobility than holes, which hints the orientation of THz emitting dipole, namely electrons being further into the bulk and holes closer to the surface. Second, the n-type GaAs, which is known to have a strong surface band bending also demonstrates the same polarity as n-InSb, implying the drift of electrons towards the bulk. The conductivity types of TMDs determined from thermoelectricity and Hall-effect measurements show opposite THz pulse polarities between n-type $MoSe_2$ and p-type MoS_2 and WSe_2 suggesting that the surface field is playing a considerable role in the ultrafast photocurrent dynamics in TMDs. Similarly, in[31] the THz pulse polarity flips over when the investigated type II WS_2/MoS_2 heterostructure is inverted.

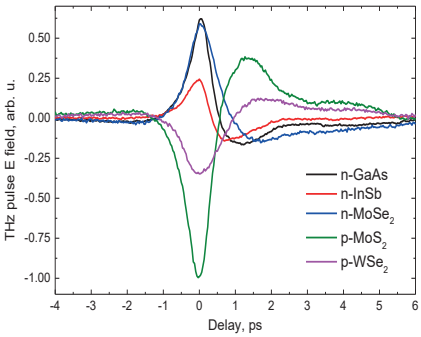

Figure 3. The shape of THz pulses emitted from semiconductors of various doping types when excited by 1.89 eV quanta at irradiation level of ~2 μJ/cm^2.

OPTICAL PUMP – THZ PROBE MEASUREMENTS

The optical pump – THz probe (OPTP) experiments are performed on all samples at various optical pump wavelengths. Generally, the main goal of such experiments is by measuring light induced THz absorption transients to evaluate the characteristics of photoexcited electrons: their lifetime, density, and carrier mobility. However, the obtained transients are highly unconventional. Their amplitudes (usually mirroring the photoconductivity of an illuminated sample) are the highest when pump photon energies are lower than the direct energy gaps contradicting with the observed TES features. When measuring optically induced THz absorption a ~10 μJ/cm^2 excitation fluence and different wavelength pulses from OPA are used in the pump beam, while the THz probe pulses are generated from a p-type InAs crystal illuminated by a 1030 nm wavelength PHAROS laser beam. Both the pump and the probe beams impinged TMD samples along their surface normal, and the transmitted THz pulse amplitude is measured at its maximum at various pump and probe delays.

Figure 4a,b presents the results of OPTP measurements performed on the multilayered MoS_2 sample. This experiment is based on a time-resolved determination of THz absorption induced by the photocarriers. The signal measured is caused by the free-carrier absorption that is directly proportional to the light induced conductance and to the probe (THz pulse) wavelength. Therefore, it is expected to observe the highest OPTP signals at a pump wavelength range where the photocurrent is the highest and generated THz pulses are the most intense. However, the experiments evidence an opposite tendency: there is a sudden drop of the induced THz absorption at pump photon energies corresponding to the highest THz generation efficiencies.

Similar results, though not so clearly expressed as in MoS_2, were also obtained for the other two TMD materials: $MoSe_2$ and WSe_2 (see Figure 4c,d). Another feature of these experimental traces is the induced THz absorption decay time (directly related to the free-carrier lifetime) dependence on pump pulse wavelength, which is also best seen on the MoS_2 results. From these observations, one can conclude that the photocarrier lifetimes excited from indirect optical transitions are longer than those from direct interband transitions. In MoS_2 this leads to the appearance of background THz absorption level despite the fact that the period of laser pulse train is as long as 5 μs implying residual free carriers when the next optical pulse arrives.

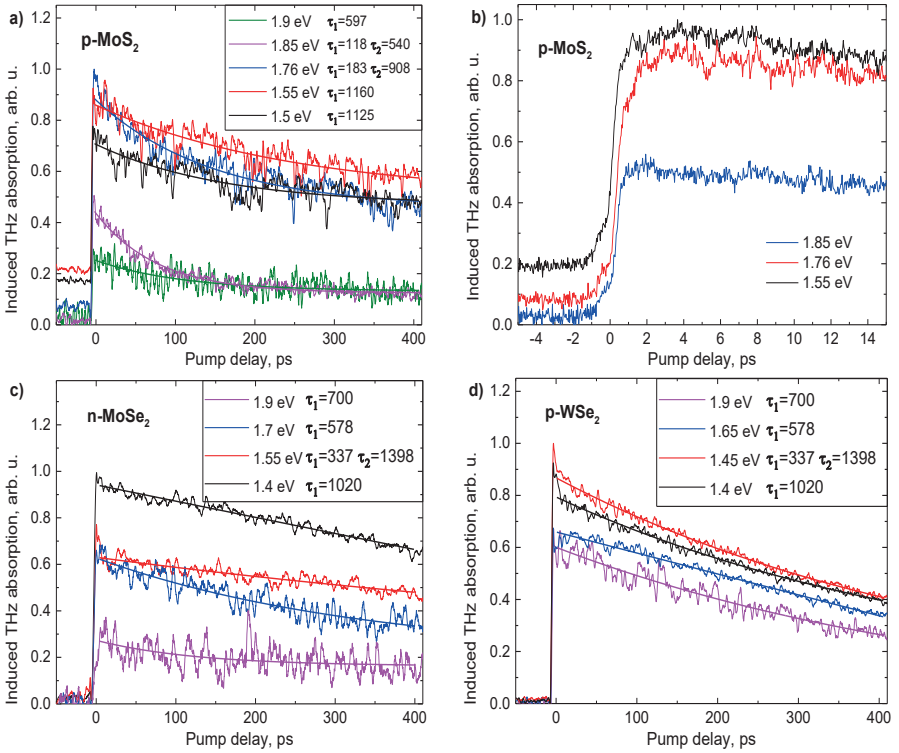

Figure 4. Optical pump – THz probe traces of MoS_2 (a and b), $MoSe_2$ (c) and WSe_2 (d) for different pump photon energies. The transients are normalized to a constant pump photon number. The excitation fluence is ~10 μJ/cm^2. The curves are fitted with one or two exponential decay functions and their corresponding decay times, τ, are given in picoseconds.

A significant increase of carrier lifetimes has been also observed in germanium crystals excited by the laser photons with energies lower than direct interband transition gap[14]. It is explained by the longer light absorption lengths leading to a reduced influence of the surface recombination in that spectral region. On the one hand, this mechanism is hardly applicable to a multilayered MoS_2, because the surface recombination lifetimes in this material is tens of picoseconds and even longer[32]. On the other hand, the OPTP traces measured in germanium excited at photon energies equal to direct bandgap energy have a sharp peak in their initial part of optically induced THz absorption[14], whereas the TMD samples demonstrate a THz absorption decrease. One has to point out that the OPTP traces shown in Figure 4 are normalized to a constant photon number and thus the same number of electrons should be excited in all spectral regions, though the direct band gap excitation induces the carriers over a much narrower distance from surface, which participate in the most intense THz pulse emission.

The question arises why the carriers that effectively contribute to THz emission do not modulate the THz absorption? A possible explanation to this contradiction could be that the majority of photoexcited electrons and holes are free only for a very short period of time after their creation – at later time moments they are bound into the excitons that are electrically neutral and cannot absorb the electromagnetic radiation. The exciton nucleation times in TMDs can be tens of femtoseconds long[33], i.e., they are of a shorter duration than the probe THz pulses resulting in a temporal resolution of the experiment that is not sufficient for the observation of the initial stages of carrier dynamics.

MECHANISM OF TERAHERTZ EMISSION

Though the electron mobility in monolayer samples is higher than the hole mobility (800 cm^2/Vs and 150 cm^2/Vs in MoS_2[34]), it is not known what is the ratio of these two material parameters in multilayer samples, especially in K valleys and in the direction perpendicular to the layer planes. From the THz pulse polarity inversion in n- and p-doped samples it appears that the surface field spatially separates carriers by the drift current. Nevertheless, the decreasing induced THz absorption at higher photon energies in OPTP measurements implies that excitons can be the cause of THz radiation themselves.

If the photoexcited electrons and holes are spatially separated by drift and one type of carriers are localized in further layers from the surface, there is an electrical dipole appearing with its axis parallel to the surface normal. The excitons are nucleated[35], the photoexcited carriers are eliminated from the electrical conduction process and they do not contribute to the THz absorption. However, a dipole field is continuously growing during the illumination causing a monopolar THz pulse radiation. In this case, the process leading to THz emission reminds of the shift current effect that is theoretically predicted in several early articles discussing the origin of an ultrafast semiconductor response to femtosecond excitation[36]. Because the dark, interlayer, or defect-bound excitons[35] can have exceptionally long lifetimes[37,38] and 100 meV binding energies[38] they are stable at room temperature and robust against dissociations when electric fields are applied. The THz pulse emission of a lower intensity can be also present at exciting photon energies below the direct energy gap of TMD semiconductors. The carriers photoexcited from defect states inducing an ultrafast photocurrent surge in the surface fields can be behind the origin of this emission. In the latter case, the photoexcited electrons remain mobile (and are not bound into excitons as in the case of photoexcitation with higher energy photons) and absorb the THz radiation, which explains the difference in OPTP traces measured in both these spectral regions.

A good proof of this novel THz generation mechanism – the accumulation of an electrical dipole field from excitons – could be a double optical pulse experiment. The first pulse with the photon energy at a TES maximum creates excitons and causes the appearance of a built-in electric field, whereas the second pulse creates photocarriers that screen this field and, therefore, generates a THz pulse with the opposite polarity. To realize this experimentally, an optical chopper modulated the first optical pulse branch at all times (Figure 1), while moving the second delay line. The results of double pulse experiments performed on n-$MoSe_2$ are presented in Figure 5 and 6. Figure 5 shows the shape of THz pulses generated by the first and the secondary optical pulses at different time delays between them, while Figure 6 presents the temporal dependence of the secondary THz pulse amplitude. These Figures clearly evidence the polarity inversion of THz pulses generated by secondary optical pulses caused by the built-in electric field screening of trapped photocarriers from the first optical pulse. The amplitude of secondary THz pulses changes weakly with increasing time delay between both photoexcitations (Figure 5). Moreover, these secondary THz pulses are generated even in the case when a photon energy is lower than the indirect energy gap of $MoSe_2$ (Figure 6). It is convincing that the electrons photoexcited by a second pulse from mid-gap defect states are moving in the built-in electric field created by the first optical pulse; no THz signal is generated when the first optical pulse is absent.

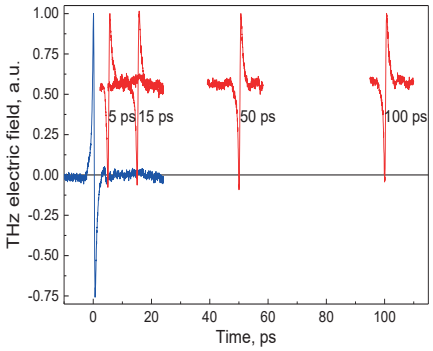

Figure 5. Results of the double pulse experiment performed on $MoSe_2$ with 1.55 eV photon energy optical pulses. The THz pulse at 0 ps is generated by the first ~6 μJ/cm^2 optical pulse, and the others are generated by the second ~2.5 μJ/cm^2 optical pulse at various delays. The second optical pulse generated THz pulses are of opposite polarity. They are shifted upwards for clarity.

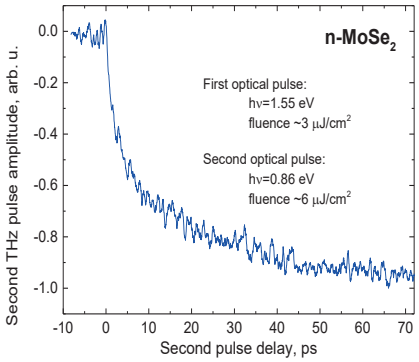

Figure 6. The amplitude of a THz pulse generated by the second optical pulse as a function of its delay with respect to the first optical pulse (see Figure 1). The parameters of optical pulses are stated in the graph.

CONCLUSIONS

The amplitudes of THz pulses radiated from multi-layered surfaces of MoS_2, $MoSe_2$, and WSe_2 were measured as a function of femtosecond optical pulse photon energy over a range from 1 eV to 2eV. It was found that for all crystals the maxima of THz excitation spectra coincided with corresponding energies of the direct interband transitions. The optical pump – THz probe experiments performed at various pump pulse wavelengths evidenced a decrease of optically induced THz absorption when photon energies were higher than the interband K-K electron transitions. This behavior was explained by the formation of electrically neutral excitons that significantly reduce the number of free carriers and the photoconductance of samples. It was proposed that excitons can be localized with the dipoles aligned perpendicular to the sample surface. The accumulation of these dipoles during femtosecond optical pulse excitation could have induced a fast-growing internal electric field and led to the THz pulse emission. The experiments with double optical pulses supported this assumption and showed that the induced built-in field remained in crystals for several nanoseconds. This photovoltaic effect could have an important aftermath for TMD applications in solar cells or optical memory devices where the prolonged state of built-in fields is desired.

AUTHOR INFORMATION

Corresponding Author

* ignas.nevinskas@ftmc.lt

Funding Sources

This research was funded in part by a grant from the European Social Fund, Measure No. 09.3.3-LMT-K-712-01-0032.

REFERENCES

1. Kolobov, A. V.; Tominaga, J. Two-Dimensional Transition-Metal Dichalcogenides. *Springer Series in Materials Science*. **2016**.

2. Wang, K.; Feng, Y.; Chang, C.; Zhan, J.; Wang, C.; Zhao, Q.; Coleman, J. N.; Zhang, L.; Blau, W. J.; Wang, J. Broadband ultrafast nonlinear absorption and nonlinear refraction of layered molybdenum dichalcogenide semiconductors. *Nanoscale* **2014**, 6(18), 10530–10535.

3. Wang, Q. H.; Kalantar-Zadeh, K.; Kis, A.; Coleman, J. N.; Strano, M. S. Electronics and optoelectronics of two-dimensional transition metal dichalcogenides. *Nat. Nanotech.* **2012**, 7(11), 699-712.

4. Jariwala, D.; Sangwan, V. K.; Lauhon, L. J.; Marks, T. J.; Hersam, M. C. Emerging device applications for semiconducting two-dimensional transition metal dichalcogenides. *ACS Nano* **2014**, 8(2), 1102–1120.

5. Radisavljevic, B.;Radenovic, A.; Brivio, J.; Giacometti, V.; Kis, A. Single-layer MoS_2 transistors. *Nat. Nanotechnol.* **2011**, 6, 147-150.

6. Zhou, F.; Chen, J.; Tao, X.; Wang, X. and Chai, Y. 2D Materials Based Optoelectronic Memory: Convergence of Electronic Memory and Optical Sensor. *Research* **2019**, 1-17.

7. Tsai, M.-L.; Su, S.-H.; Chang, J.-K.; Tsai, D.-S.; Chen, C.-H.; Wu, C.-I.; Li, L.-J.; Chen, L.-J.; He, J.-H. Monolayer MoS_2 heterojunction solar cells. *ACS Nano* **2014**, 8, 8317-8322.

8. Liu, Y.;Weiss, N. O.; Duan, X.; Cheng, H.-C.; Huang, Y.; Duan, X. Van der Waals heterostructures and devices. *Nature Reviews Materials* **2016**, 1, 16042.

9. Guo, B.; Xiao, Q. L.; Wang, S.; Zhang, H. 2D Layered Materials: Synthesis, Nonlinear Optical Properties, and Device Applications. *Adv. Sc. News* **2019**, 13, 1800327.

10. Mak, K. F.; Lee, C.; Hone, J.; Shan, J.; Heinz, T. F. Atomically thin MoS_2: a new direct-gap semiconductor. *Phys. Rev. Lett.* **2010**, 105, 136805.

11. Splendiani, A.; Sun, L.; Zhang, Y. B.; Li, T. S.; Kim, J.; Chim, C. Y.; Galli, G.; Wang, F. Emerging Photoluminescence in Monolayer MoS_2. *Nano Lett.* **2010**, 10, 1271–1275.

12. Arlauskas, A.; Krotkus, A. THz excitation spectra of AIIIBV semiconductors. *Semicond. Sci. Technol.* **2012**, 27, 115015, doi: 10.1088/0268-1242/27/11/115015.

13. Karpus, V.; Norkus, R.; Butkutė, R.; Stanionytė, S.; Čechavičius, B.; Krotkus, A. THz-excitation spectroscopy technique for band-offset determination. *Optics Express* **2019**, 26, 33807-33817.

14. Norkus, R.; Nevinskas, I.; Krotkus, A. Spectral dependences of terahertz emission from femtosecond laser excited surfaces of germanium crystals. *J. Appl. Phys.* **2019**, 126, 225704.

15. Adomavičius, R.; Nevinskas, I.; Treu, J.; Xu, X.; Koblmuller, G.; Krotkus, A. Pulsed THz emission from wurtzite phase catalyst-free InAs nanowires. *J. Phys. D: Appl. Phys.* **2020**, 53, 19LT01.

16. Zhang, X. C.; Auston, D. H. Optoelectronic Measurement of Semiconductor Surfaces and Interfaces with Femtosecond Optics. *J. Appl. Phys.* **1992**, 71, 326–338.

17. Huang, Y.; Zhu, L.; Zhao, Q.; Guo, Y.; Ren, Zh.; Bai, J.; Xu, X. Surface Optical Rectification from Layered MoS_2 Crystal by THz Time-Domain Surface Emission Spectroscopy, *ACS Appl. Mater. Interfaces* **2017**, 9, 4956–4965.

18.Huang, Y.; Zhu, L.; Yao, Z.; Zhang, L.; He, C.; Zhao, Q.; Bai, J.; Xu, X. Terahertz Surface Emission from Layered MoS_2 Crystal: Competition between Surface Optical Rectification and Surface Photocurrent Surge. *J. Phys. Chem. C* **2018**, 122, 481–488.

19. Si, K.; Huang, Y.; Zhao, Q.; Zhu, L.; Zhang, L.; Yao, Z.; Xu, X. Terahertz surface emission from layered semiconductor WSe_2, *Applied Surface Science* **2018**, 448, 416–423.

20. Zhang, L.; Huang, Y.; Zhao, Q.; Zhu, L.; Yao, Z.; Zhou, Y.; Du, W.; Xu, X. Terahertz surface emission of d-band electrons from a layered tungsten disulfide crystal by the surface field, *Phys. Rev. B* **2017**, 96, 155202.

21. Zhang, L.; Huang, Y.; Zhu, L.; Yao, Z.; Zhao, Q.; Du, W.; He, Y.; Xu, X. Polarized THz Emission from In-Plane Dipoles in Monolayer Tungsten Disulfide by Linear and Circular Optical Rectification, *Adv. Optical Mater.* **2019**, 1801314.

22. Kopaczek, J.; Polak, M. P.; Scharoch, P.; Wu, K.; Chen, B.; Tongay, S.; Kudrawiec, R. Direct optical transitions at K- and H-points of Brillouin zone in bulk MoS_2, $MoSe_2$, WS_2, and WSe_2. *J. Appl. Phys.* **2016**, 119, 235705.

23. Ghosh, S.; Winchester, A.; Muchharla, B.; Wasala, M.; Feng, S.; Elias, A. L.; Krishna, M. B. M.; Harada, T.; Chin, C.; Dani, K.; Kar, S.; Terrones, M.; Talapatra, S. Ultrafast Intrinsic Photoresponse and Direct Evidence of Sub-gap States in Liquid Phase Exfoliated MoS_2 Thin Films. *Scientific Reports* **2015**, 5, 11272.

24. Xu, S.; Yang, J.; Jiang, H.; Su, F.; Zeng, Z. Transient photoconductivity and free carrier dynamics in a monolayer WS_2 probed by time resolved Terahertz spectroscopy. *Nanotechnology* **2019**, 30, 265706.

25. Junpeng, L.; Hongwei, L. A critical review on the carrier dynamics in 2D layered materials investigated using THz spectroscopy. *Optics Communications* **2018**, 406, 24–35.

26. Docherty, C. J.; Parkinson, P.; Joyce, H. J.; Chiu, M.-H.; Chen, C.-H.; Lee, M.-Y.; Li, L.-J.; Herz, L. M.; Johnston, M. B. Ultrafast Transient Terahertz Conductivity of Monolayer MoS_2 and WSe_2 Grown by Chemical Vapor Deposition. *ACS Nano* **2014**, 8, 11147.

27. Schmidt, P.; Binnewies, M.; Glaum, R.; Schmidt, M. Chemical Vapor Transport Reactions–Methods, Materials, Modeling. *Advanced Topics on Crystal Growth*, edited by Sukarno Ferreira, **2013**, Chapter 9, 227-305, doi: 10.5772/55547.

28. Ubaldini, A.; Jacimovic, J.; Ubrig, N.; Giannini, E. Chloride-Driven Chemical Vapor Transport Method for Crystal Growth of

Transition Metal Dichalcogenides. *Cryst. Growth Des.* **2013**, 13, 10, 4453-4459.

29. Mak, K. F.; Lee, C.; Hone, J.; Shan, J.; Heinz, T. F. Atomically thin MoS_2: a new direct-gap semiconductor. *Phys. Rev. Lett.* **2010**, 105, 136805.

30. Duan, X.; Wang, C.; Pan, A.; Yu, R.; Duan, X. Two-dimensional transition metal dichalcogenides as atomically thin semiconductors: opportunities and challenges. *Chemical Society Reviews* **2015**, 44(24), 8859-8876.

31. Ma, E.; Guzelturk, B.; Li, G.; Cao, L.; Shen, Z.; Lindenberg, A; and Heinz, T. Recording interfacial currents on the subnanometer length and femtosecond time scale by terahertz emission. *Sci. Adv.* **2019**, 5, p.eaau0073.

32. Wang, H.; Zhang, C.; Rana, F. Surface recombination limited lifetimes of photoexcited carriers in few-layer transition metal chalcogenide MoS_2. *Nano Letters* **2015**, 15, 8204.

33. Selig, M.; Berghäuser, G.; Raja, A.; Nagler, P.; Schüller, C.; Heinz, T. F.; Korn, T.; Chernikov, A.; Malic, E.; Knorr, A. Excitonic linewidth and coherence lifetime in monolayer transition metal dichalcogenides. *Nature Communications* **2016**, 7, 13279.

34. Yu, S.; Xiong, H. D.; Eshun, K.; Yuan, H.; Li, Q. Phase Transition, Effective Mass and Carrier Mobility of MoS2 Monolayer under Tensile Strain. *Appl. Surf. Sci.* **2015**, 325, 27–32.

35. Mueller, T.; Malic, E. Exciton physics and device application of two-dimensional transition metal dichalcogenide semiconductors. *NPJ 2D Materials and Applications* **2018**, 2, 29.

36. Khurgin, J. Optical rectification and terahertz emission in semiconductors excited above the band gap. *JOSA B* ***1994***, 11, 2492.

37. Moody, G.; Tran, K.; Lu, X.; Autry, T.; Fraser, J. M.; Mirin, R. P.; Yang, L.; Li, X.; Silverman, K. L. Microsecond Valley Lifetime of Defect-Bound Excitons in Monolayer WSe_2. *Phys. Rev. Lett.* **2018**, 121, 057403.

38. Ovesen, S.; Brem, S.; Linderälv, C.; Kuisma, M.; Korn, T.; Erhart, P.; Selig, M.; Malic, E. Interlayer exciton dynamics in van der Waals heterostructures. *Communications Physics* **2019**, 2, 23.

Paper 7 [P7]

I. Nevinskas; Z. Mockus; R. Juškėnas; **R. Norkus**; A. Selskis , E. Norkus; A. Krotkus "Terahertz Photoconductivity Spectra of Electrodeposited Thin Bi Films", Materials, 14, 3150. (2021)

The article can be accessed online at https://doi.org/10.3390/ma14123150

materials

MDPI

Article

Terahertz Photoconductivity Spectra of Electrodeposited Thin Bi Films

Ignas Nevinskas *, Zenius Mockus, Remigijus Juškėnas, Ričardas Norkus, Algirdas Selskis, Eugenijus Norkus and Arūnas Krotkus

Center for Physical Sciences and Technology, Saulėtekio al. 3, LT-10257 Vilnius, Lithuania; zenius.mockus@ftmc.lt (Z.M.); remigijus.juskenas@ftmc.lt (R.J.); ricardas.norkus@ftmc.lt (R.N.); algirdas.selskis@ftmc.lt (A.S.); eugenijus.norkus@ftmc.lt (E.N.); arunas.krotkus@ftmc.lt (A.K.)
* Correspondence: ignas.nevinskas@ftmc.lt

Abstract: Electron dynamics in the polycrystalline bismuth films were investigated by measuring emitted terahertz (THz) radiation pulses after their photoexcitation by tunable wavelength femtosecond duration optical pulses. Bi films were grown on metallic Au, Pt, and Ag substrates by the electrodeposition method with the Triton X-100 electrolyte additive, which allowed us to obtain more uniform films with consistent grain sizes on any substrate. It was shown that THz pulses are generated due to the spatial separation of photoexcited electrons and holes diffusing from the illuminated surface at different rates. The THz photoconductivity spectra analysis has led to a conclusion that the thermalization of more mobile carriers (electrons) is dominated by the carrier–carrier scattering rather than by their interaction with the lattice.

Keywords: bismuth film; electrodeposition; terahertz emission; terahertz photoconductivity spectra; femtosecond laser

Citation: Nevinskas, I.; Mockus, Z.; Juškėnas, R.; Norkus, R.; Selskis, A.; Norkus, E.; Krotkus, A. Terahertz Photoconductivity Spectra of Electrodeposited Thin Bi Films. *Materials* **2021**, *14*, 3150. https://doi.org/10.3390/ma14123150

Academic Editor: Masato Sone

Received: 17 May 2021
Accepted: 4 June 2021
Published: 8 June 2021

1. Introduction

Bismuth is a semimetal that has many extraordinary characteristics because of its high electron energy band structure anisotropy, small electron and hole effective masses, and due to their high mobilities [1]. In addition, Bi is the first material in which the electron quantum confinement effects were demonstrated [2]. A two-dimensional (2D) carrier confinement results in the semimetal—semiconductor transition in thinner than ~30 nm Bi layers [3]; quantum confinement effects are also evidenced in Bi nanowires [4] and Bi nanocrystals [5]. Few monolayer thick Bi layers, epitaxially grown on Si substrates, were reported to have a large bulk bandgap indicating possible topological insulator properties at room temperature [6]. Due to this diversity of its physical characteristics, bismuth is sometimes considered as the key material in nanoelectronics, when quantum effects rather than doping would be exploited to mimic traditional microelectronics [7].

Furthermore, due to stability in air and negligible toxicity, Bi layers are finding significant applications in energy-related applications such as electrocatalytic CO_2 reduction [8–10], N_2 reduction [11], glucose oxidation [12], or sodium-ion storage [13]. Bi is also used as an efficient catalyst in organic synthesis reactions [14]. An overview of Bi applications in different areas of catalysis was published recently in [15]. It is worth noting that both—bulk bismuth [16] as well as bismuth film electrodes [17,18]—are used for electroanalytical purposes.

As a consequence of these new and important applications, a wider investigation of thin Bi film growth technologies is required. In this contribution, the growth of Bi layer by electrodeposition was performed. This technology appears to be one of the most suitable to grow Bi since it is a fast and cost-effective procedure to obtain large area, high-quality layers on different substrates [19–23]. It should be noted that according to the literature data, the electrodeposited bismuth coatings are comparatively thick for our below-mentioned

intensions, i.e., coating thicknesses exceed 1 μm, while Bi grain sizes are 500 nm or larger. In this study, we developed an original electrolyte for the electrodeposition of bismuth films thinner than 1 μm (details in the Experimental Part).

Bismuth layers of various thicknesses (from 50 nm to 600 nm) were electrodeposited on an Au substrate, while on Ag and Pt substrates the deposited Bi film thicknesses were 100 nm. The structures were characterized by the X-ray diffraction (XRD) and scanning electron microscopy (SEM). Then, the Bi layers were investigated by the terahertz (THz) emission spectroscopy—the measurement of the THz radiation pulse amplitudes emitted from the Bi surfaces after their photoexcitation by femtosecond optical pulses of different wavelengths. This contact-less measurement technique that is essentially related to a high temporal resolution of the photoconductivity spectrum could provide unique information on the electrical and optical characteristics of the investigated materials [24].

2. Layer Growth Methods and Structural Characterization

The above-mentioned methods of bismuth electrodeposition form 1 μm or thicker coatings consisting of 500 nm or larger Bi grains. To fabricate thinner Bi films, the experimental search for proper Bi electrodeposition electrolyte was carried out. A nitrate electrolyte was developed, allowing the electrodeposition of thin (50–600 nm) Bi films.

The analytical-reagent-grade chemicals and deionized water used for solution preparation are listed in Table 1 together with the plating conditions. The electrodeposition experiments were performed in a two-electrode magnetically stirred cell by applying galvanostatic method with current density of 20 $mA \cdot cm^{-2}$ (potentiostat/galvanostat Reference 600 (Gamry Instruments)). The cathodes (working electrodes) were Au, Pt sheets, and on Pt electroplated 1μm thick Ag (from cyanide bath). The anode was a Pt disc. Prior to each experiment, the Au and Pt cathodes were chemically etched in a 3:1:1 water solution of H_2SO_4 ~ 96 wt %, H_2O_2 ~ 30 wt %, and then washed with deionized water and dried with nitrogen. The Pt/Ag substrates were used as deposited without any additional pre-treatment.

Table 1. Bath composition and plating conditions for thin Bi film electrodeposition.

Chemicals	Concentration (M)
$Bi(NO_3)_3 \cdot 5H_2O$	0.15
HNO_3	1.5
KNO_3	1.0
Triton X-100 $C_{14}H_{22}O(C_2H_4O)_n$ n = 9–10	0.0015
Current density	20 $mA \cdot cm^{-2}$
Bath temperature	Room temperature
Magnetic stirring	500 rpm
Electrodeposition rate	500 $nm \cdot min^{-1}$
pH	~0

Triton X-100 is a non-ionic surfactant with a hydrophilic polyethylene oxide chain (on average it has 9.5 ethylene oxide units) and an aromatic hydrocarbon hydrophobic group, namely, 4-(1,1,3,3-tetramethylbutyl)-phenyl. In the processes of metal electrodeposition, it may act as a suppressor for three-dimensional growth of metals. It is worth noting that the surface-active substance Triton X-100 for Bi electrodeposition was applied for the first time. The influence of Triton X-100 additive on the shape and run on the cathodic polarization curve is shown in Figure 1a, whereas the influence of different substrates is shown in Figure 1b. It can be seen that the initial potential of Bi electrodeposition depends on the nature of the substrate, and it is more positive when Bi is deposited on a Bi electrode (Figure 1b). In all substrate cases, the values of the limiting currents remain approximately the same.

Obviously, Triton X-100 adsorbs on Bi deposition sites suppressing crystal growth, which results in a negative polarization curve shift. The negative shift increases the Bi electrodeposition over-potential at a constant current density, which leads to an increase in

nucleation density, reduction in grain sizes followed by the formation of a flat and rather smooth surface, as can be seen in Figure 2a. The morphology of Bi coatings obtained in an electroplating bath without the surface-active substance Triton X-100 differs significantly (Figure 2b). In this case, the Bi coating consists of varying sized, non-uniform crystallites. Therefore, the Triton X-100 allows us to obtain thin Bi films with uniform finely grained crystallites. A dual beam system Helios Nanolab 650 with an energy dispersive X-ray (EDX) spectrometer INCA Energy 350 and an X-Max 20 mm^2 detector was used to estimate the thicknesses of films. The EDX data were processed with a ThinFilmID ver. 1.3.0 software, and the thicknesses of Bi layers were recalculated from 9.78 g/cm^3 bismuth density.

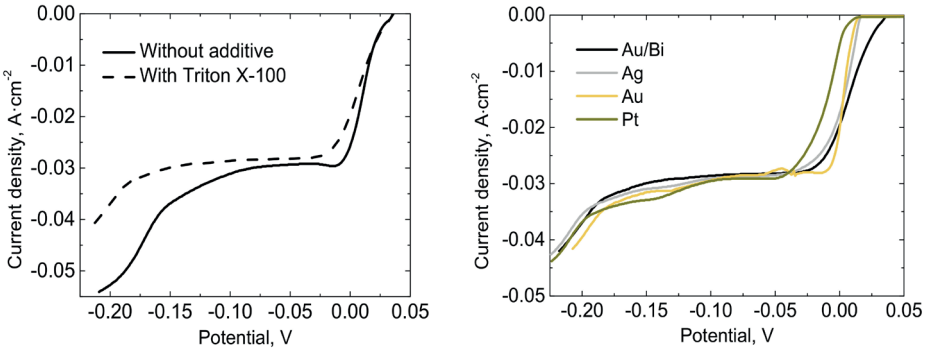

Figure 1. (**a**) Cathodic polarization curves of Bi electrodeposition on Bi-coated (100 nm) Au electrode from solutions with and without the additive Triton X-100. (**b**) Cathodic polarization curves of Bi electrodeposition on Bi, Au, Pt and Ag substrates from solutions with the Triton X-100 additive.

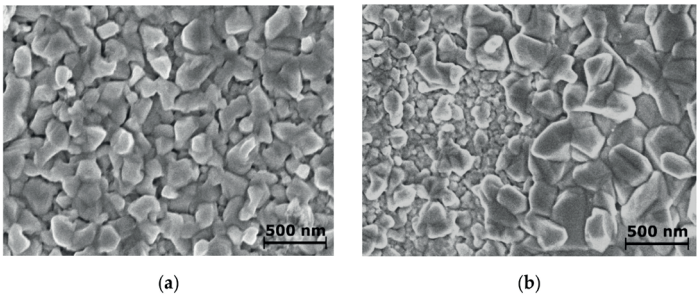

Figure 2. SEM images of 100 nm thick Bi coatings on Au obtained from Bi electrodeposition solution with the additive Triton X-100 (**a**) and without it (**b**).

The XRD measurements were carried out using X-ray diffractometer SmartLab (Rigaku) equipped with a 9 kW X-ray source with a rotating Cu anode. The grazing incidence technique (also known as the out-of-plane method) was applied to obtain a high-quality XRD pattern of the electrodeposited Bi film only 100 nm in thickness. The angle between the film surface and the incident parallel beam of X-rays, ω, equaled 0.5°. The electrodeposited Bi film's XRD pattern evidenced the film was polycrystalline of a trigonal crystalline structure (Figure 3). Even the thinnest 50 nm Bi film on gold did not present prevailing crystallographic orientation. This means that neither the XRD pattern nor SEM images

of the electrodeposited Bi films are related to the substrate origin. Despite the grazing incidence technique, the XRD peaks of Au substrate were also present in the pattern. The Bi peaks coincided very well with those presented in the ICDD database card #00-044-1246. The average size of Bi crystallites calculated using Halder–Wagner method was 19.7 ± 0.7 nm.

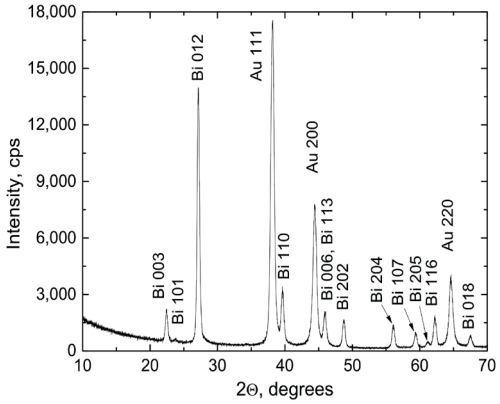

Figure 3. The XRD pattern of the electrodeposited 100 nm thick Bi film on Au substrate.

3. Ultrafast Measurements

3.1. Experimental Setup

The THz time-domain spectroscopy (THz-TDS) setup used for the investigations contained a Yb:KGW (λ = 1030 nm), 200 kHz pulse repetition rate PHAROS laser (Light Conversion Ltd., Vilnius, Lithuania). A small fraction of this laser beam of about 1 mW of average power was guided to illuminate the GaAsBi photoconductive antenna detector from Teravil Ltd. The rest of the beam was directed to an optical parametric amplifier (OPA) ORPHEUS (also Light Con. Ltd., Vilnius, Lithuania) with a capability to tune the wavelength of femtosecond pulses from 640 to about 2000 nm. The bismuth films were illuminated with these *p*-polarized various wavelength pulses at an angle, and the generated THz pulses were detected in the quasi-reflection direction (Figure 4).

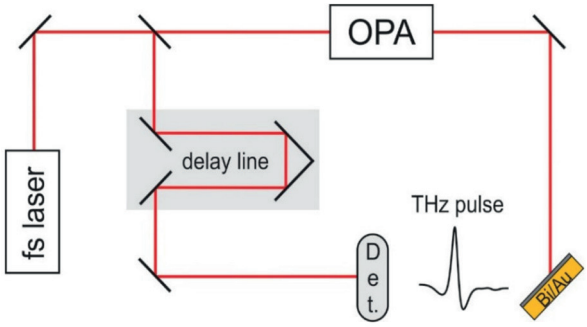

Figure 4. Terahertz time-domain spectroscopy setup.

3.2. Measurements

Figure 5a shows the temporal shape of a THz pulse radiated from the surface of a Bi layer grown on gold and its comparison with the pulses generated under exactly the same conditions from *n*- and *p*-type GaAs crystals. The amplitude of pulses emitted by Bi layer is about 100 times lower than those emitted by the GaAs crystals. Correspondingly narrower is the frequency spectrum of the bismuth layer emission (Figure 5b). These results are not surprising, because similar low THz emission levels from polycrystalline Bi have already been documented before [25]; however, the main reason behind this experiment is the comparison of the THz pulse polarities in all three cases. As it can be seen in Figure 5a, the THz pulse radiated from the Bi layer is of the same polarity as the pulse radiated from the *n*-type GaAs, which means that the dynamically changing electric dipole responsible for THz emission in both of these cases has the same direction. The photoexcited electrons are moving towards the bulk leaving the holes closer to the surface.

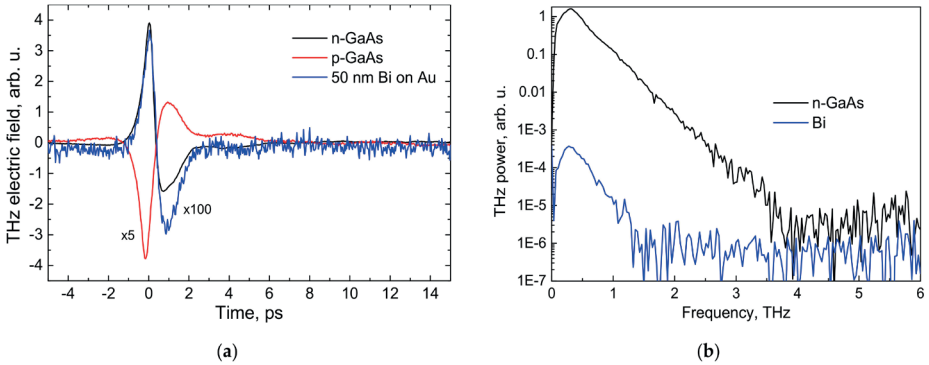

Figure 5. THz pulses (**a**) and their Fourier spectra (**b**) radiated from *n*-type GaAs ($n = 2 \times 10^{18}$ cm^{-3}, black line), *p*-type GaAs ($p = 4 \times 10^{18}$ cm^{-3}, red line) single crystals and from the surface of a 50 nm thick Bi on Au layer (blue line). The optical pulse wavelength was 780 nm, and the average power of the beam was 300 mW.

There are two main mechanisms causing the spatial separation of photoexcited electrons and holes by femtosecond optical pulses: the photocurrent, J_{ph}, can be caused by the built-in electric field at a semiconductor surface [26] and by the different diffusion rates of both types of current carriers—the so-called photo-Dember effect [27]. In both of these cases, the THz pulse electric field amplitude, E_{THz}, is proportional to the time derivative of the photocurrent, $E_{THz} \sim dJ_{ph}/dt$. Therefore, the maximum photocurrent, which is more convenient for theoretical modeling, can be determined by integrating the THz electric field temporal dependence such as shown in Figure 5a.

4. Results and Discussion

The dependences of THz pulse amplitudes on exciting photon energy, $h\nu$, measured on three Bi layers of different thicknesses shown in Figure 6 are presented in a standard way used for THz excitation spectra of crystalline semiconductors [24]—with pulse amplitudes normalized to a constant photon number. It can be seen that the measured spectra are practically identical for all the investigated samples, which indicates that the physical processes leading to THz pulse emission are taking place at a rather thin layer close to the Bi/air boundary. Some reduction in the THz pulse amplitudes was observed only for thinner than 50 nm Bi films, most probably due to the incomplete coverage of the Au substrate.

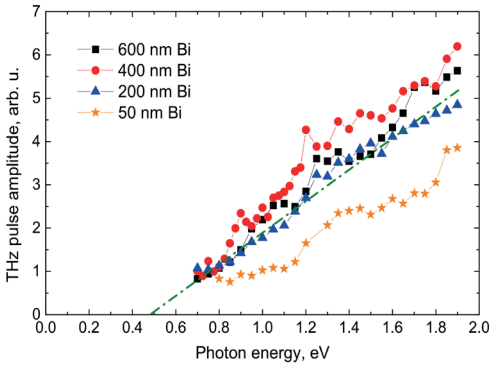

Figure 6. THz pulse amplitudes normalized to the number of photons in femtosecond optical pulses as a function of the photon energy. The experiment was performed on the four different thickness Bi layers grown on gold substrates.

In the case of direct bandgap materials, the shape of THz excitation spectra, such as shown in Figure 6, would be straightforwardly interpreted in terms of the energy bandgap $\varepsilon_g \approx 0.5$ eV determined from the approximated energy value at $E_{THz} = 0$ and the linear THz intensity growth at higher $h\nu$ caused by the increase of the photoelectron velocity with its increasing excess energy [24]. However, this interpretation cannot be applied to the semimetallic bismuth case. The energy bandgap in Bi is absent; there are no electron transitions between a pair of valence and conduction bands with their extrema at the same point of the Brillouin zone. The absorbed photon can excite numerous electron transitions at different points of this zone (see, e.g., [28,29]). Electron and hole excess energies for each optical transition can be different; therefore, the relation of a particular sole excess energy for each absorbed optical quantum energy becomes meaningless. Instead, it would be more sensible to analyze the electron-hole system that is heated up by a femtosecond laser pulse of a constant amount of energy but with differing its $h\nu$ portions.

Therefore, in Figure 7, the THz excitation spectra measured on 100 nm thick Bi layers grown on three different metallic substrates are presented as normalized to a constant optical beam intensity. The average power of the optical beam for different OPA wavelengths was changing from 200 mW to ~400 mW; in a separate experiment (not shown), it was found out that the THz signal amplitude changes nearly linearly with the optical beam intensity. Moreover, the peak values of the photocurrent transients obtained after integrating THz pulses rather than THz pulse amplitudes were plotted on those graphs. From Figure 7, it can be seen that the THz excitation spectra of polycrystalline Bi layers grown on three different substrates show only slight quantitative differences. Qualitatively, all three dependences have the same main features: a linear increase at lower photon energy range without any particular onset energy and saturation at $h\nu > 1$ eV.

Since the energy band bending and built-in electric fields in semi-insulating Bi are absent, the most probable cause of the ultrafast photocurrents and THz pulse emission is the photo-Dember effect. In the following, we will try to explain the obtained experimental dependences by using a simple model of this effect proposed by M. Tonouchi in [30] together with spectral characteristics of the polycrystalline bismuth optical response [31]. In general, the diffusion current at the photoexcited layer's surface is proportional to the diffusion coefficient, D, and the carrier density gradient:

The polarity of THz pulses shown above (Figure 5a) evidences that electrons are more mobile carriers, thus the electron transport parameters should be inserted into the equation. It was shown in [29] that the photoexcited electrons in Bi thermalize via carrier–carrier scattering and this thermalization takes place at the femtosecond time scale; the phonon

scattering being few orders of magnitude slower. One can, therefore, assume that the electrons participating in THz emission would have thermal distribution with a characteristic temperature $T_e \sim h\nu$. On the other hand, $D \sim \mu_e T_e$ and the electron mobility μ_e in Bi under dominating intercarrier scattering may be described by a power function $\mu_e \sim 1/T_e^{0.7}$ [29]. The carrier density gradient can be roughly approximated by the ratio of the absorbed photon number and the absorption depth, $dn/dz \sim P_{op} \cdot (1 - R)/h\nu \cdot \alpha$, where P_{op} is the optical beam intensity, R is the reflectance, and α is the absorption coefficient. After inserting these expressions into Equation (1), one obtains a functional dependence of the photocurrent amplitude on photon energy:

$$J_d \sim D\frac{dn}{dz} \tag{1}$$

The spectral photocurrent, J_d, is calculated by using Equation (2) together with spectral dependences of the absorption depth, α^{-1}, and the reflectance, R, impinging on the Bi layer surface at a 45° angle, both taken from [31] (see Figure 8a). The calculated shape of the photocurrent spectrum closely repeats the shape of the experimental dependences shown in Figure 7. The onset of the saturation is coinciding with the spectral range, where the change of the absorption depth is also becoming slower. It evidences that THz pulse emission observed in our experiments is indeed originating from the photo-Dember effect, and that the observed THz photocurrent saturation is caused by the absorption spectrum peculiarities of the polycrystalline Bi.

$$J_d \sim \frac{h\nu}{(h\nu)^{0.7}} P_{op} \frac{(1-R)}{h\nu}\alpha \rightarrow \frac{(1-R)}{h\nu^{0.7}}\alpha \tag{2}$$

As an additional proof of these conclusions in Figure 8b, we present the results obtained for two different angles at which the femtosecond optical pulses are impinging the Bi layer surface. Briefly, 70° is close to the Brewster angle in Bi; therefore, the enhanced light absorption is the main cause of the photocurrent increase. Theoretical curves coincide with the experimental points in the photocurrent saturation range; a significant disagreement, most probably caused by the roughness of the model, is observed at the initial parts of the spectra.

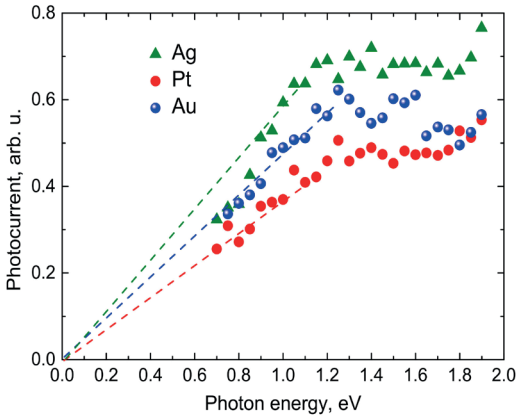

Figure 7. THz photocurrent as a function of the photon energy. Three 100 nm thick bismuth films on different substrates were measured.

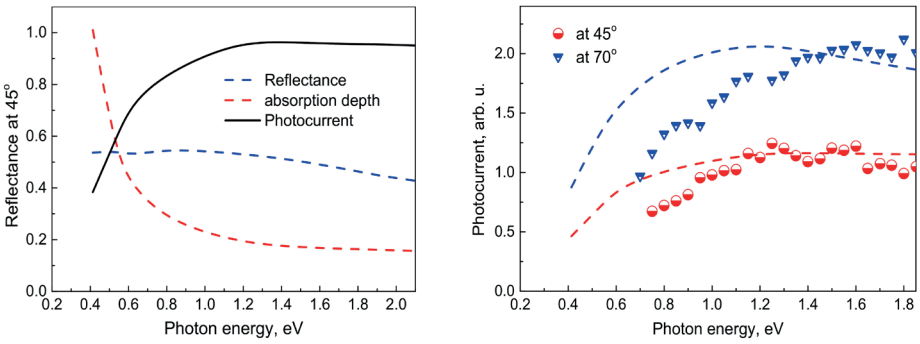

(**a**) (**b**)

Figure 8. (**a**) THz photocurrent spectrum calculated using Equation (2) and the reflectance (blue line) and absorption depth (red line) spectra. (**b**) THz photocurrent spectra measured on 100 nm thick Bi on Au layer excited at different illumination angles. Points—experiments; dashed lines—calculations.

5. Conclusions

Polycrystalline bismuth films were electrodeposited on three different noble metals: Au, Ag, and Pt. It was found that the addition of the surface-active substance Triton X-100 significantly improves the deposition conditions and allows us to obtain 50 nm to 600 nm thick Bi films consisting of uniform finely grained crystallites. These films were investigated with femtosecond optical pulses of a tunable wavelength from 0.6 μm to 2 μm. Spectral dependences of the pulsed THz radiation emission were measured, and the photoconductivity spectra of Bi films were determined from these measurements. It was established that the photoconductivity spectrum does not depend on Bi film thickness and it is only slightly dependent on the substrate material. This led us to the conclusion that the photoconductivity effect in polycrystalline bismuth films is originating from nonequilibrium carrier diffusion and that the photoexcited electrons thermalize during THz pulse generation due to the intense carrier–carrier scattering events.

Author Contributions: Main idea, modeling and original draft writing, A.K.; preparation of samples and fabrication methodology, Z.M. and E.N.; terahertz photoconductivity measurements, I.N. and R.N.; review and editing, I.N.; SEM and XRD measurements, R.J. and A.S. All authors have read and agreed to the published version of the manuscript.

Funding: This research was funded by a grant from the European Social Fund, Measure No. 09.3.3-LMT-K-712-01-0032.

Data Availability Statement: Publicly available datasets were analyzed in this study. This data can be found here: https://github.com/Indulgence21/Bismuth-film-on-Metal.

Conflicts of Interest: The authors declare no conflict of interest.

References

1. Hartman, R. Temperature Dependence of the Low-Field Galvanomagnetic Coefficients of Bismuth. *Phys. Rev.* **1969**, *181*, 1070–1086. [CrossRef]
2. Ogrin, Y.F.; Lutskii, V.N.; Elinson, M.I. Observation of Quantum Size Effects in Thin Bismuth Films. *J. Exp. Theor. Phys. Lett.* **1966**, *3*, 71.
3. Huber, T.E.; Nikolaeva, A.; Gitsu, D.; Konopko, L.; Foss, C.A., Jr.; Graf, M.J. Confinement Effects and Surface-Induced Charge Carriers in Bi Quantum Wires. *Appl. Phys. Lett.* **2004**, *84*, 1326–1328. [CrossRef]
4. Rogacheva, E.I.; Lyubchenko, S.G.; Dresselhaus, M.S. Semimetal–Semiconductor Transition in Thin Bi Films. *Thin Solid Films* **2008**, *516*, 3411–3415. [CrossRef]
5. Butkutė, R.; Niaura, G.; Pozingytė, E.; Čechavičius, B.; Selskis, A.; Skapas, M.; Karpus, V.; Krotkus, A. Bismuth Quantum Dots in Annealed GaAsBi/AlAs Quantum Wells. *Nanoscale Res. Lett.* **2017**, *12*, 1–7. [CrossRef] [PubMed]

6. Lu, Y.; Xu, W.; Zeng, M.; Yao, G.; Shen, L.; Yang, M.; Luo, Z.; Pan, F.; Wu, K.; Das, T.; et al. Topological Properties Determined by Atomic Buckling in Self-Assembled Ultrathin Bi(110). *Nano Lett.* **2015**, *15*, 80–87. [CrossRef]
7. Gity, F.; Ansari, L.; Lanius, M.; Schüffelgen, P.; Mussler, G.; Grützmacher, D.; Greer, J.C. Reinventing Solid State Electronics: Harnessing Quantum Confinement in Bismuth Thin Films. *Appl. Phys. Lett.* **2017**, *110*, 093111. [CrossRef]
8. Han, N.; Wang, Y.; Yang, H.; Deng, J.; Wu, J.; Li, Y.; Li, Y. Ultrathin Bismuth Nanosheets from in Situ Topotactic Transformation for Selective Electrocatalytic CO_2 Reduction to Formate. *Nat. Commun.* **2018**, *9*, 1–8. [CrossRef] [PubMed]
9. Rabiee, H.; Ge, L.; Zhang, X.; Hu, S.; Li, M.; Smart, S.; Zhu, Z.; Yuan, Z. Shape-Tuned Electrodeposition of Bismuth-Based Nanosheets on Flow-through Hollow Fiber Gas Diffusion Electrode for High-Efficiency CO_2 Reduction to Formate. *Appl. Catal. B Environ.* **2021**, *286*, 119945. [CrossRef]
10. Li, L.; Cai, F.; Qi, F.; Ma, D.-K. Cu Nanowire Bridged Bi Nanosheet Arrays for Efficient Electrochemical CO2 Reduction toward Formate. *J. Alloys Compd.* **2020**, *841*, 155789. [CrossRef]
11. Li, L.; Tang, C.; Xia, B.; Jin, H.; Zheng, Y.; Qiao, S.-Z. Two-Dimensional Mosaic Bismuth Nanosheets for Highly Selective Ambient Electrocatalytic Nitrogen Reduction. *ACS Catal.* **2019**, *9*, 2902–2908. [CrossRef]
12. Shi, H.; Tang, C.; Wang, Z.; Zhang, Z.; Liu, W.; Ding, Y.; Shen, X. Nanoporous Bismuth Electrocatalyst with High Performance for Glucose Oxidation Application. *Int. J. Hydrog. Energy* **2021**, *46*, 4055–4064. [CrossRef]
13. Huang, Y.; Zhu, C.; Zhang, S.; Hu, X.; Zhang, K.; Zhou, W.; Guo, S.; Xu, F.; Zeng, H. Ultrathin Bismuth Nanosheets for Stable Na-Ion Batteries: Clarification of Structure and Phase Transition by in Situ Observation. *Nano Lett.* **2019**, *19*, 1118–1123. [CrossRef]
14. Potenti, S.; Gualandi, A.; Puggioli, A.; Fermi, A.; Bergamini, G.; Cozzi, P.G. Photoredox Allylation Reactions Mediated by Bismuth in Aqueous Conditions. *Eur. J. Org. Chem.* **2021**, *2021*, 1624–1627. [CrossRef]
15. Odularu, A.T. Bismuth as Smart Material and Its Application in the Ninth Principle of Sustainable Chemistry. *J. Chem.* **2020**, *2020*, 9802934. [CrossRef]
16. Pauliukaitė, R.; Hočevar, S.B.; Ogorevc, B.; Wang, J. Characterization and Applications of a Bismuth Bulk Electrode. *Electroanalysis* **2004**, *16*, 719–723. [CrossRef]
17. Pauliukaitė, R.; Brett, C.M.A. Characterization and Application of Bismuth-Film Modified Carbon Film Electrodes. *Electroanalysis* **2005**, *17*, 1354–1359. [CrossRef]
18. Grincienė, G.; Selskienė, A.; Verbickas, R.; Norkus, E.; Pauliukaite, R. Peculiarities of Electrochemical Bismuth Film Formation in the Presence of Bromide and Heavy Metal Ions. *Electroanalysis* **2009**, *21*, 1743–1749. [CrossRef]
19. Sato, H.; Homma, T.; Kudo, H.; Izumi, T.; Osaka, T.; Shoji, S. Three-Dimensional Microfabrication Process Using Bi Electrodeposition for a Highly Sensitive X-Ray Imaging Sensor. *J. Electroanal. Chem.* **2005**, *584*, 28–33. [CrossRef]
20. O'Brien, B.; Plaza, M.; Zhu, L.Y.; Perez, L.; Chien, C.L.; Searson, P.C. Magnetotransport Properties of Electrodeposited Bismuth Films. *J. Phys. Chem. C* **2008**, *112*, 12018–12023. [CrossRef]
21. Moral-Vico, J.; Casañ-Pastor, N.; Camón, A.; Pobes, C.; Jáudenes, R.M.; Strichovanec, P.; Fàbrega, L. Microstructure and Electrical Transport in Electrodeposited Bi Films. *J. Electroanal. Chem.* **2019**, *832*, 40–47. [CrossRef]
22. Prados, A.; Ranchal, R. Electrodeposition of Bi Films on H Covered N-GaAs(111)B Substrates. *Electrochim. Acta* **2019**, *305*, 212–222. [CrossRef]
23. Coelho, D.; Gaudêncio, J.P.R.S.; Carminati, S.A.; Ribeiro, F.W.P.; Nogueira, A.F.; Mascaro, L.H. Bi Electrodeposition on WO3 Photoanode to Improve the Photoactivity of the $WO_3/BiVO_4$ Heterostructure to Water Splitting. *Chem. Eng. J.* **2020**, *399*, 125836. [CrossRef]
24. Arlauskas, A.; Krotkus, A. THz Excitation Spectra of AIIIBV Semiconductors. *Semicond. Sci. Technol.* **2012**, *27*, 115015. [CrossRef]
25. Ilyakov, I.E.; Shishkin, B.V.; Fadeev, D.A.; Oladyshkin, I.V.; Chernov, V.V.; Okhapkin, A.I.; Yunin, P.A.; Mironov, V.A.; Akhmedzhanov, R.A. Terahertz Radiation from Bismuth Surface Induced by Femtosecond Laser Pulses. *Opt. Lett. OL* **2016**, *41*, 4289–4292. [CrossRef]
26. Zhang, X.-C.; Auston, D.H. Optoelectronic Measurement of Semiconductor Surfaces and Interfaces with Femtosecond Optics. *J. Appl. Phys.* **1992**, *71*, 326–338. [CrossRef]
27. Dekorsy, T.; Auer, H.; Waschke, C.; Bakker, H.J.; Roskos, H.G.; Kurz, H.; Wagner, V.; Grosse, P. Emission of Submillimeter Electromagnetic Waves by Coherent Phonons. *Phys. Rev. Lett.* **1995**, *74*, 738–741. [CrossRef]
28. Bronner, C.; Tegeder, P. Relaxation Dynamics of Photoexcited Charge Carriers at the Bi(111) Surface. *Phys. Rev. B* **2014**, *89*, 115105. [CrossRef]
29. Faure, J.; Mauchain, J.; Papalazarou, E.; Marsi, M.; Boschetto, D.; Timrov, I.; Vast, N.; Ohtsubo, Y.; Arnaud, B.; Perfetti, L. Direct Observation of Electron Thermalization and Electron-Phonon Coupling in Photoexcited Bismuth. *Phys. Rev. B* **2013**, *88*, 075120. [CrossRef]
30. Tonouchi, M. Simplified Formulas for the Generation of Terahertz Waves from Semiconductor Surfaces Excited with a Femtosecond Laser. *J. Appl. Phys.* **2020**, *127*, 245703. [CrossRef]
31. Hagemann, H.-J.; Gudat, W.; Kunz, C. Optical Constants from the Far Infrared to the X-Ray Region: Mg, Al, Cu, Ag, Au, Bi, C, and Al_2O_3. *J. Opt. Soc. Am.* **1975**, *65*, 742–744. [CrossRef]

Paper 8 [P8]

V.L Malevich, P.A. Ziaziulia; **R. Norkus**; V. Pačebutas, I. Nevinskas; A. Krotkus, “Terahertz Pulse Emission from Semiconductor Heterostructures Caused by Ballistic Photocurrents”, Sensors, 21, 4067. (2021)

The article can be accessed online at https://doi.org/10.3390/s21124067

sensors

MDPI

Article

Terahertz Pulse Emission from Semiconductor Heterostructures Caused by Ballistic Photocurrents

Vitaly Leonidovich Malevich [1,2], Pavel Aliaksandravich Ziaziulia [3], Ričardas Norkus [4,*], Vaidas Pačebutas [4], Ignas Nevinskas [4] and Arūnas Krotkus [4]

[1] Stepanov Institute of Physics, National Academy of Science, Nezavisimosti Avenue 68, 220072 Minsk, Belarus; v.malevich@ifanbel.bas-net.by
[2] Belarusian State University of Informatics and Radioelectronics, P. Browki Str. 6, 220013 Minsk, Belarus
[3] Belarusian State University, Nezavisimosti Avenue 4, 220030 Minsk, Belarus; zezyulya@bsu.by
[4] Center for Physical Sciences and Technology, Sauletekio av. 3, LT-10257 Vilnius, Lithuania; vaidas.pacebutas@ftmc.lt (V.P.); ignas.nevinskas@ftmc.lt (I.N.); arunas.krotkus@ftmc.lt (A.K.)
* Correspondence: Ricardas.norkus@ftmc.lt

Abstract: Terahertz radiation pulses emitted after exciting semiconductor heterostructures by femtosecond optical pulses were used to determine the electron energy band offsets between different constituent materials. It has been shown that when the photon energy is sufficient enough to excite electrons in the narrower bandgap layer with an energy greater than the conduction band offset, the terahertz pulse changes its polarity. Theoretical analysis performed both analytically and by numerical Monte Carlo simulation has shown that the polarity inversion is caused by the electrons that are excited in the narrow bandgap layer with energies sufficient to surmount the band offset with the wide bandgap substrate. This effect is used to evaluate the energy band offsets in GaInAs/InP and GaInAsBi/InP heterostructures.

Keywords: THz; THz emission spectroscopy; heterojunction; GaInAsBi/InP; band offset; THz pulse generation; ballistic electrons; MBE

Citation: Malevich, V.L.; Ziaziulia, P.A.; Norkus, R.; Pačebutas, V.; Nevinskas, I.; Krotkus, A. Terahertz Pulse Emission from Semiconductor Heterostructures Caused by Ballistic Photocurrents. *Sensors* **2021**, *21*, 4067. https://doi.org/10.3390/s21124067

Received: 5 May 2021
Accepted: 9 June 2021
Published: 12 June 2021

1. Introduction

When photoexcited by femtosecond optical pulses, most materials emit ultrashort pulses of electromagnetic radiation containing frequencies at the terahertz (THz) frequency range. THz pulse emission has been observed from semiconductors [1], dielectric crystals [2], metals [3], and even from gases [4], and liquids [5]. This universal effect became an effective and popular tool for a contact-less investigation of various materials. Moreover, some semiconductor or ferromagnetic material structures that are most efficient surface emitters can replace photoconductive antennas as the THz radiation sources in the time-domain spectroscopy (TDS) systems, especially in those that are activated by long-wavelength femtosecond lasers [6]. As yet, the most efficient THz pulse emitting surfaces are the narrow bandgap group A3B5 semiconductors such as InAs or InSb [7,8]. This is because the photoexcited electrons and holes move away from the illuminated surface at different velocities, which creates fast changing electrical dipole radiating THz waves. During the first few hundreds of femtoseconds, when the dipole is developing, the photoexcited electrons in narrow-gap A3B5 semiconductors are moving ballistically [9] over the distances reaching several hundred nanometers [10]. Due to the electrons not being scattered during this stage, the initial optical orientation of their momenta [11] is conserved and it is also reflected in the azimuthal angle dependences of THz emission for certain photoexcited crystal planes [12,13].

THz emission due to ballistic photoexcited electron propagation has been exploited for the measurements of conduction band offsets in GaAsBi/GaAs [14] and GaInAsBi/InP [15] heterojunctions. Femtosecond optical pulses with a tunable central wavelength were

illuminating the interface between the air and the narrower bandgap material layer. The electrons excited at this interface with lower energy photons could not move farther than the thickness of the narrow-gap layer, and the amplitude of a THz pulse was relatively small. The THz pulse amplitude started to increase only when the excess energy of ballistic electrons was higher than the conduction band offset at the heterojunction between the layer and the wider bandgap substrate. Therefore, the heterostructure offset values could be directly found from the THz excitation spectra measurement. In fact, this band offset measurement technique is an optical equivalent of the so-called ballistic-electron-emission-microscopy (BEEM) [16], where subsurface electronic structure is probed by electrons injected into material from differently biased scanning tunneling microscope tip.

From what is said above, it is clear that femtosecond photoexcitation and THz pulse emission can be used to study the ballistic electrons in semiconductors. One of the important objects of such a study could be the realization of optics-like effects in electronic systems. Ballistic electrons are coherent de Broglie waves that can be reflected or refracted at the heterointerfaces between different semiconductors, much like the electromagnetic waves [17,18]. Their behavior would be exposed more unanimously, if the electrons would be generated at the proximity of the interface rather than away from it, at the air/semiconductor boundary. In this contribution, we present the investigation of THz emission from femtosecond laser-excited heterostructures between InP substrate and GaInAs and GaInAsBi epitaxial layers. Several nontrivial characteristics of this effect, such as different THz excitation spectra dependences and different tilt angles of THz electrical dipoles created after illuminating the structure from the substrate and the layer sides were observed. These differences have been explained by the influence of quasi-ballistic photoelectrons that are entering into the substrate and are refracted there at larger angles fostering more efficient THz radiation outcoupling from the semiconductor structure.

2. Materials and Methods

The heterostructures were grown by molecular-beam-epitaxy (MBE) on semi-insulating (001) InP:Fe substrates. Two heterostructures' samples were investigated: a sample with lattice-matched 600 nm thick $Ga_{0.47}In_{0.53}As$ layer on InP (sample A) and $Ga_{0.47}In_{0.53}As_{1-x}Bix/InP$ structure with 4% Bi (sample B). Native oxides were desorbed by heating InP substrates at 500 °C under arsenic flux and monitoring the process by observation of a distinctive (2×4) surface reconstruction pattern by the reflection high energy electron diffraction. The GaInAs layer was grown at standard growth conditions keeping high substrate temperature at T ~490 °C and the beam equivalent pressure (BEP) ratio As_2/Ga from 7 to 10. The growth temperature was adjusted by a thermocouple-based controller calibrated by the use of melting points of Sn and InSb. In order to enhance the bismuth incorporation into the growing layer and to avoid its segregation on the surface, the growth of the $Ga_{0.47}In_{0.53}As_{0.96}Bi_{0.04}$ layer was performed at substrate temperature of 240 °C, which is significantly lower than typical MBE growth temperatures for GaInAs. The BEP of group 3 and 5 atomic flux ratio was calibrated by monitoring the surface reconstruction change on separate substrate before the samples' growth. The growth rate of bismide layer was 0.6 µm/h. The atomic composition of the GaInAsBi layer was determined from X-ray diffraction (XRD) measurements, carried out with Smart Lab Rigaku diffractometer (Rigaku corporation, Tokyo, Japan) by monitoring the (004) diffraction peak with respect to its position in InP.

THz-TDS experiments were performed on the samples described above. The set-up of these experiments (Figure 1) was based on an amplified Yb:KGW femtosecond laser system (PHAROS, Light Conversion Ltd., Vilnius, Lithuania) operating at 1030 nm at 200 kHz pulse repetition rate with a cavity-tuned optical parametric amplifier (OPA, ORPHEUS, Light Conversion Ltd., Vilnius, Lithuania). Optical pulses of ~160 fs duration and central wavelengths tunable from 640 nm to 2600 nm were used for sample photoexcitation, while the emitted THz pulses were detected by a GaAsBi photoconductive antenna (TeraVil Ltd., Vilnius, Lithuania) activated by a small part of the Yb:KGW laser beam.

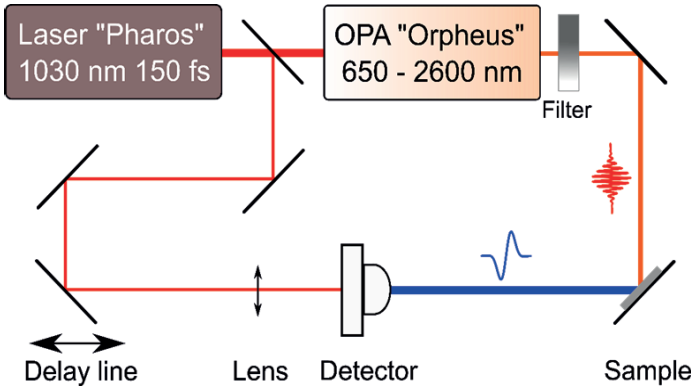

Figure 1. Experimental set-up of THz excitation spectra measurements.

3. Results

3.1. THz Excitation Spectra Measurements

Results of the measurements are illustrated in Figure 2, where the THz radiation pulses emitted from the sample A surface are shown. Femtosecond optical pulses were impinging the sample's surface at a 45° angle from the substrate side (Figure 2a), and from the GaInAs layer-side (Figure 2b), THz pulses were measured in the quasi-reflection direction. THz pulses emitted after photoexcitation at two different optical wavelengths are presented. It can be seen that the amplitudes are almost five times higher when the optical pulses are incident on the sample from the epitaxial layer-side, which could be explained by the presence of additional reflections of both optical and THz pulses at the heterointerface in the substrate-side excitation case. Another characteristic feature of these graphs is more unexpected: the THz pulses radiated from this sample when excited from the substrate side have opposite polarities at different exciting photon energies. No such change is present when the sample is illuminated from the epitaxial layer-side.

THz pulse emission from the semiconductor surfaces is mainly caused by the ultrafast changing photocurrents leading to a dynamic electrical dipole formation [1]. These photocurrents appear either due to the built-in electric fields or due to the different electron and hole propagation velocities away from photoexcited location. As the THz field amplitude measured in the far field is proportional to the first derivative of the photocurrent in time $E_{THz} \sim dJ_{ph}/dt$, the temporal shape of J_{ph} can be determined by integrating the expression. The results of integration are shown in Figure 2c,d. The photocurrent rather than the THz electric field amplitude spectra are more appropriate for the experiment and theory comparison which will be presented in this contribution later.

The experimentally determined peak photocurrent dependences on laser photon energy measured from both heterostructure samples are shown in Figure 3. The THz pulse polarity inversion is present in both samples when illuminated from the substrate side. One has to point out that in the bismide-containing layer (sample B), this effect sets on at lower photon energies than in sample A. The polarity inversion takes place at a photon energy range where a characteristic kink is observed on a THz excitation spectrum measured from the sample B epitaxial layer-side (Figure 3b—green triangles). It has been shown that similar shapes of the THz excitation spectra are indicating the onset of photoelectron propagation above the conduction band offset from the narrow-gap layer into the wide bandgap part of a heterostructure [15], which suggests that the observed polarity inversion effect is also of a similar origin. An analogous comparison of the THz excitation spectra measured from both sides of sample A is not possible, because the epitaxial layer in this

sample is much thicker, and only a few of the electrons generated at the layer/air interface reach the heterointerface location.

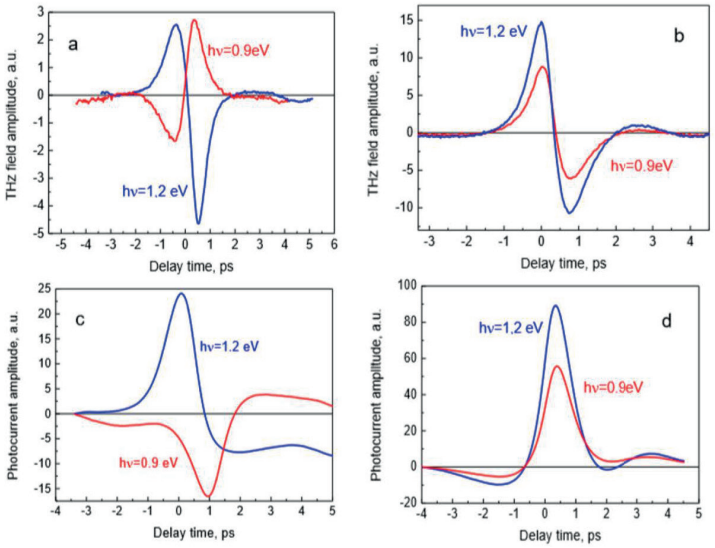

Figure 2. THz electric field (**a**,**b**) and photocurrent (**c**,**d**) pulses measured at two different optical wavelength beams impinging on sample A from the InP substrate side (**a**,**c**) and from the GaInAs epitaxial layer side (**b**,**d**).

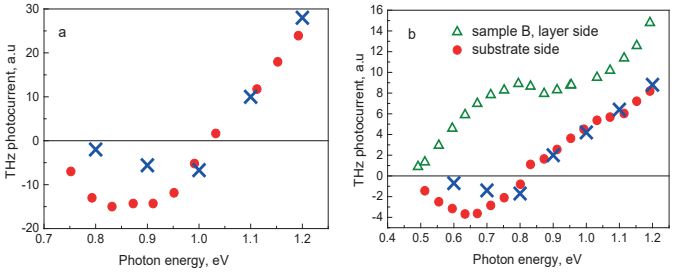

Figure 3. THz excitation spectra of GaInAs/InP (**a**) and GaInAsBi/InP (**b**) heterostructure samples measured for cases of the layer-side photoexcitation (empty green triangles) and the substrate-side photoexcitation (full red circles). Blue crosses show the Monte Carlo simulation results.

The main part of the THz pulse is generated during the first 100–200 fs after photoexcitation, that is, at the ballistic stage of photocarriers' movement. When analyzing THz surface emission, it is generally assumed that the transient photocurrent is directed perpendicular to the illuminated semiconductor surface, along the built-in surface electric field direction [1] or the induced spatial separation of photoexcited electrons and holes [19]. However, in cubic semiconductors, the absorption of linearly polarized radiation results in the photoexcited electron momenta from heavy-hole valence subband directed mainly in the plane perpendicular to the electric field of a light wave [11]. This optical alignment of electron momenta can also result in the appearance of a lateral (parallel to the illuminated semiconductor surface) transient photocurrent component. The THz radiation induced by

this photocurrent component is predominantly directed perpendicular to the illuminated surface, and hence it will be more efficiently out-coupled from the semiconductor [12].

When the photon energy is low and electrons with excess energy below the conduction band offset U are excited in the narrow-gap part of the heterostructure, the photocurrent arises as a result of electron reflections from the surfaces of the epitaxial layer and is directed towards the layer/air interface. At higher photon energies, when the excess energy becomes larger than U and is sufficient enough to overcome the potential step, the electrons moving towards the substrate of the structure also start to take part in the photocurrent. This photocurrent has an opposite direction to the current flowing in the epitaxial layer. Starting from a certain photon energy slightly exceeding the threshold energy $\varepsilon_g + U$, the contribution into the photocurrent of electrons transmitted into the substrate and electrons reflected from the external surface at $z = 0$ can prevail over the photocurrent caused by the reflection of electrons from the epitaxial layer from heterointerface, which results in polarity inversion of THz field amplitude.

3.2. Model Calculations

Let us first consider a simple theoretical model for the formation of a photocurrent in a heterostructure excited by femtosecond laser pulses. The structure under study is a narrow-gap semiconductor layer grown on a wide-gap semiconductor substrate. We only take into account the optical transitions of electrons from the heavy-hole subband, and neglect the motion of holes. In addition, we neglect the screening effect caused by spatially redistributed photocarriers and assume that the optical pulse is instantaneous with the shape approximated by the δ-function. As the THz pulse reaches its peak during optical excitation pulse, we neglect the bulk collisions of photoelectrons.

When optical radiation is incident on the structure from the narrow-gap top layer- side located at $0 \le z \le L$, the kinetic equation for distribution function $f_{\mathbf{p}}(z,t)$ of photoelectrons in this layer takes the form:

$$\frac{\partial f_{\mathbf{p}}}{\partial t} + v_{\mathbf{p}z}\frac{\partial f_{\mathbf{p}}}{\partial z} = W_{\mathbf{p}}\delta(t)e^{-\alpha z}, \tag{1}$$

where $v_{\mathbf{p}z} = p_z/m_1$ is the z-component of electron velocity, $\varepsilon_{\mathbf{p}}$ is the energy of an electron with momentum $\mathbf{p}$, α is the optical absorption coefficient (the photon energy is assumed to be lower than the wide-gap semiconductor's bandgap). The rate of direct optical transitions from heavy-hole subband to conduction band $W_{\mathbf{p}}$ is given by [11]:

$$W_{\mathbf{p}} = \frac{n}{g(\varepsilon_{\mathbf{p}})}(1 - P_2(\cos\gamma))\delta(\varepsilon_{\mathbf{p}} - \varepsilon_0), \tag{2}$$

where n is the photoexcited electron density at the surface $z = 0$, $P_2(x)$ is the second order Legendre polynomial, γ is the angle between the $\mathbf{p}$-vector and the exciting radiation's electric field, $\varepsilon_0 = (\hbar\omega - \varepsilon_g)/(1 + m_1/m_{1h})$ is the excess energy of photoelectrons excited by femtosecond optical pulses with photon energy of $\hbar\omega$, ε_g is the bandgap of a top-layer semiconductor, m_1 and m_{1h} are the electron and heavy-hole effective masses, and $g(\varepsilon) = \sqrt{2m_1^3\varepsilon}/(\pi^2\hbar^3)$ is the density of electron states in the conduction band. We assume that for electrons at the boundary $z = 0$ that the mirror reflection condition is satisfied, and hence $f_{\mathbf{p}_\parallel,p_z}(z = 0,t) = f_{\mathbf{p}_\parallel,-p_z}(z = 0,t)$, $\mathbf{p}_\parallel$, is the two-dimensional electron momentum parallel to the surface.

At the heterointerface $z = L$, the boundary condition is written in the form $f_{\mathbf{p}_\parallel,-p_z}(z = L,t) = (1 - T)f_{\mathbf{p}_\parallel,p_z}(z = L,t)\ p_z > 0$, which takes into account the possibility of photoelectron penetration through the potential step into the wide-gap semicon-

ductor. The transmission coefficient for electrons with energy ε incident on a potential step at an angle θ is written as [20]:

$$T(\varepsilon, \cos\theta) = \frac{4\sqrt{m_1 m_2 \varepsilon(\varepsilon - U)}\cos\theta\cos\theta_t}{\left(\sqrt{m_2\varepsilon}\cos\theta + \sqrt{m_1(\varepsilon - U)}\cos\theta_t\right)^2}, \quad (3)$$

where m_2 is the electron effective mass in a wide-bandgap semiconductor, U is the conduction band offset; the angle θ_t between electron momentum and z-axis in a wide-bandgap semiconductor is determined from the relation:

$$\frac{\sin\theta_t}{\sin\theta} = \sqrt{\frac{m_1\varepsilon}{m_2(\varepsilon - U)}}. \quad (4)$$

Multiple electron reflections from the boundaries of the narrow-gap layer lead to a quasiperiodic character of its motion along z-axis (at $T = 0$, the motion becomes strictly periodic with a period $2L/v_{\mathbf{p}z}$). The solution to Equation (1) is found by the method of characteristics and it is represented by an infinite series of terms. Below, we neglect the multiple reflections and restrict ourselves to considering the motion of electrons at times not exceeding the time of one flight over a narrow bandgap layer ($t < L/v_0$ ($v_0 = (2\varepsilon_0/m_1)^{1/2}$). The distribution function $f_{t\mathbf{p}}(z, t)$ of electrons transmitted into a wide-gap semiconductor ($z > L$) is found from the equation

$$\frac{\partial f_{t\mathbf{p}}}{\partial t} + v_{t\mathbf{p}z}\frac{\partial f_{t\mathbf{p}}}{\partial z} = 0, v_{t\mathbf{p}z} = p_z/m_2, \quad (5)$$

together with the boundary condition of the electron flux continuity at $z = L$.

The in-plane vectors of the incident and transmitted electron momenta coincide ($\mathbf{p}'_{\parallel} = \mathbf{p}_{\parallel}$), while the z-component of transmitted electron momenta is determined as

$$p'_z = \sqrt{2m_2(\varepsilon - U)}\cos\theta_t = \sqrt{2m_2(\varepsilon - U) - 2m_1\varepsilon + p_z^2}. \quad (6)$$

The surface photocurrent determining the amplitude of a THz pulse is defined as

$$\mathbf{J} = -\frac{e}{4\pi^3\hbar^3 m}\left(\int_0^L dz\int d^3p\,\mathbf{p}f_{\mathbf{p}}(z,t) + \int_L^\infty dz\int d^3p\,\mathbf{p}' f_{t\mathbf{p}'}(z,t)\right). \quad (7)$$

Substituting the obtained electron distribution functions into (7) and carrying out the integration over z, and, in a spherical coordinate system over absolute value of electron momentum p and azimuthal angle φ, we obtain the surface photocurrent components to be equal to

$$\begin{aligned} J_z &= -\tfrac{3env_0^2t}{8}\int_0^1 d(\cos\vartheta)\cos\theta\left(2 - 2\sin^2\vartheta_r\cos^2\theta - \cos^2\vartheta_r\sin^2\theta\right)\times\left[2\cos\theta\times\right. \\ &\left.\times\left(1 - e^{-\alpha L}\right) + \mathrm{T}(\varepsilon_0, \cos\theta)e^{-\alpha L}\left(\cos\theta + \tfrac{m_1}{m_2}\sqrt{\cos^2\theta - \cos^2\theta_{cr}}\right)\right] \end{aligned}, \quad (8)$$

$$J_x = \frac{3env_0^2te^{-\alpha L}\sin 2\vartheta_r}{8}\left(1 - \frac{m_1}{m_2}\right)\int_0^1 d(\cos\vartheta)\cos^2\theta\sin^2\theta\mathrm{T}(\varepsilon_0, \cos\theta) \quad (9)$$

where ϑ_r is the refraction angle of the optical radiation, which is supposed to be polarized in xz plane, $\theta_{cr} = \cos^{-1}\sqrt{1 - m_2(\varepsilon_0 - U)/(m_1\varepsilon_0)}$ is the critical angle–electrons incident at angles greater than θ_{cr} are totally reflected from the potential step. Here we assume that the optical absorption length is higher than the thickness of the top layer, and hence, in the ballistic mode which we are concerned about, the parameter $\alpha v_0 t$ can be assumed to be

small. Therefore, when introducing Equations (8) and (9), we limited ourselves to the first order in this small parameter.

Further on, for the sake of simplicity, we approximate the transmission coefficient $T(\varepsilon_0, \cos\theta)$ by the step function: $T = 1$ for $\theta < \theta_{cr}$, and $T = 0$ for $\theta > \theta_{cr}$. After integration over the variable $\cos\theta$ in (8) and (9) we get the final expressions for the surface photocurrent components

$$J_{1z} = -\frac{env_0^2 t}{5}\left\{\left(1-e^{-\alpha L}\right)\left(1+\cos^2\theta_r\right)+\frac{e^{-\alpha L}}{2}\left[1+\cos^2\theta_r - \right.\right. \\ \left.\left. -\frac{5s^3}{4}\left(2-\cos^2\theta_r\right)-\frac{3s^5}{4}\left(3\cos^2\theta_r-2\right)\right]\right\} \quad (10)$$

$$J_{2z} = -\frac{env_0^2 te^{-\alpha L}}{4}\frac{m_1}{m_2}\left(1-s^2\right)^{3/2}\left(\cos^2\theta_r - \frac{\left(1-s^2\right)}{5}\left(3\cos^2\theta_r-2\right)\right), \quad (11)$$

$$J_x = \frac{env_0^2 te^{-\alpha L}\sin 2\vartheta_r}{20}\left(1-\frac{m_1}{m_2}\right)\left(1-\frac{5}{2}s^3+\frac{3}{2}s^5\right), \quad (12)$$

where s is defined as

$$s = \begin{cases} 1, & \varepsilon_0 < U \\ \cos\theta_{cr}, & U<\varepsilon_0 < U/(1-m_1/m_2) \\ 0, & \varepsilon_0 > U/(1-m_1/m_2). \end{cases} . \quad (13)$$

Equations (10) and (11) represent the contributions to the normal component of electron photocurrent in the upper narrow bandgap layer and in the substrate, respectively. Thus, the normal component of the total photocurrent is defined as $J_z = J_{1z} + J_{2z}$.

The expressions of the surface photocurrent components for the substrate-side excitation case are calculated in a similar way. The corresponding expressions for the components J_{2z} and J_x are obtained from Equations (11) and (12) by omitting the factor $\exp(-\alpha L)$; the contribution from the top-layer photoelectrons to the normal photocurrent component is obtained from Equation (10) after removing the factor $\exp(-\alpha L)$ before the second term in the square bracket and changing the sign in the first term.

Using Equations (10)–(13), we calculate the dependencies of photocurrents' contributions on exciting photon energy (Figure 4). In the calculation, the following parameters are used: $L = 0.24$ μm, $\varepsilon_g = 0.5$ eV, $U = 0.28$ eV, $m_1 = 0.042\ m_0$ (GaInAsBi), $m_2 = 0.078\ m_2$ (InP); the optical absorption coefficient is approximated as $\alpha = 2.87{\cdot}10^4\left(\hbar\omega - \varepsilon_g\right)^{\frac{1}{2}}/\hbar\omega$ [cm^{-1}].

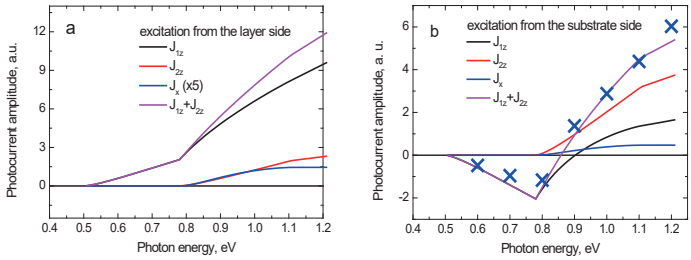

Figure 4. Results of the analytical calculations of different photocurrent components by use of Equations (10)–(13), for the excitation from the GaInAsBi layer side (**a**) or the InP substrate side (**b**) Blue crosses show the Monte Carlo simulation results.

In the subthreshold photon energy range, when $\varepsilon_0 = \hbar\omega - \varepsilon_g < U$, electrons cannot surmount the potential step and only the carriers in the narrow-gap layer contribute to the photocurrent. The corresponding expression follows from Equation (10) at $s = 1$ and

for the excitation from the top layer-side $J_z = -env_0^2 t\left(1-e^{-\alpha L}\right)\left(1+cos^2\theta_r\right)/5$ (for the excitation from the substrate side, this expression changes signs). It is evident that, in this case, the photocurrent tends to zero when the top layer-width is narrower than the optical penetration length ($\alpha L > 1$) and it disappears completely for a uniform photoelectron distribution. A slight growth of the photocurrent in the spectral region $\varepsilon_g < \hbar\omega < \varepsilon_g + U$ is caused by the dependences of parameters α and v_0 on photon energy.

When the photon energy is higher than $\varepsilon_g + U$, the photoelectrons acquire enough energy to pass into the wide bandgap substrate. At the excess electron energy slightly exceeding the threshold energy U, only a small fraction of electrons traveling almost perpendicularly to the interface pass into the substrate; most of the photoelectrons undergo reflection. With increasing excess electron energy, the angle of total internal reflection increases, therefore, the photoelectrons incident on the heterointerface at greater angles can also penetrate into the substrate. This leads to an increase in the fraction of electrons that pass into the substrate and to a steeper growth of the substrate photocurrent in the spectral range $\varepsilon_g + U < \hbar\omega < \varepsilon_g + U/(1 - m_1/m_2)$. At photon energies $\hbar\omega > \varepsilon_g + U/(1 - m_1/m_2)$ which corresponds to electron energy $\varepsilon_0 > U/(1 - m_1/m_2)$, the angle of total internal reflection is $\theta_{cr} = \pi/2$ and all electrons incident on the interface pass into the substrate.

Figure 4 shows that after exciting the heterojunction from the substrate side, the photocurrent depends on photon energy non-monotonically: at low photon energies, it is negative, and at $\hbar\omega \approx 0.85$ eV, it changes sign to positive. This feature is explained by the fact that in the subthreshold photon energy range, photoexcited electrons in the narrow bandgap layer move away from the substrate and, therefore, their contribution to the photocurrent is negative. As the photon energy increases above the threshold value $\hbar\omega < \varepsilon_g + U$, the contribution of J_{1z} to the photocurrent decreases in absolute value due to a decrease in the fraction of photoelectrons reflected from the heterointerface, and changes its sign at a photon energy of $\hbar\omega \approx 0.9$ eV. On the other hand, the contribution of photoelectrons in the substrate J_{2z} is positive and rises with increasing photon energy. As a result, at photon energies lower than 0.85 eV, the total photocurrent is negative because J_{1z} contribution prevails, while at higher photon energies, the dominant contribution is of those photoelectrons that are passed into the substrate, and the total photocurrent becomes positive.

As it follows from Equation (12), the anisotropy of photoelectron momentum distribution can lead to the appearance of a lateral (parallel to the heterointerface) photocurrent component J_x. This photocurrent component arises when the effective masses of electrons in the narrow-gap layer and the substrate do not coincide, which leads to a difference in the lateral components of the photoelectron velocities reflected from the interface and transmitted to the substrate. When the structure is excited from the substrate side, the photoelectrons are mainly located near the heterointerface and, in this case, the lateral photocurrent is higher than under excitation from the layer side.

Equations (10)–(13) do not describe the time dependences of photocurrents; more detailed analysis of the photoexcited carrier transport in the heterostructures was performed by the ensemble Monte Carlo (MC) method. The optical absorption coefficient, electron and hole effective masses, conduction band non-parabolicity, deformation potentials, optical phonon energies, and other parameters determining carrier scattering probabilities in GaInAsBi were assumed to be equal to those of $Ga_{0.47}In_{0.53}As$ and were taken from [21]; the corresponding parameters for InP were as in [22]. The calculations for different photon energies had been carried out under the condition of a constant photon flux of $W/\hbar\omega = 5 \cdot 10^{11}$ cm^{-2}, at $\hbar\omega = 1.2$ eV, it corresponds to $W = 0.48$ μJ/cm^2. In the calculation, an ensemble of 1,000,000 particles was used; the electric field was recalculated for each 1 fs time step, the spatial step was 1 nm. The emitted THz electric field in the far field region was defined by the time derivative of the surface transient photocurrent.

Figure 5 shows the time dependences of THz electric field emitted from the GaInAsBi-InP heterojunction excited by 160-fs laser pulses with photon energies of 0.7, 1.0, and 1.2 eV

from the layer and the InP substrate sides. It can be seen that at the excitation from the top layer-side (Figure 5a), the amplitude of a THz field monotonically grows with increasing photon energy. At photon energies higher than ~0.9 eV, this growth becomes faster because the electrons have energies sufficient to surmount the barrier at the heterostructure interface. When photoexciting from the substrate side (Figure 5b), this effect leads to the inversion of THz field polarity at higher photon energies, because of the contributions of electrons from the layer, and from the substrate to photocurrent having opposite signs. This is confirmed by the MC simulation results shown in Figure 6, where the time dependencies of photocurrents in the narrow-gap layer and the substrate are separately presented. It can be seen that in the case of excitation from bismide layer-side, both contributions to the photocurrent have the same sign (Figure 6a), while under excitation from the substrate with 0.8 eV and 1.2 eV photons, the signs of these contributions are opposite (Figure 6b). Figure 4b also shows that analytical calculations are in agreement with the MC simulation.

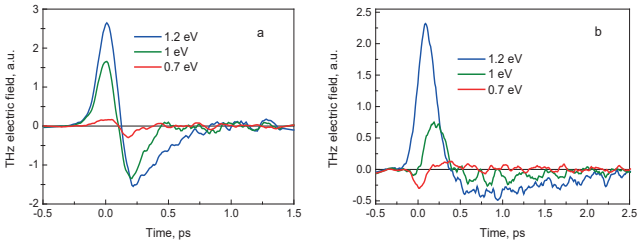

Figure 5. THz electric field pulses calculated by MC method for three different femtosecond optical pulse photon energies. The heterostructure is illuminated from the GaInAsBi layer-side (**a**) or from the InP substrate side (**b**).

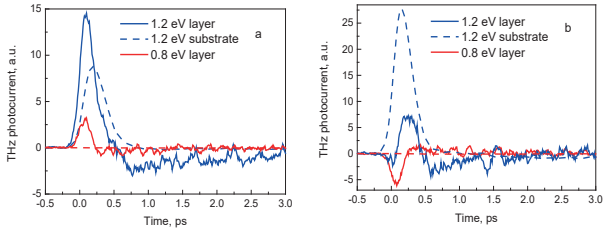

Figure 6. The MC calculated contributions of GaInAsBi layer (solid lines) and InP substrate (dashed lines) to the photocurrent for a heterojunction excited by femtosecond pulse optical radiation from the top layer (**a**) and from the substrate side (**b**); the blue and red lines correspond to the photon energies of 0.8 and 1.2 eV, respectively. The photocurrent in the substrate at 0.8 eV is zero.

In Figure 6, the MC method calculated photocurrents for substrate-side excitation by femtosecond optical pulse with different photon energies are shown. It is seen that for both structures, the MC simulation shows the polarity inversion of photocurrent at photon energies close to the experimentally observed values. In the subthreshold region of exciting photon energies, the calculations lead to the lower values of photocurrent amplitude in comparison with the experimentally measured ones. This difference is most likely due to the fact that the MC simulation took into account only the electric field caused by the spatial separation of photoexcited electrons and holes, but neglected the built-in electric field near the heterojunction boundary. In the considered heterostructures, the built-in electric field would lead to an increase in the photocurrent.

4. Conclusions

THz radiation pulses emitted from the $Ga_{0.47}In_{0.53}As/InP$ and $Ga_{0.47}In_{0.53}As_{1-x}Bi_x/InP$ (x = 4%) heterostructures illuminated by femtosecond optical pulses from the narrow bandgap layer-side and from the wide bandgap substrate-side were measured for a wide range of optical pulse wavelengths. These pulses changed their polarity to the opposite when the excess energy of the photoexcited electrons became comparable with the conduction band offset in the investigated Bi-containing heterostructure. This effect was analyzed both analytically and numerically by the Monte Carlo simulation, taking into account the optical alignment of photoexcited carrier momenta and the quasi-ballistic non-equilibrium electron propagation during the THz pulse emission. Good agreement between the experiment and the theory was obtained when analyzing the results of a well-known $Ga_{0.47}In_{0.53}As/InP$ heterostructure; the conduction band offset U = 0.28 eV was obtained for the heterostructure containing a $Ga_{0.47}In_{0.53}As_{0.96}Bi_{0.04}/InP$ layer grown on InP substrate. These results evidence that, at least for pure A3B5 semiconductors, the carrier separation due to the optically aligned ballistic electron movement rather than their random diffusive propagation (the photo-Dember effect) is responsible for the dynamic electrical dipole formation and THz emission. Moreover, the proposed THz excitation spectroscopy can be used as a direct method to analyze the energy band line-ups in semiconductor heterostructures.

Author Contributions: Conceptualization, A.K.; Formal analysis, V.L.M. and P.A.Z.; Investigation, R.N. and I.N.; Resources, V.P.; Supervision, A.K.; Writing—original draft, V.L.M. and A.K.; Writing—review and editing, R.N. and I.N. All authors have read and agreed to the published version of the manuscript.

Funding: This research was funded by a grant from the European Social Fund, measure number 09.3.3-LMT-K-712-01-0032.

Institutional Review Board Statement: Not applicable.

Informed Consent Statement: Not applicable.

Data Availability Statement: Not applicable.

Conflicts of Interest: The authors declare no conflict of interest.

References

1. Zhang, X.-C.; Auston, D.H. Optoelectronic measurement of semiconductor surfaces and interfaces with femtosecond optics. *J. Appl. Phys.* **1992**, *71*, 326. [CrossRef]
2. WFisher, W.M.; Rand, S.C. Optically-induced charge separation and terahertz emission in unbiased dielectrics. *J. Appl. Phys.* **2011**, *109*, 064903. [CrossRef]
3. Kadlec, F.; Kužel, P.; Coutaz, J.-L. Study of terahertz radiation generated by optical rectification on thin gold films. *Opt. Lett.* **2005**, *30*, 1402. [CrossRef] [PubMed]
4. Johnson, K.; Price-Gallagher, M.; Mamer, O.; Lesimple, A.; Fletcher, C.; Chen, Y.; Lu, X.; Yamaguchi, M.; Zhang, X.C. Water vapor: An extraordinary terahertz wave source under optical excitation. *Phys. Lett. A* **2008**, *372*, 6037–6040. [CrossRef]
5. Jin, Q.; Yiwen, E.; Gao, S.; Zhang, X.C. Preference of subpicosecond laser pulses for terahertz wave generation from liquids. *Adv. Photonics* **2020**, *2*, 015001. [CrossRef]
6. Molis, G.; Adomavicius, R.; Krotkus, A.; Bertulis, K.; Giniunas, L.; Pocius, J.; Danielius, R. Terahertz time-domain spectroscopy system based on femtosecond Yb: KGW laser. *Electron. Lett.* **2007**, *43*, 190–191. [CrossRef]
7. Adomavičius, R.; Urbanowicz, A.; Molis, G.; Krotkus, A.; Šatkovskis, E. Terahertz emission from p-lnAs due to the instantaneous polarization. *Appl. Phys. Lett.* **2004**, *85*, 2463–2465. [CrossRef]
8. Adomavičius, R.; Molis, G.; Krotkus, A.; Sirutkaitis, V. Spectral dependencies of terahertz emission from InAs and InSb. *Appl. Phys. Lett.* **2005**, *87*, 261101. [CrossRef]
9. Malevich, V.L.; Ziaziulia, P.A.; Adomavičius, R.; Krotkus, A.; Malevich, Y.V. Terahertz emission from cubic semiconductor induced by a transient anisotropic photocurrent. *J. Appl. Phys.* **2012**, *112*, 073115. [CrossRef]
10. Sasa, S.; Umino, S.; Ishibashi, Y.; Maemoto, T.; Inoue, M.; Takeya, K.; Tonouchi, M. Intense terahertz radiation from InAs thin films. *J. Infrared Millim. Terahertz Waves* **2011**, *32*, 646–654. [CrossRef]
11. Zemskii, V.I.; Zakharchenya, B.P.; Mirlin, D.N. Polarization of hot photoluminescense in semiconductors of the GaAs type. *Pis'ma Zh Eksp.Teor. Fiz.* **1976**, *24*, 96.

12. Cicėnas, P.; Geižutis, A.; Malevich, V.L.; Krotkus, A. Terahertz radiation from an InAs surface due to lateral photocurrent transients. *Opt. Lett.* **2015**, *40*, 5164–5167. [CrossRef] [PubMed]
13. Nevinskas, I.; Vizbaras, K.; Trinkūnas, A.; Butkutė, R.; Krotkus, A. Terahertz pulse generation from (111)-cut InSb and InAs crystals when illuminated by 1.55-μm femtosecond laser pulses. *Opt. Lett.* **2017**, *42*, 2615–2618. [CrossRef] [PubMed]
14. Karpus, V.; Norkus, R.; Čechavičius, B.; Krotkus, A. THz-excitation spectroscopy technique for band-offset determination. *Opt. Express* **2018**, *26*, 33807–33817. [CrossRef] [PubMed]
15. Pačebutas, V.; Norkus, R.; Karpus, V.; Geižutis, A.; Strazdienė, V.; Stanionytė, S.; Krotkus, A. Band-offsets of GaInAsBi–InP heterojunctions. *Infrared Phys. Technol.* **2020**, *109*, 103400. [CrossRef]
16. WBell, L.D.; Kaiser, W.J. Observation of interface band structure by ballistic-electron-emission microscopy. *Phys. Rev. Lett.* **1988**, *61*, 2368. [CrossRef]
17. DWilson, D.W.; Glytsis, E.N.; Gaylord, T.K. Quantum well, voltage-induced quantum well, and quantum barrier electron waveguides: Mode characteristics and maximum current. *Appl. Phys. Lett.* **1991**, *59*, 1855–1857. [CrossRef]
18. Wilson, D.W.; Glytsis, E.N.; Gaylord, T.X. Electron waveguiding characteristics and ballistic current capacity of semiconductor quantum slabs. *IEEE J. Quantum Electron.* **1993**, *29*, 1364–1382. [CrossRef]
19. Dekorsy, T.; Auer, H.; Waschke, C.; Bakker, H.J.; Roskos, H.G.; Kurz, H.; Wagner, V.; Grosse, P. Emission of submillimeter electromagnetic waves by coherent phonons. *Phys. Rev. Lett.* **1995**, *74*, 738. [CrossRef] [PubMed]
20. Gaylord, T.K.; Brennan, K.F. Electron wave optics in semiconductors. *J. Appl. Phys.* **1989**, *65*, 814–820. [CrossRef]
21. Adachi, S. *Physical Properties of III–V Semiconductor Compounds. InP, InAs, GaAs, GaP, InGaAs and InGaAsP*; Wiley: New York, NY, USA, 1992. [CrossRef]
22. Semiconductors on NSM. Available online: http://www.ioffe.rssi.ru/SVA/NSM/Semicond/ (accessed on 11 November 2020).

Paper 9 [P9]

J. Devenson, **R. Norkus**, R. Juškėnas, A. Krotkus, "Terahertz emission from ultrathin bismuth layers," Optic Letters 46, 3681-3684 (2021)

The published article can be accessed online: https://doi.org/10.1364/OL.425271

Terahertz emission from ultrathin bismuth layers

JAN DEVENSON, RIČARDAS NORKUS*, REMIGIJUS JUŠKĖNAS, ARŪNAS KROTKUS

Center for Physical Sciences and Technology, Saulėtekio av. 3, LT-10257, Vilnius, Lithuania
**Corresponding author: ricardas.norkus@ftmc.lt*

Received XX Month XXXX; revised XX Month, XXXX; accepted XX Month XXXX; posted XX Month XXXX (Doc. ID XXXXX); published XX Month XXXX

Thinner than 10 nm layers of bismuth were grown on (111) Si substrates by molecular beam epitaxy. Terahertz (THz) radiation pulses from these layers excited by tunable wavelength femtosecond optical pulses were measured. THz emission sets-on when the photon energy exceeds 0.45 eV, which was explained by the semimetal-to-semiconductor transition at this bismuth layer thickness. THz signal has both isotropic and anisotropic components that could be caused by the lack of balance of lateral photocurrent components and the shift currents, respectively.

Terahertz (THz) frequency range measurement techniques have greatly improved over the last decades and are applied in many different application areas such as sensing, spectroscopy, imaging, and material characterization. Technique utilizing THz radiation to characterize materials is lately becoming very popular – the emission of THz pulses from materials photoexcited by femtosecond laser pulses. In the investigated material laser pulses are inducing ultrafast changing photocurrents, which cause electrical dipoles radiating in the THz frequency range. THz pulse emission induced by femtosecond optical pulses has been observed in different semiconductors [1, 2], gases [3, 4], and liquids [5]. As a broadband and contactless measurement technique it is especially useful when investigating novel material systems such as graphene [6], topological insulators [7], or two-dimensional materials [8]. THz time-domain spectroscopy provides reliable information on charge carrier mobility [9], whereas the THz pulse emission induced by femtosecond optical pulses and its spectral dependencies – on the details of the electron energy band structure in the material [10,11].

In this letter, we describe the effect of femtosecond optical pulse induced THz pulse emission from thin bismuth layers. Thin bismuth (Bi) films are an interesting research object because of their rich variety of physical properties. Due to its small electron and hole effective masses Bi has an extremely long Fermi wavelength (λ_F~30 nm), therefore quantum confinement effects can easily appear in the direction perpendicular to the surface of the layers [12]. Energy bandgap opening and semiconductor-semimetal phase transition were also documented in Bi nanowires with smaller than 46 nm diameters [13] and in Bi quantum dots [14]. Bi is also the basis of many topological insulators; thin bismuth films may themselves be topologically nontrivial, as theoretical studies predict them to be. [15,16]. To the best of our knowledge, THz pulses were used for investigating bismuth only in two contributions [17,18]. In Ref. 17 THz emission from bulk Bi crystals photoexcited by femtosecond Ti:sapphire laser pulses was measured, whereas 30 nm to 100 nm thick, magnetron sputtered

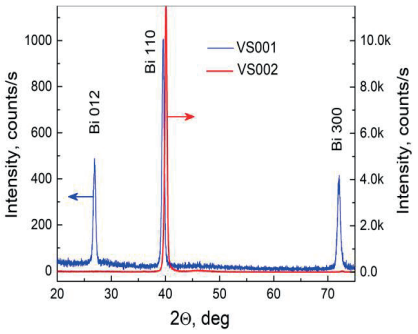

Fig. 1 The In-plane XRD patterns of Bi films VS001 (blue) and VS002 (red).

polycrystalline Bi layers were investigated in [18]. Here we will present more complex investigations of THz surface emission from a few nanometres thick Bi films grown by the molecular beam epitaxy (MBE) on Si (111) substrates using tuneable wavelength optical pulses from femtosecond optical parametric amplifier (OPA).

Several Bi samples were grown using solid source Veeco GEN Xplor MBE system, equipped with a conventional Dual Filament bismuth source on (111) oriented Si substrates. To remove the native oxide layer, before the growth of Bi layer, the Si substrate was heated up to ~1100 °C in the growth chamber. The RHEED (Reflection High-Energy Electron Diffraction) pattern and saturation of the average intensity of the main reflection point were monitored to determine the completion of the oxide removal process. The substrate temperature was controlled by a thermocouple. In the following, we will compare the results obtained on two of the samples: VS001 and VS002. Both samples

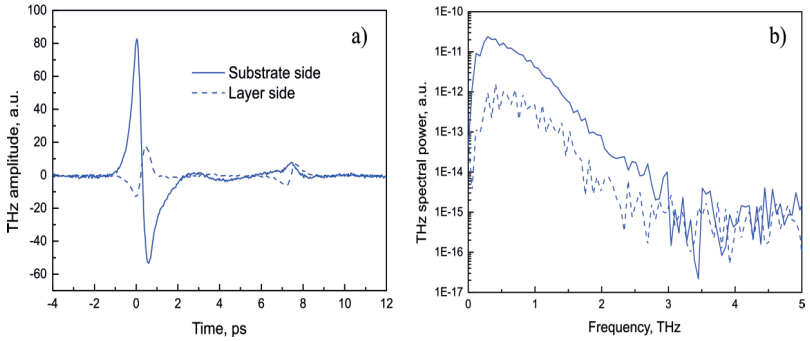

Fig. 2 THz field amplitudes (a) and Fourier spectra (b) of the pulses radiated from the sample VS001 illuminated by femtosecond optical pulses with a photon energy of 0.91 eV and average optical power – 120 mW from the Bi layer side (dashed line) and from the Si substrate side (solid line). Optical pulses were impinging at 30° angle; THz pulses were detected in the transmission direction.

were grown at the same Bi beam equivalent pressure of $8 \cdot 10^{-8}$ Tor and the layer growth rate was also the same - ~4 nm/h. The main difference in technological conditions of both growth runs was different substrate temperatures. It was equal to 100 °C for the layer VS001 and 20 °C for VS002. Low temperature growth is not uncommon for bismuth films due to its low melting point of 271°C. And the growth process is rather complex. It starts with ML thick wetting layer growth, proceeds with polycrystalline, rombohedral (pseudocubic) sublayer, and finally – with hexagonal sublayer growth [19].

The structure of the layers was studied by In-plane X-ray diffraction (XRD) and their thickness by X-ray reflectivity (XRR), respectively. The measurements were carried out using X-ray diffractometer SmartLab (Rigaku) with a 9 kW power rotating Cu anode X-ray source. The goniometer of this device was equipped with a special In-plane axis. According to the XRR measurements, the thickness of the both Bi films was approximately the same: 7.7 ± 0.5 and 8.8 ± 0.5 nm, while the surface roughness was 0.88 ± 0.04 nm and 0.93 ± 0.05 nm for VS001 and VS002, respectively.

Figure 1 shows the In-plane XRD patterns of Bi films VS001 (blue) and VS002 (red). The observed XRD peaks can be attributed to a rhombohedral Bi structure, space group R3m [20]. The peak Bi 012 may also be treated as peak Bi 100 of the pseudocubic phase, which is characteristic for film thicknesses up to 6 nm according to Ref. 21. It has been found in [21] that the pseudocubic phase becomes transformed into the hexagonal Bi phase when film thickness increases to 25 nm. In our work, the XRD pattern of VS001 presented peaks Bi 110 and Bi 300 along with Bi 012, while sample VS002 yielded only one very strong peak Bi 110 at $2\Theta \sim 40°$. The XRD pattern suggests that Bi film of sample VS001 resembles a polycrystalline film with prevailing orientation [001] perpendicular to the sample surface, while the XRD pattern of the sample VS002 that resembles that of the epitaxial layer or single crystal with the hexagonal plane coinciding with the sample's surface. It is worth to notice, that the XRD peaks of both Bi films are shifted towards higher diffraction angles as compared with the known data for trigonal bismuth PDF-#00-005-0519 [22], which points out to lower values of lattice parameter a in the Bi film plane and indicates the presence of compressive stresses in the film.

THz pulse emission from the Bi layers was investigated using femtosecond optical pulses from OPA Orpheus (Light Conversion) and a GaAsBi photoconductive antenna detector (UAB Teravil). The central wavelength of the optical pulses was varied in the range from 2.4 μm to 0.64 μm, the pulse duration was around 150 fs, and the pulse repetition rate was 200 kHz. A more detailed description of the experimental set-up was provided in Ref.10. The samples were illuminated along their surface normal and at the incline to it angles; THz pulses were monitored either in the transmission or in the reflection directions. Linearly polarized (p polarization) optical pulses were used: all measurements were performed at room temperature.

Figure 2a shows THz pulses radiated from the sample VS001 after the photoexcitation by 1360 nm wavelength, 120 mW average power optical pulses in the transmission direction. The

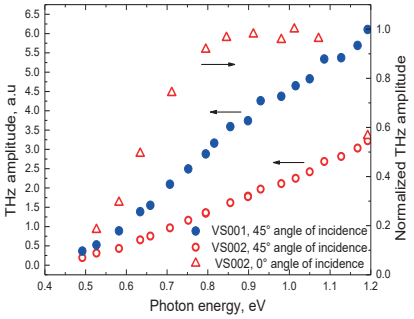

Fig. 3 THz excitation spectra of two thin Bi film samples. The spectra corresponding to the reflection geometry at 45° angle of incidence were measured at 20 mW average optical power. The spectrum measured in the transmission geometry at 0° angle of incidence on the sample VS002 was obtained using 80 mW average optical power. All spectra are normalized to a constant photon number in the optical pulse.

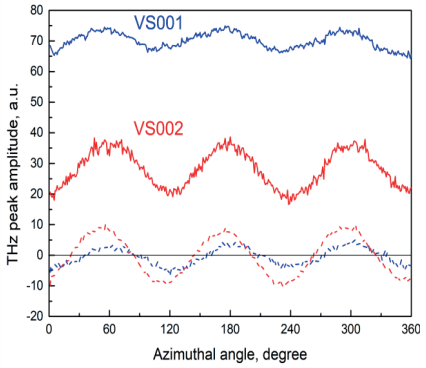

Fig. 4 Azimuthal angle dependences of THz emission from two samples: VS001 (blue) and VS002 (red). The spectra were measured in the transmission geometry: θ=30° (full lines) and θ=0° (dashed lines). Average power of photoexciting optical beam was 120 mW, photon energy – 0.91 eV

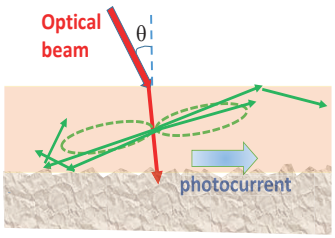

Fig. 5 Mechanism of the THz pulse emission from thin hexagonal Bi films. Azimuthal angle independent, isotropic component appears due to the difference in the electron propagation in two opposite lateral directions. Electrons moving to the right reach a flat interface with air and are there reflected without changing their lateral velocity component, whereas electrons moving to the left are diffusively scattered after reaching the polycrystalline part of the film. The resulting lateral photocurrent (blue arrow) creates fast changing electrical dipole

pulses were impinging on the samples surface at a 30° angle to its normal, from the Si substrate or Bi layer side. It can be seen that THz pulse amplitude is ~ 4 times larger when the Bi layer is excited from the substrate side. For the case of the excitation from the Si substrate side, the Fourier spectrum of the pulses (Fig. 2b) reaches a maximum frequency of around 2.5 THz, most probably limited by the THz detector response, and has a signal-to-noise ratio of 40 dB. These numbers are lower for the spectrum corresponding photoexcitation from the Bi layer side. One has to point out that when THz pulses are monitored in the reflection direction the amplitude is higher for the excitation from layer side rather than substrate side.

Figure 3 compares THz pulse amplitudes generated by samples VS001 and VS002 when photoexcited by different wavelength optical pulses from femtosecond OPA. These THz excitation spectra were measured in the reflection geometry, the optical beam was impinging the sample's surface at θ=45° angle to its normal from the Bi film side. THz excitation spectrum of the sample VS002 measured in transmission geometry with the excitation beam impinging from the substrate side along the surface normal is shown in Fig. 3 for comparison. It can be seen that THz emission sets-on when the photon energy becomes larger than ~0.45 eV, which suggests that the energy band gap of these layers is of a similar order of magnitude. This energy is comparable to the values obtained by theoretical simulation [21]. THz generation sets on when photo-carriers are excited in other direct bandgap semiconductors [10] as well. THz pulse amplitude monotonously increases at higher photon energies. THz pulses radiated by sample VS001 grown at a higher substrate temperature have larger amplitudes.

Figure 4 shows the emitted THz pulse amplitude dependencies on the azimuthal angle φ between the optical field direction and the crystalline axes for both samples. These dependencies were measured in the transmission geometry with optical beam, with 0.91 eV photon energy, impinging on the substrate side at θ=30° (full lines) and θ=0° (dashed lines). It is evident from Fig.4 that there are two different contributions to the azimuthal angle dependences of THz signals radiated by thin Bi films: the component independent on φ and proportional to cos(3φ). The first of these components depends on the optical beam incidence angle θ, disappears when θ=0°, and changes its polarity to the opposite when the sign of θ is reversed (not shown). Azimuthal angle independent component is stronger in the sample VS001. On the other hand, the component proportional to cos(3φ), which is more clearly manifested for sample VS002, it is less dependent on the incidence angle θ and does not disappear for θ = 0°.

As it has been pointed out above, in both reflective and transmission geometries of the experiment THz pulse amplitude is higher when the pulse exits the sample from the Bi layer side. Taking into account the fact that this layer consists of two parts: polycrystalline pseudocubic part close to the Si substrate and hexagonal on top of it, one can assume that the main processes leading to THz emission are taking place in the more structurally impeccable top hexagonal Bi sublayer.

The amplitude of the isotropic component depends on the light beam incidence angle θ. It changes its sign when this angle becomes equal to - θ, and disappears for θ = 0. Such behavior is typical for the so-called photo-Dember effect, which explains THz pulse emission by a spatial separation of photoexcited electrons and holes propagating from the illuminated surface of the sample towards its bulk by diffusion [23]. However, such an effect is rather unlikely in less than 10 nm thick Bi layers - thinner than the de Broglie wavelength in the investigated material. The same could be told about the possible effect of the photocurrent surge at the Bi-Si interface depletion layer. In that case, the electric dipole could be created by the carriers entering the substrate from Bi film, however, the THz emission sets on at significantly lower photon energies than the Schottky barrier height of 0.6 eV to 0.73 eV [24, 25] at this interface.

An alternative explanation could be photoexcited lateral currents. In hexagonal crystals such currents can be excited by optical beams polarized perpendicular to the main c axis [26]. If the optical beam impinges the crystal surface along its normal, the carriers propagating to the opposite directions compensate each other's effect and total photocurrent in the lateral direction is

absent. However, this compensation disappears even after a minor deflection from the normal. In that case, a half of the carriers will move towards the flat interface of the hexagonal Bi layer with the air; their mirror-like reflections from the interface will not interrupt the lateral propagation. In contrast, the remaining carriers will be diffusively scattered at the rough interface with the polycrystalline Bi layer that will effectively interrupt their directional movement. As a result, the mutual compensation of both parts of photocurrent will disappear and a dynamically changing lateral electric dipole will be created (Fig. 5). VS001 sample has a higher isotropic component amplitude due to thicker polycrystalline layer so carrier propagation in the vicinity of two opposite surfaces is differing more.

The azimuthal angle dependent component of the radiated THz signal could be explained in terms of optical rectification or the linear photogalvanic effect also called the shift current [27, 28]. The first of these effects is more typical for thicker dielectric material samples. On the other hand, the shift current can appear in all non-centrosymmetric crystals, when the electrons are photoexcited from lower to higher energy states along the bond from one atom to the nearest lying another atom in the lattice. The buckled structure of hexagonal β-Bi [29] has no inversion center, therefore, the shift photocurrents are likely to appear in this material. The shift current and the electric dipole caused by it will appear instantaneously during the photoexcitation; its amplitude will depend only on the absorbed photon number. This explains the saturation of the anisotropic part of THz excitation spectrum that is normalized to the constant photon number at higher photon energies (see Fig. 3). The amplitude of azimuthal angle dependent component is similar in both samples, which suggests hexagonal layer is of the same quality in both samples. The shift currents have been also used by interpreting the azimuthal angle dependent THz emission from thin layers of Bi_2Te_3 [30] and ultrafast photocurrents in another topological insulator Bi_2Se_3 [7].

In summary, thin bismuth films were grown by MBE on (111) oriented silicon substrates. Their structural properties were characterized by the XRD and XRR techniques. Two approximately 8 nm thick layers grown at the substrate temperatures of 20°C and 100°C were studied. Both layers contained two structurally different parts: the polycrystalline wetting sublayer at the substrate and hexagonal sublayer on the top of it. The thickness of the latter was larger for the film grown at a lower temperature. It has been found that THz radiation pulse is predominantly generated in the top hexagonal part of the film. The THz emission sets-on when the photon energy in the optical pulse becomes larger than 0.45 eV. This is evidencing that a transition from the semimetal to semiconductor with the corresponding bandgap is taking place in the Bi film due to the quantum confinement. The dependences of THz pulse amplitude on the azimuthal angle φ between the optical field vector and the crystalline axes have both isotropic and anisotropic, proportional to cos3φ components. We suggest that the anisotropic component is caused by the shift current, and the isotropic - by the lateral photocurrents originating from different carrier propagation conditions in opposite directions.

Acknowledgments. This research was funded by a grant from the European Social Fund, Measure No. 09.3.3-LMT-K-712-01-0032.

Disclosures. The authors declare no conflicts of interest.

References

1. X. C. Zhang, D. H. Auston,, J.Appl. Phys., 71, 326–338 (1992).
2. R. Adomavičius, A. Urbanowicz, G. Molis, A. Krotkus, and E. Šatkovskis, Appl. Phys. Lett., 85, 2463 (2004).
3. T. Bartel, P. Gaal, K. Reimann, M. Woerner, and T. Elsaesser, Opt. Lett., 30, 2805 (2005).
4. Y. Chen, M. Yamaguchi, M. Wang, and X.-C. Zhang, Appl. Phys. Lett., 91, 251116 (2007).
5. Q. Jin, Y. E, K. Williams, J. Dai, and X.-C. Zhang,, Appl. Phys. Lett., 111, 071103 (2017).
6. P. A. Obraztsov, N. Kanda, K. Konishi, M. Kuwata-Gonokami, S. V. Garnov, A. N. Obraztsov, and Y. P. Svirko, Phys. Rev. B 90, 241416 (2014).
7. L. Braun, G. Mussler, A. Hruban, M. Konczykowski, T. Schumann, M. Wolf, M. Münzenberg, L. Perfetti, and T. Kampfrath, Nat. Commun., 7, 13259 (2016).
8. L. Zhang, Y. Huang, L. Zhu, Z. Yao, Q. Zhao, W. Du, Y. He, and X. Xu, Adv. Optical Mater. 7, 1801314 (2019).
9. "Terahertz Spectroscopy: Principles and Applications", Edited by Susan L. Dexheimer, CRC Press (2008).
10. A. Arlauskas and A. Krotkus, Semicond. Sci. Technol., 27, 115015 (2012).
11. V. Karpus, R. Norkus, R. Butkutė, S. Stanionytė, B. Čechavičius, and A. Krotkus, Optics Express, 26, 33807 (2018).
12. Y. F.Ogrin, V. N. Lutskii, M. I. Elinso, JETP Lett., 3, 71 (1966).
13. J. Heremans, C. M. Thrush, Yu-Ming Lin, S. Cronin, Z. Zhang, M. S. Dresselhaus, and J. F. Mansfield, Phys. Rev. B, 61, 2921 (2000).
14. R. Butkutė, G. Niaura, E. Pozingytė, B. Čechavičius, A. Selskis, M. Skapas, V. Karpus, and A. Krotkus, Nanoscale Research Letters, 12, 436 (2017).
15. Y. Ma, Y. Dai, L. Kou, T. Frauenheim, and .T Heine, Nano Letters, 15, 1083 (2015).
16. M Wada, S Murakami, F Freimuth, G Bihlmayer, Phys. Rev. B, 83, 121310 (2011).
17. I. E. Ilyakov, B. V. Shishkin, D. A. Fadeev, I. V. Oladyshkin, V. V. Chernov, A. I. Okhapkin, P. A. Yunin, V. A. Mironov, and R. A. Akhmedzhanov, Opt. Lett., 41, 4289 (2016).
18. Y. Hirai, N. Yoshikawa, H. Hirose, M. Kawaguchi, M. Hayashi, and R. Shimano, Phys. Rev. Appl., 14, 064015 (2020).
19. H. Hirayama, Advances in Physics: X, 6:1 (2021)
20. T. Shirasawa, M. Ohyama, W. Voegeli, and T. Takahashi, Phys. Rev. B, 84, 0754 (2011).
21. S. Xiao, D. Wei, and X. Jin, Phys. Rev. Lett. 109, 166805 (2012).
22. Gates-Rector, S.; Blanton, T. Powder Diffr., 34 (4), 352–360 (2019)
23. T. Dekorsy, H. Auer, H. J. Bakker, H.G. Roskos, and H. Kurz, Phys. Rev. B, Condens. 53, 4005 (1996)
24. A. Bannani, C. Bobisch, R. Möller, Science, 315, 1824 (2007).
25. K. Hricovini, G. Le Lay, A. Kahn, and J.E. Bonnet, Appl. Surf. Sc., 56-58, 259 (1992).
26. P. Tronc, Yu. E. Kitaev, G. Wang, M. F. Limonov, A. G. Panfilov, and G. Neu, phys. stat. sol. (b), 216, 599 (1999).
27. J. E. Sipe and A. I. Shkrebtii", Phys. Rev. B, 61, 5337 (2000).
28. N. Laman, M. Bieler, and H. M. van Driel, , J. Appl. Phys., 98, 103507 (2005).
29. S. Zhang, S. Guo, Z. Chen, Y. Wang, H. Gao, J. Gomez-Herrero, P. Ares, F. Zamora, Z. Zhu, and H. Zeng, Chem. Soc. Rev., 47, 982 (2018).
30. H. Zhao, X. Chen, C. Ouyang, H. Wang , D. Kong, P. Yang, B. Zhang, C. Wang, G. Wei, T. Nie, W. Zhao, J. Miao, Y. Li, L. Wang, and X. Wu, Advanced Photonics, 2, 066003 (2020).

NOTES

Vilniaus universiteto leidykla
Saulėtekio al. 9, III rūmai, LT-10222 Vilnius
El. p. info@leidykla.vu.lt, www.leidykla.vu.lt
bookshop.vu.lt, journals.vu.lt
Tiražas 20 egz.